

**Combinatorial Low-Binding Affinity
Polymersomes for Targeting Dendritic Cells:
Towards Cancer Vaccine Development**

Chiara Cursi

Supervisor: Prof Giuseppe Battaglia

Thesis submitted for the degree of Doctor of Philosophy

University College London

Faculty of Mathematics and Physical Sciences

Department of Chemistry

2023

To Giorgia,

so that you can always believe in your dreams.

'Nothing in life is to be feared, only to be understood'

(Marie Salomea Skłodowska- Curie)

Declaration of Authorship

I, Chiara Cursi, hereby declare that the work presented in this thesis is my own. Where information has been derived from other sources, I confirm that this has been indicated in the thesis.

Chiara Cursi
University College London
Department of Chemistry
London, UK

Acknowledgements

One of the most wonderful things in science is its collaborative nature and there are many people without whom this thesis would not have been possible.

Firstly, I want to express my gratitude to my supervisor Prof Giuseppe Battaglia for accepting me and welcoming in his group as his PhD student and for the constant and precious supervision throughout the years. I would like to also thank my industrial supervisor Dr Carl Webster for his guidance and supervision during these years and for offering me all the help, support and trainings from AstraZeneca. Dr Aidan Riley, collaborator at the AstraZeneca R&D department, for his mentorship and training in the lab, especially during first years of my training. I want to express my gratitude also to Dr Pablo Scodeller, for providing the mUNO peptide used in this work. I thank my sponsors, AstraZeneca and Engineering Physical Science Research Council (EPSRC) for funding this project.

I also want to thank everyone in the Battaglia's group for their help when it was most needed. For the *in vivo* experiments, I want to thank Dr Matias and Miss Ibarzo for their contribution. For the help with the TEM, Dr Forth and Mr Ing. For the molecular modelling, Prof Battaglia and Dr Gutierrez. For the polymer synthesis, Dr Duro Castano and Dr Deng. I owe a great deal to Dr Matias, Dr Leite, Dr Rizzello and Dr Scarpa for their supervision in the lab, teachings, guidance, support and encouragement. Thank you, people of G17 and 460 labs. You know who you are and how much I love you. You became friends. You made the lab a great place where to be, even in the darkest times. Barbs, Vale, Belen, Miko, Melis, Safa, Azzu, Gab, Ce', Carlos, Virgy, and The Diana's. You all have a special place in my heart and memories. Holly, you have been the constant rock of my everyday life and took care of me when I most needed, thank you. I am extremely grateful to my family and friends. To my mum Simonetta, for always being there, giving me the strength to pursue my dreams. My brother Lamberto, my sister-in-law Diletta and my beautiful niece Giorgia. Thank you to my best friends in the world Angela, Marina and Erica, you are the big deal. Barbs, we did it. Never Again.

COVID19 Impact Statement

The following research project, like many others, has been deeply affected by three UK national lockdowns enforced between 2020 and 2021. Furthermore, shipments and deliveries of goods and reagents were delayed due to new border controls enforcement following the UK leaving the EU.

During those unprecedented times, access to laboratories and other facilities across the UCL campus was denied to everyone but COVID-related personnel. I took alternative steps to mitigate the impact COVID restrictions had on the project, such as learning computational skills and writing a scientific literature review. Moreover, during first national lockdown, I voluntarily joined the COVID Force-Task Team instituted by Prof Giuseppe Battaglia, for the encapsulation of anti-viral drugs for the active targeting of the ACE2 receptor in lung cellular model. I personally contributed to the project with experiments involving use of cell lines and nanoparticle cytotoxicity characterisation. I was involved in this line of work until June 2021 and it was not possible to work on any thesis-related experiments during this time.

During second and third national UK lockdowns (January-April 2021), the UCL Chemistry Department enforced a cohort system of access to laboratories and other facilities to guarantee social distancing. Furthermore, all 1:1 training (e.g., animal procedures, flow cytometry trainings, etc.) were suspended until October 2021 to respect social distancing.

The sudden increased demand of personal protection equipment (PPE) and sterile single-use plastic (pipette tips, tissue culture flasks, etc) by hospitals and research labs involving work with Sars-CoV-2, resulted in a general difficulty to access sterile plastics, a problem shared across many research labs in Europe. For these exceptional circumstances, it was granted a funded extension of 6 months to finalise the last few experiments for this project. The national lockdowns, the cohort system and Brexit-related delays contributes to a substantial backlog of experiments and trainings which unfortunately was not possible to fully recover.

Abstract

Conventional DNA cancer vaccines fail to adequately stimulate the adaptive immune system and to establish proper immunisation. This is reflected in clinical practice, where only a handful of them have been approved by the FDA. Within this project the use of the pH-sensitive polymer Poly (2-(methacryloyloxyethyl phosphorylcholine)-poly(2-(diisopropylamino-ethyl methacrylate) (PMPC-PDPA) has been investigated for DNA antigen encapsulation and intracellular delivery. By implementing a dendritic cellular model (DC2.4), it was demonstrated the expression and surface presentation of the antigen model (SIINFEKL). Furthermore, exploratory experiments highlighted the inflammatory power of the immunomodulator cyclic guanosine monophosphate–adenosine monophosphate (cGAMP) in *in vitro* settings, with potential implications for *in vivo* cancer vaccines.

Moreover, current strategies of design for active targeting nanoparticles (NPs) are suboptimal and characterised by off-target binding and side effects. In this work, it was demonstrated a paradigm shift in the design of active targeting nanoparticles based on the concepts of the ‘range selectivity’ theory. Specific Ligands for the phenotypic targeting of dendritic cells (DCs) were selected (PMPC, mUNO and PEP4) and conjugated to the respective polymer, such as PMPC-PDPA or polyethylene glycol-poly (lactic acid) (PEG- PLA). Multivalent and multiplexing POs were prepared and tested *in vitro*, proving experimentally the validity of computational hypotheses. Multivalent and combinatorial POs were also intradermally injected into animal models to further corroborate *in vitro* experimental evidence. It was envisioned that the implementation of empirical observation combined with *in silico* simulation would help to define the optimal range of the number of ligands on a vesicle for the phenotypic targeting of DCs, ultimately improving the intracellular co-delivery of antigen and adjuvant for the development of a cancer vaccine.

Impact Statement

Cancer, a disease defined by the uncontrolled division of aberrant cells in the body, is one of the leading causes of mortality worldwide, accounting for around 13 million deaths each year. There are more than 200 distinct forms of cancer, each defined by its location and cell type of origin. Breast cancer, melanoma, colon and cervical cancer are the most common types of cancer diagnosed in adults aged 25-49 years old. This disease, along with cardiovascular and Alzheimer's disease, has possibly the most significant impact on society. Each year, approximately 250,000 people in England are diagnosed with cancer, and over 130,000 people die from it. The annual cost of cancer services to the NHS is £5 billion, but the total cost to society is £18.3 billion [1].

Scientists worldwide are focused on unravelling mechanisms underlying the failure of certain treatments in the hope of providing answers to hundreds of unsolved problems. In just a decade, we assisted in the approval of many clinical trials and the commercialisation of immunotherapy drugs in combination with chemotherapy and radiotherapy treatments, providing a better outcome for patients. Nevertheless, some types of tumours do not respond to these therapies. Hence, a further investigation on the intracellular mechanisms behind these results is necessary.

In parallel, scientists are working on optimising existing treatments, reducing side effects and increasing their effectiveness. It is in this space that the following research project finds the opportunity to give its contribution. With the phenotypic targeting of immune cells by multiplex low-binding affinity polymersomes, it is anticipated to improve the effectiveness of therapeutic cancer vaccines by overcoming the present limitations of antigen and adjuvant co-delivery.

List of Contents

ACKNOWLEDGEMENTS	3
COVID19 IMPACT STATEMENT	4
ABSTRACT	5
IMPACT STATEMENT	6
LIST OF CONTENTS.....	7
LIST OF ABBREVIATION.....	10
GLOSSARY	14
LIST OF FIGURES	17
LIST OF TABLES	20
LIST OF SUPPLEMENT FIGURES	21
1 INTRODUCTION.....	22
2 THE IMMUNE SYSTEM.....	24
2.1 INNATE IMMUNE RESPONSE.....	25
2.1.1 Intracellular Inflammatory Response.....	25
2.1.2 Molecular Defence	26
2.1.3 Cellular Defence.....	28
2.1.3.1 DCs.....	29
2.1.4 Adaptive Immune Response.....	31
2.2 CANCER IMMUNO-EDITING.....	32
2.3 CANCER IMMUNOTHERAPIES.....	35
2.3.1 Therapeutic Cancer Vaccines.....	36
2.3.1.1 DNA Delivery for Cancer Vaccines.....	39
2.3.1.2 STING Agonists.....	41
2.4 NANOMEDICINE	43
2.4.1 Polymersomes.....	43
2.4.2 Supramolecular Forces in Self-Assembly.....	45
2.4.3 The Diblock Copolymers: Structure and Properties.....	47
2.4.3.1 PMPC-PDPA Diblock Copolymer	48
2.4.3.2 PEG-PLA Diblock Copolymer.....	51
2.5 NEW PERSPECTIVE FOR THE ACTIVE TARGETING	53
2.5.1 Superselectivity Theory	56
2.5.2 Macromolecular Crowding and Steric Hindrance.....	58

2.5.3	<i>Multiplexing Polymersomes</i>	60
2.5.4	<i>Range Selectivity</i>	61
2.5.5	<i>Targeting Skin APCs</i>	64
2.5.5.1	Langerin Receptor	65
2.5.5.2	Mannose Receptor	66
2.5.5.3	Scavenger Receptors (SRs) Family	66
3	HYPOTHESIS AND AIMS	69
4	MATERIALS AND METHODS	72
4.1	POLYMERSOMES PREPARATION AND CHARACTERISATION	72
4.1.1	<i>pH Switch and DNA Encapsulation</i>	72
4.1.2	<i>Solvent Switch</i>	73
4.1.2.1	cGAMP Encapsulation	73
4.1.3	<i>Solvent Displacement</i>	74
4.1.4	<i>Purification of Polymersomes</i>	75
4.1.5	<i>Polymersomes Characterisation</i>	75
4.1.5.1	Dynamic Light Scattering (DLS).....	75
4.1.5.2	Transmission Electron Microscopy (TEM)	78
4.1.5.3	Reverse Phase- High Performance Liquid Chromatography (RP- HPCL).....	78
4.1.6	<i>Encapsulant Quantification and Loading Efficiency</i>	80
4.1.6.1	Calculation of Number of Ligands.....	83
4.2	PHAGE DISPLAY	85
4.2.1	<i>Cloning, Transfection and Expression of CD207 Receptors</i>	85
4.2.2	<i>Phage Display for CD207-Targeting Ligands</i>	89
4.3	CYCLE-ADDITION OF LIGANDS TO PEG-PLA	93
4.3.1	<i>Quantifying Peptide-Conjugation</i>	95
4.4	EXPERIMENTS <i>IN VITRO</i>	96
4.4.1	<i>Cell Culture Maintenance</i>	96
4.4.2	<i>Cell Viability</i>	97
4.4.3	<i>Transfection Experiments</i>	99
4.4.4	<i>Flow Cytometry</i>	100
4.4.5	<i>Laser Scanning Confocal Microscopy (LSCM) Imaging</i>	104
4.4.6	<i>Enzyme-Linked Immuno-Staining Assays (ELISA)</i>	105
4.4.7	<i>Caspase 3/7 Apoptosis Assays</i>	106
4.4.8	<i>Western Blot</i>	106
4.4.9	<i>Lectin staining</i>	108
4.4.10	<i>In Vitro Binding Assay</i>	108
4.5	<i>IN VIVO</i> EXPERIMENTS	109
4.5.1	<i>cGAMP Delivery In Vivo</i>	109

4.5.2	<i>Intradermal Injection of Combinatorial POs In Vivo</i>	110
4.6	STATISTICAL ANALYSIS	112
5	DNA ENCAPSULATION AND DELIVERY	113
5.1	INTRODUCTION AND AIMS	113
5.2	RESULTS AND DISCUSSION.....	115
5.2.1	<i>Self-assembly of pH-Sensitive Polymersomes and DNA Encapsulation</i>	115
5.2.2	<i>Biosafety Profile of Polymersomes in Cells in vitro</i>	119
5.2.3	<i>GFP Expression and SIINFEKL Presentation in Cells</i>	120
5.3	SUPPLEMENT MATERIAL	124
6	cGAMP ENCAPSULATION AND DELIVERY	126
6.1	INTRODUCTION AND AIMS	126
6.2	RESULTS AND DISCUSSION.....	129
6.2.1	<i>Polymersomes Preparation and cGAMP Encapsulation</i>	129
6.2.2	<i>Inflammatory Effect of cGAMP-loaded Polymersomes in vitro</i>	133
6.2.3	<i>Pro-inflammatory Behaviour Induced by cGAMP-POs in DC2.4 and B16F10-OVA Cells</i>	136
6.2.4	<i>Effect of cGAMP-Polymersomes in Cell Death</i>	138
6.2.5	<i>cGAMP Delivery In Vivo</i>	140
6.3	SUPPLEMENT MATERIAL	142
7	PHENOTYPIC TARGETING OF DCS.....	144
7.1	INTRODUCTION AND AIMS	144
7.2	RESULTS AND DISCUSSION.....	146
7.2.1	<i>Protein Expression of Surface Receptors</i>	146
7.2.2	<i>Screening and Validation of DC207-targeting Ligands</i>	149
7.2.3	<i>Binding with PMPC-Ligand</i>	152
7.2.4	<i>Binding with PEP4 and mUNO-Ligands</i>	158
7.2.5	<i>Binding Assay with Combinatorial POs</i>	163
7.2.6	<i>Intradermal Injection In Vivo</i>	166
7.3	SUPPLEMENT MATERIAL	173
8	FINAL REMARKS AND FUTURE DIRECTIONS.....	186
	BIBLIOGRAPHY	199

List of Abbreviation

ACT	Adoptive Cell Therapies
ADCC	Antibody-Dependent Cellular Cytotoxicity
APC	Antigen Presenting Cells
BCA	Bicinchoninic Acid
BECs	Brain Endothelia Cells
CAC	Critical Aggregation Concentration
CAR T cell	Chimeric Antigen Receptor T cells
CASP	Collected Solution After Purification
CD	Cluster of differentiation
cDCs	circulating DC progenitors
CDN	Cyclic Dinucleotides
CDPs	Common DC progenitors
cGAMP	Cyclic guanosine monophosphate-adenosine monophosphate
cGAS	Cyclic guanosine-adenosine synthase
CHO	Chinese hamster ovary
CTL	Cytotoxic T lymphocyte
CTLA-4	Cytotoxic T-lymphocyte associated protein 4
CTLD	Carbohydrate-binding C-type lectin domain
CMFs	Common myeloid progenitors
DC	Dendritic Cell
DMSO	Dimethyl sulfoxide
DMF	Dimethylformamide
DMXAA	5,6-dimethyl- xanthenone-4-acetic acid
ELISA	Enzyme-Linked Immuno-Staining Assays
Fc	Fragment Crystallizable
GFP	Green Fluorescent Protein
GM-CSF	Granulocyte-macrophage CSF
GMPs	granulocyte macrophage progenitors

HLA	Human Leukocyte Antigen
HSCs	Hematopoietic stem cells
huCD207	Human CD207
ICI	Immune Checkpoint Inhibitors
IDO	Indoleamine 2,3-dioxygenase
Ig	Immunoglobulin
IFN	Interferon
IFNR	type I IFN receptor
IL	Interleukin
irAEs	Immune-related Adverse Events
IRES	Internal Ribosome Entry Sequence
ISGs	Interferon-stimulated genes
i.v.	Intravenous
LAG-3	Lymphocyte Activation Gene-3
LC	Langerhans cells
LDL	Low-density lipoprotein
l.n.	Lymph node
LRP1	LDL Receptor Related Protein 1
LPS	Lipopolysaccharide
MDPs	macrophage DC progenitors
MPS	Mononuclear Phagocyte System
MTT	3-(4,5-dimethyl-2-thiazolyl)-2,5-diphenyl-2H-tetrazoliumbromide
moCD207	Mouse CD207
MNAs	Micro-Needles Arrays
NAD	Nicotinamide adenine dinucleotide
NK	Natural Killer
NLRP3	NOD-like receptor family, pyrin domain-containing-3
NLT	Nonlymphoid tissue
NP	Nanoparticle
OVA	Ovalbumin

PAGE	Polyacrylamide gel electrophoresis
PAMPs	Pathogen-Associated Molecular Patterns
PBAE	poly(beta-amino ester)
PC	Phosphorylcholine
pDCs	plasmacytoid DCs
PDI	Polydispersity Index
pDNA	Plasmid DNA
PDPA	Poly(2- (diisopropylamino)ethyl methacrylate)
PE	Production Efficiency
PEG	poly(ethylene glycol)
PEG-DBP	poly(ethylene glycol)-block-[(2-(diethylamino)ethyl methacrylate)-co-(butyl methacrylate)-co-(pyridyl disulfide ethyl methacrylate)]
PEI	polyethylenimine
PMPC	Poly(2-methacryloyloxyethyl phosphorylcholine)
POs	Polymersomes
PRRs	Pattern Recognition Receptors
PTA	Phosphotungstic Acid
Rho	Rhodamine B
RES	Reticuloendothelial System
RT	Room temperature
RP-HPLC	Reverse Phase- High Performance Liquid Chromatography
SDS	Sodium dodecyl sulphate
SFKL	SIINFEKL peptide
SRs	Scavenger Receptors
SR-B1	Scavenger receptor type B1
TAA	Tumour Associated Antigens
TCR	T cell receptor
TILs	Tumour infiltrating lymphocytes
TME	Tumour Microenvironment
TNF	Tumour Necrosis Factor
TFA	Trifluoroacetic acid

Tg	Glass transition temperature
THF	Tetrahydrofuran

Glossary

Abscopal Effect	Hypothesis describing the reduction or elimination of lesions in areas of the body not directly targeted by local treatment (e.g., radiotherapy).
Adaptive Immunity	Generally composed by B and T lymphocyte cells which specifically recognise non-self antigens. Major part of the adaptive immune response is mediated by antibodies released by B cells, helper CD4 T cell and cytotoxic CD8 T cell.
Aliphatic polyester	Carbon atoms in an open chain
Amorphous polymer	Polymers that have randomly packed molecules with no crystalline regions.
Antigen	Virtually any molecule capable to stimulate the immune response
APC	APCs are specialised in presenting antigens on their exterior surface to initiate the adaptive immune response resulting in a specific immunisation.
Cold Tumour	Describes a tumour that is unlikely to generate a significant immune response. Cold tumours are typically surrounded by cells that dampen the immune response and prevent T cells from attacking and destroying the tumour cells. Typically, immunotherapy is not effective.
Colloidal Solution	Colloidal solutions, or colloidal suspensions, are a mixture of small material that are evenly suspended in a fluid.
CpG motif	The innate immune system can discriminate bacteria DNA from vertebrate DNA by detecting unmethylated CpG dinucleotides motif the DNA sequence. These CpG motifs act as PAMPs and are detected by TLR9, which belongs to the PRRs family, to initiate the innate immune response.
CAC	In colloid chemistry, it is the lowest concentration of which amphiphilic molecules start to self-assemble in a particle
CTL	Generally referred as effector CD8+ T Cells with cytotoxic functions using perforins or apoptosis via Fas ligand pathway
C-type Lectin Receptor	Important PRRs family receptor (e.g., CD206, Clec9A, DEC205, DC-SIGN, CD207, etc) expressed on DCs and macrophages for initiating the inflammation. Most of these receptors bind carbohydrates moieties of the pathogen in a calcium-dependent manner.

DAMPs	Endogenous molecules released by infected, damaged or dying cells and trigger a type I IFN response. Examples are heat shock proteins, ATP, ADP, adenosine and DNA.
Epitopes	Molecular portion of the antigen to which the antibody bind
<i>Ex vivo</i>	(latin: 'out if the living') refers to experiments conducted on tissue/organ/ cell outside the original organism (eg., skin biopsies).
GFP	Fluorescent protein extensively used as gene reporter model in transfection experiments.
Glass transition temperature	It is defined as the temperature at which amorphous or semi-amorphous polymers transition from glassy to viscous state.
HLA class I and II	Human MHC molecules involved in self- non-self-recognition and are clinically important as transplantation antigens. HLA class I are expressed on the surface of almost nucleated cells, while HLA class II are expressed only on APCs, B and T cells.
Hot Tumour	A tumour that is likely to provoke a robust immune response and immunotherapy is typically effective against hot tumours.
Immuno-proteasome	Highly efficient proteolytic multi-protein complex for protein degradation and abundantly expressed in immune cells.
Innate Immunity	Quick but unspecific immunological response to a pathogen activated by pre-existing defences, such as mucosal barriers, proteins of the complements and cellular phagocytosis.
IRES	This sequence allows the entry of a ribosome for the translation of a second gene reporter along the same mRNA transcript thus allowing the expression of two different proteins simultaneously under the control of the same promoter.
Log P	The Partition Coefficient (P) represent the ratio of concentrations of a biomacromolecule in a liquid biphasic (e.g., octanol/water). It predicts encapsulation, toxicity and drug clearance.
LPS	Lipopolysaccharide present on the membrane of Gram-negative bacteria (i.e., E.Coli)
MHC I and II	Major histocompatibility complex (MHC I) is presented on nucleated cells and are recognized by cytotoxic CD8+ T cells. The presentation of MHCII by APC, activate CD4+ T cells, leading to the coordination and regulation of effector cells. In either case, it is a clonotypic T cell receptor that interacts with

	a given MHC complex, potentially leading to sustained cell:cell contact formation and T cell activation.
Neoantigen	Mutated form of proteins expressed by cancer cells as results of mutation occurred in the DNA.
NKT cells	NKT cells. Heterogenous sub-group of T cells that express semi-invariant T cell receptor along with NK cells.
Opsonisation	Immune process by which a pathogen is marked for phagocytosis upon recognition by antibodies.
Ovalbumin	Main protein found in egg white (up to 55% of total protein) and conveniently used for a variety of uses in laboratory.
PAMPs	Small molecular structures or motif highly conserved in pathogens (e.g., virus and bacteria) which are used by the host cell to uniquely identify an exogenous invasion. Examples are LPS,
Perforin	Component of cytolytic granules that participates in the permeabilization of plasma membranes, allowing granzymes and other cytotoxic components to enter target cells
RES	Also associated with the mononuclear phagocyte system (MPS). It refers to a system of cells (e.g., macrophages, scavenger endothelial cells) specialised in effectively clear the circulatory system from debris and other material
SIINFEKL	Small antigen derived from the immunoproteasome degradation of ovalbumin protein. Represent one of the most popular peptides utilised for antigen presentation in inflammatory study <i>in vitro</i> and <i>in vivo</i>
Steric Hindrance	Steric hindrance is the overall steric repulsion caused by steric bulk between intramolecular contacts, with the final result of decreasing the energy of binding
TAA's	Proteins highly expressed by tumour cells, but also expressed at lower level by healthy cells.
Thermoplastic polymer	Mouldable polymer material at a certain elevated temperature and solidifies upon cooling.
TILs	Immune cells found in the tumour biopsy of a patient can be used for ACT therapy in co-administration with IL-2 cytokine or CTLA-4, for example. TILs are also associated with better outcomes.

List of Figures

Figure 1: cGAS-STING DNA sensing and pathway of inflammation.....	26
Figure 2: Immune cells of the innate and adaptive immune system.	29
Figure 3: Antigen Processing and Presentation in DCs.	31
Figure 4: The Immuno-editing Process. Image created using Biorender.	34
Figure 5: Different strategies for cancer immunotherapy.	36
Figure 6: Cancer-Immunity Cycle.....	37
Figure 7: Representative Figure of a Polymersome.....	45
Figure 8: Electrostatic interaction and predicted geometry of self-assembly.	47
Figure 9: PMPC-PDPA Structure and Self-assembly.....	50
Figure 10: POs Cellular Entry.....	51
Figure 11: Chemical structure of PEG ₄₅ PLA ₁₁₃ used in this work.	52
Figure 12: Schematic Representation of the Degeneracy Factor (Ω).	55
Figure 13: Principles of the STT.....	58
Figure 14: Macromolecular Crowding in the Extracellular Environment.....	59
Figure 15: Schematic Representation of the Steric Hindrance between the POs and the glycocalyx on the surface of a cell membrane. Image edited from [221].	60
Figure 16: Achieving the Superselectivity with Multiplex Multivalent NPs. Image taken from [221].	61
Figure 17: Achieving the Phenotypic Targeting with the Range Selectivity method.	63
Figure 18: Molecular Modelling of Surface Receptors for phenotypic targeting of DCs.....	68
Figure 19: Graphic Abstract of Main Research Hypothesis of this Project.....	71
Figure 20: Set-up for pH switch self-assembly method.....	72
Figure 21: Schematic representation of solvent switch method for POs preparation.....	73
Figure 22: Chemical Structure and Properties of cGAMP. Source PubChem.	74
Figure 23: Examples of correlograms from a sample containing large samples (left) and a sample containing smaller vesicles (right).....	77
Figure 24: PMPC-PDPA Chromatogram at RP-HPLC (220nm).....	79
Figure 25: Schematic representation of a transversal section of POs.	82
Figure 26: representative cartoon of unimers arranged in the hydrophobic interface membrane.	85
Figure 27: Representative structure of plasmid pDEST for expression of huCD207 and moCD207 CTL domain.....	87

Figure 28: Cartoon representing the phage display method.	91
Figure 29: chemical structure of azide-PEG-PLA used for click-chemistry.	94
Figure 30: Copper-catalysed cyclo-addition. [270]	95
Figure 31: Standard curves obtained by BCA method for the peptide-conjugation quantification for PEP4-PEG-PLA and mUNO-PEG-PLA polymers, respectively.	96
Figure 32: Chemical reaction of MTT to Formazan by mitochondrial reductase activity.	98
Figure 33: Chemical Structure and Properties of RU.521. (Source PubChem).	100
Figure 34: Representation of the gating strategy for GFP and SIINFEKL detection in DC2.4.	102
Figure 35: Gating Strategy for Skin and Lymph Node Samples.	103
Figure 36: Representative cartoon of the <i>in vitro</i> binding assay	109
Figure 37: Experiment Layout for Tumour Survival Experiment in C57Bl6 mice.	110
Figure 38: Graphical abstract.	114
Figure 39: Characterisation of empty and pDNA-SFKL encapsulated POs.	116
Figure 40: Loading Efficiency of pDNA-SFKL in PMPC-PDPA POs.	118
Figure 41: MTT assay for empty and pDNA-loaded PMPC-PDPA POs on DC2.4 and HEK293T.	120
Figure 42: GFP and SIINFEKL Expression Analysis.	123
Figure 43: Graphical abstract.	128
Figure 44: Quality analysis of cGAMP-loaded POs.	130
Figure 45: Loading Efficiency (L.E.) of cGAMP in PMPC-PDPA Polymersomes.	132
Figure 46: MTT Assay in DC2.4 and B16F10-OVA cells.	134
Figure 47: Single-dose MTT Assay in DC2.4 and B16F10-OVA cells.	136
Figure 48: Cytokines Quantification from DC2.4 and B16F10-OVA supernatant.	137
Figure 49: Cell Apoptosis in DC2.4 and B16F10-OVA.	139
Figure 50: cGAMP-POs delivery in B16F10-OVA tumour bearing mice.	141
Figure 51: Graphical Abstract.	145
Figure 52: Receptors expression in different cell lines validated by WB assay.	146
Figure 53: Confocal imaging of surface receptors in cell lines.	148
Figure 54: Staining of the cellular surface glycocalyx.	149
Figure 55: Sequences of DCs- targeting peptides.	150
Figure 56: ELISA test for validating synthetic peptides interacting with huCD207 and moCD207.	150

Figure 57: EC50 ELISA for the human CD207 receptor with respective EC50 values for each peptide.....	152
Figure 58: Cellular uptake in DC2.4 cells by confocal microscopy.....	155
Figure 59: Contour map of multi-time point binding assay with multivalent PMPC-ligand POs.	156
Figure 60: Binding assays using PMPC, PEP4 or mUNO ligands in multivalent POs.	161
Figure 61: Binding assay of combinatorial POs <i>in vitro</i>	165
Figure 62: Results from flow cytometry analysis upon i.d. injection from samples derived from skin biopsies (top graph) and I.n. (bottom graph).....	170
Figure 63: Analysis of fluorescent signal in the serum upon i.d. injection after 1,2 or 4h..	171
Figure 64: Organ biodistribution for each formulation after 1, 2 or 4 hours from time of i.d. injection.	172
Figure 65: Conceptual model of peptides embedded within the polymer-brush.	196

List of Tables

Table 1: Abbreviations and definitions for the Stokes-Einstein equation.	76
Table 2: Abbreviation and definition used to calculate the Loading Efficiency.....	83
Table 3: Initial concentrations of treatments for the serial dilution MTT assay in DC2.4 and B16F10-OVA.	98
Table 4: Final concentrations of treatments used for the single concentration MTT assay, cytokine quantification and Caspase 3/7 assay.	99
Table 5: List of Antibody and Markers used in Flow Cytometry for analysis of <i>ex vivo</i> biopsies upon i.d. injection.	103
Table 6: List of Antibodies used for Confocal Imaging.	105
Table 7: List of Primary and Secondary Antibodies Used for WB.	107
Table 8: Ingredient List for Preparing the Digestion Cocktail Mix.....	111
Table 9: Polymer %Molar mass in *PMPC-PEG-PDPA formulations prepared by solvent switch for the binding experiment.....	154
Table 10: Schematic representation (figure) and polymer molar percentage (table) of each componen for the self-assembly of PEG-PLA POs used in binding assay experiments...	159
Table 11: Polymer mix for preparation of combinatorial POs for <i>in vitro</i> binding assay....	164
Table 12: Polymer mixes for <i>in vivo</i> experiment.....	167

List of Supplement Figures

S 1: Schematic representation of pDNA-SIINFEKL (SFKL).....	124
S 2: PMPC-PDPA effect in cell viability in different cell lines by MTT assay.....	124
S 3: Positive controls for transfection.....	125
S 4: cGAMP Chromatogram at RP-HPLC.....	142
S 5: RP-HPLC Chromatogram of analysis of cGAMP:PMPC-PDPA formulation.....	142
S 6: Comparison Analysis of Empty PMPC-PDPA before and after electroporation.	143
S 7: EC50 of cGAMP:PMPC-PDPA formulation.	143
S 8: WB to confirm successfull expression and release in CHO supernant of huCD207 and moCD207.	173
S 9: Homology prediction between huCD207 and moCD207.	173
S 10: DLS (left) and TEM (right) analysis of *PMPC-PEG-PDPA POs.	174
S 11: DLS (left) and TEM (right) analysis of *PEP4-PEG-PLA POs.	175
S 12: DLS (left) and TEM (right) analysis of *mUNO-PEG-PLA POs.....	176
S 13: DLS (top) and TEM (bottom) analysis of combinatorial POs for <i>in vitro</i> binding assay.	177
S 14: DLS (left) and TEM (right) analysis of POs batch for <i>in vivo</i> i.d. injection.....	178
S 15: Heatmap of Binding for the *PMPC-PEG-PDPA batch formulation on cell models.	179
S 16: Heatmap of Binding for *PMPC , *PEP4 and *mUNO ligands on the three cell lines.	180
S 17: Combinatorial Formulation binding Heapmap.....	181
S 18: Gating for Cy5.5 + and CD45- cells.	182
S 19:Gating for Cy5.5+ and CD45+ cells, representative of gating strategy for analysis of samples after 1h from time of injection.....	183
S 20: Cy5.5+ cells indicating PO internalisation gated for CD207+ receptor expression..	184
S 21: Cy5.5+ cells indicting internalisation of POs gated for CD206+ receptor expression. Cells were collected after 1h from i.d. injection.	185

1 Introduction

Despite tremendous medical advances, cancer continues to be one of the top causes of mortality worldwide, accounting for more than 8 million deaths each year [2].

Cancer represents a group of more than 200 distinct illnesses classified according to severity, localisation and etiological origin; heterogeneity exists both within the tumour mass and across metastases, which has substantial consequences for drug therapy application [3], [4].

When the illness is detected early and is placed in an easily accessible location, surgery is the preferred method of eradicating the neoplasia more efficiently; it remains the best option for cancer patients in terms of safety and result. Typically, surgical excision of a tumour is followed by combinatorial rounds of chemotherapy and radiation, the other two primary therapeutic options [5]. However, in the instance of a blood or lymphatic system tumour, such as leukaemia or lymphoma, or in the case of metastatic tumours that have spread and invaded other organs and tissues, surgery is no longer an option. Chemotherapy and radiation remain the sole treatments for minimising disease severity and optimising tumour control [5]. Unfortunately, both radiation and chemotherapy have harmful effects that extend beyond the malignant cells themselves. This is the primary constraint on these medicines, since they have significant adverse effects on patients, crippling their already vulnerable health [6].

Scientists have been able to illuminate several points of intervention thanks to the growing understanding of the field. It is known that cancer cells thrive in the body host by hiding from the immune system and new treatment strategies, such as immunotherapies, are increasingly being developed and implemented [7].

The vertebrate immune system is characterised by a sophisticated network of cells and proteins that have developed to recognise and eliminate infections and cancer cells as potential threats for the host [8]. The immune system is divided into two distinct branches: innate and adaptive responses, which differ in terms of specificity, activation time, and response components. The role of the immune

system in the progression and regression of cancer has been intensively studied and discussed in the last couple of decades [9]. During the process known as cancer immuno-editing, the immune system unwillingly selects the fittest cancer clone to survive in the tumour microenvironment (TME) [9], [10].

Immunotherapies take a novel approach to cancer treatment by reawakening the body's immune system against the tumour, fighting, and eliminating it from inside. Several types of immunotherapies can be used to treat cancer, each with its own set of advantages and disadvantages, which must be considered for each type of cancer and patient.

Among all existing cancer immunotherapies, therapeutic cancer vaccines are the most promising since they are the only ones that give lifelong immune protection against a particular tumour with few adverse effects [11].

At the central core of these treatments is the activation of dendritic cells (DCs). DCs ingest and display tumor-associated proteins externally, consequently triggering inflammation and eradicating the tumour.

For the development and clinical use of therapeutic cancer vaccines, several protocols for antigen loading into DCs have been developed, either *ex vivo* (outside the body) or *in vivo* (within the body) procedures [11]. Both systems have drawbacks that can be solved by developing a unique platform for drug delivery based on biocompatible nanoparticles such as polymersomes.

Polymersomes are nanoparticle-sized vesicles made of amphiphilic polymers that serve as an effective drug delivery platform. The surface can be functionalized with specific ligands for precise cell or tissue targeting.

Active targeting is often accomplished by high-affinity protein-ligand interactions, but with a significant risk of off-target binding risk and consequent loss of material.

A new rationale for the design of active targeting nanoparticles is given in here, namely 'range selectivity'. The range selectivity theory is based on the counterintuitive concept that only a small number of ligands on a particle's surface are capable of selective targeting. Number of ligands exceeding or falling short of this threshold hinder the interaction.

2 The immune System

The mammalian immune system is a remarkable network of cells and molecular pathways that enable the host to defend itself against potential dangers. The immune system includes physical (i.e., skin and mucosa) and chemical barriers (e.g., acidic pH and enzymes), as well as cells and blood proteins, such as the complement system and soluble mediators (i.e., cytokines) [12].

The immune system has been designed to prevent and control infections, and eliminate infected, damaged, abnormal, or dead host cells [13], [14], [15]. At the heart of the immune system is a series of molecular and protein-protein interactions that enable the body host to distinguish between itself ('self') and potentially harmful external components ('non-self', e.g. virus and bacteria), which must be recognised to initiate the appropriate immune response [13]. An unbalance of these powerful molecular or cellular mechanisms can lead to debilitating severe auto-immune conditions for the body host, such as diabetes type I, multiple sclerosis, Chron's disease and rheumatoid arthritis, just to name a few [16], [17].

One of the first line of defences put in place to protect the organism is the skin. The skin functions as both a physical and chemical barrier. The outermost layer of epidermis is composed mostly of keratinocytes, which functions as physical barrier and also possess sensor receptors capable of inducing inflammation, an antimicrobial response which culminates with the release of soluble factors (e.g., cytokines, chemokines and antimicrobial peptides) and microbial lysis [12]. In addition, the sebaceous glands associated with hair follicles produce huge quantities of fatty acids, which create an acidic environment unfriendly to microbes. Mucous membranes of the digestive, respiratory, and genitourinary systems contain a continuous epithelium that blocks the entry of germs [13], [14].

Based on their functions in host defence, immune processes have historically been classified into two large, interconnected subsystems: the innate and adaptive immune systems (Figure 2) [14]. The former generates a rapid and nonspecific immune response against infections and malignant cells. Whereas the latter generates a highly specific targeted immune response after a period of maturation,

resulting in a final immune reaction against that particular pathogen. The adaptive response can be further classified as primary or secondary, depending on whether the body is encountering the foreign agent for the first or second time [13], [18]

2.1 Innate Immune Response

2.1.1 Intracellular Inflammatory Response

Multicellular organisms are constantly subjected to various stress signals (e.g., reactive oxygen species, heat stress, infections, etc.) and, in order to survive, they have evolved defence mechanisms against them. Where the damage is beyond control or repair, cells can initiate programmed cell death, such as apoptosis and pyroptosis [19], [20]. In other situations (i.e., infections or cancerogenesis) it is essential to alert the body system with inflammatory signals. The inflammation usually starts with the recognition of pathogen-associated molecular patterns (PAMPs) or damage-associated molecular patterns (DAMPs) by their respective pattern recognition receptors (PRRs) (see Glossary for further details) [21] [22], [23]. PRRs are ubiquitously expressed in every cell type of the host and once activated culminate with the activation and nuclear translocation of the Nuclear Factor- κ B (NF- κ B) transcription factor followed by the secretion of type I IFNs (IFN α and IFN β) that bind to the type I IFN receptor (IFNR) in an autocrine and paracrine manner and expression of several interferon-stimulated genes (ISGs) [24], [25].

Within the repertoire of a vast group of PRRs can be found NOD-like receptors (NLRs), Toll-like receptors (TLRs), RIG-I -like receptors (RLRs) and cytosolic DNA sensors. For example, while self-DNA is compartmentalized in the nucleus or mitochondria, pathogen DNA is released into the cytosol during infection of cells. DNA found in this unusual location is sensed by a repertoire of PRRs, including TLR-9, Z-DNA binding protein (ZBP-1/DAI) and the cytosolic Cyclic GMP–AMP synthase (cGAS) [26]–[28] In particular, cGAS binds DNA present in the cytosol, dimerises and converts ATP and GTP into 2'3'-cyclic GMP-AMP (cGAMP). In turns, cGAMP acts as a second messenger to activate the adapter protein stimulator of interferon genes (STING) embedded in the endoplasmic reticulum membrane [29],[30]. Upon STING

activation, a signalling cascade is triggered and culminates with the translocation into the nucleolus of transcription factors IRF3 and NF- κ B for the transcription of cytokines and activation of type I IFN response (Figure 1) [31]. Furthermore, it has been shown that STING activation can lead to apoptosis via Caspase3/7 as a defence to eliminate infected cell [32] [33].

In the last decades, the sensing of nucleic acids has emerged with a prominent position both during inflammation and cancer eradication [34]. It paved the way for advancement in preventive and therapeutic vaccines and for a new class of cancer therapeutics that will be discussed in more details in Paragraph 2.3.1.2.

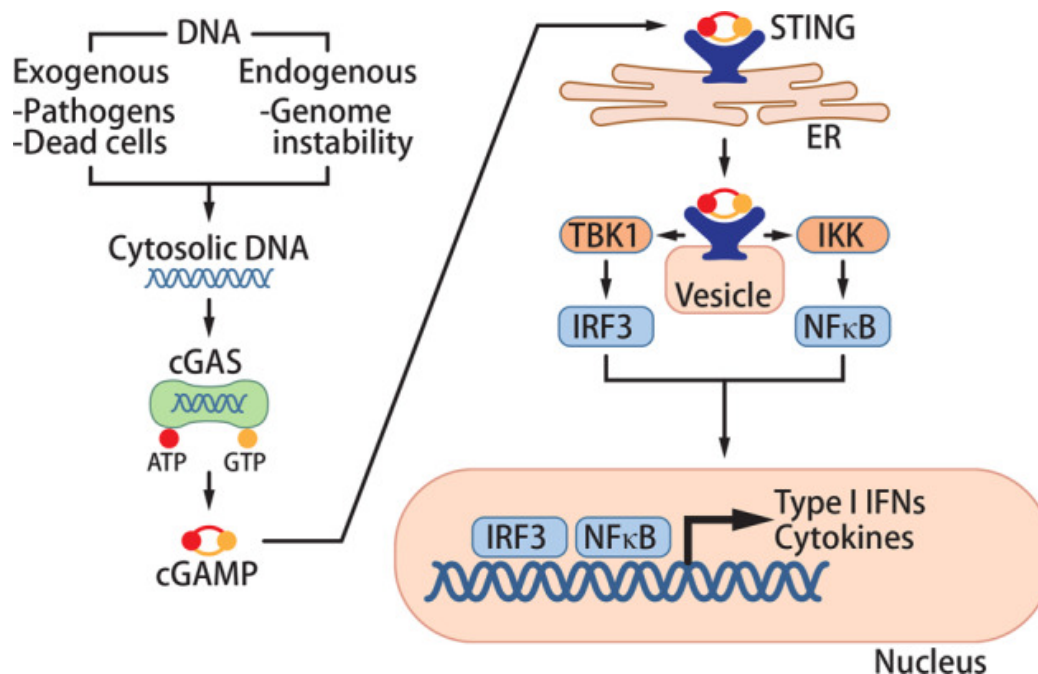


Figure 1: cGAS-STING DNA sensing and pathway of inflammation. Image edited from [35].

2.1.2 Molecular Defence

At molecular level, the protection is offered by different sets of proteins released by cells in the bloodstream and capable of exercising different actions. Examples are the proteins of the complement system and cytokines, with the latter

being a superfamily of different proteins, which includes cytokines, interferons (IFNs) and tumour necrosis factors (TNFs).

The complement system is an evolutionary ancient system of defence, comprised by proteins released mainly by the hepatocytes and some immune cells [36], [37]. The complement system is part of the innate immune system with the main functions of chemotaxis, and microbial opsonisation and lysis [36]. Based on the recognition of different molecules, the complement system can be activated in three different modalities: the canonical, the lectin and the alternative pathways [36]. As an example, in the canonical pathway, proteins of the complement (i.e., C1q) recognise and interact with class of surface-bound antibodies (e.g., IgG and IgM) and with one another, to opsonise pathogens and trigger a cascade of responses that culminate in inflammation and microbial lysis, via formation of a pore complex in the pathogen's membrane [38].

Another important class of small soluble factors involved in the perfect orchestration of the interactions and communications across immune cells is represented by the superfamily of proteins called cytokines [39]. Cytokines are physiologically released by innate immune cells and other types of cells, such as fibroblast and endothelial cells upon specific signals and hold anti- or pro-inflammatory activities, with the ability to modulate cellular growth, survival and differentiation [39] [40]. Several cytokines (e.g. IL-1, IL-2, IL-6, IL-10, IL-12, just to name a few) have been characterised, each with specific receptors and functions [41].

Chemokines, or chemotactic cytokines, are involved in immune cells migration from blood to tissue and vice versa, as well as in the induction of cell movement in response to a chemical gradient (chemotaxis). Chemokines are involved in regulating the lymphoid organ development and T-cell migration [39].

The Interferon (INF) family of cytokines are involved in the first line of defence against pathogens invasion and can be further classified into type I (IFN- α and - β), type II (IFN- γ) and type III (IFN- λ) [42] . Virus-infected cells release extracellularly type I IFN to activate the inflammation, which include innate and adaptive immune responses such as the production of pro-inflammatory cytokines, as well as increasing

expression of MHC class I molecules and promote cytotoxic T cell activation [43]. Similarly, IFN- γ is involved in promoting the host immune response but with a pivotal role in cancer immunosurveillance and antitumour immunity and it is mainly secreted by activated lymphocytes such as CD4 T helper type 1 (Th1) cells and CD8 cytotoxic T cells, $\gamma\delta$ T cells and natural killer (NK) cells [44], [45]. Finally, the IFN- λ family, with four members so far identified, has been described with overlapping expressions and functions to type I IFNs. However, IFN- λ operates primarily at epithelial barrier surfaces (e.g., respiratory and gastrointestinal tracts, and the blood-brain barrier), in contrast to type I IFNs, whose receptors are ubiquitously expressed [46]. A final example of group of cytokines is presented by the tumour necrosis factor (TNF) family (e.g., TNF- α and TNF- β and LT- β). These transmembrane proteins are synthesised as pro-protein which are activated and released as a result of a cleavage by a cell-surface metalloprotease. Once released in the extra-cellular environment, the TNF bind its specific receptor expressed on the surface of a variety of cells to induce a pro-inflammatory response, release of other cytokines and production of fever [41]. TNF also plays a fundamental role in cellular differentiation, proliferation and apoptosis in the lymphoid tissue [47][48].

2.1.3 Cellular Defence

Besides molecular responses, the immune system offers a defence at a cellular level through specialised cells, patrolling blood vessels and organs, promptly eradicating potential threats. Cells belonging to innate or adaptive branch bear different properties and functions for their specific role in the immune response, although there are some exceptions (e.g., $\gamma\delta$ T and Natural Killer (NK) T cells) [37], [49].

Cells of the adaptive immune system comprises B cells and T cells (see Paragraph 2.1.4 for further details). While cells of the innate immune system are represented by NK cells, macrophage and dendritic cells (DCs), to mention a few (Figure 2) [50] [15]. In particular, DCs are a type of innate immune cell heavily involved in the immune response [51]. DCs belong to a diverse group of immune cells collectively referred to as antigen-presentation cells (APCs; see Glossary), which are specialised in

presenting antigens on their external surface to trigger the adaptive immune response [21], [52].

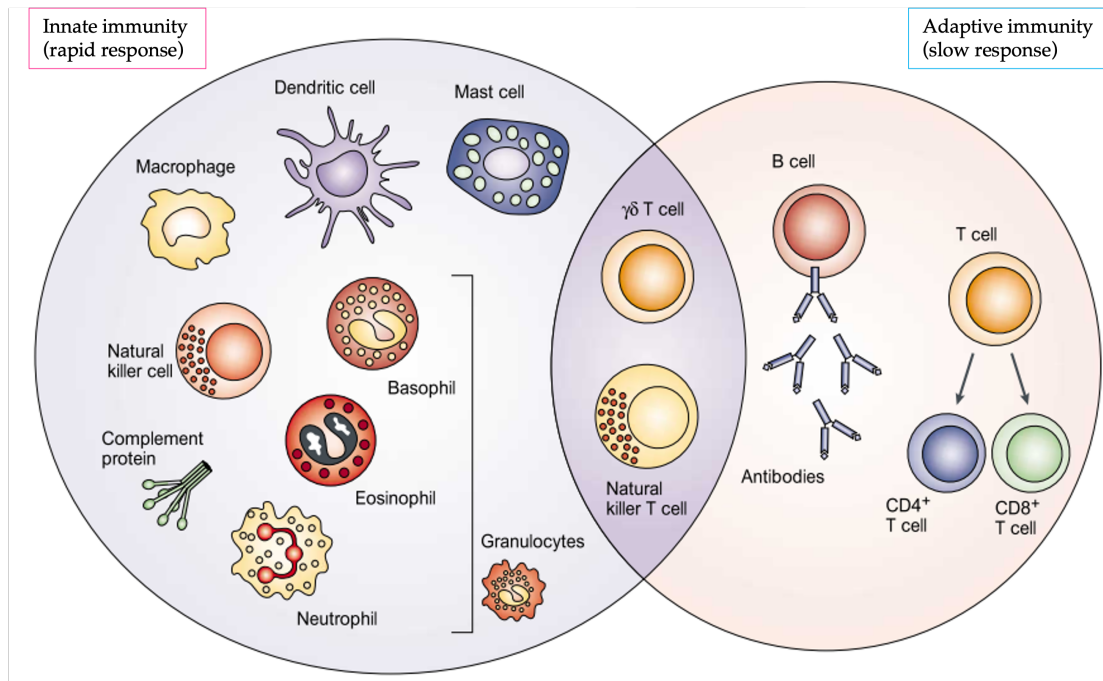


Figure 2: Immune cells of the innate and adaptive immune system.
Picture edited from [50].

2.1.3.1 DCs

Dendritic Cells (DCs) are a family of diverse immune cells that connect innate and adaptive immunity [14]. Referred to the most important class of antigen-presenting cells (APCs), the primary purpose of these innate cells is to collect, process, and deliver antigens to adaptive immune cells and to mediate the polarisation of their effector cells (Figure 3) [14].

Firstly discovered in the 1970s by Steinman and Cohn, DCs own their name to the peculiar tree-like morphology (in Greek ‘dendron’ means tree) [53], [54], [55]. Due to their short life span, DCs are continuously replenished [56]. Derived from common hematopoietic stem cells (HSCs), DCs are classified according to their location, ontogeny, phenotype, and functions [56]. In the bloodstream, three main subsets of DCs can be identified in the circulatory bloodstream: plasmacytoid DCs (pDCs), myeloid DCs (mDCs) and conventional DC (cDCs) [57]. In particular, pDCs and mDCs are able to identify various types of PAMPs thanks to their broad expression

of PRRs. Consequently, mDCs and pDCs are capable of stimulating CD4+ and CD8+ T cell responses against various pathogens. Moreover, both mDCs and pDCs are able to interact with Natural Killer (NK) cells, which are especially important during viral infections [57].

Populations of immature DCs reside in every tissue or surface prone to disease-relevant stimuli, such as skin (e.g., Langerhans DCs), pharynx, upper oesophagus, as well as internal mucosal surfaces (e.g., respiratory and gastrointestinal apparatus). They are continuously patrolling and sampling the areas by extending their protrusions through the epithelia tight junctions and sampling for antigens [58]. A signalling cascade is triggered at the detection of microbial or other danger signals, resulting in the functional maturation of DCs and migration to the lymph node. Each step is well-regulated by a series of transcription factors [59].

DCs have a crucial role in initiating an immune response against pathogens and cancer, as they can identify tumour-associated antigens (TAAs) and neoantigens (refer to Glossary). The pathogen is recognised, engulfed, cleaved and digested into distinct antigens through the immunoproteasome (see Glossary) and subsequently exposed on the surface via MHC class II molecules, a process known as antigen presenting (

Figure 3) [60], [61]. Upon sensing of PAMPs or DAMPs, PRRs activations induces a conformational change to mature DCs that enables them to traffic to lymph nodes to activate the immune system [62]. Upon internalisation, the pathogen is degraded and digested in the phagosome. Bacterial proteins are then further degraded by the immunoproteasome into distinct antigens (antigen processing), which then are captured by MHC class II receptor and exposed on the cellular surface (antigen presentation) for the initiation of the adaptive immune response followed by immunisation [60].

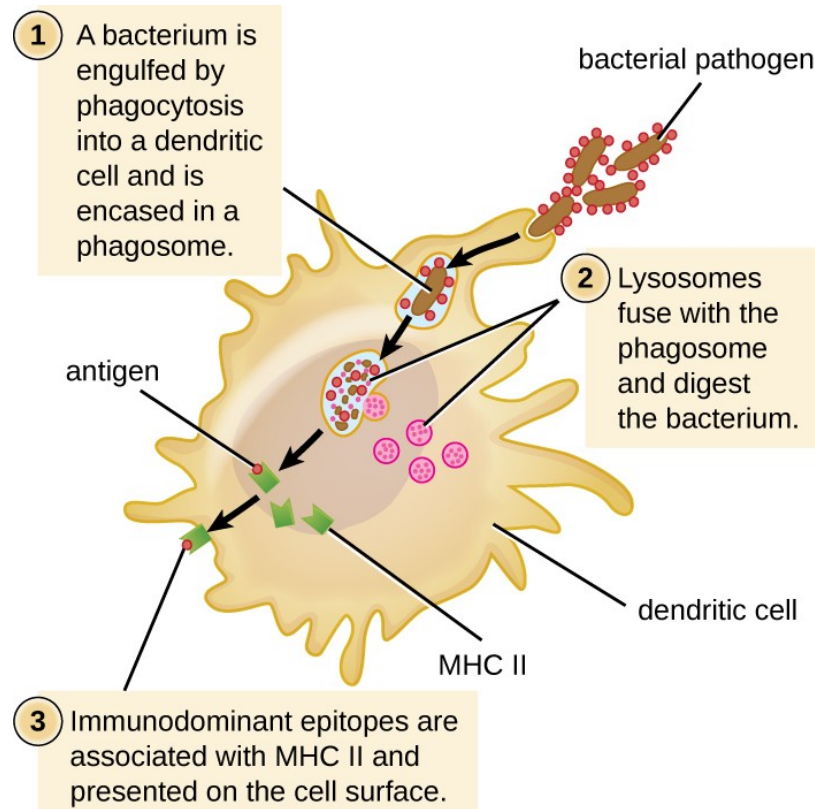


Figure 3: Antigen Processing and Presentation in DCs.

Image taken and adapted from www.coursehero.com, access on 19/05/2022.

2.1.4 Adaptive Immune Response

The other branch of the immune system is represented by the adaptive immune response, which orchestrates the specific and immunologic memory that protects the host against pathogens. The adaptive immune system mainly employs lymphocytes that originate from the primary lymphoid organs, such as **T cells**, which mature in the thymus, and **B cells**, which arise from the bone marrow and produce high-affinity antibody proteins [63], [64]. These cells travel to secondary lymphoid organs (i.e., lymph nodes and the spleen) where they intercept circulating antigens exposed on activated APCs [65],[66]. Lymphocytes can now circulate into several sites of the body host to exert their functions [65].

T cells originate from hematopoietic stem and precursor cells in the bone marrow and migrate to the thymus and acquire T-cell identity, where they can respond to stimuli. Here they begin the proliferation while initiating their T cell receptor

(TCR) rearrangement and differentiating into distinctive lineages, such as CD4⁺ T, CD8⁺ T, natural killer T (NKT) and regulatory T (Treg) cells [67]. Altogether, different T cells play distinctive functions that contribute to the immunosurveillance and homeostasis of the immune system. The recognition of the antigen/MHC complex presented on an APC by the TCR, known as immunological synapse, triggers the T-cell activation [67]. As a result, a complex intracellular molecular signalling pathway is activated and culminates with a rapid increase of intracellular calcium and subsequent translocation of NF- κ B into the nucleus of the transcription of genes involved in the function of activated T cells [68].

B cells arise from hemopoietic stem cells in the bone marrow and produce antibodies after differentiation and maturation in the spleen and upon directive signalling received from activated T cells or DCs [69]. The antibody-mediated immunity, or humoral response, begins when the B cell's antigen-binding receptor recognises and binds the antigen in its native form, neutralising the threat [70]. Antibodies are subdivided into five major classes, of which IgG is the most predominant circulatory and extensively studied type [70]. IgG antibodies recognise and 'flag' the pathogen to neutralize specific pathogens by targeting their epitopes (see Glossary) [71]. The IgG constant domain (or fragment crystallizable, Fc) is then recognised by the Fc receptors (i.e., Fc γ R), broadly expressed in immune cells and involved in phagocytosis and inflammatory response [72]. Alternatively, C1q complement complex can recognise and bind to the Fc region of IgG/antigen complex and trigger the classical complement pathway, which culminates with the pathogen opsonisation and elimination [73].

2.2 Cancer Immuno-Editing

The first to suggest the concept of immunological surveillance (immuno-surveillance) was the German physiologist Paul Ehrlich in 1909 [74], [75]. He advanced the hypothesis that the immune system plays a fundamental role in the surveillance against tumours. Although he did not prove experimentally the

hypothesis due to the lack of tools and knowledge, he envisioned the central role of the immunological control of neoplasia, initiating a contentious debate on the matter [74], [75].

Throughout their lifetime, cells are exposed to carcinogenic triggers such as genetic alterations, toxic substances, and oncogenic viruses [76]. The immune system's role is to recognise and fight against these threats as quickly as possible. In particular, during carcinogenesis, cells acquire a series of characteristics essential for malignant transformation such as angiogenesis, uncontrolled proliferation, escape from apoptosis, immune evasion and immunosuppressive microenvironment [77], [78]. Mutated cells might start expressing TAAs and neoantigens, which might be quickly recognised as 'non-self' by host immune system in a process known as cancer immunosurveillance [79], [80]. To survive, cancer cells evolve mechanisms that evade and/or suppress the immune system. The process that selects malignant clones with immunosuppressive features is named 'cancer immune-editing' (Figure 4) [9].

Cancer immuno-editing is now a well-recognised process that drives malignant cells to evolve immune suppressive mechanisms to escape the immunosurveillance and proliferate. Immunogenic therapy is used to restore antitumor immune responses and may be critical to the long-term efficacy of cancer treatment [80].

As depicted in Figure 4, the first cancerous cells express and expose on their surface the neoantigens, which are perceived as 'non-self' by the immune system cells such as NK, NK-T cells and macrophages [81]. Some of the cancerous clones might be immunogenic, increasing the level of awareness in nearby cells, which respond with the secretion of signalling molecules such as cytokines and type I and II IFN to create an *in loco* inflammation and leading to antiproliferative tumour control [81]. In particular, type I IFN is considered a fundamental link between innate and adaptive immunity as it activates DCs and increase the cytotoxic activity of NK cells [82], [83]. Tissue-resident DCs take up dead tumour cell debris. Once activated, they migrate to the tumour-draining lymph node activating the cancer-immunity cycle (further details in Paragraph 2.3.1 and Figure 6).

Non-immunogenic cancer cells acquire several abilities to suppress immune recognition and ultimately provide the cancer with substances and nutrients, including overexpressing of receptors PD-1 and its ligand PD-L1, CTLA-4, the release of immunosuppressive cytokines (e.g., IL-10 and TGF- β), the creation of an unfavourable metabolic environment with hypoxia, amino acid depletion, and acidic pH [84], [85], [86]. Notably, the most aggressive tumours can evade the immunosurveillance at a very early stage and skip the equilibrium phase, entering into the high replicative state directly [9].

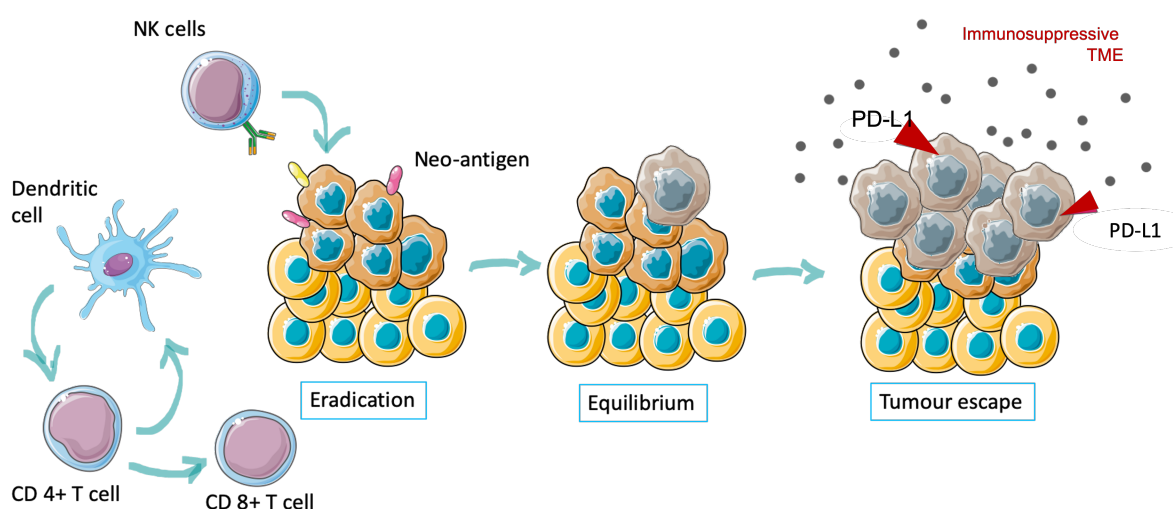


Figure 4: The Immuno-editing Process: Eradication, Equilibrium and Tumour Escape. A healthy cell (yellow) is subjected to a plethora of stimuli that can start the process of cancerogenesis. During this process, cancerous cells (dark orange) might express abnormal surface proteins (neoantigens, pink and yellow surface epitopes) that can be quickly recognised as ‘non-self’ by NK cells during the phase of eradication. During the eradication phase, material from cancer cell lysis can be released in the immediate extracellular environment and internalised by DCs, which in turn activate the adaptive response via CD4+ and CD8+ T cells. However, tumors can also develop strategies to evade immune surveillance and destruction during the equilibrium phase, which can lead to tumor progression (grey cells) and metastasis (escape). Understanding the mechanisms underlying tumor elimination by the immune system, as well as the mechanisms of tumor escape, such as expression of PD-L1 (red triangles) and other immunosuppressive mechanisms, is critical for the development of effective cancer immunotherapies. Image created using Biorender.

2.3 Cancer Immunotherapies

One of first attempt of treatment with immunotherapy was performed by Dr William Coley in 1891. Heat-killed bacteria (namely Coley's toxins) were injected in patients with inoperable sarcoma and where obtained astonishing positive results were obtained with complete eradication of the neoplasia [87], [88]. Since then, tremendous advancements have been made in the field, with several classes of immunotherapy being developed (Figure 5). Amongst this vast plethora of therapies, the adoptive cell therapies (ACT) and immune checkpoint inhibitors (ICI) have entirely transformed the panorama of cancer medical treatment, owning their very effective results against a broad variety of tumours [89], [90]. Chimeric Antigen Receptor (CAR) T cells have distinguished themselves as one of the most effective ACT in the treatment of blood cancers like leukaemia and lymphoma [91]. On the other hand, ICI is aimed at inhibitory receptors in T cells, like PD-1, and its ligand PD-L1 in tumour cells, or the CTLA-4, with proven clinical benefit in both solid and blood tumours [92]–[94]. Despite the excellent results, immunotherapies are only efficient in the 10-30% of patients [92]–[94], and off-target binding events can render secondary effects which range from bearable to the development of immune-related adverse events (irAEs), leading to auto-inflammatory reactions in patients [95], [96]. Adverse events such as dermatitis, vitiligo, colitis and liver and lung toxicity have been observed. In some rare cases, irAEs lead to auto-immune diseases, such as diabetes and lupus [97], [98].

Compared to ACT or ICI therapies, therapeutic cancer vaccines have been less impressive clinically, with only a handful of them having been approved by the FDA. Nonetheless, they represent a viable alternative among immunotherapies due to their simplicity, low cost, and low risk of irAEs [99][100]. Cancer vaccines are generally considered safer, with a lower profile of immuno-toxicity and are expected to preserve the quality of life in patients with minor side effects (flu-like symptoms, fever and local inflammation in the injection site) [101]. Therapeutic vaccinations help expand the pool of tumour-specific T cells from the naïve repertoire and reawaken those that are latent or inactive [102]. To optimally activate T lymphocytes, DCs, which play a

significant role in adaptive response activation, must be stimulated *ex vivo* by tumour-specific antigens and the appropriate adjuvants for both purposes [102].

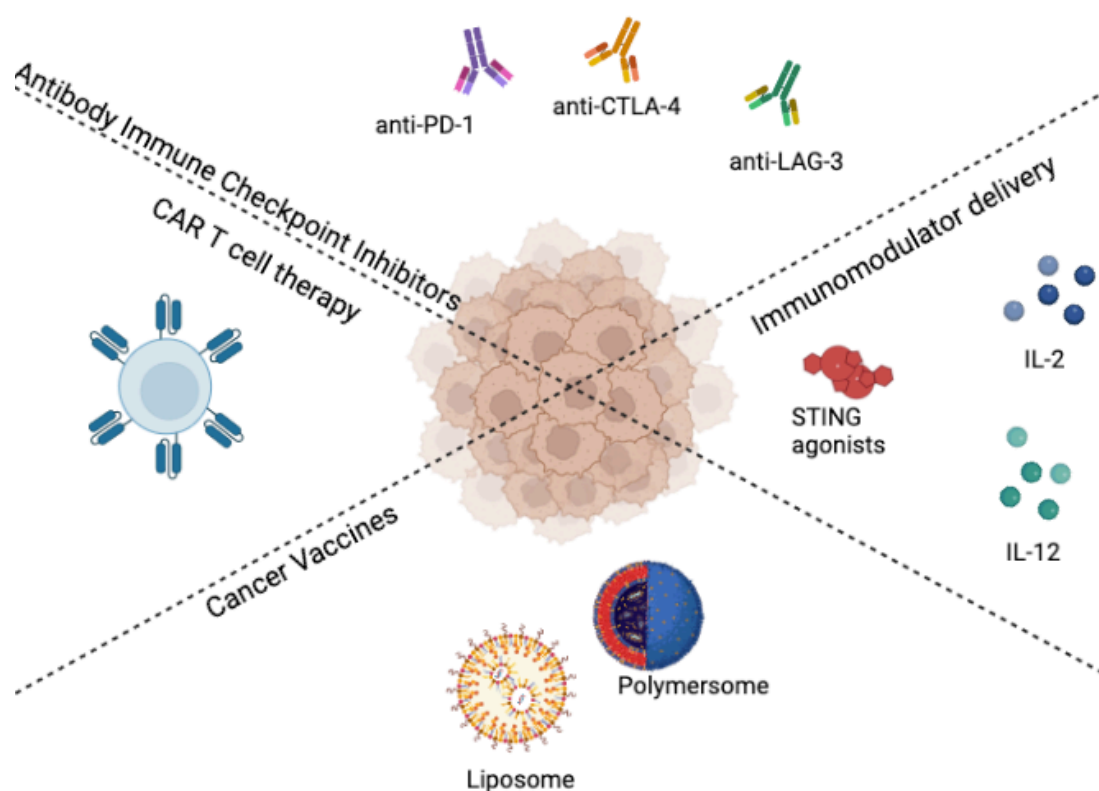


Figure 5: Different strategies for cancer immunotherapy.

From the left to the right clockwise: 1) CAR T cell treatment is based on engineering patient's own T cells to present on the surface receptors for targeting cancer; 2) blockade ICIs antibodies are used to inhibit the inhibition of immune cells in the tumour microenvironment; 3) Immunomodulators molecules have been investigated alone or in combination with current approved therapy to increase tumour inflammation; and 4) cancer vaccines are based on the administration of TAAs for the DCs presentation of the antigen in order to trigger an immune response against the cancer. New drug delivery platforms such as liposome and polymersome are under investigation for the delivery of nucleic acids for cancer vaccination (to be discussed in the next paragraphs). Image created using Biorender.

2.3.1 Therapeutic Cancer Vaccines

Antitumour immunity typically begins at the tumour site, where fragments of dying cancer cells (i.e., DAMPs) are taken up and processed by DCs to initiate the cancer-immunity cycle (Figure 6) [60], [103]. The process requires a finely regulated network of maturation signals, without which DCs might promote tolerance rather than activation [104]. As previously mentioned, once DCs are activated, they migrate

to the lymph node, where they will present tumour antigens to induce cytotoxic T lymphocyte (CTL, see Glossary) responses (Figure 6) [105].

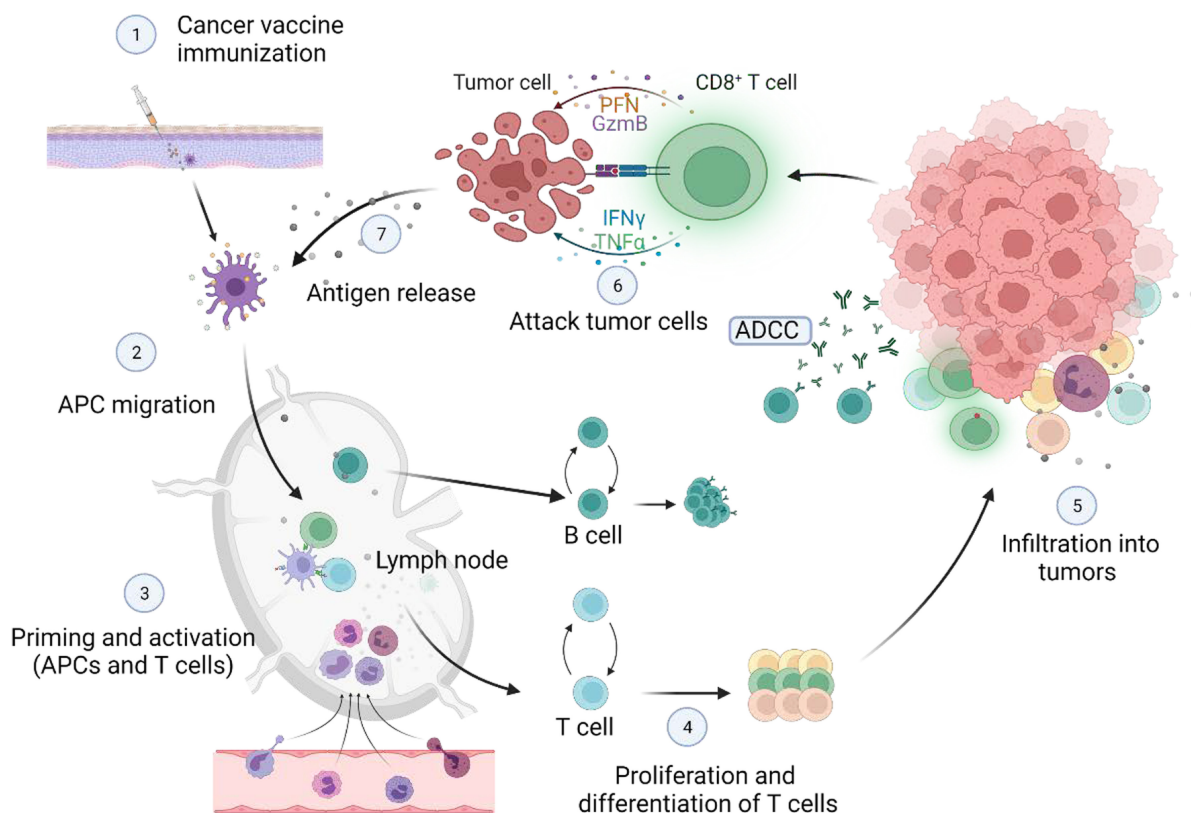


Figure 6: Cancer-Immunity Cycle.

DCs constitute the link between innate and adaptive immunity. Once they have uptaken antigens and cross-presented them on MHC I molecules (2), they migrate to the draining lymph nodes (3), where T cells are primed. Mature DCs present to naïve CD4⁺ and CD8⁺ T lymphocytes with processed antigen epitopes on MHC I and MHC II molecules, and IL-12 and IFN- γ are secreted to boost the costimulatory factor synthesis. Tumor-specific T cells are activated and develop into memory or effector T cells. Effector tumor-specific T lymphocytes multiply (4) and transported to the TME (5), where they drive tumour cell death through cytotoxicity via perforin (PfN) and granzyme B (GzmB) action (6). Furthermore, activated B lymphocytes induce tumour death via antibody-dependent cellular cytotoxicity (ADCC) or complement-dependent cytotoxicity. The immunogenic cell death release tumour antigens and DAMPs, which in turns are captured (7), processed and presented again by DCs/APCs to induce polyclonal T cell response (3), thereby increasing the antigenic range of anti-tumor-immune responses in the so-called cancer-immunity cycle. Cancer vaccines aim to eradicate tumour cells mainly by activating cellular immunity, initiating the cancer-immunity cycle. Image adapted from [106].

CD4⁺ T lymphocytes collaborate with other immune cells. They can stimulate T cell activation and growth, boosting the anti-tumour T cell repertoire [107]. The IFN- γ released by Th1 CD4⁺ T cells upregulates MHC I on tumor cells, enhancing the activity of effector CD8⁺ T cells and increasing the inflammation of the TME with CTLs, which are essential for tumour control [108]. Activated CTLs will pierce the

core of the tumour and attack target cells through different mechanisms based on the production and release of cytotoxic particles. Hence, their presence in the TME is crucial for a positive prognosis [105]. In addition, CTLs might release IFN- γ and TNF- α , which have a cytotoxicity effect on cancer cells [107].

Loss or modification of surface antigens in malignant cells is an efficient strategy to elude the immunosurveillance and avoid tumour eradication [101]. Therefore DC-based vaccines aim to mend this negligence of the immune system by providing the body host with *ex vivo* (see Glossary) DCs-pulsed with tumour antigens or tumour cell lysates and stimulated with a defined maturation cocktail [109].

In 2010, FDA approved the first cancer vaccine, namely Sipuleucel-T (Provenge®), for the treatment of asymptomatic or minimally symptomatic metastatic castration-resistant prostate cancer [110]. With this vaccination, a higher patient survival rate was observed and cancer vaccines were reintroduced as a new therapy option. This vaccine immunogen is a fusion protein consisting of the prostate cancer-specific antigen and adjuvant granulocyte-macrophage colony-stimulating factor (GM-CSF), to promote DCs maturation [110]. However, the response of the malignancy to Sipuleucel-T was minimal, resulting in a relatively short window of benefit and the drug's eventual withdrawal from clinical use for some time [111]. With a similar approach, NeuVax™ (Galena) cancer vaccine was designed for the treatment of breast cancer. The immunogenic portion of the protein HER2 is fused with the GM-CSF to induce tumour control. A phase II clinical study, showed a reduction from 26% to 6% of the five-year recurrence rate of breast cancer [112], [113].

A parallel strategy to develop cancer vaccines is to use tumour cells to elicit spontaneous immune responses. GVAX (Aduro Biotech) is a cancer vaccine made from autologous tumour cells that have been genetically engineered to release GM-CSF. GVAX was found able to stimulate a prolonged, long-lasting and anti-tumour activity with some success in clinical trials [114]–[116].

The lack of clinical success of cancer vaccines might be due to the sub-optimal antigen presentation and T cell stimulation [117]. To overcome this limitation, several attempts to improve antigen and adjuvants delivery in DCs to elicit a successful immunisation [118]. Intuitively, factors that contribute to an optimal antigen

presentation, are the intracellular delivery of the antigen and the 'quality' of the antigen itself, in terms of stability and type (e.g., whole cell lysate, protein or nucleic acid) [119], [120]. Several approaches for antigen delivery *in vivo* and *ex vivo* have been developed over the years, each with advantages and disadvantages [119], [120], [121]. The most effective strategy for tumour antigen delivery *in vivo* is to couple the TAA to a monoclonal antibody directed against DC-specific receptor [119]. Internalization of the complex occurs, and the antigen is processed for cross-presentation via MHC-I and II class molecules. Adjuvants, which are needed to activate DCs and increase the immune response, are typically co-administered to augment the cytotoxic T cells and tumour inflammation. The first works based on this method were generated in the mid-1980s. Snider and Segal were able to execute tailored antigen delivery *in vitro* and *in vivo* by coupling it with antibodies against FcγRs, boosting T cell presentation and hence the antitumor immune response [119]. However, the material can be lost by diffusion or establish non-specific interactions upon the injection, raising the chance of developing irAEs, as has been demonstrated [113]. On the other hand, in *ex vivo* protocols, DCs are collected from the patient, loaded with antigen through electroporation of whole tumour cell lysate or antigen proteins, or transfected with nucleic acid encoding for the antigen (DNA or RNA), and then re-injected into the body [122] [123]. However, these methods require extensive culture periods, which might negatively affect the healthy cellular state [122] [123].

2.3.1.1 DNA Delivery for Cancer Vaccines

The selection of antigen is one of the most important parts of cancer vaccine development. The ideal antigen would be highly and selectively expressed by cancer cells and immunogenic. Because relatively few antigens possess all these characteristics, great effort has gone into developing novel and more effective antigens. Protein-based cancer vaccines can be easy to be manufactured, but very expensive [120]. Nucleic acid delivery for cancer vaccines, such as DNA and RNA, provides a safer, simpler, and cheaper alternative to protein-based cancer vaccines [124]. The nucleic acid delivered intracellularly, encodes for the tumour antigens using the cell machineries, which then are processed to induce immunisation. Because of structural differences and ubiquity of RNase enzymes, DNA molecules

present higher stability and longer permanence in the body host. The downside is that they need to cross two physical barriers (cellular and nuclear membranes) to initiate the mRNA transcription. However, a single plasmid DNA can encode for multiple copies of mRNA, hence more antigens to present. On the other hand, RNA encoding for antigen protein needs to cross only the cellular membrane and the production of antigen is quick and effective. However, RNA vaccines result to be more expensive to produce and maintain due to their instability [125].

Delivery of nucleic acids can be achieved via *ex-vivo* methods (taking place outside the organism), followed by re-injection of loaded DCs into the body. For the intracellular delivery, can be implemented chemical methods, such as cationic polymers like Lipofectamine. Or physical methods, such as electroporation, which is based on destabilising the membrane potential to deliver internally the nucleic acid. These protocols, however, are technically very challenging. In particular, *ex vivo*-loaded DCs require extensive culture period, which might negatively affect their functionality [123].

Besides *ex vivo* protocols, *in vivo* strategies for DC-antigen loading, are under intense investigation [126]. A new platform for antigen delivery *in vivo* is required to overcome the loss of material by diffusion and unspecific binding. As an example, nanoparticles can encapsulate both antigen and adjuvant for a specific (active) targeting of DCs for antigen-loading and improving cancer vaccines [127].

Furthermore, the plasmid DNA itself can act as co-stimulant of the immune response. In fact, CpG motifs (see Glossary) present in the bacterial plasmid are recognised by TLR9, a PRR receptor [28], [128]. The TLR9 cascade activates a signalling pathway that culminate with the nuclear translocation of NF- κ B and consequent synthesis and release of pro-inflammatory cytokines. Additionally, the DNA double-stranded structure is recognised by the cytosolic PRRs cGAS, which dimerise around the plasmid and utilise the change of conformation to synthesise cGAMP (for further details refer to Paragraph 2.1.1) [129]. Several studies have shown that the activation of the cGAS-STING axis is essential for a robust adaptive response [130]. Nowadays, multiple STING-agonists molecules have been

developed for therapeutic use, some have already been tested in clinical trials, holding great promises for triggering the robust tumour inflammation needed to overturn immune-unresponsive (cold) tumours (see Glossary) [131]. Therefore, STING-agonists represent a new class of immunomodulators to be utilised alone or in combination with other therapy for therapeutic immunisation [132], [131].

Despite bearing several advantages, DNA vaccines have only achieved minor progress in clinical trials due to their poor immunogenicity and therefore several efforts are made towards a more effective cancer immunisation [133].

2.3.1.2 **STING Agonists**

A cancer vaccine is considered successful if able to overcome the immune suppressive TME and to transforming "cold" tumours into "hot" tumours (see Glossary), whilst establishing a robust adaptive immune response [134]. Among the several optimisation strategies taken in consideration, there is the use of immunomodulators to be co-administered with the TAA [135]. Besides the canonical immunostimulatory cytokines, such as IL-2, GM-CSF, IL-12 and IFN ([136]–[139]), a new class of adjuvants has appeared in the clinical panorama. The potential therapeutic of the STING agonists and other cyclic dinucleotides (CDNs) have found a prominent spot in the investigation of potent immunomodulators in vaccination. STING agonists, including its natural ligand cGAMP, have all shown encouraging results in anti-tumour pre-clinical studies. One of the studies conducted in C57Bl6 mice bearing B16F10 melanoma tumour showed that the intratumoral injection of cGAMP induced potent STING activation in the TME, promoting TILs in an IFN-dependent manner. The growth of both injected and the contralateral tumour were significantly delayed [140]. Furthermore, when cGAMP was tested in combination with anti-CTLA-4 and anti-PD-1 it was found that the anti-tumour activity was greatly enhanced, holding great promises for future clinical application [140]. Finally, and unexpectedly, it was found that endothelial cells in the TME, and not DCs, were the main producer of IFN- β required to boost antitumour activity [140].

In a similar work, immuno-competent tumour-bearing mice were intratumorally injected with 5,6-dimethyl- xanthenone-4-acetic acid (DMXAA), one of the most promising STING agonists in pre-clinical studies. Results of the study demonstrated

the potent tumour inflammation properties of DMXAA in animal model, with anti-tumour growth control and TILs in the TME in several solid tumours models [141]. DMXAA showed potent anti-tumour activity in mice models, holding therapeutic promises, which however were not met in human clinical studies, abruptly interrupting the line of research [142].

STING agonists belong to a new emerging class of adjuvants that holds great therapeutic potential and which requires further investigation.

For example, it was found that STING expression is highest on T cells and its activation leads to cell apoptosis. However, comparable effects are not observed in macrophages and DCs [143].

The potential therapeutic benefit of STING agonists has been translated into the investigation and development of other CDN molecules [144]. To avoid T cell death while using a STING agonist in a cancer vaccine, a delivery strategy that solely targets myeloid cells in vivo would be required and the lack of delivery control might impede the development of effective cancer vaccines. One approach might be to deliver intracellular to specific myeloid cell phenotypes the ingredients needed for a robust adaptive immune response by implementing biocompatible pH-sensitive materials and nanoparticle formulation. In other words, the customisable platform of nanomedicine might offer the delivery tools required to overcome the present obstacles[145].

2.4 Nanomedicine

Despite the encouraging clinical results of cancer immunotherapy, the outcome vary according to tumour type and patient [146]. Effective treatments typically comprise a combination of two or more types of therapies, including both immunotherapy and/or chemotherapy regiment. However, these combinations usually come at the price of off- target toxicities [147], [148], [149]. Furthermore, many therapeutical molecules come with significant restrictions including poor pharmacokinetics, instability and toxicity. Drug delivery via designed nanocarrier systems holds the potential to improve therapeutic efficacy while reducing the side effects [150]. The emerging discipline of nanotechnology and nanomedicine can help to achieve significant progresses in detection, diagnosis and treatments.

Nanomedicine (defined as 'the use of materials at the level of molecules and atoms, ranging from few nm to 1000nm in diameter [151]), emerges as customisable delivery platform at the nanoscale that has the potentiality to overcome present drawbacks in the therapeutic space [152]. Nanocarriers can 1) encapsulate poorly soluble or hydrophobic molecules, 2) prevent payload mechanical or enzymatic degradation and enable controlled drug release, 3) decrease clearance and improve tissue distribution, and 4) can be tailored to overcome physiological barriers, such as vascular endothelium, extracellular matrix and cell membrane [153]. Taken together, these advantages made nanomedicine a very attractive field of study for the oncologists. Examples of this success are represented by the liposome-encapsulated doxorubicin (Doxil) and the albumin-stabilized paclitaxel (Abraxane) [154], [155].

2.4.1 Polymersomes

Researchers have investigated a wide range of NPs for use as delivery systems alone or in combination with other treatments [156], [157]. These include bilayer nanovesicles such as liposomes and polymersomes, micelles, carbon nanotubes, mesoporous silica and gold NPs [158]. Liposomes (lipidic bilayer nanovesicles) are one of the most successful NP in clinic, with more than 40 liposome-based treatments approved by the FDA in the last two decades [159]. Their

biocompatibility, non-immunogenicity and versatility are the fundamentals of this success [159], [160]. Furthermore, the nanosized dimension of liposomes allows them to be a suitable platform for the quick trafficking to the lymph node, where they can be uptaken up by APCs and release their cargo intracellularly [159], [160]. Liposomes can be used to deliver antigens, RNA or DNA to increase the immunogenicity and improve cancer vaccines in pre-clinical studies [161]. In 2016, BioNTech has developed a lipid-based scaffold for the delivery of therapeutic RNA into DCs [162], [163]. Firstly, it was observed that the RNA-lipoplex so formulated were able to efficiently protect the RNA molecules from degradation upon intravenous (i.v.) injection, thus prolonging circulation time and therapeutic potential. Moreover, the precise targeting of DCs to mount a proper immunisation was achieved by finely tuning the physiochemical characteristics of the RNA-lipoplex, such as charge, size and lipid composition.

However, since the introduction of the first liposomal formulation, other drawbacks have surfaced. In particular, liposomes display low encapsulation efficiency, poor physical and chemical stability (e.g., high critical aggregation concentration (CAC), see Glossary), and limited chemical flexibility [164]. In reality, liposome formulations have a shorter shelf life as a result of a lesser degree of molecular entanglement of the hydrophobic tails [164]. Thus, in the last decade, the attention has been re-directed towards the development of biocompatible amphiphilic block copolymers, which can self-assemble into polymersomes (POs) [164]. The chemical and physical characteristics of polymers, together with their high molecular weight, make them a viable alternative to phospholipids. Biocompatible and biodegradable polymers, such as poly (ethylene glycol) (PEG), poly (lactic acid) (PLA), poly (-caprolactone) (PCL), poly lactic glycolic acid (PLGA), and cationic poly (b-amino esters) PBAE, have been developed for this purpose and have been approved by both the FDA and EMA [165], [166].

Polymersomes, bilayer nanovesicles made of diblock polymers offer various benefits over liposomes due to their membrane and entangled hydrophobic chains, which provide greater stability and cargo retention (Figure 7) [164]. Moreover, POs are characterised by higher loading and retention of biomolecules, stimuli-

responsiveness (e.g., pH sensitivity), antifouling polymeric brush and selective targeting properties.

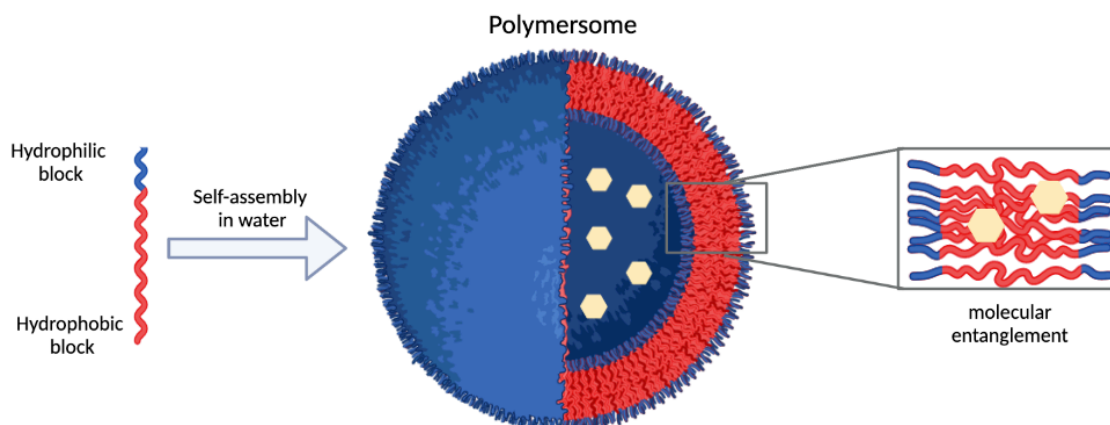


Figure 7: Representative Figure of a Polymersome.

Polymersomes offer a superior level of molecular entanglement through their hydrophobic blocks (in red) then liposomes. This is translated to a better stability and cargo retention (represented in yellow) of the NP and longer shelf life. Image created using Biorender.

2.4.2 Supramolecular Forces in Self-Assembly

In soft matter, NPs self-assembly is governed by supramolecular forces. These weak, cooperative and reversible interactions (e.g., hydrogen bonds, electrostatic interactions, hydrophobic forces, van der Waals forces etc) are at the bases of biological processes and self-assembly systems in nature. Taking inspiration from natural self-assembly structures, novel polymeric amphiphiles for drug delivery applications have been developed and synthesised.

Amphiphiles are characterised by their dual nature, with a hydrophilic and a hydrophobic portion, that behave oppositely in water [167]. As consequence, the self-assembly of polymeric amphiphiles may form a variety of structures (vesicles, micelles, cylinders, etc) for the encapsulation and delivery of biomolecules of various kind [164].

By taking into account some geometric considerations (i.e., ‘packing factor’ [168]), it is possible to govern the self-assembly of polymeric amphiphiles into the formation of nanoscopic vesicles, such as polymersomes, with an internal aqueous

core and a double-layer membrane, ideal configuration for trapping both hydrophobic and hydrophilic biomolecules [154].

A di-block copolymer is a molecule composed by two polymers: one is hydrophilic whilst the other one is hydrophobic [167], [169]. In a water solution, hydrophobic blocks prefer to reduce their contacts with the polar solvent and maximise their interactions with one another (hydrophobic effect), whereas hydrophilic blocks interact with the solvent *via* hydrogen bonding, electrostatic and van der Waals interactions [167], [169]. Depending on the geometry of the amphiphile and preparation method, the self-assembly process can form a wide range of structures, such as micelles, vesicles and like vermicelli-like shapes [170] (Figure 8).

The dimensionless parameter 'packing factor' (p) can be used to approximately predict the final spatial rearrangement:

$$p = \frac{v}{a_0 l} \quad (1)$$

where v is the hydrophobic molar volume, l is the length of the hydrophobic block and a_0 is the optimal interfacial area occupied by the amphiphile. With a good approximation, the packing factor can predict the final geometry of the nanoparticle in solution (Figure 8) [170].

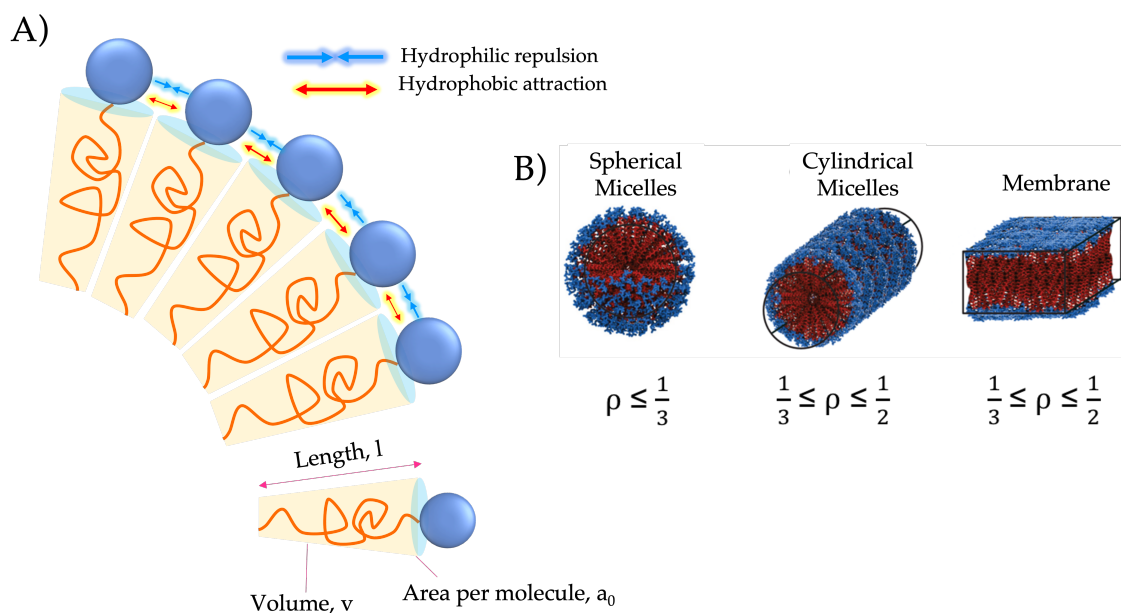


Figure 8: Electrostatic interaction and predicted geometry of self-assembly. Figure in A) shows the intermolecular electrostatic interactions between the hydrophilic heads (blue) and hydrophobic tails (yellow) during self-assembly. Figure B) represent shows packing factor value determines tri-dimensional structure of self-assembly. Generally, high-curvature structures (e.g., spherical micelles) are generated when $p < 1/3$, as cylindrical micelles when $1/3 \leq p < 1/2$ and low-curvature bilayer membranes (like polymersomes) when $1/2 \leq p < 1$ [171] [168]. Image readapted from [172].

2.4.3 The Diblock Copolymers: Structure and Properties

To better explicate their functions, POs should be made of biodegradable, biocompatible, non-toxic, and non-immunogenic polymers. Ensuring a prolonged circulation duration in the bloodstream of materials and an acceptable concentration in target tissues have been the two main research objectives in the field. But one of the main obstacles of NP-based therapies is their accumulation in the spleen and liver as a result of the reticuloendothelial system actions (RES; see Glossary). Ensuring a prolonged circulation duration in the bloodstream of materials and an acceptable concentration in target tissues have remained objects of further scientific studies [173]. POs surface characteristics, such as charges and chemistry, determine the composition of the surrounding matrix of biomolecules, known as “protein corona”. The protein corona determines the destiny of POs in biological systems, defining their physiological response, such as cellular uptake and targeting

efficacy [174]–[176]. For these reasons, the choice of antifouling polymer as building block of NPs it is a rather fundamental part in nanomedicine [174], [175].

Amongst the antifouling diblock copolymers developed, two require particular attention for their therapeutic potential: poly (2-(methacryloyloxy) ethyl phosphorylcholine) - poly (2- (di-isopropylaminoethyl methacrylate) (PMPC-PDPA) and the poly(ethylene oxide)- poly (lactic acid) (PEG-PLA). The first is a viable option for the intracellular delivery of biomolecules (e.g., DNA, antigens, etc.) thanks to the pH-sensitivity and its ease of use for transfection; while the latter is one of the most prominent amphiphilic polymers certificated for clinical use by the FDA thanks to its biodegradability and biocompatibility.

2.4.3.1 **PMPC-PDPA Diblock Copolymer**

The PMPC-PDPA diblock copolymer has been extensively studied in different therapeutic and physiological set ups. Besides traditional application of intracellular delivery of anticancer drugs, such as doxorubicin and paclitaxel ([177], [178]), PMPC-PDPA POs have been implemented for a wide range of therapeutic applications. One of the most recent works used PMPC-PDPA for the intracellular delivery of the anti-rheumatic drug methotrexate in *in vivo* model of arthritis [179]. In this study, it was shown the ability of the loaded-POs were able to target macrophages and to successfully dampen the chronic inflammation, both *in vitro* and *in vivo* [179]. It was also observed that the prolonged administration of PMPC-PDPA POs *in vivo* did not manifest subacute systemic toxicity, nor immunogenic effects. Notably, it was also observed a mild anti-inflammatory effect in the empty PMPC-PDPA PO group control, which is currently under investigation [179].

PMPC-PDPA polymer is also known for its ease of internalisation *via* receptor-mediated endocytosis by interacting with the ubiquitously expressed Scavenger Receptors (SRs) family, such as type B class 1 (SRB1), CD36 and CD81 *via* phosphorylcholine (PC) groups present in the PMPC blocks [180]. Thus, PMPC polymer can be used as natural ligand for the targeting of cells with high expression of SR-B1 and CD36, such as cancer and immune cells [181]–[183]. The specific interaction of PC with CD81 is current subject of investigation. The CD81 receptor belongs to the superfamily of tetraspanin, transmembrane receptors involved in cell-

to-cell interactions and recently reported its implication during hepatitis C virus (HCV) [184], [185]. It has been shown that SR-B1 and CD81 were found to associate and interact upon HCV infection, assuming a similar dynamism upon PC binding [186],[187].

Additionally, PMPC-PDPA PO is an ideal intracellular delivery system because of their pH-sensitivity [188]. The amine group of the DPA monomer is a weak cationic polyelectrolyte with a pKa of 6.3 (Figure 9, [189]). At acidic pH, the PDPA is a hydrophilic block fully dissolved in acidic water but becomes hydrophobic at higher pH. Hence, self-assembled PMPC-PDPA vesicles are stable when maintained in physiological condition (i.e., pH 7.4) but start disassembling once internalized via endocytosis [190] [191][192]. Subsequently, the sudden increase in number of charged molecules leads to an osmotic pressure, which release the cargo into the cytoplasm (endosome escape, Figure 10) [193], [190].

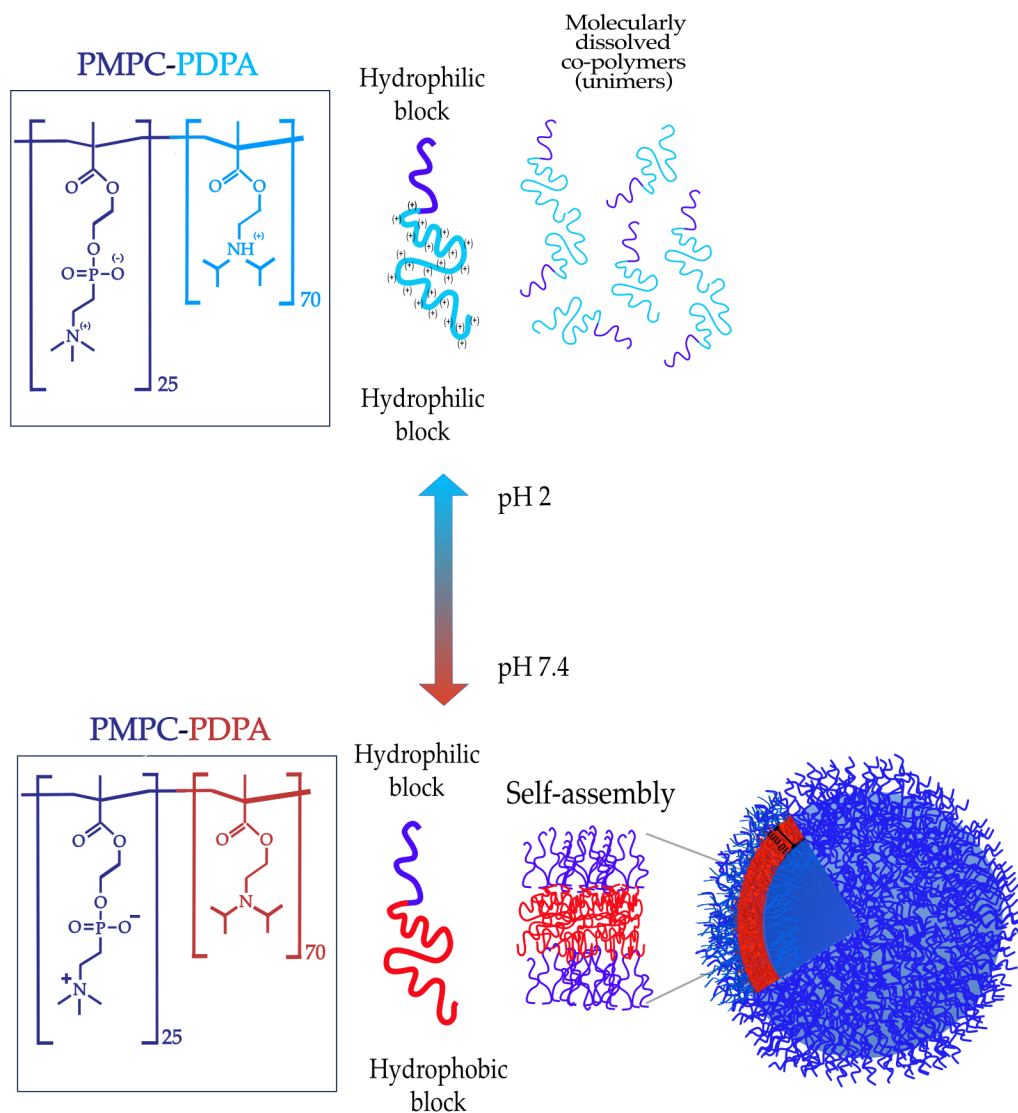


Figure 9: PMPC-PDPA Structure and Self-assembly.

Cartoon representation of PMPC-PDPA self-assembly by pH switch is reported in A). Both PMPC and PDPA are hydrophilic in a water solution with pH under 6.4 (top). When pH is higher than 6.4, PMPC-PDPA start to self-assemble into vesicles (bottom). Image created using Affinity and Biorender.

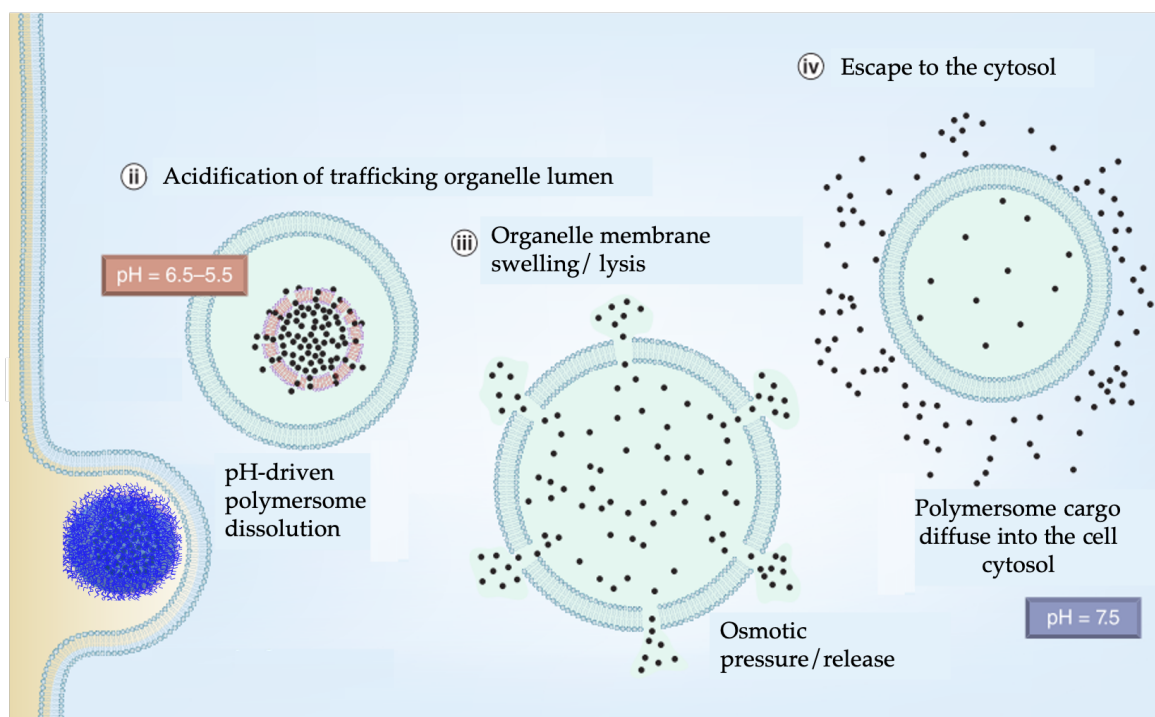


Figure 10: POs Cellular Entry.

POs enter cells via SR-B1 and CD36 receptors forming the early endosome via membrane fusion. Endocytic vesicles are maintained to a range of 6.5–4.5 thanks to ATP-dependent proton pumps [194]. The endosome couple with a lysosome vesicle in the proximity of the membrane and as the pH drops (around pH 6) the vesicles dissemble. Finally, due to the osmotic pressure raising up, with consequent swelling of the endolysosome, the payload is released into the cytoplasm. Image readapted from [171].

PMPC-PDPA copolymer nanocarriers are of recent formulation and have not enter in clinical trials yet, but they have been proven to be an efficient carrier for a variety of molecules *in vitro* and *in vivo* [177], [178], [195].

Their efficiency of delivering intracellularly is thanks to their the pH-sensitiveness, their ease in being uptaken by immune cells and their capability to be loaded with DNA, which makes them an ideal candidate for cancer vaccine development [171], [181], [196], [197].

2.4.3.2 PEG-PLA Diblock Copolymer

The polyethylene glycol (PEG) polymer is one of the most extensively used antifouling polymers in nanomedicine, being classified as safe to use by the FDA back in the 1990s [198]–[200]. Another polymer widely used in pre-clinical and clinical studies is the poly(lactic acid) (PLA). PLA is a biodegradable, compostable aliphatic polyester. It is considered a thermoplastic characterised by high-strength and is

degraded by simple hydrolysis into water and carbon dioxide through a citric acid cycle. [201]. For these reasons the PLA has been widely used as scaffold material for drug-loaded NPs and when combined with PEG (Figure 11), the resulting diblock copolymer is an ideal material for drug delivery *in vivo* [202].

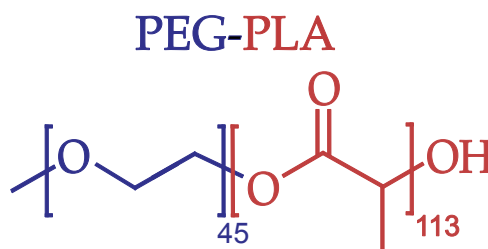


Figure 11: Chemical structure of PEG₄₅PLA₁₁₃ used in this work.

After decades of clinical use, an increasing body of evidence indicates the production of anti-PEG IgM antibodies and immune response upon PEGylated drugs administration, posing a new challenge for the researchers [203], [204]. Anti-PEG immunity has been already observed in healthy blood human donors, raising concerns over the general acceptance of non-immunogenic and non-antigenic properties of PEG and its future application in clinic studies [205].

There is an increasing attention from scientists to overcome this limitation. In a recent study, different functional groups such as methoxy (OCH₃), hydroxyl (OH), carboxyl (COOH), or amino (NH₂) were introduced to a PEGylated liposome. Their cross-reactivity with anti-PEG IgM was evaluated *in vitro* and it was observed that hydroxyl-PEGylated liposomes presented the less immunogenic alternative across the different preparations [206].

2.5 New Perspective for the Active Targeting

The scientific community has devoted considerable effort to the design of NPs for the targeting of cancer cells and, more recently, immune system cells, which play a vital role in tumour clearance [207],[208]. Precise and specific delivery of drugs comprises one of the most challenging goals in medicine.

In cancer treatment, the fine control of the selectivity of the treatment towards the target tissue is ultimately essential to avoid systemic side effects raised from the toxicity of the drug on healthy cells and tissues.

With this notion in mind, drugs, peptides, and antibodies for therapeutic purposes have been screened and selected as the ones with the highest strength of the binding for the respective receptor (affinity) remaining at the core of modern medicine discoveries. From this, arises an important problem. In many diseases, cancer being the prime example, the dysfunction is frequently related to endogenous receptors that are expressed in both healthy and cancer cells. It is impossible for the therapeutic drug selected with high affinity for its receptor to discriminate healthy vs unhealthy target, based purely on the presence of its receptor. Because of this, most medications have side effects, and many have failed to make it through the clinical pipeline.

One way to overcome this setback, it is once again to look at biological systems. Nature has evolved ways to perfectly regulate complex interactions with chemicals, proteins, nucleic acids, and cells interfacing with one another with the highest degree of selectivity by implementing a multitude of interactions (multivalency, or polyvalency) at the same time [209]. In many instances, cells require a variety of ligand-receptor interactions (multiplex) as well. The cell membrane is a remarkable example of spatiotemporal modulation of intricate biological interactions, based on perfected multivalent and multiplex-combinatorial bindings [210]. Perhaps, the key to selectivity in nanomedicine is in the multivalent and multiplex bindings between nanoparticles and their target.

Affinity can be defined by the amount of drug binds to the receptor and it is governed by the similar thermodynamic principles that can be regulated or modelled

as a reversible reaction. It can be mathematically represented by the inverse proportion of the potency of the drug ($\frac{1}{K_d}$), where K_d is the dissociation constant [211], [212], [213].

The binding between the ligand (L) and its receptor (R) modelled as reversible reaction can be usually expressed with the law of mass action for a reversible reaction: ‘the number of receptors site $[R]$ occupied by a drug depends on the plasma drug concentration $[L]$ and the association and dissociation rate constants K_{on} and k_{off} of drug receptor complex” [213]. It is assumed that the components can freely diffuse in solution and can be expressed as follows:



Where k_{on} and k_{off} are, respectively, the rates of association and dissociation (or binding and non-binding).

At the equilibrium, the K_d can be expressed as

$$K_d = \frac{k_{off}}{k_{on}} = \frac{[L][R]}{[LR]} \quad (3)$$

While the energy of binding can be expressed with a simple model of interaction between two rigid objects (or ‘lock and key’ model,[214]), as it follows:

$$E_{bind} = -kT \ln\left(\frac{\rho_0}{K_d}\right) \quad (4)$$

Where k is the Boltzmann constant, T is temperature, ρ_0 is the standard concentration.

However, the binding between the ligands on the NP’s surface and their receptors is more complex than the simple ‘lock and key’ model and the ‘degeneracy’ factor must be included in the equation. Degeneracy (Ω) is defined as “the number of ways in which i bonds can be formed between two multivalent entities and depends on the spatial arrangement of both ligands and receptors” [209] (Figure 12).

Therefore, the energy of binding can be expressed as:

$$E_{bind} = -kT \ln\left(\Omega_{tot} \frac{\rho_0}{K_d}\right) \quad (5)$$

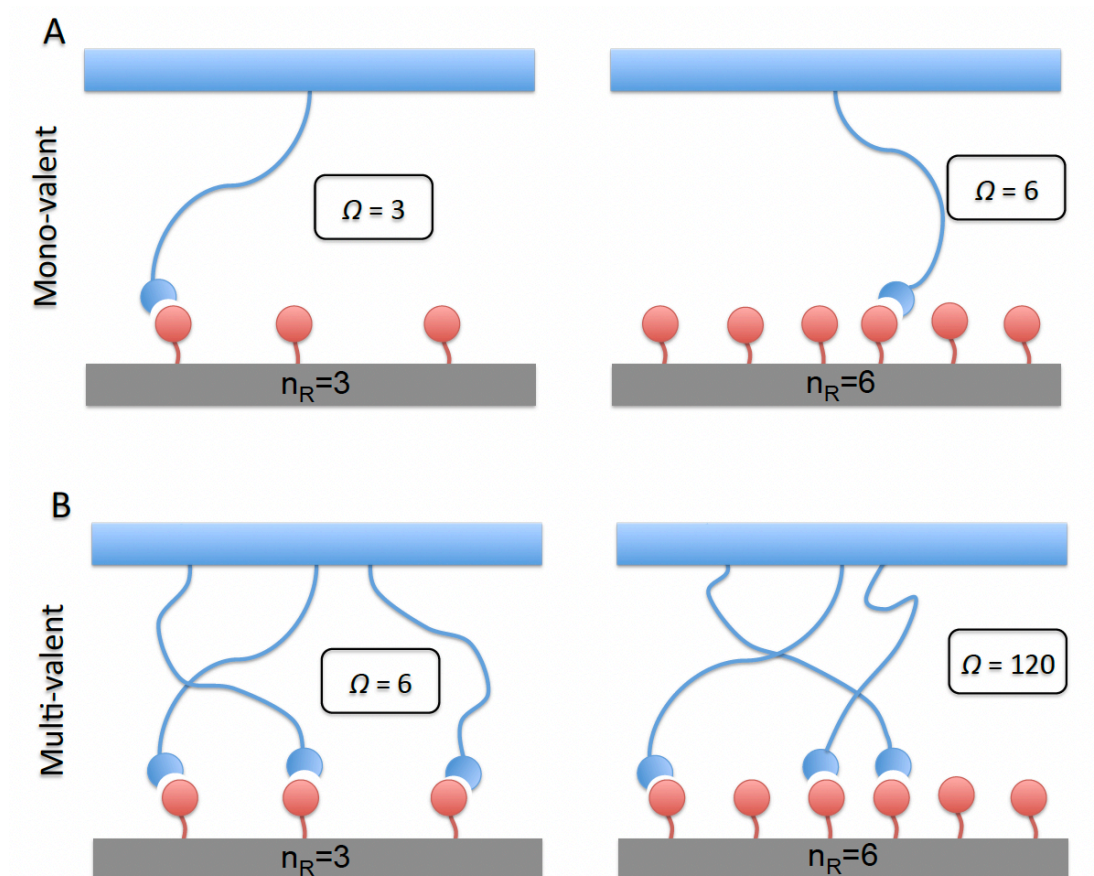


Figure 12: Schematic Representation of the Degeneracy Factor (Ω). In the case of monovalent binding (section A of the figure) between one ligand and 3 or 6 receptors, the degeneracy factor results to be $\Omega = 3$ or $\Omega = 6$. Whereas, in the case of multivalent binding with flexible poly-chain ligands, the Ω notably increase. Therefore, degeneracy depends by both the number of receptors (n_R) and the number of ligands linked to a flexible polymer-chain. Figure adapted from [209].

As previously stated, the high-affinity ligand against a specific receptor might not provide sufficient discrimination [215]. Once more, biology systems provide an excellent starting point for enhancing the selectivity of precise targeting, as specific interactions are in perfect place as a result of thousands of years of biological evolution [210]. Multivalent interactions are critical in most biological processes. They allow the translation of weak bonds into strong ones, thanks to cooperativity. For example, the building blocks of DNA are highly selective while pairing, although the underlying interactions are rather weak (hydrogen bonding and $\pi - \pi$ stacking). To this end, the “superselectivity theory” (SST) hold the promise to achieve the precise active targeting of cells, discriminating from the others by the different level of expression of the same receptor [216]. Further refinements of this model involve

taking into consideration other factors involved in the binding, such as the steric hindrance and ligands multiplexing on NPs, reaching for what is considered a 'range of selectivity', which is determined by a specified window of number of receptors on a surface that uniquely identify a cell phenotype [217].

The approach is particularly important for improving cancer vaccines, where the precise targeting of DCs, amongst all other cell types, is crucial for the co-delivery of antigens and adjuvants [215].

2.5.1 Superselectivity Theory

Examples of multiple low-affinity interactions as tool of refined discrimination between cell phenotypes are already present in literature [210], [218], [219]. For instances, in work published in 2006 by Carlson et al., it was demonstrated with a series of elegant experiments that the complement-mediated cell death was in fact induced only on cell lines with high receptor expression, by low affinity and multivalent interactions, effectively discriminating across different cell lines classified by the receptor expression [219].

Noting such peculiar behaviour in physiological conditions, Martinez-Veracoechea and Frenkel proposed the concept of 'superselectivity theory' (SST) [216]. With their statistical mechanical simulations, they elegantly demonstrated that the fine discrimination between cell types can be achieved by employing multivalent nanoparticles with low-binding affinity for receptors expressed at medium- high level on a given membrane/surface [216]. It was shown that the resulting binding system is sensitive to the amount of receptors on the membrane surface, generating a highly non-linear dependence (*superselectivity*) with an 'on-off' binding behaviour (Figure 13) [216]. According to the theory, multivalent particles with weak interactions for the receptor are needed for the superselectivity [216]. Thus, monovalent particles with strong binding energy (mono-strong, blue curves in Figure 13.A) for the receptor immediately saturate the surface already with very few receptors. In a physiological setting, this translates to a widespread, non-specific binding of particles in organs/tissues presenting the same receptor expressed at a low level. On the other hand, weak-monovalent particles saturate the surface at high-level of expression,

which is not suitable for physiological applications (Figure 13.A). Instead, multivalent particles with weak affinity are refractory to the binding at low numbers of receptors on the surface, whereas they quickly saturate when receptors reach a specific number, creating the 'on-off' binding behaviour. Such behaviour offers a very selective tool, sensitive to the number of receptors on the surface (Figure 13.A).

The adsorption of the nanoparticles on the cell surface can be described using the Langmuir-Hill isotherm equation:

$$\theta = \frac{zq}{1+zq} \quad (6)$$

Where θ is the fraction of the bound particles to the surface, z is the nanoparticle activity and q is the partition function that describes the interaction between a single particle and the surface.

However, the SST presents two major setbacks. Firstly, weak single bond binding to untargeted receptors can nonetheless collectively result in a large binding energy, which drives non-specific adsorption; and secondly, the computational model creates the superselective profile by employing a very low affinity of ligands, corresponding to binding energies of few $k_B T$. This is poorly realistic, with water hydrogen bond being $-8 k_B T$ one of the lowest binding energies [216].

One way to lower the total binding free-energy of the system could be to induce steric hindrance (see Glossary) between the nanoparticles and the surface [220]. Such objective can be achieved (1) by embedding the targeting ligands within a nanoparticle brush of the hydrophilic block and (2) by using a combination of different types of targeting ligands in the same PO (multiplexing), enabling targeting of cells that overexpress distinct combinations of receptors [221].

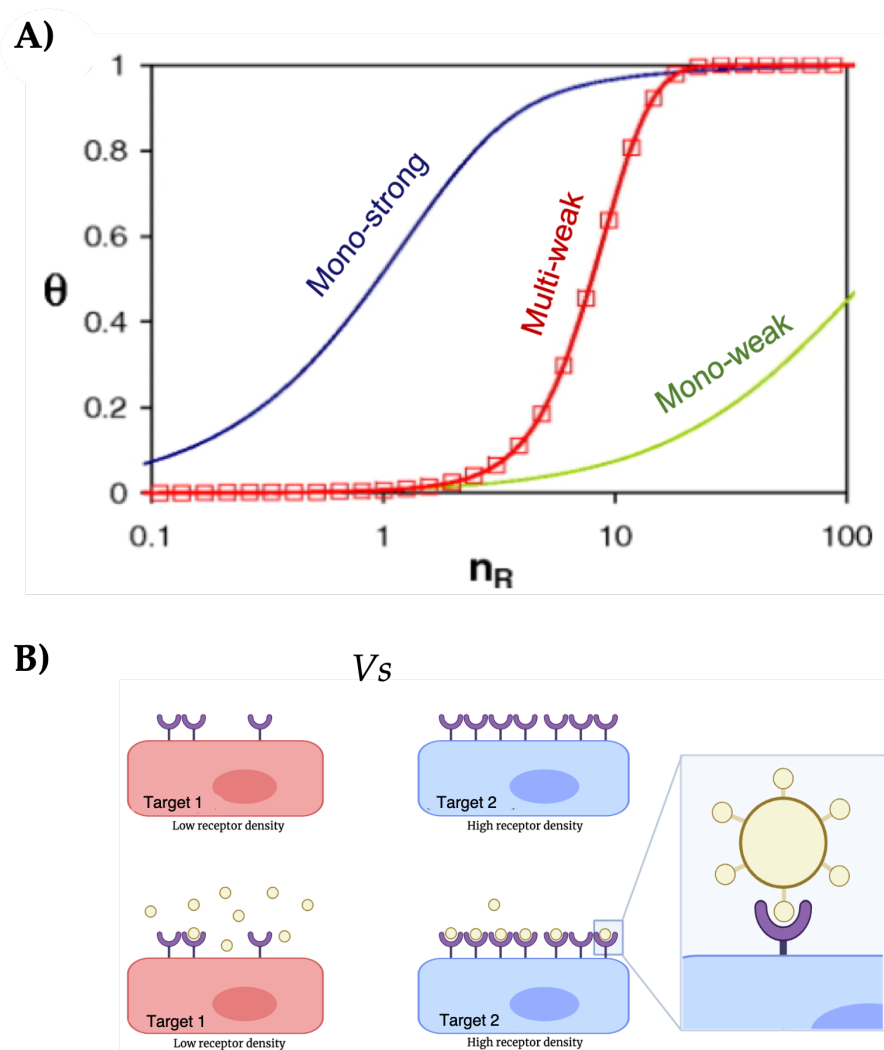


Figure 13: Principles of the STT.

Figure in A) represents results from in silico analysis, which demonstrates that neither strong (in blue) nor weak (in green) monovalent particles can achieve the appropriate targeting sensitivity; rather, multivalent particles with weak interactions (in red) with the receptor are required for superselectivity. In fact, monovalent particles with strong affinity for the receptor quickly saturate the surface receptors, not ideal for physiological applications. Figure B) represents the concept of multivalency in particles for the selective binding of a surface with medium-high number of receptors. Such behaviour could be favourable in physiological condition for the selected targeting of tissues or cells that are presenting on their surface the specific receptor highly expressed. Image adapted from [216].

2.5.2 Macromolecular Crowding and Steric Hindrance

Surprisingly, the majority of the experiments of NP binding and cellular uptake are conducted without taking into consideration the macromolecular crowding on the extracellular surface [222]. A major contributor to the macromolecular crowding is the

glycocalyx, a brush-like layer of glycolipids and glycoproteins located in the outermost region of the cell membrane [212]. (Figure 14). Physiologically, any interaction between a ligand and its receptor on two different cells that need to communicate, has to encompass the steric repulsion (hindrance) originating from the glycocalyx being in close proximity. Indeed, the glycocalyx plays important roles in a variety of cellular functions, such as cell-cell recognition, cell-surface signalling and adhesion [223].

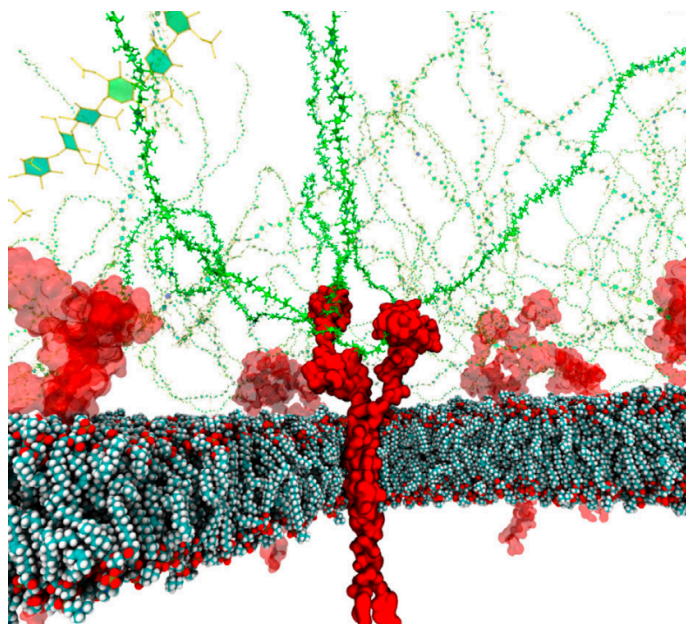


Figure 14: Macromolecular Crowding in the Extracellular Environment. Figure depicts the MD computational modelling of the glycocalyx. The sugar chains (green) are linked to the transmembrane proteins (in red) that are embedded within the phospholipid cellular membrane (blue-light beads). Image adapted from [224].

Like cells, POs made of diblock copolymers also have a brush-like layer on their external surface. Such polymer brush will inevitably come in close contact with the cell glycocalyx. The optimal balance of attraction and repulsion could offer the fine level of selectivity required for the precise active targeting.

In a recent paper from the Battaglia's group the concept of decreasing the overall energy of interaction of the system was explored by embedding ligands within the POs brush itself and taking in consideration the contribution of the glycocalyx during the interaction for the final design of NP 's architecture (Figure 15) [221].

As shown in the *in silico* work done by Martinez-Veracoechea and Frenkel in 2011, the binding affinity utilised for the multi-weak particle is exceedingly low, below any known physiological binding energy [216]. In this new strategy of NP design, it has been proposed that the possibility of including the steric hindrance originated from the polymer brush and glycocalyx coming in close proximity into the final equation of the total energy of binding.

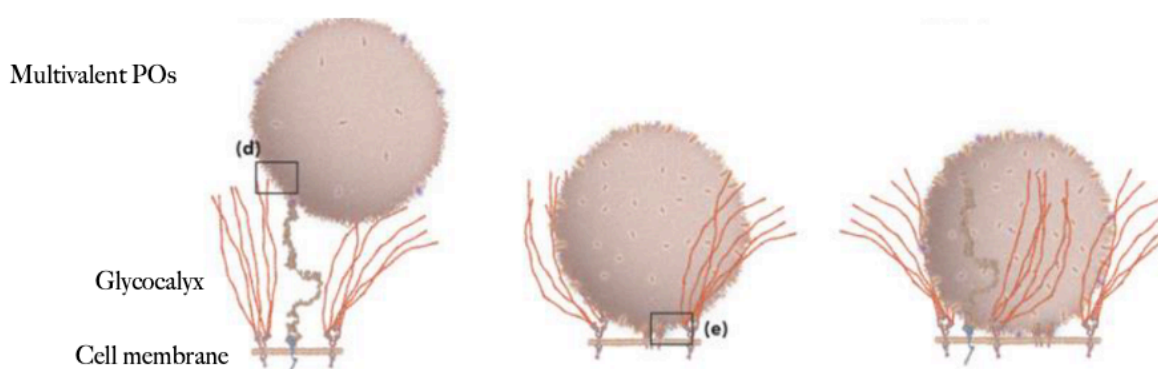


Figure 15: Schematic Representation of the Steric Hindrance between the POs and the glycocalyx on the surface of a cell membrane. Image edited from [221].

2.5.3 Multiplexing Polymersomes

Multiplex nanovesicles have been conceptualized as a means of achieving the desired avidity and hence the best possible superselectivity. Multiplex nanovesicles are functionalized with several ligand types to target distinct receptors and might be embedded into the PO brush at different length, using hydrophilic block. Thus, the suboptimal targeting ligands affinity will co-operate for a better targeting of cell/tissue with a certain amount of receptor expressed on their surface (also known as range selectivity) [221]. In a work published in 2020 by Tian et al., the idea of superselectivity of brain endothelial cells (BECs) with a combination of experimental and analytical analysis was explored. BECs can be targeted using targeting ligand for the lipoprotein receptor-related protein 1 (LRP1), namely Angiopep. Angiopep-decorated POs were proven to target and cross BECs, as described elsewhere [225]. Models of targeting were first simulated *in silico*, observing the energy of binding and taking into consideration contributions from steric hindrance from the glycocalyx/polymer brush. Next, the model was validated experimentally

using fluorescent angiopep and PMPC-decorated POs with different density of targeting ligands. Fluorescent signal derived by the cellular uptake was detected and analysed by confocal laser scanning microscope, generating a sigmoidal progression in cells. The binding profiles obtained experimentally were combined together to generate a binding landscape reported in figure [225]. Although some assumptions were made in the computational modelling and the theory being still at embryonic stage, it was anticipated that a multivalent-multiplexing POs might present a synergistic binding behaviour with higher selectivity for the targeting in respect of multivalent POs.

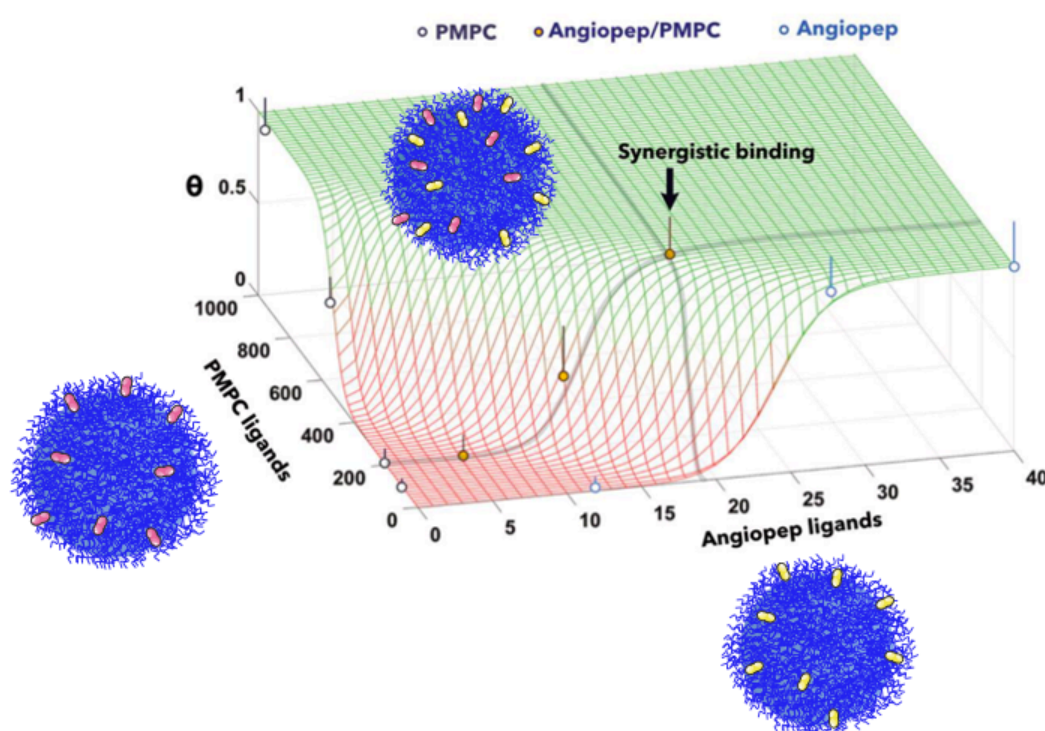


Figure 16: Achieving the Superselectivity with Multiplex Multivalent NPs. Image taken from [225].

2.5.4 Range Selectivity

Generally, one of the major setbacks of the active targeting in anticancer therapy is the considerable unspecific binding due to multi-organ receptor expression at different density and lack of exclusive receptors. This setting may appear challenging for the preparation of targeting-NPs with conventional design method,

yet it is ideal for exploring new architectural approaches and shifting from strong affinity targeting ligands, to weak and multivalent ones. In recent years, many computational studies have been able to uncover the potential benefits of multivalent NPs, considering a multitude of variables including the steric repulsion and the multiplexing as ways to reach a higher degree of selectivity. In a 2020 publication, authors implemented a combination of theory, numerical modelling and experiments, to explore the new concept of *range selectivity* as in “the ability, under appropriate conditions, to only bind to targets where the receptor density is within a certain range, but not below nor above” (Figure 17) [226].

The range selectivity approach would enable the identification of an exact range of receptor density in which the binding is effective. In other words, at lower receptor density levels, the multi-weak binding total energy is not adequate [226]. At high receptor density, the overall steric repulsion resulting from the confinement of ligands and receptors, the compression of the polymer brush and cell glycocalyx, prevent the absorption of the NP to the surface (Figure 17, left) [226]. As a result, a 'sweet spot' of N_R may be uniquely targetable for that cell (Figure 17, right). Every cell type may presumably be recognised by a distinct surface phenotype. The combination of the different type of receptors expressed at distinctive density levels in combination with the cell glycocalyx, makes each cell phenotype a target that can be aimed with a unique '*combinatorial*' PO (multiplex and multivalent), achieving the *phenotypic targeting*.

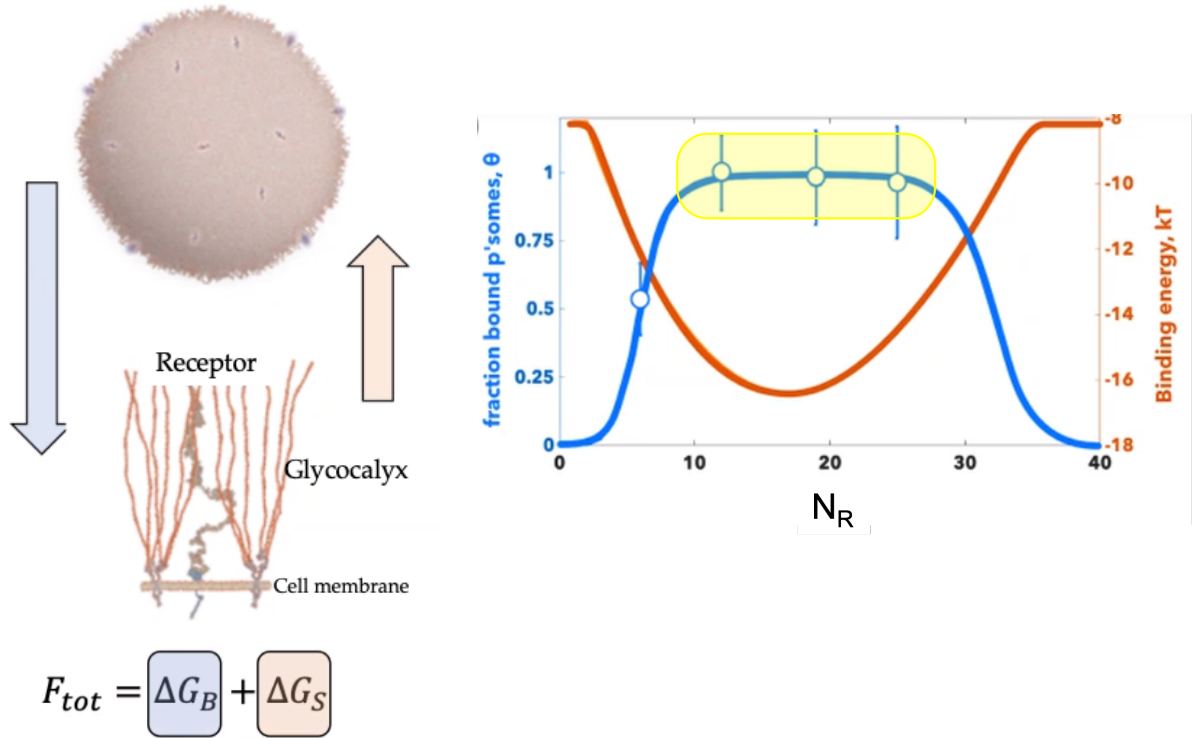


Figure 17: Achieving the Phenotypic Targeting with the Range Selectivity method. On the left, schematic representation of the total energy of binding is the sum between the free energy of binding (ΔG_B) and free energy from steric repulsion (ΔG_S). The latter takes in consideration the compression of the polymer brush upon the binding, the excluded volume interactions from the cell glyocalyx and the confinement of ligands between the cells and NP surface. Figure on the right, represents a schematic model of progression of θ (fraction of bound particles.) in function of the binding energy in kT and number of receptors on the surface (N_R). The model should help identifying the 'range' of N_R (in yellow) for the active targeting of cell phenotypes. Image adapted from [226].

As previously mentioned, one of the major setbacks for cancer vaccine development is the direct delivery of antigens and adjuvants in the correct cell phenotype, such as DCs, to initiate a robust adaptive immunity response.

To enhance their development, a novel *in vivo* antigen-loading platform is needed. Implementing the Range Selectivity theory for the architectural design of POs, might help to overcome these limitations.

2.5.5 Targeting Skin APCs

In terms of drug delivery, the route of administration is a rather crucial aspect of the disease management itself. The gold standard of immunotherapy administration in clinic is the intravenous (i.v.) injection [89]. Systemic infusion presents obvious advantages, such as predictable serum pharmacokinetics, practical and technical simplicity of administration and widespread of available infrastructures. Nonetheless, i.v. infusion of immunotherapies has a few of downsides. These are associated with heavy side-effects derived from the route of administration of the treatment, which then has to be administrated at sub-optimal doses [89]. Moreover, the drug circulating in the blood system has to overcome physical barriers to infiltrate into solid tumour [227].

On the other hand, several pre-clinical studies have shown a superior tumour control upon intratumoral injection of ICI or PRR agonists, along with decreased toxicity, improved efficacy as well as abscopal effects (see Glossary) [228], [229], [230]. Regrettably, it is rather invasive technique for the patients and certain location of the body are not of easy access, therefore intratumoral injection of cancer therapies are still a seldom in clinic [231].

An alternative route of administration of immunotherapy, including cancer vaccines, is the intradermal (i.d.) injection. The skin is a highly active immunological organ that defends the body against environmental hazards, inducing protective immunity against pathogens. This involves several complex cutaneous immunological systems controlled by various cells in the skin [232], [233]. The skin is enriched with various types of APCs (e.g., macrophages, Langerhans cells and dermal DCs) ready to detect exogenous invaders [232], [233]. Importantly, as previously stated, APCs, such as DCs, offer a crucial connection between innate and adaptive immune responses by migrating to skin-draining lymph nodes to present antigens to T and B cells in order to mount the adaptive immune response [232], [233]. Thus, topical immunisation is a very appealing method for patients. However, the stratum corneum (top layer of the skin) hinders topical administration of antigens and adjuvants from penetrating the skin efficiently. Topical immunisation can be

administered with conventional needles, but this procedure is uncomfortable and technically demanding

Despite the benefits of cutaneous vaccination over current immunisation routes, the skin has been underutilised for clinical immunisation due to a lack of effective drug delivery systems that enable safe, reproducible, and patient-friendly deployment of antigens to skin microenvironments [234]. In recent decades, significant developments in biomaterials science, nanotechnology, and microfabrication have facilitated the creation of sophisticated intracutaneous drug delivery devices, such as micro-needles arrays (MNAs). Normally, MNA designs consist of multiple micron-scale sharp-tipped projections linked to a supporting substrate. The micro-needles have diameters, ranging from 100 to 1000 μm , and made by different materials, such as silicon, glass, sugar etc. [235]. They might represent the valid device that is able to pierce into the skin with in a minimally invasive and pain-free manner [235].

Moreover, NP-based vaccines can further improve the immunisation thanks to the prolonged release of antigen, the possibility to co-deliver the adjuvant within the same NP and to enhance uptake in APCs and more specifically DCs or macrophages thanks to the phenotypic targeting [236].

In fact, as previously stated, DCs play a crucial role in immunizations and cancer management. Methods for delivering tumour antigens in DCs are still sub-optimal, with extensive culture periods and cell manipulation which negatively affect the DC activation and cytokines production [126]. Nanomedicine might offers an effective platform for antigen delivery in DCs *in vivo via* DC-specific surface receptors, such as CD207, CD206 and other members of the Scavenger Receptor family.

2.5.5.1 Langerin Receptor

Langerin, a C-type lectin receptor and PRR (see Glossary) also known as CD207 (Figure 18), is a PRRs predominately expressed on Langerhans cells (LC) which, were first identified and characterised in 1869 by Paul Langerhans [237], [238]. LCs are a sub-population of DCs present in the epidermis and on stratified mucosal tissue. They are in the frontline for interaction with pathogens and they constitute approximately 2-4% of all epidermal cells [239] [233].

Several studies have highlighted the LCs as promising targets for cutaneous vaccine, as they are able to cross-presenting antigens to CD8+ T cells and to strongly activate CD4+ T cells responses [240], [241]. These dendritically shaped cells in the skin are distinguishable for their typical internal rod-shaped structures, named Birbeck granules [238],[242]. These granules form a component of the endosomal recycling system that has been found to implicated in internalisation and degradation of pathogens, including HIV [243]. Because of its role in antigen processing and inflammation, Langerin is an attractive targeting for immunisation studies. Liposomes functionalised with heparin-inspired glycomimetic ligands were employed for the development of a platform targeting for transcutaneous cancer vaccines [244]. Crystallography studies indicate that this receptor trimerizes at the time of binding, which might be of relevance for binding studies with combinatorial POs [237].

2.5.5.2 Mannose Receptor

The mannose receptor (MR, MRC1, or CD206, Figure 18) belongs to the C-type lectin receptor superfamily and it's first member of endocytic receptors family that include CD205, CD280 and M-type phospholipase A₂ receptor (PLA₂R) [245]. CD206 is expressed in cells of the mononuclear phagocyte (MNP) lineage, such as macrophages, immature DCs, endothelia cells, dermal fibroblasts and keratinocytes [245]–[248]. Although some studies indicate CD206 expression as marker of immature DCs, it also marks the alternatively activated macrophages, known as M2, in contrast with classically activated macrophages (M1) [249]. CD206 recognise specific glycoproteins on the surface of bacteria, fungi or other pathogens. Similar to Langerin, CD206 belongs to the class of PRRs and plays a role in immune recognition of pathogens, internalisation and presentation [250], [251]. For its role in inflammation and pattern expression in dermal cells, CD206 can be exploited as novel target for cancer immunisation [252].

2.5.5.3 Scavenger Receptors (SRs) Family

Scavenger receptors (SRs) are a 'superfamily' of membrane-bound receptors that are involved in the bind and internalisation of low-and high- density lipoprotein (LDL and HDL). In recent years, new families of SRs and their features have been found and categorised into 10 eukaryotic groups, designated as Classes A-J

[253],[254], [255]. Amongst all SRs, it is worth mentioning the SR-B and CD36 receptors (Figure 18) for their interaction with PC molecules in the hydrophilic block of PMPC as previously described (Paragraph 2.4.3.1). Besides their role in the uptake and cholesterol metabolism ([255]), It is now recognised that several ligands, including endogenous proteins and pathogens, bind to SRs. As example, some studies have highlighted their role in mediating the entry of Hepatitis C Virus [256], [257]. SR-B1 and CD36 sequences are highly conserved across species and expressed ubiquitously in mammalian cells, especially in intestine, immune cells, endothelial cells, smooth muscle cells, keratinocytes, adipocytes, and placenta [258]. Regardless the ubiquitous expression of SR-B1 and CD36, these receptors still represent a valid DC-targeting options nowadays, thanks to the principles of the range selectivity theory [187].

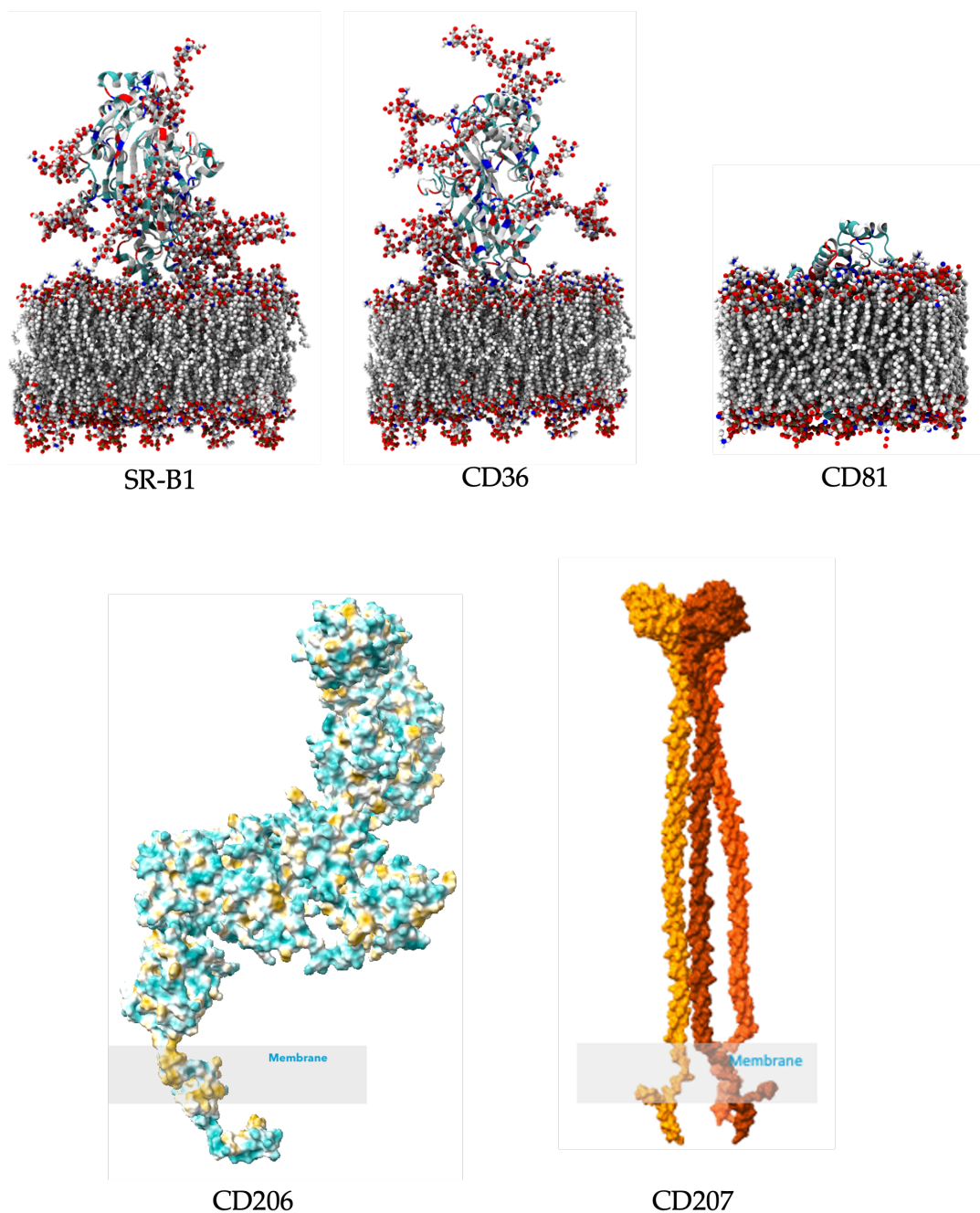


Figure 18: Molecular Modelling of Surface Receptors for phenotypic targeting of DCs.

Structure models on top row (left to right) represent SR-B1, CD36 and CD81, known to interact with PMPC blocks. SR-B1 and CD36 are members of the SRs family and are known to interact with the PC molecules of the PMPC hydrophilic blocks. CD81 belongs to the superfamily of tetraspanin, involved in cell-cell interactions. Interestingly, it has been found to be associated with SR-B1 during HCV infection. If PC is natural ligand for CD81 is still under investigation.

CD206 and CD207 are PRRs and expressed at different levels in macrophages or DCs, immune cells with pivotal roles in inflammation and adaptive immune response. They represent pivotal target for immunotherapy and tumour control. The thickness of the cellular membrane was arbitrary set at 4 nm for all receptors. The author thanks Dr Acosta and Prof Battaglia for providing the modelling structure.

3 Hypothesis and Aims

The main hypothesis of this PhD is the design of a combinatorial (multivalent and multiplex) PO for phenotypic targeting of DCs for the development of a new class of DNA cancer vaccines (Figure 19).

The project tested three different hypotheses through specific aims:

Hypothesis (I)

POs can be used to efficiently encapsulate plasmid DNA encoding for antigen model (OVA) for the intracellular delivery in DCs and to prove the antigen surface presentation.

Aims:

- To produce and characterise PMPC-PDPA POs loaded with plasmid DNA encoding for OVA antigen protein.
- To quantify the number of loaded plasmid DNA molecules in POs.
- To assess the PO cellular uptake in dendritic cells model (DC2.4), the intracellular delivery of the cargo and surface presentation of SIINFEKL peptide through MHC class I protein.

Hypothesis (II)

PMPC-PDPA POs loaded with STING agonist cGAMP can activate the IFN type I response and inflammation in targeted DCs cellular model but not in 'cold tumour' cellular model.

Aims:

- To produce and characterise PMPC-PDPA POs loaded with STING agonist cGAMP.
- To quantify the number of loaded cGAMP molecules in POs
- To assess the PO cellular uptake in dendritic cells model (DC2.4) and cold tumour cellular model (B16F10-OVA)
- To investigate the inflammatory power of loaded-cGAMP in PMPC-PDPA POs as adjuvant in cancer vaccine and immunogen in tumour eradication in animal model

Hypothesis (III)

Functionalised combinatorial PEG-PLA POs designed with the 'range selectivity' theory can identify and target specifically different cell phenotypes based on the differential expression of surface receptors.

Aims:

- To identify and select surface receptors for the phenotypic targeting of DCs, such as SR-B1, CD36, CD81, CD207 and CD206.
- To screen and validate suitable CD207-specific peptides through phage display.
- To perform and quantify the efficiency of the click-addition of peptides on PEG-PLA polymer for the production of multivalent POs.
- To produce and characterise multivalent POs
- To characterise and quantify differential receptors expression on designated cellular models, such as DC2.4, MutuDC and NIH3T3.
- To perform binding assays *in vitro* in designed cellular model.
- To validate the phenotypic targeting *in vitro* using multivalent and multiplex PEG-PLA POs.
- To assess the phenotypic targeting of multivalent and multiplex PEG-PLA POs *in vivo* upon intradermal injection.

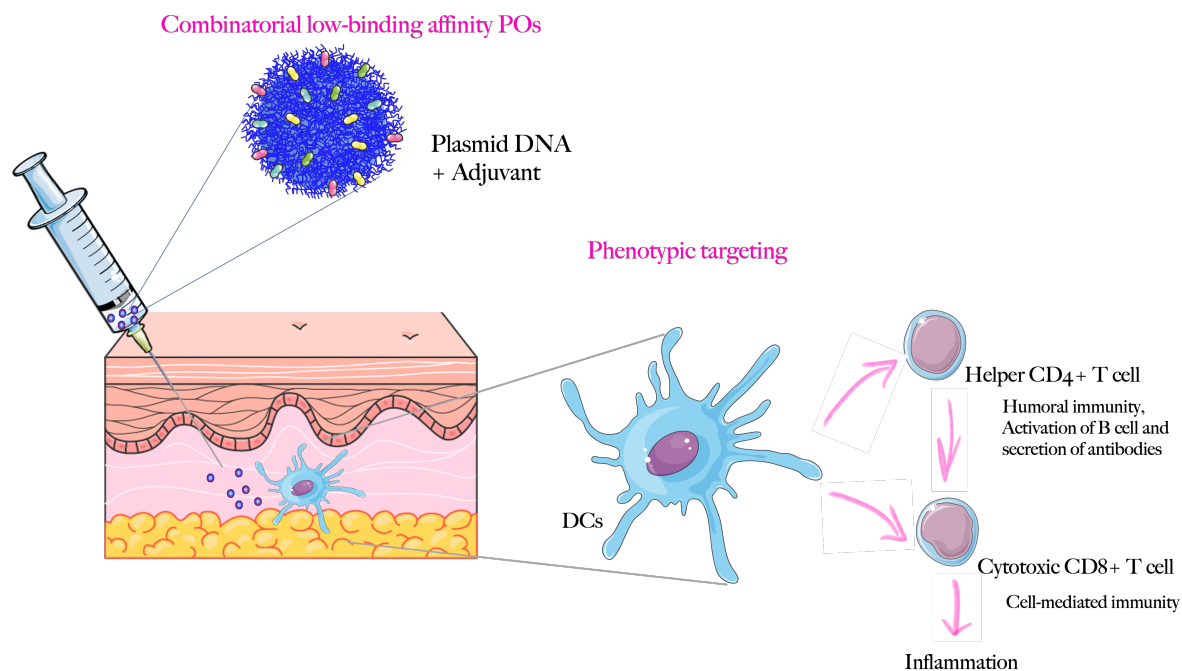


Figure 19: Graphic Abstract of Main Research Hypothesis of this Project.

In this investigation, biocompatible pH sensitive POs are used for the intracellular delivery of antigen encoding plasmid and adjuvants molecules in DCs. In parallel, biocompatible and biodegradable POs are functionalised with multiplex low-affinity binding ligands for the phenotypic targeting of skin DCs. Ultimately, upon intradermal injection, low-binding combinatorial POs loaded with antigen and adjuvant will be taken up by the DCs resident in the skin and activating an immune response through antigen presentation to CD4+ and CD8+ T cells in the afferent lymph node, leading to tumour inflammation and elimination. Image created using Servier Medical Art.

4 Materials and Methods

4.1 Polymersomes Preparation and Characterisation

4.1.1 pH Switch and DNA Encapsulation

Self-assembly of PMPC-PDPA POs and plasmid DNA (pDNA) encapsulation were obtained by pH switch method (Figure 20). Briefly, 10 mg of PMPC-PDPA polymer (synthesised by ATRP by Dr Duro-Castano as described elsewhere [189]) was dissolved in a glass vial containing an organic mixture of 2:1 chloroform: methanol. The vial was placed in a vacuum desiccator at 37°C for 48 hours upon which the polymer film was rehydrated with 2 mL of sterile PBS pH 2. The solution was then filtered through syringe filter (Millex, Syringe Filter 0.22 μ m, PES membrane, # SLGP033RS) into an autoclaved glass vial with a sterile stirring magnet. The pH of the solution was brought to 6.0 by injecting 0.5M NaOH with a syringe pump at the constant rate of 2 μ L/min while monitoring the pH with a pH meter (Mettler Toledo, #LE422). Once the pH stabilised around 5.9 - 6, 500 μ g of pDNA

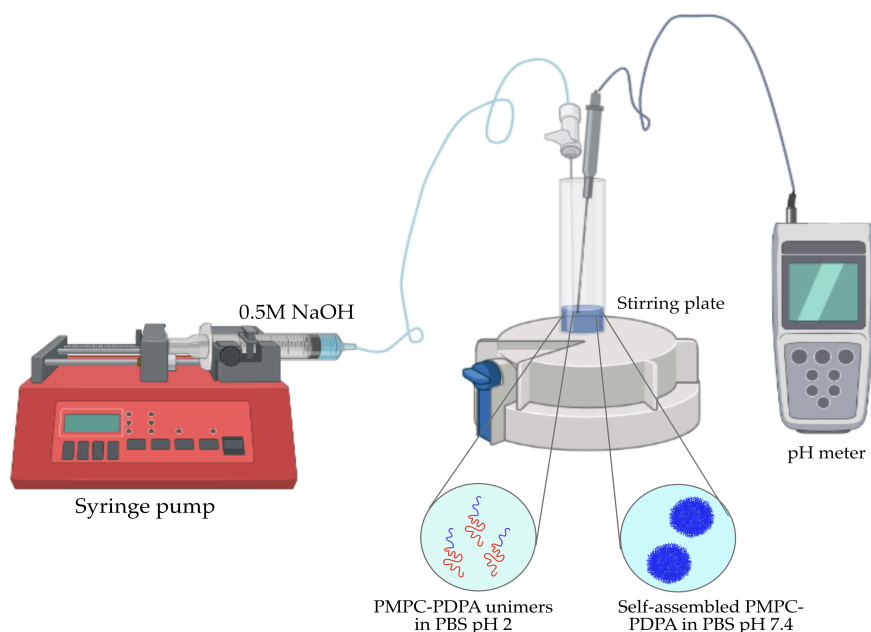


Figure 20: Set-up for pH switch self-assembly method

(pDNA-PresentER-SIINFEEKL-GFP; Addgene #102944, Supplement Material S 1) were added into the solution. Finally, the pH of the solution was brought to the final pH of 7.4.

4.1.2 Solvent Switch

Empty PMPC-PDPA POs were obtained by using solvent switch method. PMPC-PDPA diblock polymer (10 mg) were initially dissolved in 3:1 (v/v) methanol (MeOH): tetrahydrofuran (THF) into a sterile glass vial with a magnet. Then, the polymer solution was stirred at 350-400rpm, while PBS (2.3mL) at pH 7.4 was injected at the steady rate of 2 μ L/min over the course of 19h using a syringe pump (Figure 21). To remove the organic solvent from the preparation, the sample was left in dialysis against PBS at pH 7.4 (8 changes for minimum of 4h each time). Finally, the excess of PBS was removed from the formulation using a hollow fiber filter (MicroKros, cut-off of 500kDa, #C02-S05U-05-S, Spectrum Labs).

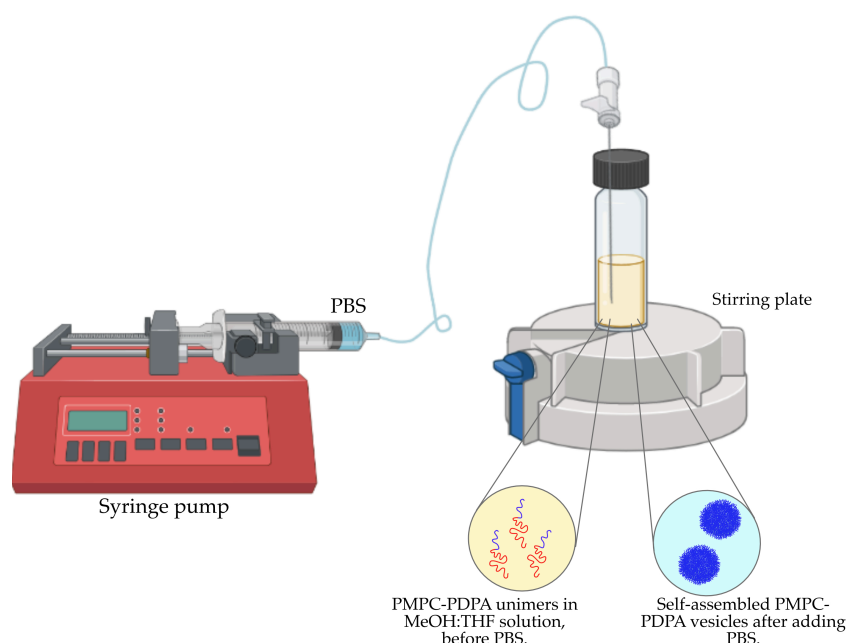


Figure 21: Schematic representation of solvent switch method for POs preparation.

4.1.2.1 cGAMP Encapsulation

Following the preparation of the empty PMPC-PDPA POs by solvent switch, 2'3'-cGAMP STING ligand (#tlrl-nacga23, Invitrogen, Figure 22) was encapsulated

by electroporation. In this method, a high-voltage electric pulse is applied to the PO, the bilayer membranes of POs temporally destabilised, allowing small molecules to cross the membrane [259].

Briefly, equal volumes of empty PMPC-PDPA vesicles (200µl at 5.5.mg/mL) and cGAMP (dissolved in LPS-free dH₂O at 2 mg/mL) were added into a cuvette and 5 pulses at 2500V were applied. The sample was left to recover overnight at 4°C and then purified from unloaded cGAMP by size exclusion chromatography (SEC, asdescribed in Paragraph 4.1.4) using LPS-free PBS.

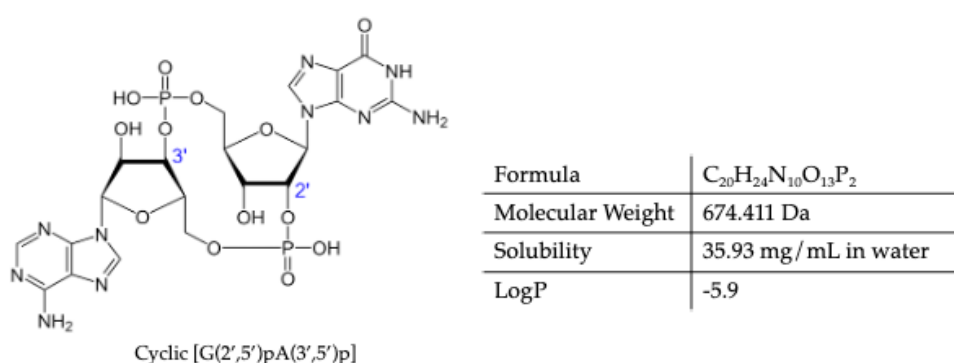


Figure 22: Chemical Structure and Properties of cGAMP. Source PubChem.

4.1.3 Solvent Displacement

For the binding assay, several batches of fluorescent PEG-PLA formulation with different %molar amounts of ligand were prepared by solvent displacement method as it follows.

Each polymer mixture (20mg of total polymer mass) was first dissolved in 1 mL of dimethylformamide (DMF) and loaded into a glass syringe. A sterile glass vial and magnet containing 2.3 mL of sterile milliQH₂O was placed over stirring plate and the temperature was set at 42°C (above the transition glass temperature (T_g) of the PEG-PLA polymer). The polymer solution was injected into the milliQH₂O at the steady rate of 50 µl/min. Once the injection was completed, 1.7mL of sterile milliQH₂O were added to stabilise the colloidal suspension. For fluorescent POs, a 5% molar percentage of Rhodamine B octadecyl ester perchlorate (Sigma-Aldrich, #83683, ex543/em570) was added to the polymer mixture before self-assembly.

Fluorescent PEG-PLA POs were detected by confocal imaging and by plate reader to confirm the cellular uptake.

The same protocol was performed for the preparation of POs for i.d. injection *in vivo*. New batch of formulation was made to meet the requirements of animal experiment. As fluorophore was chosen Cy5.5-PEG-PLA polymer at 5% molar mass, rather than Rhodamine as previously described. This fluorophore has been proved to provide a better signal and easier to track in *ex vivo* validation experiments in our labs.

4.1.4 Purification of Polymersomes

After preparation by self-assembly, PO formulations were centrifuged for 10 min at 1000xg to eliminate large aggregates formed during the self-assembly. A Size Exclusion Column (SEC) was used to separate POs (30-120 nm) from non-encapsulated biomolecule, such as Rhodamine, free cGAMP or free pDNA-SFKL. The column was packed with porous beads of agarose (Sephacrose 4B Sigma, #4B200) that allow small molecules to pass through the solid phase with a longer retention time, compared to larger molecules.

As a precautionary step, pDNA-loaded samples were treated with DNase I enzyme (New England Biolabs, #M0303S) to digest free pDNA-SFKL molecules, as they might interfere with quantification. For the DNase I digestion reaction mix, 10 μ L of enzyme were added to 800 μ L of POs solution containing 90 μ L of buffer enzyme 10X. The reaction was left in incubation for 20 min at 37° C before proceeding with SEC.

4.1.5 Polymersomes Characterisation

4.1.5.1 Dynamic Light Scattering (DLS)

Information about sizes and distribution for all prepared formulations were obtained using the dynamic light scattering (DLS).

Two assumptions are made in order to obtain particles size information: (i) particles in the fluid are subjected to Brownian motion and (ii) any particle is assumed to be a hard sphere [260]. Essentially, the method analyses the fluctuation of the

scattered light yielded from the detector and correlates it with the average intensity of particle diameter in solution. A Helium-Neon laser (with $\lambda = 633\text{nm}$) is used to illuminate the particles, the intensity of the light scattered fluctuates over very short timescales at a rate that is dependent upon the size of the particles; smaller particles are displaced further by the solvent molecules and move more rapidly. Analysis of these intensity fluctuations correlates with the velocity of the Brownian motion and hence with the particle size estimated as hydrodynamic diameter (d_H). Due to the assumptions previously described, the hydrodynamic diameter can diverge from the physical diameter when calculated using the Stokes-Einstein equation (abbreviations and their definition in Table 1:

$$d_H = \frac{kT}{3 \pi \eta D} \quad (3)$$

Abb	Definition	Abb	Definition
d_H	Hydrodynamic diameter	k	Boltzmann's constant
T	Absolute temperature	η	Viscosity
D	Diffusion coefficient		

Table 1: Abbreviations and definitions for the Stokes-Einstein equation.

The correlation function compares the similarity between two signals or one signal with itself at different time intervals, and it is used to determine the diffusion coefficient of the particles. If signals are comparable at time t, the correlation curve will decrease from 1 to 0 in a smooth sigmoidal curve. The curve quickly decays if particles are small and moving rapidly but will persist for a more extended period if large particles are present, offering a first indication of the mean size of the sample (Figure 23).

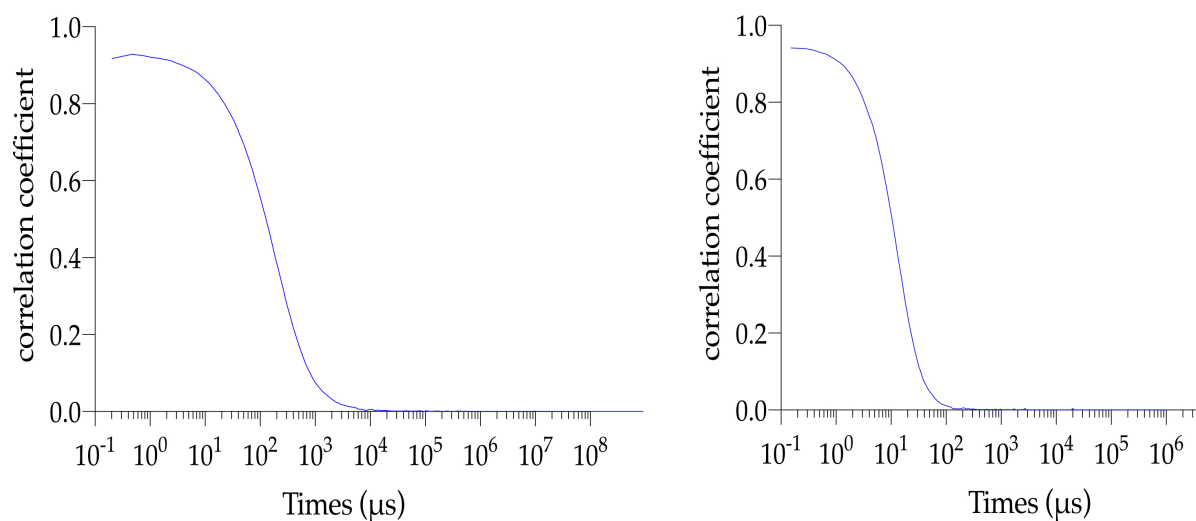


Figure 23: Examples of correlograms from a sample containing large samples (left) and a sample containing smaller vesicles (right). Graphs obtained during POs preparation.

The particle diffusion is measured by its scattering intensity in function of time generating an autocorrelation function (ACF). The ACF is based on the number of scattered light strikes measured and it is proportional to the concentration of the sample being analysed, with values comprised between 0.8 and 1 [261].

Variation in particle size during the manufacture of polymersomes is referred to as polydispersity and the Polydispersity Index (PDI) is a dimensionless value comprised between 0.05 (highly monodisperse) and 0.7 (broad size distribution) [167]. Experimentally, polymersomes formulations with PDI between 0.1 and 0.3 are generally observed and considered monodispersed. Any preparation with a PDI greater than 0.4 should be carefully analysed prior usage, to determine if such polydispersity is an artefact of the instrument or a trustworthy representation of the sample [262].

For the analysis, samples were diluted in phosphate buffered saline (PBS, pH 7.4) at the final concentration of 50 ng/μL in a final volume of 500 μL in a polystyrene cuvette (DTS0012), analysed using Malvern Zetasizer Nano ZS laser light scatterer equipped with a He-Ne 4mW 633 nm laser, with an average of 3 runs at a set angle of 173°.

The electro-kinetic potential (ζ -potential) of particles in a colloid system was also analysed using DLS. For the analysis, 5 μL of each sample was added into 995 μL of dH_2O and placed into a disposable capillary cuvette.

4.1.5.2 **Transmission Electron Microscopy (TEM)**

TEM was used to confirm the morphology and size of the POs. This microscopy technique uses a focused electron beam, generated by an incandescent filament, to image micro- and nano-sized materials. A few microliters of POs dispersion were deposited onto the glow-discharged copper grid side for one min, then the excess of the sample was removed with filter paper. Heavy metal stains can promote heavy atom deposition on the sample to enhance sample structural details from the background. For this purpose, samples are treated with 75% (w/w) phosphotungstic acid (PTA) for 5 seconds before being removed. Grids were then dried under vacuum and imaged using a JEOL microscope using 100kV voltage tension

4.1.5.3 **Reverse Phase- High Performance Liquid Chromatography (RP-HPCL)**

The concentration of PMPC-PDPA in each formulation was quantified using RP- HPLC using a Jupiter C18 column (#00G-4057-U0, 5 μm , 300 \AA , 4.60 mm x 250 mm, Phenomenex). The instrument allows the separation of different molecules based on their hydrophobicity, which depends on their binding to the stationary phase [263].

As the ratio between different solvents in the mobile phase changes, it reaches a critical value for each analyte which desorbs from the stationary surface and elutes from the column. The elution is followed by the detection of absorbance, which results in a peak that can be used for identification and quantification.

For the analysis of PMPC-PDPA samples, it was utilised a gradient method with 0.05% (v/v) trifluoroacetic acid (TFA) in methanol (phase A) and 0.05% (v/v) TFA in ultra-pure water (Phase B). The separation method used is described as follows: 5% A to 100% A in 10 min following a linear gradient. Then, 100% A was maintained for 15 min and returned to 5% A in one min in a linear gradient, then maintained for

6 min. The flow was set at the constant elution of 1 mL/min. Samples were dissolved in PBS pH2 and measured at 220nm.

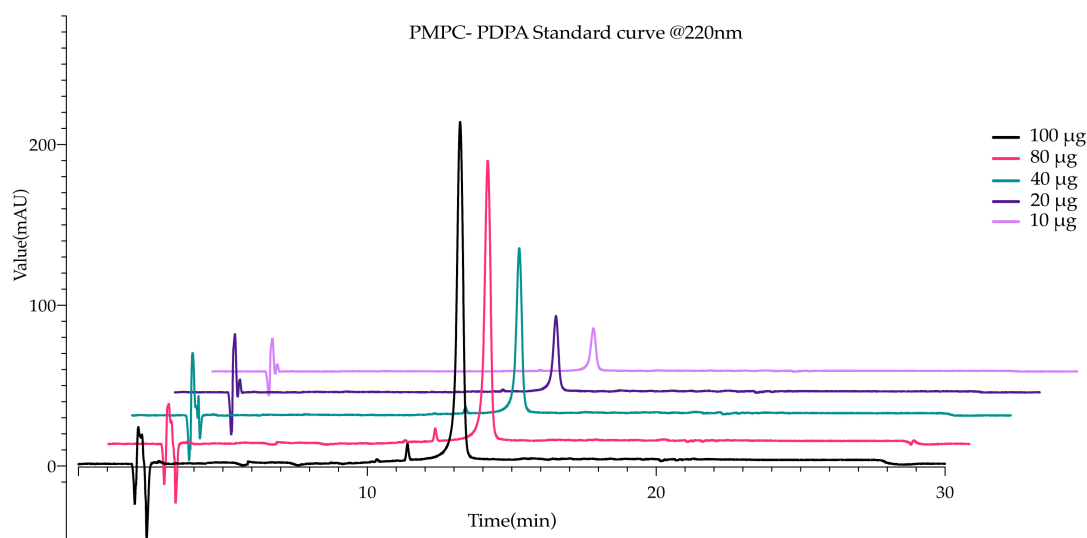


Figure 24: PMPC-PDPA Chromatogram at RP-HPLC (220nm). Graph is reporting absorbance peaks obtained using a wavelength of 220nm at RP-HPLC. Peak's areas were interpolated with respective mass of polymer injected, obtaining a standard curve which was then used for quantifying PMPC-PDPA concentration in formulations.

For quantifying PEG-PLA formulations, samples were dissolved in acetonitrile (sample to solvent 1:3, (v/v)) and analysed with same gradient method implemented for PMPC-PDPA utilising acetonitrile (phase A) and ultrapure H₂O (phase B). Data were analysed with Thermo Scientific Chromeleon Chromatography data system software. Representation of PMPC-PDPA standard curve measured at 220nm is reported in Figure 24.

The parameter of Production Efficiency (PE) was used to assess the efficiency with which POs were formed, both empty and pDNA-loaded. PE is defined as the percentage of final polymer mass recovered after self-assembly and purification over the initial total mass, and is expressed as:

$$Production\ Efficiency\ (\%) = \frac{Final\ polymer\ mass}{Initial\ polymer\ mass} \times 100 \quad (7)$$

RP-HPLC Quantification of the encapsulated cGAMP was obtained by RP- HPLC using absorbance at 260nm, and different amount of free cGAMP were injected for the analysis. Relative peak areas were used to build a standard curve which was then used to estimate cGAMP encapsulated into PMPC-PDPA (Supplement Material S 4).

4.1.6 Encapsulant Quantification and Loading Efficiency

Due to the risk of DNA precipitation in presence of organic solvents within the column, it was not possible to quantify the mass of encapsulated pDNA-SFKL by RP-HPLC. To overcome this limitation, the quantification of the encapsulated pDNA-SFKL was done by using a Quant-iT PicoGreen dsDNA kit (#P7589). The assay is based on the fluorescence emitted by the PicoGreen upon binding to a dsDNA molecule. Prior to the assay, PicoGreen was diluted 1:200 in 1x TE buffer (ThermoFisher, #J62285.AK) at pH 7.4 as recommended by the manufacturer. A calibration curve was obtained using empty POs (diluted in TE Buffer at 0.2 mg/mL) spiked with 1:2 serial dilutions of pDNA-SFKL from 1 to 0.03125 µg/mL final concentration. A volume of 10 µL of pDNA-SFKL:PMPC-PDPA formulation was added in the PicoGreen solution. The plate was left in the dark at room temperature (RT) for 5 min, and then fluorescence was measured using a microplate reader (Tecan) at absorption/emission 502/523 nm. The signal from empty POs was subtracted as blank from the raw values.

With the quantification of encapsulated biomolecules, it was possible to estimate the encapsulation efficiency (E) and the loading efficiency (L_E) [264]. E represents the ratio between the mass of biomolecule encapsulated within the lumen of POs and the initial total mass, and can be found as follows (abbreviations and definitions in Table 2):

$$E = \frac{M_D}{M_{D0}} 100 \quad (8)$$

Where:

$$M_D = [D] V_s \quad (9)$$

$$M_{D0} = [D]_0 V_s \quad (10)$$

L_E expresses the ratio between the measured number of biomolecules encapsulated per POs (L_N) and the number of biomolecules that can be theoretically loaded within the POs (L_N^T). L_E can be found with the following expressions:

$$L_E = \frac{L_N}{L_N^T} \quad (11)$$

where

$$L_N = \frac{N_b}{N_p} \quad (12)$$

$$N_b = \frac{M_b}{M_{wb}} N_A = \frac{C_b V_s}{M_{wb}} N_A \quad (13)$$

The total numbers of POs (N_p^i), can be calculated thanks to the size distribution for width as followed:

$$N_p^i = \frac{M_c}{M_{wc} N_a^i} N_A R^i = \frac{C_c V_s}{M_{wc} N_a^i} N_A R^i \quad (14)$$

where

$$N_a^i = \frac{\rho_{PDPA} V_{PDPA}^i}{M_{wPDPA}} N_A \quad (15)$$

$$V_{PDPA}^i = \frac{4}{3}\pi [(r-d)^3 - (r-d-l)^3], \text{ see Figure 25} \quad (16)$$

Then the total number of POs is equal to:

$$N_p = \sum_l^n N_p^i \quad (17)$$

The L_N^T value is calculated assuming that the concentration of biomacromolecule encapsulated within the collected POs is equal to the initial concentration:

$$L_N^T = \frac{N_b^T}{N_p} \quad (18)$$

where

$$N_b^T = \frac{M_b^T}{M_{wb}} N_A \quad (19)$$

$$M_b^T = M_b^0 \frac{V_p}{V_s^0} \quad (20)$$

$$V_p = \sum_l^n (N_p^i V_p^i) \quad (21)$$

The value obtained by implementing the formula in (13) provides the first indication if the process of encapsulation is driven by diffusion ($L_E = 1$), by positive supramolecular interaction ($L_E > 1$) or hindrance ($L_E < 1$) [264].

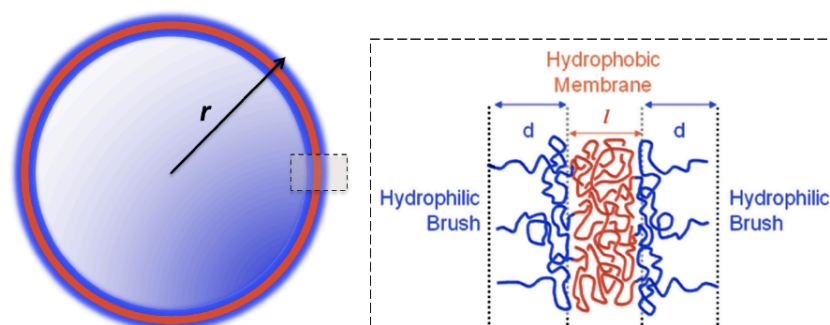


Figure 25: Schematic representation of a transversal section of POs.
Figure edited from [264].

Abb	Definition	Abb	Definition
M_{D0}	Initial moles of pDNA	M_D	Moles of biomolecule in the collected solution after purification (CSAP)
$[D]_0$	Initial molar concentration of biomolecule	$[D]$	Molar concentration in the CSAP
L_N	Loading Nb of pDNA per POs	L_N^T	Theoretical loading Nb
M_b^0	Initial mass of pDNA	M_b	Mass of pDNA in the CSAP
C_b^0	Initial concentration of pDNA	C_b	Concentration of the pDNA in the CSAP
V_s^0	Initial volume of the solution	V_s	Volume of the CSAP
N_b	Number of pDNA in the CSAP	N_p	Number of POs in the CSAP
M_b^T	Theoretical mass of pDNA withing the PO		
C_c	Concentration of the copolymer in the CSAP	M_c	Mass of the POs in the CSAP
M_{wb}	Molecular weight of the pDNA	M_{wc}	Molecular weight of PMPC-PDPA copolymer
N_A	Avogadro's number	N_p^i	Number of POs in the CSAP
N_a^i	Copolymer aggregation number of single PO	R^i	POs number ratio of each population measured by DLS
M_{wPDPA}	Molecular weight of the PDPA block	ρ_{PDPA}	Density of the PDPA block (1.05 g/cm) ³
V_{PDPA}^i	Volume of the PDPA block in a single PO	r	POs radius
d	Hydrophilic PMPC block brush length	l	Hydrophobic PDPA block thickness
N_b^T	Theoretical number of pDNA within the collected POs in which with the C_b^0	M_b^T	Theoretical mass of pDNA within the collected POs in which with the C_b^0
V_p	Total internal volume of POs	V_p^i	Internal volume of a single PO

Table 2: Abbreviation and definition used to calculate the Loading Efficiency.

4.1.6.1 Calculation of Number of Ligands

By approximating the diblock copolymer to a cylinder embedded in a curved surface, it is possible to estimate the total number of 'cylinders' that constitute a PO

(Figure 26) [265]. From this, it is possible to obtain an estimation of the number of ligands pre implementing simple geometric considerations. For these calculations it has been assumed that each PO present in the sample preparation is a perfect bilayer sphere with an internal core.

Based on Hyde's work, it could be assumed that the packing factor can be determined with the following equation:

$$p = 1 + Hl + \frac{Kl^2}{3} \quad (22)$$

Where H is defined as the mean curvature of the amphiphilic monolayer, K is the Gaussian curvature of a surface and l is the length of the polymer block.

For the final estimation of the total number of ligands present on a single PO, calculations have been made for both the external monolayer curvature hydrophobic interface (left) and internal monolayer hydrophilic interface (right), as it follows:

$$K_{ext} = \frac{1}{(r - l_H)^2} \quad \left| \quad K_{int} = 1 \frac{1}{(r - l_H - l_L)^2} \quad (23)$$

$$H_{ext} = \frac{1}{(r - l_H)} \quad \left| \quad H_{int} = -1 \frac{1}{(r - l_H - l_L)} \quad (24)$$

packing factor of external layer:

$$p_{ext} = 1 + H_{ext} l_L + (K_{ext} l_L^2)/3$$

packing factor of internal layer:

$$p_{int} = 1 + H_{int} l_L + (K_{int} l_L^2)/3 \quad (25)$$

Where l_H is the length of the hydrophilic block (i.e., PMPC) and l_L is the length of the hydrophobic block (i.e., PDPA) represented in Figure 26.

To estimate the total number unimers present in each hydrophilic and hydrophobic monolayer (namely 'number of aggregates', N_{agg}), it was first necessary to calculate the volume as:

$$V_{ext} = \frac{4}{3} \pi [(r - l_H)^3 - (r - l_H - \frac{l_L}{2})^3] \quad (26)$$

$$V_{int} = \frac{4}{3} \pi [(r - l_H - \frac{l_L}{2})^3 - (r - l_H - l_L)^3] \quad (27)$$

Where r is simply the radius of the particle obtained by DLS analysis (Figure 26).

Then the N_{agg} were calculated following equations as it follows:

$$N_{agg_{ext}} = \frac{p_{ext} V_{ext}}{v_l} \quad \left| \quad N_{agg_{int}} = \frac{p_{int} V_{int}}{v_l} \quad (28)$$

and v_l represent the volume of the hydrophobic block expressed as:

$$v_l = \frac{N_L M_{LH}}{\rho_L N_A} \quad (29)$$

where N_L is degree of polymerisation of hydrophobic block, N_A is Avogadro number , M_{wl} is molecular weight of hydrophobic block and ρ_L is density of hydrophobic block. Next, the total number was obtained as:

$$N_{agg_{tot}} = N_{agg_{ext}} + N_{agg_{int}}$$

Finally, it was possible to obtain the final number of ligands included in a PO

$$Nb \text{ ligands} = \left(\frac{\% \text{ conjugation eff} \times \text{Mol ligand}}{100} \right) N_{agg_{tot}} \quad (30)$$

Where the % of conjugation is calculated empirically by BCA assay and the moles of the ligand represent the ratio between the moles of the ligand conjugated and the total moles added during the click-addition reaction.

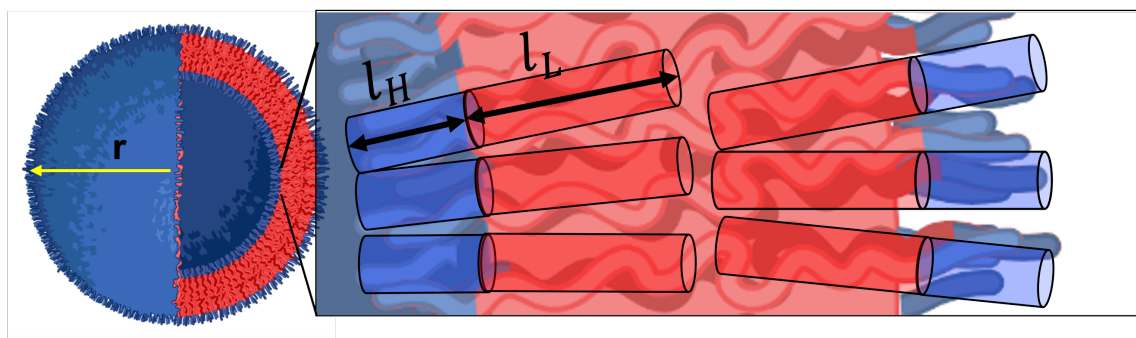


Figure 26: representative cartoon of unimers arranged in the hydrophobic interface membrane.

Image created using Biorender.

4.2 Phage Display

4.2.1 Cloning, Transfection and Expression of CD207 Receptors

For the identification and selection of CD207-targeting peptides, first step was to clone and express the extracellular domain of CD207 to be used as bait during phage display technique. The extracellular domain sequence is a carbohydrate-binding C-type lectin domain (CTLD) and it was identified using

UniProt (<http://uniprot.org>). To facilitate the expression, protein secretion and purification steps, the CTLD was cloned into a plasmid backbone along with additional features such as hCD33 secretory signal peptides, AviTag™ and His-Tag. The DNA sequence encoding murine and human CD207 were ordered from GenScript.

Cloning of Plasmids

The cloning of huCD207 or moCD207 inserts into pDEST (Invitrogen, Figure 27) was performed using NEBuilder HiFi DNA Assembly mix kit (New England Biolabs, #E2621S) allowing the assembly of linear DNA fragments, regardless their length. In an Eppendorf tube, 1 µL of linearised pDEST vector was added to 5 µL of oligo insert, 4 µL of nuclease-free water and 10 µL of NEBuilder Master mix. The reaction was incubated at 50°C for 30 min, and 2 followed by bacteria transformation using 2 µL. Next day, visible colonies were amplified and plasmids were extracted using Maxiprep Kit (Qiagen, # 12181). The correct sequences of the plasmids were confirmed by sequencing.

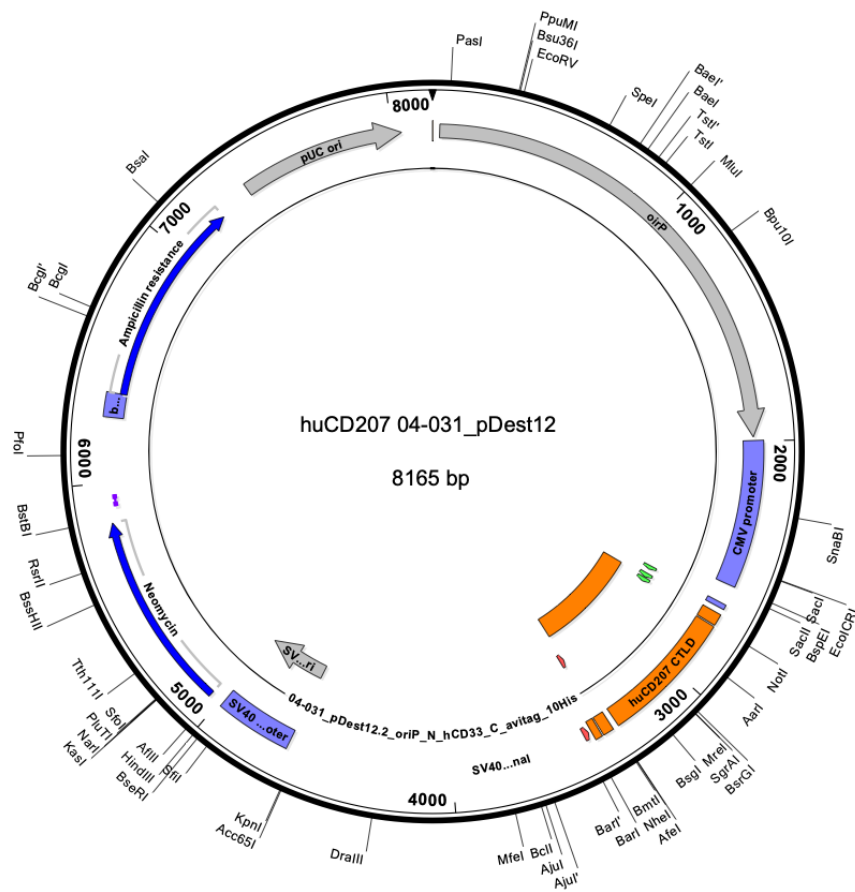


Figure 27: Representative structure of plasmid pDEST for expression of huCD207 and moCD207 CTL domain.

In the plasmid are present key features such as the CD33 signal is for protein extracellular translocation in mammalian cells (CHO), the AviTag™ sequence (GLNDIFEAQKIEWHE) for *in vitro* biotinylation and reversible binding of streptavidin to be used in protein immobilisation, purification and visualisation, and the HisTag sequences (typically 6 residues of histidine) has been inserted to facilitate purification and detection steps.

Transfection of Plasmids

For the expression of the receptors, the plasmids were transfected in Chinese hamster ovary (CHO) cell line using polyethylenimine (PEI), following a standard protocol provided by the company. Four Roller bottle 850 flasks of CHO cells were requested at a density of $\sim 2 \times 10^6/\text{mL}$. For a 5:1 (v/v) PEI: DNA with a $1 \mu\text{g}$ DNA/mL of CHO cells, a PEI mix was prepared adding 0.78 mL of PEI (initial concentration 10 mg/mL) to 49.2 mL of NaCl (at the concentration of 250 mM). For the DNA mix, 0.171 mL of pDEST DNA (at 3 mg/mL) was added to 8.02 mL of NaCl (at 250 mM). In a falcon tube, 8 mL of PEI mix was added to 8 mL of DNA mix, vortexed and incubated at RT for 1 min. The final mix was added to the 500 mL flask

of CHO cells, along with 5 mL of Pen/Strep. After 5h of incubation 37°C, 5% CO₂ and 250 rpm shaking, 17mL of feeding media (F009, produced in-house) and 1mL of extra supplements (F010, produced in-house) were added in each flask. Cells were left incubating at 34°C, 5% CO₂ and 250 rpm shaking for 72h. On day 3 and 5, more feeding media and supplements were added into each cell culture. On day 7, cells were collected into 500mL Corning tube and centrifuged at 4500rpm for 45min. The supernatant (where proteins of interests have been released) was filtered with a 0.2µm PES membrane and stored at -70°C before purification process. Protein expression was confirmed by western blot. A volume equal to 1mL was centrifuged for 5min at 3500rpm to remove debris. Of this, 40µL were added to 10µL of 4x Bolt LDS Sample Buffer (Invitrogen, #B0007) and boiled for 10min at 70°C before been loaded into pre-made Midi Protein Gels (NuPAGE™ 4-12%, Bis-Tris, 1.5mm, Invitrogen). Western blot run was performed at 200V for 20min in presence of NuPAGE™ MOPS SDS Running Buffer (Invitrogen, NP0001). Transfer of proteins to PVDF membrane was obtained using iBlot Transfer Stack (Invitrogen #IB301002) and iBlot Dry Blotting System (Invitrogen). Membrane was left incubating in 5% (w/v) skimmed milk-PBS for 1h at RT on rocking plate for blocking. Next, the membrane was incubated for 1h at RT on rocking plate with 1:10000 (v/v) anti-HisTag-horseradish peroxidase (HRP) antibody. The reaction substrate tetramethylbenzidine (TMB, Sigma #T0440) was added at 50µl/well and left incubating for 5-20min at RT. Chemical signal emitted by HRP enzyme was revealed by plate reader measuring absorbance at 450nm.

Purification of huCD207 and moCD207

All supernatant collected from cell growth was filtered to remove debris and concentrated using Amicon Ultra-15 Centrifugal Falcon tube (Merk) with a molecular weight cut off of 10K (MWCO) by centrifugating at 4000xg at 25°C for 5min.

The selection and purification of moCD207 and huCD207 proteins was achieved using AKTA Pure 25 1M chromatography system (Cytiva) comprised of a His-trap column (HiLoad 26/60 Superdex, Cytiva) that bound the His-Tag sequence

present on the proteins. Eluted solution containing moCD207 and huCD207 was probed again via western blot utilising same protocol previously described.

Biotinylation of huCD207 and moCD207

To secure proteins to a streptavidin-coated surface to perform phage display or ELISA, proteins of interests have to be biotinylated first. The biotinylation reaction of the protein huCD207 and moCD207 was performed using BirA enzyme (by AVIDITY LLC) and the protocol is described as it follows.

Purified proteins huCD207 and moCD207 were quantified via absorbance at 280 to estimate the concentration in solution. A volume equivalent of 40 μ M of each protein was added into a 1 mL Eppendorf tube where 40 μ L of BirA enzyme- biotin ligase (at initial concentration of 1 mg/mL) was added, along with 120 μ L Biomix-A (10X concentration: 0.5 M bicine buffer, pH 8.3) and 120 μ L of Biomix-B (10X concentration: 100 mM ATP, 100 mM MgOAc, 500 μ M d-biotin). The reaction was left incubating at 30°C for 40 min. Then, biotinylated-proteins were purified from all reagents using disposable PD-10 Desalting Columns (Merk #GE17-0851-01).

4.2.2 Phage Display for CD207-Targeting Ligands

Phage display is a technology based on the replicative potential of bacteriophage M13 into bacteria. Bacteriophage (phage) used for this methodology were previously engineered to introduce a short sequence of random nucleotides encoding for 12 amino acid peptide [266] [267]. Hence, each phage bears a different small peptide exposed on its surface, which will determine the selective binding to a solid phase during the screening.

In this work, and for simplicity, the protocol has been subdivided into 3 major steps: selection, screening and validation.

Selection

For the project, two engineered phage libraries (library nb° 8 and nb° 10, provided by AstraZeneca) were used to select DCs-targeting peptides.

First, 50mL of 2xTY (tryptone, yeast) medium were added in a 250mL flask with a single colony of *E.coli* TG1 cells taken from a freshly grown minimal media. The flask was left incubating at 37°C with shaking at 300rpm until bacteria culture reached mid-logarithmic growth phase ($OD_{600} = 0.5-1$). The growth was kept in ice until required for the bacteriophage infection stage.

For the first round of selection, a 50µL phage aliquot was added to 450µL of 5% (w/v) skimmed milk powder in PBS in a 1.5ml Eppendorf tube and incubated at RT for 1h. In the meantime, a volume of 100µL magnetic streptavidin beads (Dynabeads, Invitrogen) were added in a 1.5mL Eppendorf tube, pellet with a magnetic separator for 2min and resuspended in 1mL of PBS. Process was repeated a second time to wash the magnetic beads. Finally, beads were pellet down with a magnet and resuspended in 3% (w/v)milk-PBS and left in orbital shaker at 20rpm for 1h at RT for blocking.

Next, a 50µL aliquot of blocked beads was added to the volume of blocked library of phage and left incubating at RT for 1h in orbital shaker to remove phage that would bind streptavidin, reducing the risk of false positive selection. Beads were pellet down with magnet and supernatant with remaining phage was transferred in two fresh Eppendorf containing 300nM of biotinylated huCD207 or moCD207 previously purified and resuspended in 5% (w/v) milk- PBS. The phage library was left incubating with the biotinylated proteins for 1h at RT in orbital shaker at 600rpm (panning, Figure 28). Fresh magnetic beads (50µL) were added to each selection, mixed, and left equilibrating for 5min in the orbital shaker before been transferred in a deep-well 96-well plate (selection, Figure 28). To remove unbound phage and wash the beads, it was used the automatic system Kingfisher96. Magnetic beads were isolated and washed (exclusion, Figure 28) and remaining phage (selection, Figure 28) were finally eluted with the reducing agent triethylamine (TEA) at 0.1M into Eppendorf tube. Add 200uL of Tris 1M pH 8 to neutralise the TAE and stabilise the phage:biotinylated-proteins:beads complex. Beads were pellet down with a magnetic separator for 2min and supernatant (containing eluted phage) was transferred to a fresh Eppendorf tube.

The eluted phages were used to infect *E. coli* strain TG1 at mid-log phase at 30°C (amplification, Figure 28). The selection was achieved by plating phage/*E. coli* suspension in agar enriched with 100µg/mL ampicillin and 2% glucose. Selection of phage was repeated a second time, followed by enrichment of selected clones again.

Finally, phage selected were sent for sequencing the peptide sequence cloned within their genome and a glycerol stock was prepared mirroring the master plate and conserved at -70°C for future experiments (e.g., screening via ELISA).

Phage were then screened using ELISA method to reveal binding interactions between a receptor-coated plate and supernatant containing the selected phage.

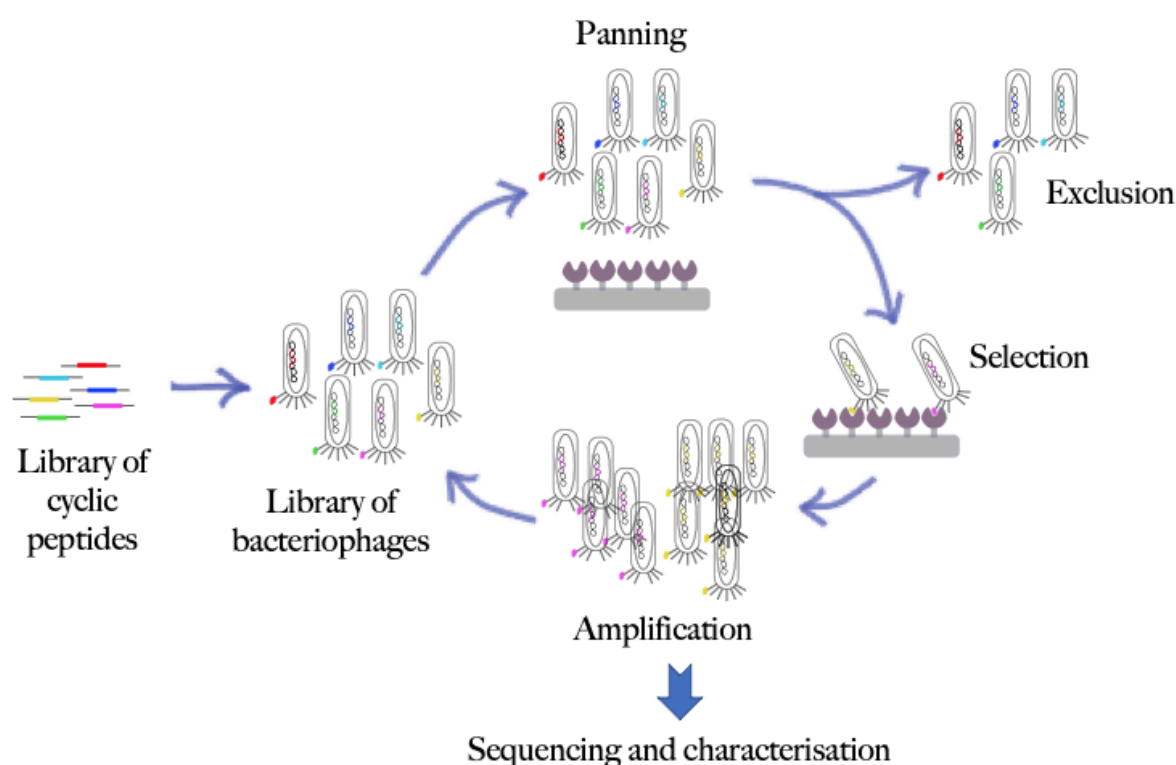


Figure 28: Cartoon representing the phage display method.

The 2018 Nobel Prize in Chemistry with one half to Frances H. Arnold for the directed evolution of enzymes and the other half jointly to George P. Smith and Sir Gregory P. Winter for the phage display of peptides and antibodies. Image created using Affinity.

Screening of Phage

For the screening, it was implemented the enzyme-linked immunosorbent assay (ELISA). ELISA is a plate-binding technique which reveals binding interactions between a receptor-coated plate and a mobile phase. In this case the mobile phase is represented by supernatant of growing culture of *E. coli* infected with phage that have been previously selected via phage display.

First, a replica plate with 2xTYAG (tryptone, yeast, ampicillin, glucose) media was prepared mirroring the master plate containing the infected *E. coli*. The replica plate was left incubating for 5h at 37°C, 280rpm to amplify the clones. In the meantime, K07 M13 Helper Phage (for safety reasons, it is used in conjunction with a phagemid of choice to produce single-stranded phagemid DNA. Stock 3×10^{13} pfu/mL was prepared by 5µL of in 10ml of 2XTYAG media. Of this, 100µl was added into each well of the replicate plate and left incubating at 37°C for 1h and shaking at 150rpm, and then incubate ON at 25°C at 280rpm.

Next day, 50µl of 5% (w/v) skimmed milk powder in PBS was added to the phage cultures and left at RT for 1h to reduce unspecificity in the coming steps. Plates were centrifuges for 5min at 3200rpm and the supernatant was transferred in a new plate and used for the selection assay *via* ELISA.

Selection of CD207-Binding Phage

Streptavidin-coated plates were first blocked for 1h at RT with 3% (w/v) milk - PBS. A total of 16 plates were prepared for the assay: testing plates, cross-reactivity plates and control plates, 4x of each. Next, biotinylated huCD207 and moCD207 proteins were diluted at 0.5µg/well (total of 200µg needed for the assay) in PBS and 50µL of this were added in each well and left incubating ON at 4°C. After the coating, plates were washed 3 times with PBS before blocking for 1h at RT in 5% milk-PBS. Plates were rinsed 3 times with PBS before adding 50µL/well of eluted blocked phage to the corresponding wells in the antigen plate and left incubating for 1h at RT. Plates were washed 3 times with PBS (v/v) 0.1% Tween and 50µL/well of anti-M13-HRP antibody diluted 1:5000 was added into each well to reveal the specific binding against the receptors. Plates were left undisturbed for 1h at RT, before been washed

with PBS (v/v) 0.1% Tween. Next, 50µL/well of TMB substrate was added to react with HRP, 0.5M of H₂SO₄ was added to stop the reaction and to proceed with absorbance reading of the plates.

The phage selected by phage display and screened by ELISA were sequenced (top 4 with the highest signal), and the corresponding peptides sequences were sent for chemical synthesis to GenScript Service. A biotin group was asked to be added at the peptides at the N-terminus to allow second step validation through ELISA.

Validation of peptides

Peptides previously selected (total of 4 peptides) were synthesised with a custom biotin group at N-terminus. This allowed to perform validation assays using streptavidin-coated plates.

Peptides were ordered in dry form and were resuspended in DMSO (stock concentration 1mg/mL) to allow the reduction on the internal sulphurs residues and to create an internal disulphuric bridge, essential to recreate the cyclic form originally presented on the surface of the phage. Streptavidin-coated plates were blocked. Peptides were diluted 1/100 and 1/1000 in 1mL of PBS and 100µL of these were added in each well and left incubating ON at 4°C. The supernatant was removed and plates were incubated with 3% milk-PBS for 1h at RT for blocking. Plates were washed with 3 times with PBS and incubated with 300µL of non-biotinylated huCD207 or moCD207 (final concentration 0.2 mg/mL). Supernatant was removed, plates were washed, and 50µL of 1/2000 anti-HisTag-HRP were added in each well for 1h at RT. Next, plates were washed and TMB substrate was added as previously described and chemiluminescent signal was detected at the plate reader.

4.3 Cycloaddition of Ligands to PEG-PLA

For the synthesis of the peptide-conjugated polymer, an alkyne-azide cycloaddition 'click' reaction using the biodegradable, biocompatible and FDA-approved PEG-PLA was performed [202], [268]. In more detail, azide-PEG₆₈ (N₃-PEG) was

purchased for the click-reaction and used for the synthesis of the PLA hydrophobic block by ring opening polymerisation (performed by Dr Deng, polymer presented in Figure 29).

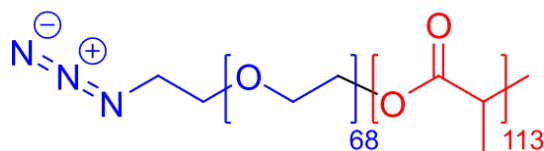


Figure 29: chemical structure of N_3 -PEG₆₈-PLA₁₁₃ polymer used for click-chemistry.

Peptides CD207-targeting (PEP1-4) and CD206-targeting (mUNO) were ordered from GenScript with an additional propargylglycine at the N'-terminal.

The copper(I)-catalysed alkyne-azide cyclo-addition (Figure 30) was performed as follows.

First, N_3 -PEG₆₈-PLA₁₁₃ polymer (20.72 mg, 1.7879 μ mol,) was added to a 25ml reaction Schlenk flask with stirring magnet and dissolved in 2.1mL of DMF:H₂O solution (1:9, v/v) previously degassed. To the solution was added degassed H₂O until turbidity was observed (micelles, not vesicles, increasing the chances to attach the peptides on the PEG-PLA polymer). Alkyne-PEP4 peptide (5mg, 2.324 μ mol) was dissolved in 1 mL of DMSO, added to the reaction flask and degassed for at least 30min. Next, NaAsc (1.77mg, 8.939 μ mol) was resuspended in degassed DMF:H₂O, added to the solution and degassed for at least 30min, followed by the catalyst of the reaction CuSO₄ * 5H₂O (0.385mg, 1.787 μ mol) . The reaction was bubbled through for a further 30min and then left in thermo oil bath at 25°C for 72h. DMF (10 mL) was added to the reaction once it was completed, and the solution was dialysed for 5 days against milliq-H₂O using a 3.5 kDa molecular-weight cut-off dialysis bag, changing the solution 4 times each day. After that, the aqueous solution was lyophilized, yielding a light-yellow powder and stored at -20 °C.

The reaction was similarly performed using N_3 -PEG₆₈-PLA₁₁₃ polymer (31.78mg, 2.742 μ mol) with alkyne-mUNO peptide (2mg, 3.565 μ mol), maintaining the ligand/polymer molar ratio 1:1.3.

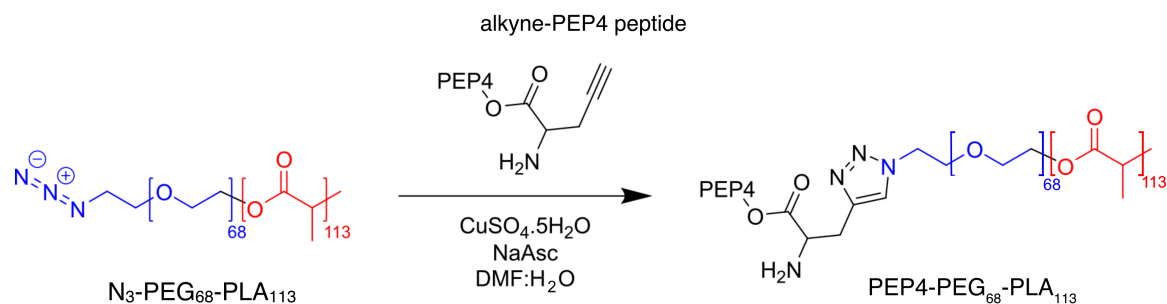


Figure 30: Copper-catalysed cycloaddition. [269]

4.3.1 Quantifying Peptide-Conjugation

The amount of peptide-polymer obtained from click chemistry was quantified by bicinchoninic acid (BCA) protein assay. The first step of the reaction is to produce a light blue complex by chelating copper with protein in an alkaline environment. Peptides with three or more amino acid residues generate a chelate complex and Cu^{2+} is reduced to Cu^{1+} . The chelation of two molecules of BCA with one Cu^{1+} ion produces a strong, purple-coloured water-soluble reaction product. The BCA/ Cu^{1+} complex has a linear absorbance at 562 nm that increases with protein quantities.

The BCA assay was used to quantify the peptide-polymer quantification as follows.

A mass of N₃-PEG₆₈-PLA₁₁₃ polymer (3.64 mg) and alkyne-PEP4 (0.99 mg) were dissolved 1.4mL and 2.06mL of DMSO respectively, samples were sonicated if necessary. Then, different volumes of 0.5 % (v/v) SDS/NaOH (0.05M) were added to each tube to obtain the final concentration of 1.85M in all samples. An equal volume (2 mL) of N₃-PEG₆₈-PLA₁₁₃ polymer and alkyne-PEP4 were added to a fresh Eppendorf tube and 200 μL of Triazole (3.72 M) were added to the mixture. Serial dilutions were conducted starting from the PEP4 concentration of 40 $\mu\text{g}/\text{mL}$ in DMSO/0.5 % (v/v) SDS/NaOH (0.05M).

In parallel, PEP4-PEG-PLA polymer (1.3 mg) was dissolved in DMSO, sonicated and diluted in 0.5 % (v/v) SDS/NaOH (0.05M) to obtain final concentration of 1.85 M. For the colorimetric assay, 150 μL of BCA working solution were added to 150 μL of standard curve dilutions or 150 μL of dissolved PEP4-PEG-PLA polymer. The 96-

well plate was left incubating at 37°C for at 2h and then absorbance was analysed with plate reader at 570nm.

Same procedure was applied for the quantification of mUNO-PEG-PLA polymer.

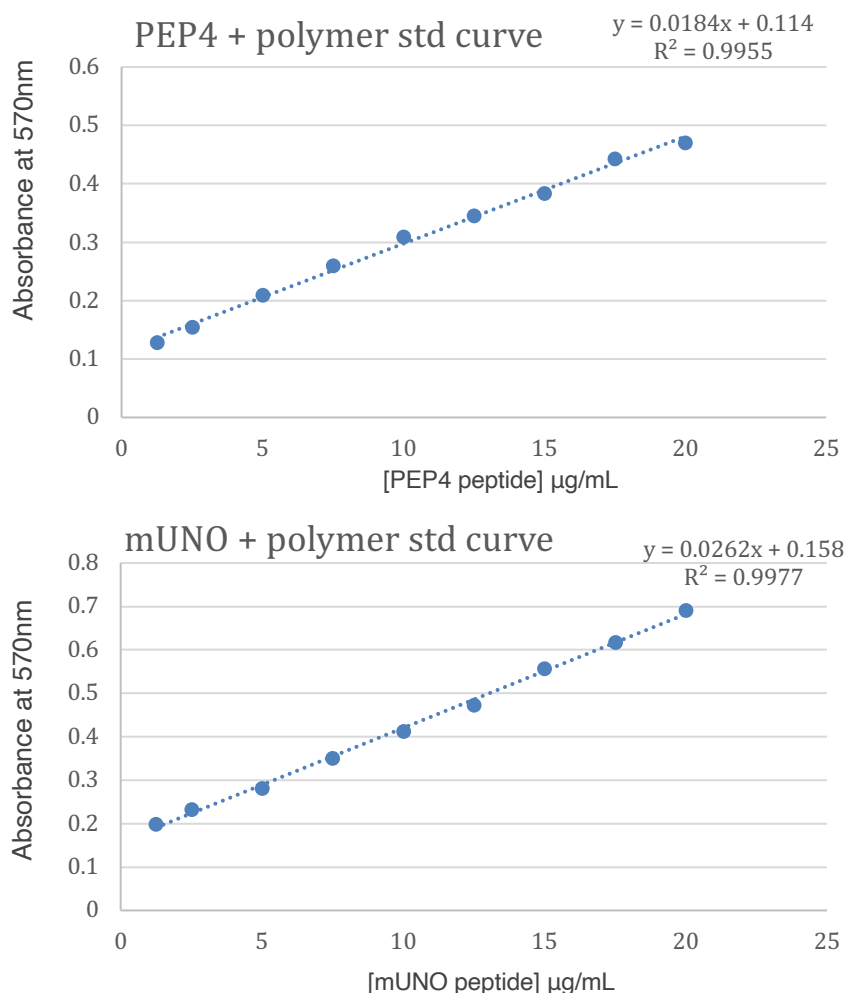


Figure 31: Standard curves obtained by BCA method for the peptide-conjugation quantification for PEP4-PEG-PLA and mUNO-PEG-PLA polymers, respectively.

4.4 Experiments *in vitro*

4.4.1 Cell Culture Maintenance

Unless otherwise specified, all cell lines were maintained in the appropriate media supplemented with 10% (v/v) fetal bovine serum (FBS, ThermoFisher, #16140071), 1% (v/v) Pen/Strep (ThermoFisher, #433), 200mM L-glutamine

(SigmaAldrich #G7513) and incubated at 37°C with 5% CO₂ saturation. Human embryonic kidney 293 (HEK293T, ATCC #12022001) and mouse melanoma (B16F10-OVA, ATCC, #CRL-6475) cell lines were maintained in complete high-glucose Dulbecco's Modified Eagle's Medium (DMEM, Gibco, #11995) media. Mouse embryonic fibroblast (NIH 3T3, ATCC, #CRL-1658) were maintained in complete high-glucose DMEM supplemented with 10% (v/v) of calf serum (ATCC, #30-2031). Mouse dendritic DC2.4 (Merk-Sigma, #SCC142) were cultured in complete RPMI 1640 (Gibco, # 21875034) media supplemented with 10mM HEPES (ThermoFisher, #15630056), 0.05% (v/v) β -mercaptoethanol (SigmaAldrich, #444203), and 2mM sodium pyruvate. and mouse dendritic cell MutuDC1940 (Abm, #T0528) were cultured in complete IMDM (1x) + GlutamaxTM (Gibco, #31980-030).

Once 70% of confluency was reached, cells were washed with PBS before adding 0.2% (w/v) Trypsin-EDTA (SigmaAldrich, #T4049) solution and incubated for 5 min at 37°C. Cells were centrifuged at 300xg for 5 min, diluted 1:10 and seeded in a new T75 flask.

4.4.2 Cell Viability

Since PMPC-PDPA POs were used in biological systems for pDNA-SFKL delivery, their biocompatibility on DC2.4 and HEK293T was assessed using 3-(4,5-dimethyl-2-thiazolyl)-2, 5-diphenyl-2H-tetrazolium bromide (MTT) assay (Figure 32). Under stressful conditions, the intracellular level of NADH provides a first glance at the cellular metabolic flux and cell viability as previously explained.

DC2.4 were seeded in 96-well plates at a cell density of 5×10^4 cells per well, whereas HEK293T were seeded at 3×10^4 cells per well. Subsequently, the cells were incubated with different concentrations of PMPC-PDPA POs, starting from the highest concentration possible (0.8 mg/mL; 7.74×10^{-9} moles) and performing dilutions 1:2. Cells were incubated for 24h then 80 μ L of the MTT reagent (1 mg/mL) was added. After an incubation period of 2h, the formed formazan crystals were dissolved in 100 μ L of dimethyl sulfoxide (DMSO) and the absorbance was

evaluated at 570 nm using a microplate reader. PBS buffer and DMSO were used for negative and positive control, respectively.

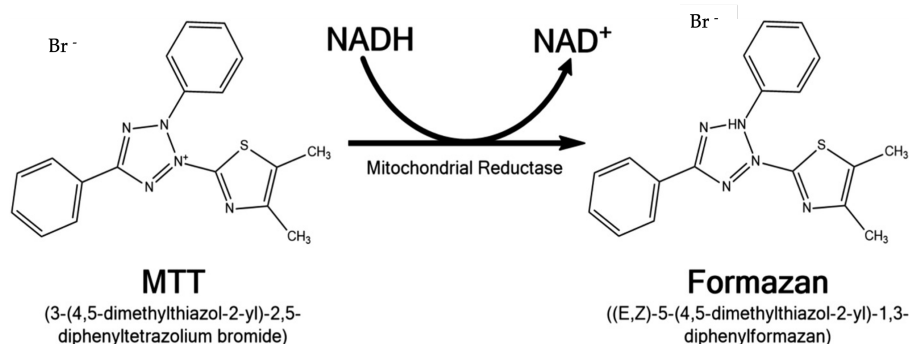


Figure 32: Chemical reaction of MTT to Formazan by mitochondrial reductase activity. The mitochondrial activity of the reductase enzyme which metabolizes the water soluble 3-(4,5-dimethyl-2-thiazolyl)-2, 5-diphenyl-2H-tetrazolium bromide (MTT) into a purple formazan salt. The more formazan salt is formed, the more cells are viable [270].

The MTT assay was performed to assess cell viability upon treatment with free cGAMP and cGAMP:PMPC-PDPA POs. For the assay, DC2.4 and B16F10-OVA cells were seeded in 96-well plates at 5×10^4 cells/well and 3×10^4 cells per well, respectively. Day after seeding, cells were incubated with 1:2 serial dilution of free-cGAMP, cGAMP:PMPC-PDPA POs and empty PMPC-PDPA. For the following studies, lipopolysaccharide endotoxin (LPS, 1000 kDa) was added as positive control of inflammation (Table 3 for concentration) [271].

Treatment	Initial Concentration	Moles in initial Volume
Empty PMPC-PDPA	1.2 mg/mL	5.7×10^{-6}
Free-cGAMP	3.36 $\mu\text{g}/\text{mL}$	5.18×10^{-9}
Encapsulated-cGAMP	3.36 $\mu\text{g}/\text{mL}$	5.18×10^{-9}
LPS	1 $\mu\text{g}/\text{mL}$	1×10^{-13}

Table 3: Initial concentrations of treatments for the serial dilution MTT assay in DC2.4 and B16F10-OVA.

Cells were incubated for 24h followed by the addition of MTT. The formed formazan crystals were dissolved in DMSO and the absorbance was evaluated at 570 nm using microplate reader. PBS buffer and DMSO were used as a negative and positive control, respectively.

The MTT for a single-dose treatment to confirm previous findings, final concentrations are reported in Table 4.

Treatment	Final Concentration	Moles in Final Volume
Empty PMPC-PDPA	0.2 mg/mL	0.95×10^{-11}
Free-cGAMP	0.56 $\mu\text{g}/\text{mL}$	0.97×10^{-9}
Encapsulated-cGAMP	0.56 $\mu\text{g}/\text{mL}$	0.97×10^{-9}
LPS	250 ng/mL	0.17×10^{-13}

Table 4: Final concentrations of treatments used for the single concentration MTT assay, cytokine quantification and Caspase 3/7 assay.

MTT assay was repeated to assess the biocompatibility of PEG-PLA formulations for binding assay, starting from the concentration of 0.8 mg/mL. Cells were left incubating for 2h before performing the MTT assay.

4.4.3 Transfection Experiments

Experiments to determine transfection efficiency using a GFP vector and a SIINFEKL antigen expressing vector were performed using HEK293T or DC2.4 cell Cells analysed by flow cytometry. DC2.4 and HEK293T cells were seeded in a 24-well plate at the concentration of 2×10^5 and 1×10^5 per well, respectively, and left undisturbed overnight in the incubator before proceeding with the experiments.

First set of studies were aimed to determine the baseline level of transfection of cells and Lipofectamine 2000 (Invitrogen, #11668027) was used as chemical transfection reagent. For the preparation of the lipo-complexes, it was used 1 μg of pDNA-SFKL per 3 μL of Lipofectamine 2000 in OptiMEM reduced serum (Invitrogen, #31985062), as indicated by the manufacture's protocol. The lipo-complexes were added in the supernatant, which was then replaced after 6h of incubation. Cells were collected after 24h from transfection, processed to single cells suspension and analysed by flow cytometry.

Next, it was investigated the capacity of pDNA-loaded POs to transfect DC2.4 cells and to release the pDNA intracellularly. For this set of experiments, DC2.4 were seeded at the concentration of 2×10^5 per well in a 24-well plate. Instead of lipo-complexes, it was added on top of the cells the equivalent volume of pDNA-

loaded POs corresponding to 1 µg of DNA. As negative controls, cells were treated either with equal volume of empty POs or DNA only (1 µg). OptiMEM was used to top up the final volume to 1 mL and the cell media was replaced after 6h. Cells were collected after 24h from transfection and processed to single cells suspension for flow cytometry analysis.

To increase the level of transfection, the murine cGAS-inhibitor RU.521 (Invitrogen, #inh-ru521, resuspended in DMSO at 2mg/mL, Figure 33) was added in the fresh media 1:1000 (v/v) 3h prior transfection, as recommended by manufacture.

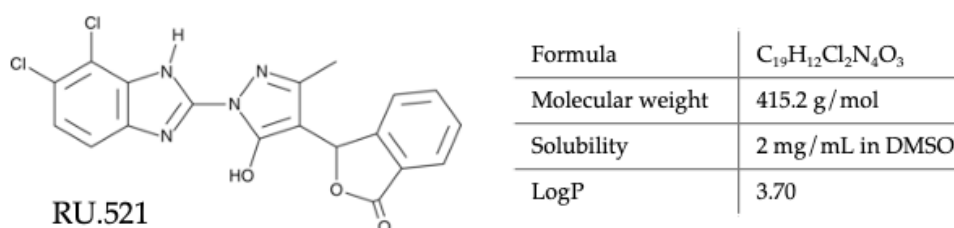


Figure 33: Chemical Structure and Properties of RU.521. (Source PubChem).

4.4.4 Flow Cytometry

The intracellular expression of GFP and SIINFEKL antigen were analysed in DC2.4 and HEK293T cells by flow cytometry. This technique allows the multiparametric analysis of individual cells suspended in a volume. Cells are ordered in line by hydrodynamic focusing, passed through a nozzle and interrogated individually with one or more beams of focused light. The light scattered in the forward direction or with an angle of 90°C are collected by the forward scatter channel (FSC) or by the side scatter channel (SSC), respectively. The first provides indication of the size of the particle, while the latter offers information about the relative complexity (i.e., granularity). Data collected by the FSC and SSC are unique and used to roughly differentiate cell types in a heterogeneous population. However, fluorescent labelling is generally required to obtain more detailed information. Monoclonal and polyclonal antibodies are generally produced against a specific target (i.e., epitope of a protein) and then conjugated to a fluorophore to specifically detect certain structures of the cell populations of interest. The downside of using antibodies is that they could be

recognised by their Fragment crystallizable (Fc) domain by receptors expressed on the surface of immune cells, resulting in false positive data. It is necessary to include a pre-treatment with Fc blocking reagents (Biolegend, #101319) before proceeding with the staining protocol [272].

Upon transfection, cells were trypsinised, centrifugated at 350xg for 5 min and washed with 1x PBS. Then, a volume of 20 μ L from the single cell suspension was used to determine the %live cells in the sample by using the automated cell counting system. Cells were analysed at flow cytometry for GFP signal using the appropriate laser of excitation.

In another experiment aimed at the detection of antigen SIINFEKL exposed on the cellular surface, single cells suspension was first incubated in ice for 15 min with 1 μ g Fc-block in 100 μ L in Cell Staining Buffer (Biolegend, #420201) containing per 10^6 of cells. This step is aimed to eliminate unwanted binding of the Fc domain to the antibody. Without washing, cells are incubated for 20 min in ice with APC-anti-SIINFEKL mouse antibody cell staining buffer (1 μ L per 10^6 of cells in, Biolegend, #141605). As negative control, cells were incubated at the same final concentration of APC anti-mouse IgG1 κ Isotype (Biolegend, #400119). Untreated cells were used for adjusting the voltage of the lasers and for the gating strategy. Cell acquisition was done using LSR Fortessa flow cytometer. Data were subsequently analysed with FlowJo software with the gating strategy reported in Figure 34.

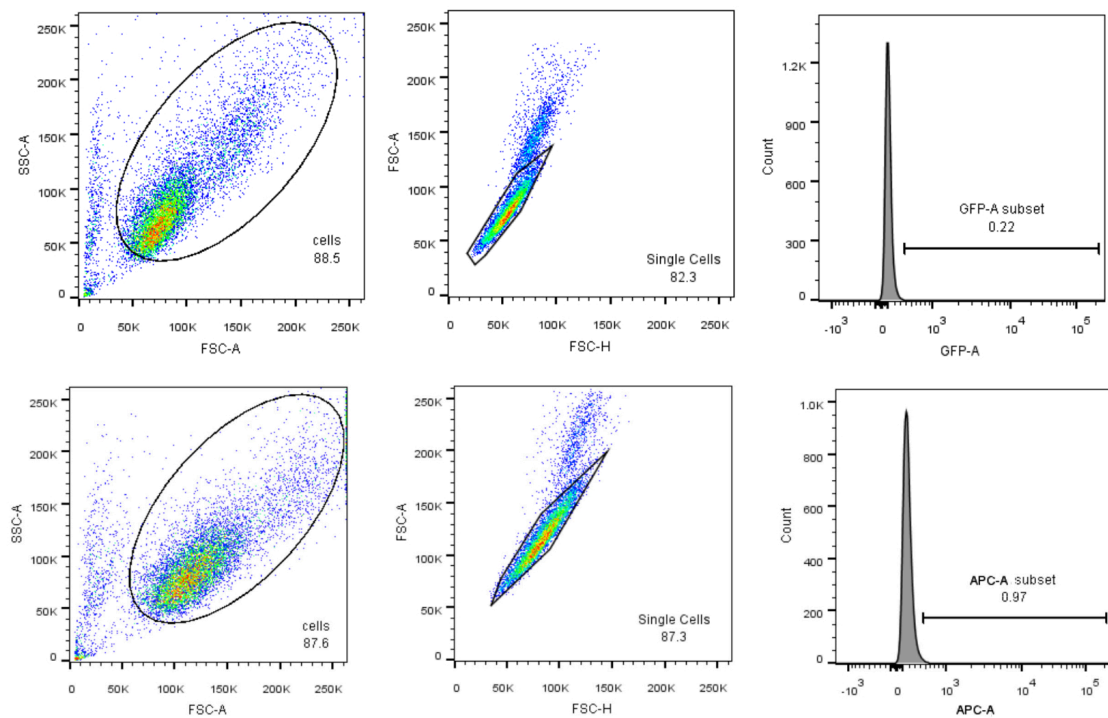


Figure 34: Representation of the gating strategy for GFP and SIINFEKL detection in DC2.4. Cells were first gated based on the physical parameters such as cell granularity complexity (Side Scatter, SSC) and cell surface area or size (Forward Scatter, FSC). Correlated measurements (FSC-H vs FSC-A) allowed the differentiation of single cell types from debris and doublets. The single cells population was gated and to obtain histogram cell counts vs GFP or APC signal.

In different experiments, aimed to characterise the binding behaviour of combinatorial POs upon i.d. injection *in vivo*, single cells suspension obtained from skin biopsies and lymph node (see Paragraph 4.5.2.1.1) were first left incubating in ice for 20 min protected from light with Fixable blue live/dead cell (at 0.2 μ l in 200 μ l of cell staining buffer per sample, ThermoFisher, #L23105). A small aliquot of untreated cells was left aside for optimisation of the laser voltage of the instrument. Live/dead discrimination allow to gate for live cells only and discard dead ones during the analysis since they unspecifically interact with antibodies and might provide false positive signals.

After incubation period, cells were washed twice at 350xg for 5 min with cell staining buffer and resuspended in 100 μ l of cell staining buffer with 1 μ g of Fc-block and left in ice for 15 min. Without washing, 100 μ l of Ab mix (1 μ l of each Antibody of

Table 5) and left incubating for 15min in ice. Next, cells were washed twice at 350xg for 5min with cell staining buffer before proceeding with flow cytometry analysis.

Cell phenotype	Marker	Colour	Clone
Keratinocytes/fibroblasts	CD45-	BV 786	Biolegend, 30-F11
DCs	CD11c ⁺ high	BV 421	Biolegend, N418
Mannose receptor	CD206	AF 488	Biolegend, 15-2
Langerin receptor	CD207	PE	Biolegend, 4C7
Polymersomes		Cy5.5 (=AF 700)	Polymer
Live/dead staining		Fixable blue	ThermoFisher

Table 5: List of Antibody and Markers used in Flow Cytometry for analysis of *ex vivo* biopsies upon i.d. injection.

Cell acquisition was done using LSR Fortessa flow cytometer with the gating strategy reported in Figure 35. Data were subsequently analysed with FlowJo software.

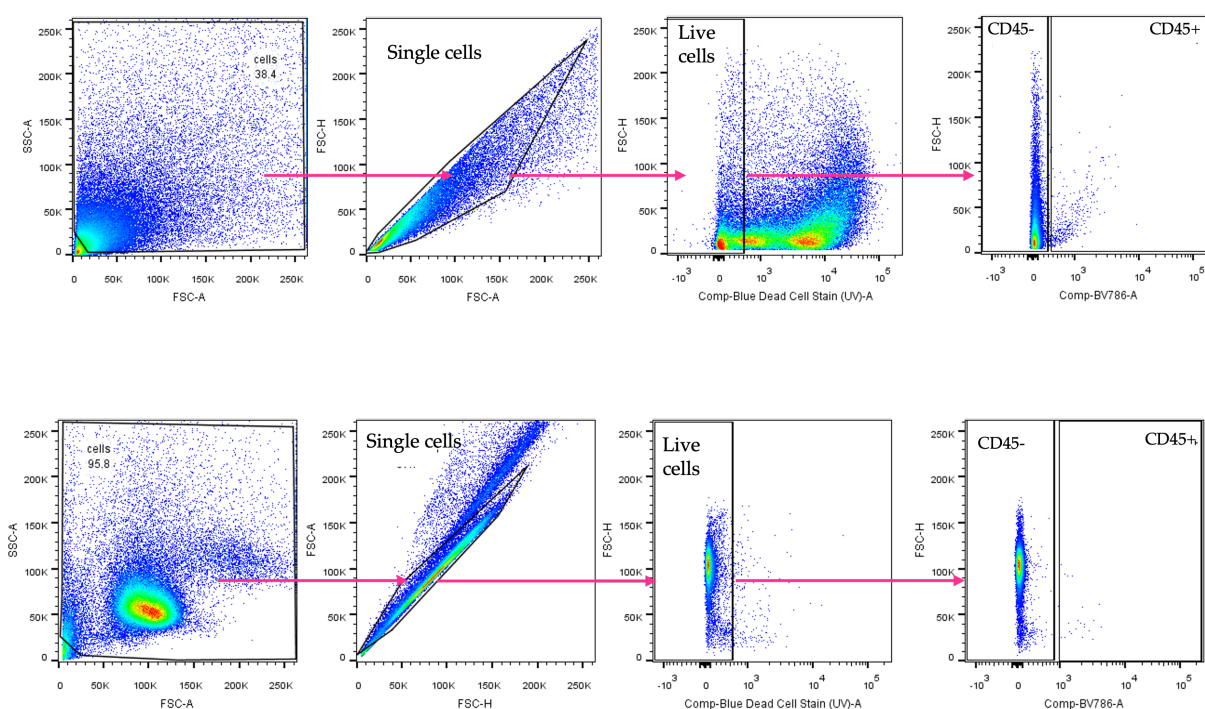


Figure 35: Gating Strategy for Skin and Lymph Node Samples.

Untreated sample of each cell population (skin or lymph node) was used to set up optimal laser voltage at the instrument. Main cell population was gated 'P1' and subsequently analysed for FSC-H/FSC-A to identify single cell population 'P2'. Events to record in P2 was set to 5×10^5 . The single cell population was analysed for live/dead channel and subsequently gated for CD45, CD206 or CD207 signal.

4.4.5 Laser Scanning Confocal Microscopy (LSCM) Imaging

To corroborate results obtained by flow cytometry, GFP and SIINFEKL signals were also detected using LSCM (Figure 42). Briefly, DC2.4 cells were seeded at a density of 0.4×10^6 cells/well in a glass-bottom dish (Ibidi, #89629) and incubated overnight. Up to 3 hours prior pDNA-SFK:PMPC-PDPA delivery, RU.521 cGAS inhibitor was added 1:1000 (as previously described) in the supernatant and left incubating at 37°C. Next, pDNA-SFKL:PMPC-PDPA POs were added to the cells. After 6h of incubation, the media was replaced. Upon 24h of incubation, cells were gently washed with PBS and were fixed with 3.7% (v/v) PFA solution for 10min at 4°C. Samples were then left in blocking solution (5% BSA in PBS) for 30min at room temperature (RT), washed and then blocked with Fc block for 30min at RT to prevent unwanted binding of the Fc region of the antibodies. APC labelled anti-mouse H-2Kb bound to SIINFEKL Antibody (Biolegend, #141605, dilution v/v 1/100) was used to detect the presented antigen on the cellular surface.

In a different experiment aimed to characterise surface receptors expression (SR-B1, CD36, CD81, CD207 and CD206) in different cell lines, confocal imaging was used to corroborate results obtained by western blot (WB) (Figure 54). Cell line NIH3T3 was seeded at 0.4×10^6 cells/well, whereas MutuDC and DC2.4 cells were seeded at 0.5×10^6 cells/well in μ -Slide 8 Well glass bottom (Ibidi, #80826) and left incubating at 37°C overnight. Upon 24h of incubation, cells were gently washed with PBS and were fixed with 3.7% (v/v) PFA solution for 10min at 4°C. Cell nuclei were stained with Hoechst Stain solution and then the cytoskeleton with Phalloidin-Atto 647 F-actin staining (Sigma, #65906). Cells were gently washed before proceeding with the immunostaining. First, cells were left incubating for 2hs at RT with 5% BSA (w/v) in PBS to reduce unspecific binding. Then cells were incubated with Fc-block as described in Paragraph 4.4.4 and without washing it was added the primary Ab (as listed in Table 6) for ON incubation at 4°C. The primary Ab was removed and cells were gently washed with PBS before adding the secondary Ab, which was left

incubating protected from the light for 1h at RT. Cells were then gently washed with PBS before proceeding with confocal imaging.

Primary Ab	Host	Reactivity	Dilution	Cat. nb
Anti-SR-B1	rabbit	Hu, Mu, Rt	1/100	Novus, NB400-104SS
Anti-CD36	rabbit	Hu, Mu, Rt	1/100	Novus, NB400-144SS
Anti-CD81	mouse	Hu, Mu, Rt	1/100	Santa Cruz, sc-7637
Anti- CD207	rabbit	Hu, Mu, Rt	1/100	Novus, NB100-56733SS
Anti-CD206	goat	Mu	1/100	Novus, AF2535

Secondary Ab	Host		Dilution	Cat. nb
Anti-rat 488	Goat		1/400	Biolegend, 405418
Anti-rabbit 488	Donkey		1/400	Biolegend, 406416
Anti-mouse 488	Goat		1/400	LifeTechnology, 0638

Table 6: List of Antibodies used for Confocal Imaging.

Primary and secondary antibodies were diluted in 1% BSA (w/v) in PBS. Abbreviation: human (Hu), mouse (Mu) and rat (Rt).

All confocal images were acquired using Leica TCS SP8 confocal microscopy equipped with Diode (405), Argon (488nm), DPSS (561) and HeNe (633nm) lasers. Data analysis was carried out using ImageJ software.

In another experiment aimed to assess the cellular uptake of fluorescent POs (Figure 58) , DC2.4 cells were seeded on a 35 mm imaging dish (Ibidi™) at a density of 0.4×10^6 cells/well and allowed to grow overnight. Cells were incubated with fluorescent PEG-PDPA vesicles at the final concentration of 0.2mg/mL and imaged. For the imaging, cells were fixed with 3.7% (v/v) PFA before staining the cell membrane with CellMask™ Deep Red Plasma Membrane Stain (1:2000 dilution in PBS) for 8 min at RT and cell nuclei with Hoechst Stain solution (1:2000 dilution in PBS) for 5 min at RT.

4.4.6 Enzyme-Linked Immuno-Staining Assays (ELISA)

As previously mentioned, second messenger cGAMP is responsible to activate a signalling cascade which culminate with the transcription of ISGs and the

secretion of pro-inflammatory cytokines. Amongst all pro-inflammatory cytokines released, $\text{INF}\beta$, IL-12, IL-6 and $\text{TNF-}\alpha$ were selected as the main ones and were object of quantification by ELISA (Peprotech ELISA kit #900-TM97/TM54/TM50 and #MIFNB0, R&D systems).

Briefly, DC2.4 and B16F10-OVA cells were seeded in 96-well plates at 5×10^4 or 3×10^4 cells per well, respectively. Cells were treated as reported in Table 4 and left incubating for 24h. Cell-free supernatant was collected for the quantification of secreted cytokines according to the manufacturer's protocols.

4.4.7 Caspase 3/7 Apoptosis Assays

The release of pro-inflammatory cytokines upon cGAMP:PMPC-PDPA treatment could be indication of cellular stress (as in reduction of cell viability) or initiation of apoptosis. To better understand the effects at single cell level, it was implemented Caspase-3/7 assay kit. If Caspase-3/7 are activated by the treatment, the four-amino acid peptide (DEVD) conjugated to a nucleic acid binding dye, which serves as substrate of activated enzymes, binds the DNA and produces fluorescence signal in response, which can be detected by confocal.

For the apoptosis assay, DC2.4 and B16F10-OVA cells were seeded in an 8-well plate (Ibidi™) at a density of 5×10^4 and 3×10^4 cells per well, respectively, and cultured overnight. Cells were then treated with empty or cGAMP-loaded POs, free-cGAMP and LPS as reported in Table 4. Cell apoptosis was assessed at 24h after the treatment. Prior imaging, CellEvent™ Caspase-3/7 was added on top of the cells at the concentration recommended by the manufacturer. Cells were then fixed using 3.7% PFA for 8 min at 4°C and washed twice with PBS. Images were acquired using a Leica TCS SP8 confocal microscope in brightfield. Green fluorescent cells were counted over the total number of cells, providing %of dead cells.

4.4.8 Western Blot

The Range Selectivity is based on the number of receptors on the cellular surface, hence their concentration. Before proceeding with the binding experiments,

the receptors of interest (SR-B1, CD36, CD81, CD207 and CD206) were validated and quantified by Western Blot (WB) and confocal imaging.

One million of cells were collected from single cell suspension and the pellet was washed twice with PBS. The cells were lysed using RIPA buffer containing proteinase inhibitor cocktail 1:50 (v/v) to prevent events of degradation. The sample was left in ice for 30 min and then centrifuged at 1200xg for 5 min at 4°C to separate the supernatant from debris. A small aliquot of the supernatant was used to quantify protein concentration using BCA Protein Assay Kit. Laemmli buffer 4x was added to the remaining part of the supernatant and samples were heated at 95°C for 5 min. Proteins (20 µg) were separated by molecular weight on 12-10% SDS-polyacrylamide gel electrophoresis (PAGE) and then transferred to polyvinylidene difluoride (PVDF) membrane previously activated with methanol. PVDF membranes were briefly immersed in Ponceau solution to confirm the successful transferring procedure before been blocked with 5% (w/v) skimmed dried milk (Malvern) in tris-buffered saline (TBS) containing 0.1% (v/v) Tween-20 (TBS-T) for 1h at RT. Membranes were incubated overnight with correspondent primary antibody at 4°C (Table 7). Upon TBS-T wash, membranes were then incubated with secondary antibody conjugated with DyLight-488 (Abcam) up for 2h at RT and imaged using Odyssey CLx (LI-COR Biosciences). Membranes were then probed with relative loading control (e.g., GAPDH or α -tubulin) listed in Table 7.

Protein size	Primary Ab	Host	Reactivity	Dilution	Cat. nb
80 kDa	Anti-SRB1	Rabbit	Hu, Mu	1/500	Novus, NB400-104
72 kDa	Anti- CD36	Rabbit	Hu, Mu	1/500	Novus, NB400-144
25kDa	Anti-CD81	Mouse	Hu, Mu	1/100	Santa Cruz Biotech, sc-7637
37kDa	Anti-CD207	Rabbit	Hu, Mu	1/300	Novus, NB100-56733
166 kDa	Anti-CD206	Goat	Hu, Mu	1/400	Novus, af2535
36 kDa	Anti-GAPDH	mouse	Hu, Mu	1/1000	Abcam, ab8245
53 kDa	Anti- α tubulin	mouse	Hu, Mu	1/2000	Novus, #NB100-690
	Secondary Ab	Host		Dilution	Cat nb.
	Anti-rabbit	Donkey		1/20000	Biolegend, 406404
	Anti-mouse	Goat		1/20000	Biolegend, 405310
	Anti-goat	Donkey		1/20000	Biolegend, 405312

Table 7: List of Primary and Secondary Antibodies Used for WB.

4.4.9 Lectin staining

Glycocalyx is surface layer comprised of glycosylated proteins and lipids (glycans) involved in major cellular functions, such as cell-cell interactions, cell migration, tissue patterning to the immune response and disease progression [223]. Because of their physical presence and contribution during the binding, glycans must be characterised in each cell types used for the binding experiments.

Their characterisation was evaluated by flow cytometry analysis and confocal imaging using carbohydrate binding proteins such as lectins (Sigma-Aldrich, #L0401, FITC-conjugated) [273], [274].

Trypsinised cells of each phenotype (DC2.4, NIH3T3 and MutuDC) were washed twice with PBS before proceeding with 5% (v/v) FBS in PBS blocking step. Cells were then incubated for 15 min with a concentration of FITC-lectin at 7.5 µg/mL in 2% (v/v) FBS in PBS to minimise unspecificity. Cells were then washed gently and analysed by flow cytometry of confocal imaging followed by PFA fixation.

4.4.10 *In Vitro* Binding Assay

To test the phenotypic targeting theory, DC2.4, NIH 3T3 and MutuDC1940 cells were seeded in transparent bottom black 96-well plate at their respective concentration to achieve 70% confluency on the day of the experiment. For each formulation to be tested, it was prepared a working concentration of 0.2 mg/mL in 5% FBS in PBS (v/v) to be added on top of the cells and left incubating at different time points (3, 5, 7, 10, 15, 20, 30, 45 and 60 min). At the end of the incubation period, the vesicles were removed and cells were gently washed once with PBS to eliminate unbound material. The plate was then read at plate reader for rhodamine fluorescence. To correlate the fluorescent signal with the uptaken material, it was generated a standard curve for each of the formulation, starting from the initial concentration of 0.2mg/mL.

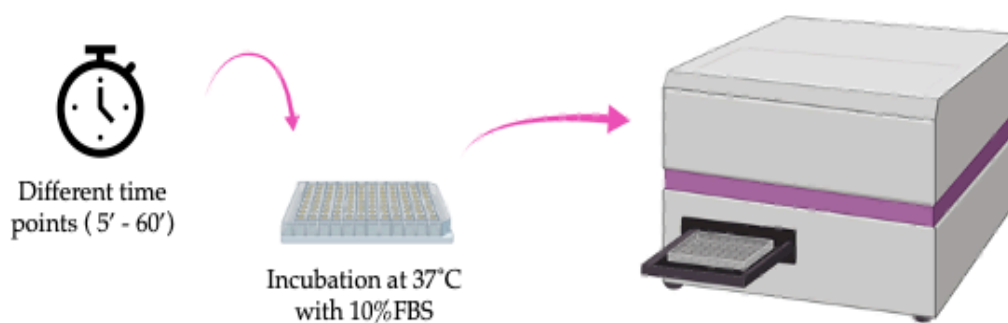


Figure 36: Representative cartoon of the *in vitro* binding assay

4.5 *In Vivo* Experiments

All animal experiments were performed in compliance with Animals (Scientific Procedures) Act 1986 and under the Project Licence PR3889251. All experiments were performed in immunocompetent C57Bl6 male mice of 6-8 weeks old and then sacrificed by neck dislocation at the end of the experiment, followed by perfusion. The i.v. and i.d. injections were performed by Dr Diana Matias. Tumour cell injection and tumour growth monitoring were performed by Barbara Ibarzo Yus.

4.5.1 cGAMP Delivery *In Vivo*

cGAMP-loaded POs were formulated following protocols described in Paragraph 4.1.2 and 4.1.2.1. Vesicles were administered into animal model to assess and validate the system to elicit a tumour inflammation by itself or as adjuvant. A total of 20 wild-type immuno competent C57Bl6 mice were ordered from the animal facility. At day zero of the experiment, 5×10^5 B16F10-OVA cells were injected on one flank of the animal (Figure 37). Animals were divided in group of five for the following treatments: PBS only, Empty PMPC-PDPA, free-cGAMP and cGAMP:PMPC-PDPA. After 3 days from injection, animals were i.v. injected with a maximum of 5 mg of material per Kg of animal weight. Animals were injected with PBS, empty PMPC-PDPA POs (initial concentration 5.3 mg/mL), cGAMP:PMPC-PDPA POs (at 1.8

$\mu\text{g/mL}$ of cGAMP in 1.3 mg/mL of PMPC-PDPA) or free-cGAMP (at 1.8 $\mu\text{g/mL}$). Injections were repeated at Day 3, 7, 10 and 12. Tumour growth was monitored and reported daily. Animals bearing tumours that exceeded 1.5 cm in one orthogonal direction of over 1 cm³ in dimension, that interfered with normal movement or become ulcerated, were scarified by neck dislocation in compliance with the Project Licence. Length size of the lesion were used to estimate the total volume of tumour growth progression and animal survival.

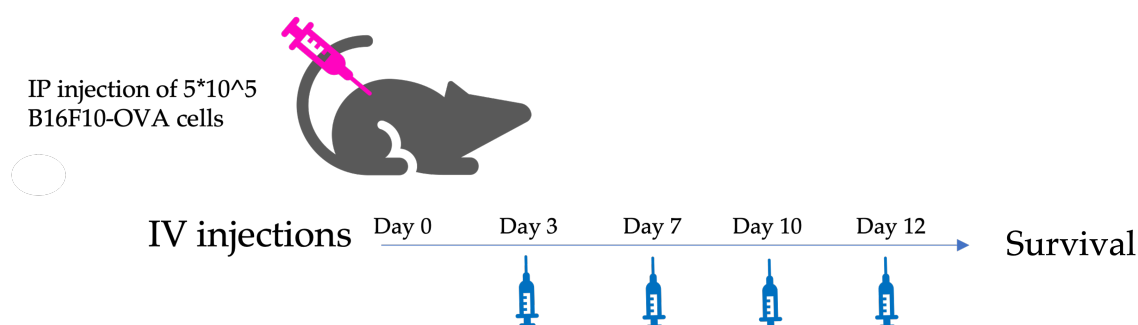


Figure 37: Experiment Layout for Tumour Survival Experiment in C57Bl6 mice.

4.5.2 Intradermal Injection of Combinatorial POs *In Vivo*

Range selectivity theory was assessed *in vitro* experiments using cellular model and a variety of multivalent and/or multiplex POs. Although encouraging, these *in vitro* experiments represent a rather simplistic model of interaction. It was then decided to investigate the binding behaviour of combinatorial POs *in vivo*. The experiment is aimed to target immune cells in the skin, following the expression of receptors such as CD206 and CD207. For the experiment Fluorescent Cy5.5-POs injected in animals were prepared following protocol described in Paragraph 4.1.3. A maximum of 20 mg/ml for a maximum of 200 μl volume of material was injected in the trunk skin of animals, which then were scarified after 1h, 2h or 4h from injection. Animals were perfused first with PBS and then with fixative solution to preserve the organs. At this point, skin biopsies, afferent lymph nodes and internal organs (brain, spleen, liver, lungs, heart, gut, kidneys, thymus, testis, pancreas) were taken for analysis of the fluorescence by plate reader or flow cytometry.

4.5.2.1.1 Preparation of Lymph Node and Skin Biopsy Suspensions

For the experiment aimed to assess the phenotypic targeting of DCs *in vivo* upon i.d. injection, area of injection and afferent lymph node of each animal were taken and processed to single cells suspension for NP trafficking analysis.

Up to 1cm² of the area of injection was cut off and gently separated it from the back muscle. Biopsies from each animal were placed in 6-well plate containing 1.5mL of the digestion cocktail mix (Table 8) and left digesting at 37°C for no more than 90 min. It is known that trunk skin samples are found to be particularly tough to digest. To help with the digestion, the skin samples were first finely cut with scissor and then with a broken glass pipette.

Name	Company	Final Concentration
Liberase TM (Enzyme TM)	SigmaAldrich, #5401119001	0.3 mg/ml
DNase I	Roche, #10104159001	50 U/mL
RPMI (v/v) 5%FBS	Merk, #R8758	Up to 1.5 mL/sample

Table 8: Ingredient List for Preparing the Digestion Cocktail Mix.

The digested skin samples were collected with a sterile Pasteur and filtered through a 70µm cell strainer (Falcon, #352350) over a 50mL Eppendorf tube kept in ice. The cell strainer was washed with 5mL of RPMI (v/v) 5% FBS and the remaining sample was squeezed through the cell strainer with the help of a syringe plunger. The cell collected were pelleted at 350xg for 5 min and washed once with PBS before proceeding with antibodies labelling for flow cytometry.

4.5.2.1.2 Organ Biodistribution

To assess the NPs distribution upon i.d. injection majority of internal organs were collected and processed, including brain, spleen, liver, lungs, heart, gut, kidneys, thymus, testis, pancreas. Each organ was carefully washed with PBS to remove any residual blood or unbound PO and after a light dump on paper to remove excess of water, they were carefully weighted. An adequate volume of Lysing Buffer containing 10mM of Tris at pH 7.4 and 0.5% (v/v) Triton X-100 was added in each tube for final concentration of 1mg/mL. Each tissue was homogenised using ceramic beads (VWR, #432-3751) and high-speed tissue homogeniser centrifuge (Bertin Instruments, Precellys 24).

For the fluorescence analysis, hence PO biodistribution, 200 μ L of tissue homogenised was added in a 96-well black plate with transparent bottom. The plate was analysed at plate reader for cy5.5 fluorescence.

A standard curve from each PO sample that was injected was obtained. The relative value of fluorescence acquired from each organ/tissue was then interpolated with the standard curve to obtain the total mass of PO uptaken.

4.6 Statistical Analysis

The results are expressed as mean \pm standard deviation (SD). Statistical differences were evaluated by Student's T test and ANOVA one-way test in GraphPad Prism 8. Statistical analysis is reported statistically significant when $p \leq 0.05$ (*), $p \leq 0.01$ (**), $p \leq 0.001$ (***) and $p \leq 0.0001$ (****).

5 DNA Encapsulation and Delivery

5.1 Introduction and Aims

Despite having the lowest risk of irAEs, cancer vaccinations fail to stimulate inflammation and cancer elimination due to poor immunogenicity and antigen presentation. Thus, their poor clinical translation does not come as a surprise [275], [276]. The specific delivery of antigens *in vivo* by APCs, such as DCs, as opposed to diffusion, is one strategy for addressing these drawbacks [275].

Four types of cancer vaccines exist, including those based on tumour or immune cells, peptides, viral vectors and nucleic acid-based (DNA or RNA) vaccines [277]. The latter class represent a viable vaccination platform for a number of reasons. First, nucleic acid vaccines provide simultaneous delivery of several antigens spanning diverse TAAs or somatic tumour alterations, inducing both humoral and cell-mediated immune responses and consequently boosting the probability of overcoming vaccine resistance [277]. Besides, nucleic acid vaccines are non-infectious, devoid of protein or virus-derived contamination during manufacture and are regarded as safe for both preventative and therapeutic use. Furthermore, DNA molecules are cheap to manufacture, robust and easy to handle [277]. Nonetheless, a persistent issue in DNA vaccination research has been the reduced immunogenicity in animal models and the inability to predict human vaccine responses accurately [277]. One way to overcome this limitation is, for example, the co-delivery with a cGAS inhibitor to prolong the half-life of the plasmid inside the cell, along with an adjuvant to stimulate the immune response.

Another way is using polymeric nanocarrier systems, such as PMPC-PDPA POs, due to their quick binding and cellular internalisation via SRs and capability to escape the endosome compartment because of the pH-sensitivity of the PDPA block [197]. Numerous studies have confirmed the PMPC-PDPA talent to deliver biomolecules of different genres intracellularly with no cytotoxicity *in vitro* and *in vivo* [181],[179].

This chapter aimed to explore the possible therapeutic use of PMPC-PDPA polymer as nanocarrier for pDNA delivery for cancer vaccines (Figure 38).

This will be achieved through the following objectives:

- Encapsulate pDNA-SFKL into PMPC-PDPA POs and verify the intracellular delivery in a DC2.4 cellular model;
- Verify the effective antigen SIINFEKL presentation on the cellular surface of DC2.4 cells;
- Assess the effect of cGAS-inhibitor compound RU.521 in antigen delivery and presentation.

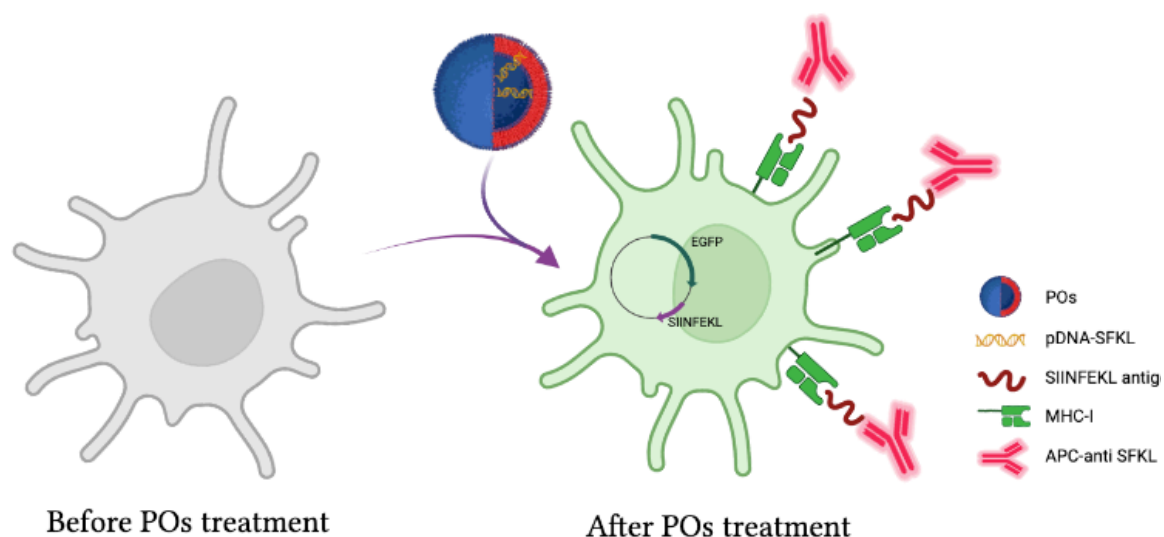


Figure 38: Graphical abstract.

To achieve project's goals, the pDNA-SFKL:PMCP-PDPA formulation was the object of investigation. The central hypothesis was to validate the capability of PMPC-PDPA POs to deliver pDNA intracellularly effectively and to validate DC2.4 as cellular model for antigen expression and presentation.

5.2 Results and Discussion

5.2.1 Self-assembly of pH-Sensitive Polymersomes and DNA Encapsulation

First, pDNA-loaded and empty control self-assembled POs were obtained by pH-switch method. To guarantee the absence of unloaded pDNA molecules, samples were treated with DNase enzyme as previously described in Paragraph 4.1.4. POs were centrifugated to eliminate large aggregates obtained during the self-assembly process, in the attempt of obtaining a monodisperse population of particles [278]. A monodisperse fraction is essential to minimise the variability in experimental procedures. SEC was then used to purify the population of spherical vesicles from bigger structures, DNase I enzyme and undigested fragments of pDNA-SFKL. Subsequently, the pDNA-SFKL:PMPC-PDPA sample and its control counterpart were imaged at TEM and analysed at the DLS (results reported in Figure 39). The analysis confirmed that self-assembly and purification steps produced a monodisperse sample of spherical vesicles, with no secondary structures to be found (i.e., worms). Moreover, it was observed that the average pDNA-SFKL:PMPC-PDPA diameters were 4 times bigger than empty vesicles (Figure 39.A). These findings were later confirmed by DLS analysis, which provided the PDI, d_H and ζ -potential. As observed in Figure 39.B, analysis of ζ -potential distributions from empty and pDNA encapsulated samples demonstrated no electro-kinetic difference upon encapsulation of anionic molecules. The two peaks presented a slight difference in height, which is corresponding to the total count of hits detected by the instrument. This is solely due to the sample's initial concentration, which has no impact on the reliability of the results.

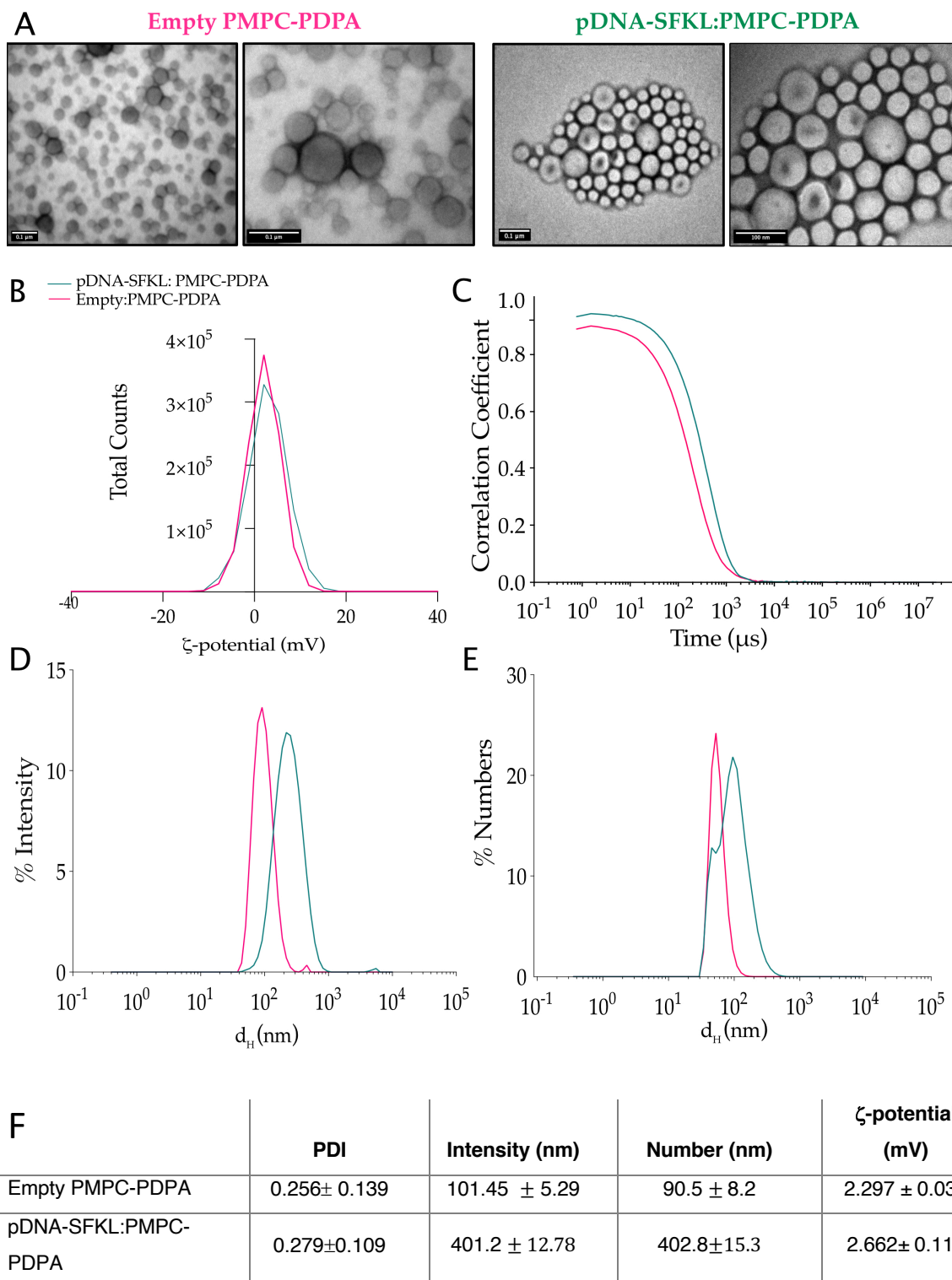


Figure 39: Characterisation of empty and pDNA-SFKL encapsulated POs.

In A) are reported representative TEM images of empty (left) and pDNA-SFKL:PMPC-PDPA vesicles (right). Phosphotungstic acid was used as contrast agent. Scale bar is 100 nm. Graphs in B) show ζ -potential distribution of empty PMPC-PDPA (red) Vs pDNA-SFKL:PMPC-PDPA (green). Correlation function smoothly decaying to zero in the time is shown in graph C). Size distribution expressed as % intensity and numbers are reported in graphs D) and E). Table in F) reports average numbers from DLS analysis.

The smooth decay over time of the correlation coefficient indicates the correct estimation of size distribution in function of intensity and numbers (Figure 39.C, D and E) of the samples. It was measured a four times bigger d_H by the intensity on average than the control sample (Figure 39 D,E). It was also observed that the size distribution for DNA encapsulated vesicles appeared to have a small detectable peak in proximity to the same d_H of empty POs sample, which might indicate a small second population of empty POs present in the formulation. It was hypothesised that during the self-assembly process, pDNA-SFKL molecules (negatively charged) might strongly interact with PDPA blocks (positively charged) of the unimers, leading to the formation of irregular large aggregates that precipitate. In fact, the observed average d_H of pDNA-SFKL:PMPC-PDPA vesicles was 4 times bigger than the empty control (DLS data in Paragraph 5.2.1). Although no further investigation was conducted at this stage, several works published in the literature confirm the strong supra-molecular interactions between molecules of pDNA and cationic polymers, which might explain the aggregate formation and the larger size of vesicles [279]–[282]. It was suggested that POs with a d_H smaller than 200 nm were left empty during self-assembly, corroborating the hypothesis that the supra-molecular interactions between pDNA and cationic polymer during self-assembly influenced both encapsulation efficiency and POs size. Results from DLS corroborate the visual observations obtained at the TEM, confirming the monodispersity of spherical vesicles. The pellet obtained upon centrifugation was visibly bigger than the control counterpart, potentially underestimating the polymer quantification concentration of encapsulated pDNA-SFKL.

Following the characterisation by DLS and TEM, samples were analysed and quantified at reverse phase-HPLC (Paragraph 4.1.4). The POs P.E. and L.E. were determined upon quantification, while the encapsulated-pDNA concentration was estimated by Quanti-PicoGreen assay. It is important to mention that due to the incompatibility of pDNA with the column used for RP-HPLC, it was not possible to directly determine the polymer concentration in pDNA-SFKL:PMPC-PDPA sample. For the estimation of the polymer concentration, it was used the control counterpart sample.

The analysis estimated the number of pDNA molecules encapsulated was 1 to 8 copies per POs. The average d_H of vesicles associated with the encapsulation was from 200 nm to 400 nm, with an average of 1.15 plasmid in this range (Figure 40.A). At the analysis of P.E., a substantial difference was observed between of pDNA-loaded POs (P.E. of 20%) in respect of their empty counterparts (P.E. 54%; Figure 40.B). As explanation of the 36% difference of total material lost during the preparation, it was hypothesised that anionic pDNA molecules strongly interact with the cationic unimers in solution, generating large aggregates that easily precipitated during the centrifugation step.

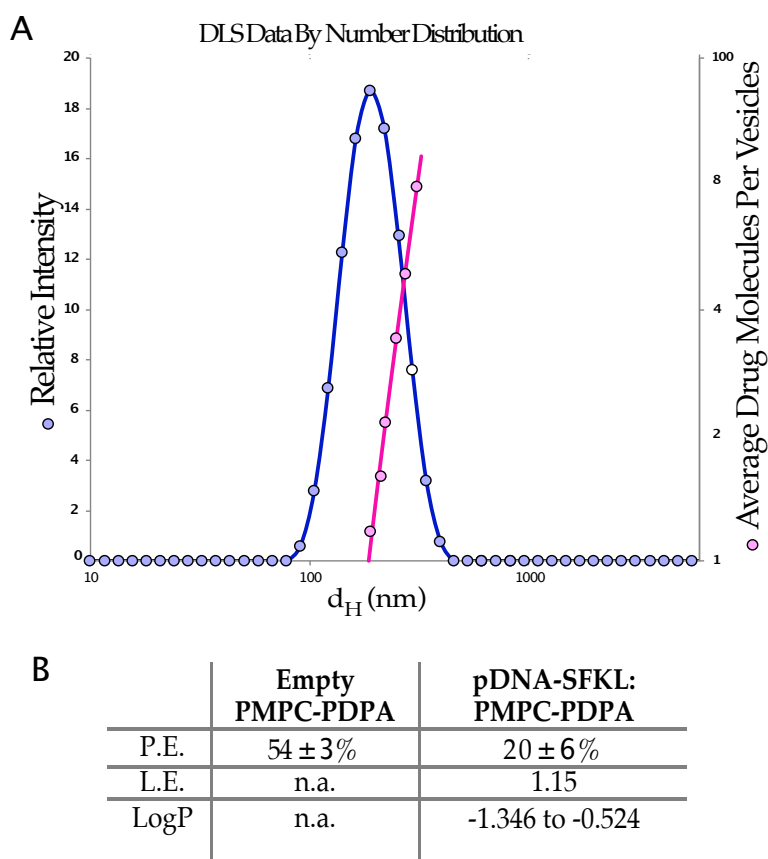


Figure 40: Loading Efficiency of pDNA-SFKL in PMPC-PDPA POs.

A) Representation of the average number of plasmids per POs in function of d_H . Table in B) reports Production Efficiency (P.E.), Loading Efficiency (L.E.) and estimated LogP value for DNA based from literature [283]. The final concentration of pDNA in the formulation was reported to be 51 $\mu\text{g/ml}$ in 1.8 mg/mL of PMPC-PDPA.

5.2.2 Biosafety Profile of Polymersomes in Cells *in vitro*

Prior to any cellular experiments, POs were tested for biocompatibility on selected cell lines to confirm biosafety profile (Paragraph 4.4.2). The copper bromide catalyst used in the polymer synthesis, the ATRP reaction, is known for its cellular cytotoxicity [284]. Although column chromatography and dialysis have been performed to purify the polymer from contaminants, polymers batches were accurately tested prior to usage in biological systems (HDF, THP1 and Bend3 cell lines). The empty PMPC-PDPA POs were tested via MTT assay, as previously described (results presented in Supplement Material S 2). POs were also tested in DC2.4 and HEK293T cells. Generally, the pDNAs used in transfection in mammalian cells, such as pDNA-SFKL, do not present a cytotoxic profile when properly purified from lipopolysaccharide (LPS) or other bacterial toxins, or in absence of cGAS/STING pathway. However, large plasmids (> 6kbp) might introduce cellular metabolic stress [285],[286]. As pDNA-SFKL is bigger than 8kbp, there was a concern over potential cytotoxicity. Therefore, cells were treated with different concentrations of pDNA-SFKL:PMPC-PDPA POs, to test their biocompatibility.

A day before the experiment, cells were seeded in a 96-well plate. Subsequently, cells were exposed for 24h to 1:2 serial dilutions of material, starting from the initial concentration of 0.8 mg/mL. Values were normalised by the PBS and DMSO control and are reported in Figure 41. No statistical difference (ns) was detected across different samples and cells. Overall, HEK293T presented around a 20% reduction of cell viability for both empty and pDNA-loaded formulations, while DC2.4 displayed metabolic stress with a 50% decrease of cellular viability at higher dose of polymer with both formulations. However, for concentrations below 0.2 mg/mL (as indicated by the vertical dotted line in Figure 41), both cell lines displayed more than 80% cell viability. Hence, this PO concentration range was proven to be safe for further *in vitro* studies.

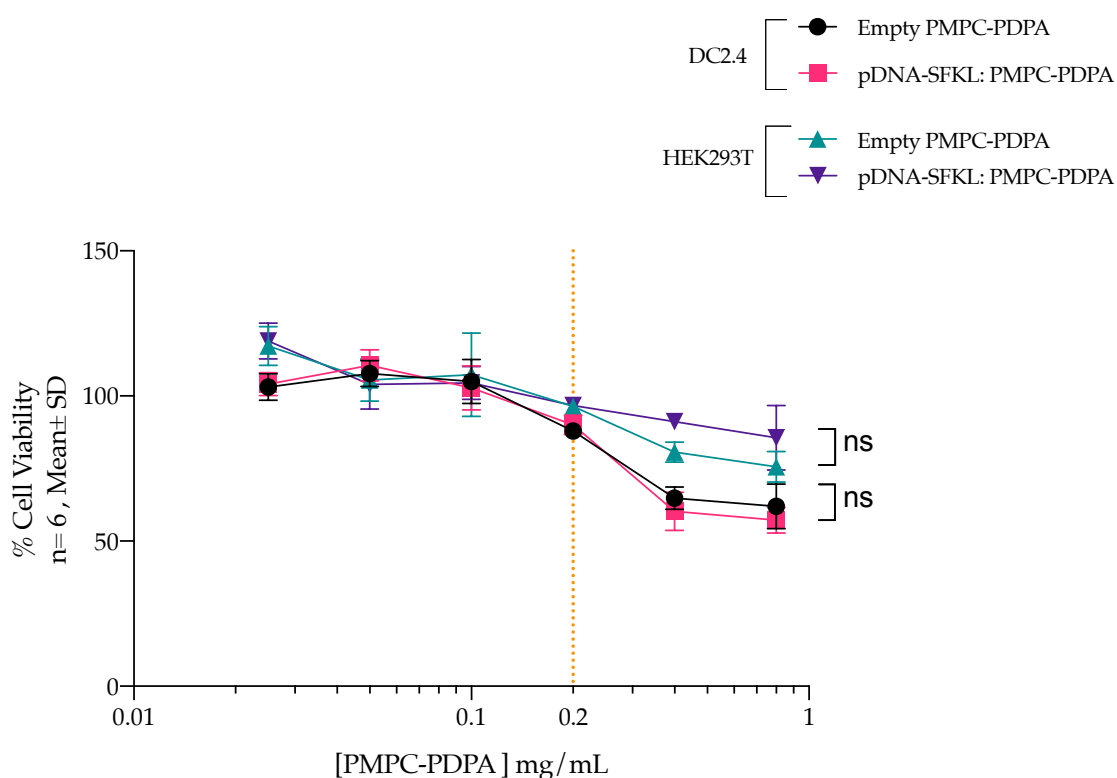


Figure 41: MTT assay for empty and pDNA-loaded PMPC-PDPA POs on DC2.4 and HEK293T.

Cells were treated with 1:2 dilutions of pDNA-loaded or empty POs. Cell viability was measured and values were normalised for PBS and DMSO controls. No statistical difference was observed between empty and DNA-loaded POs. Orange dotted line represents selected working concentration. Mean \pm SD from two independent experiments. One-way ANOVA was used for the statistical analysis (ns with $p>0.05$).

5.2.3 GFP Expression and SIINFEKL Presentation in Cells

Since empty and pDNA-loaded vesicles were found to be spherical and biocompatible for *in vitro* experiments, the system's capability to effectively deliver pDNA intracellularly was tested. To do so, POs must overcome the physical barrier represented by the cellular membrane and pDNA must escape the endosome and be transported inside the nucleus for transcription [287], [288].

The pDNA used for this work encodes for the GFP gene reporter and antigen model SIINFEKL under the control of the same promoter (for further details refer to Chapter 4).

Initially, the basal level of transfection and expression of GFP gene reporter by flow cytometry was evaluated. For these pivotal experiments, HEK293T cells, known for

their ease of transfection ([289]), were used as positive control for the gene reporter expression and compared to DC2.4 transfection efficiency.

In these initial experiments, the efficacy of pDNA-SFKL transfection in cells was determined using Lipofectamine 2000. Flow cytometry analysis confirmed the high transfection level in HEK293T ($84 \pm 7.4 \% \text{GFP}^+, S 3$) against DC2.4 ($27 \pm 3.2 \% \text{GFP}^+, S 3$), suggesting a significant mechanistic difference between the two cell lines.

Thereafter, the ability of POs to deliver pDNA-SFKL in HEK293T and DC2.4 cells after 24h from transfection was evaluated. Samples were processed to a single cell suspension and analysed at flow cytometry, with results reported in Figure 42. HEK293T showed higher transfection efficiency with around 50% of cells GFP⁺, whilst for DC2.4 up to 10% of cells were GFP⁺. As expected, control samples DNA-only did not exhibit any fluorescence, confirming that only when the DNA is effectively encapsulated into a delivery system is able to cross the cellular membrane and escape from the endosome compartment (for further details refer to Figure 9). Based on the low levels of transfection obtained in DC2.4 cells, it was hypothesised whether interference by the DNA-sensing cGAS-STING pathway is hampering the transfection ability. In physiological conditions, this pathway acts as a cellular defence, sensing potentially harmful DNA in the cytosol and triggering the inflammation, which in turns limits the protein expression by impairing the viability of the plasmid itself. The lack of similar defence mechanisms in some cell lines, such as HEK293T, is believed to be one of the hypotheses behind their ease of transfection [290].

To verify this hypothesis, RU.521, a murine cGAS-inhibitor, was used. DC2.4 were pre-treated with RU.521 before transfection, and then analysed by flow cytometry. DC2.4 exposed to RU.521 presented a level of GFP⁺ between 2-3 times higher than those without. Interestingly, levels of SIINFEKL presentation seemed to not be perturbed by the treatment (Figure 42.C-D). Results suggested a potential interference by the cGAS-STING pathway in the transfection efficiency.

To further corroborate these results, images of DC2.4 in bright field were taken under confocal microscope, looking for GFP and SIINFEKL expression. Pre-treated DC2.4

showed a higher level of GFP fluorescence than the control counterpart but not SIINFEKL detection, which was detected as clusters, rather than diffusely presented by cells (Figure 42.E).

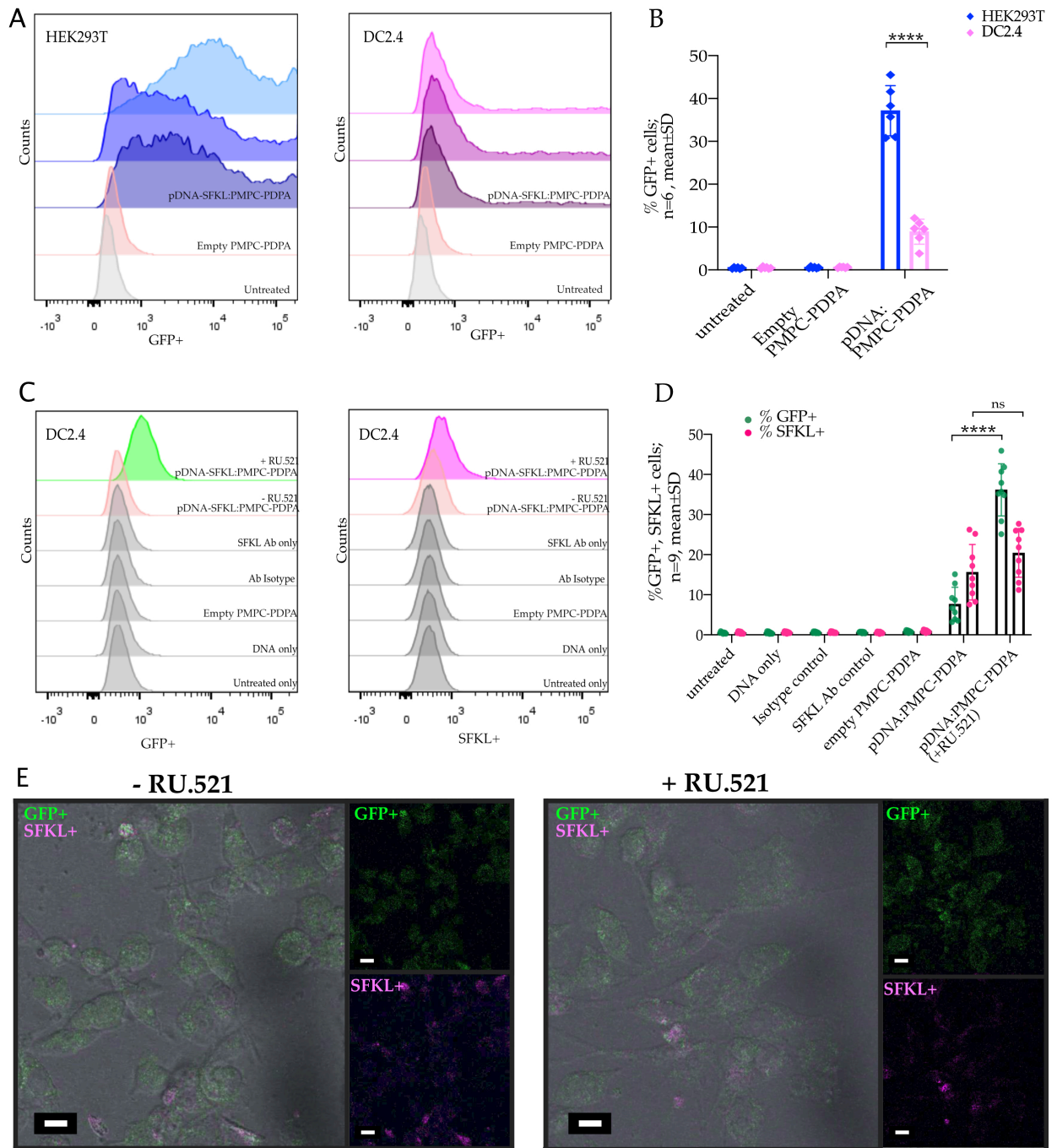
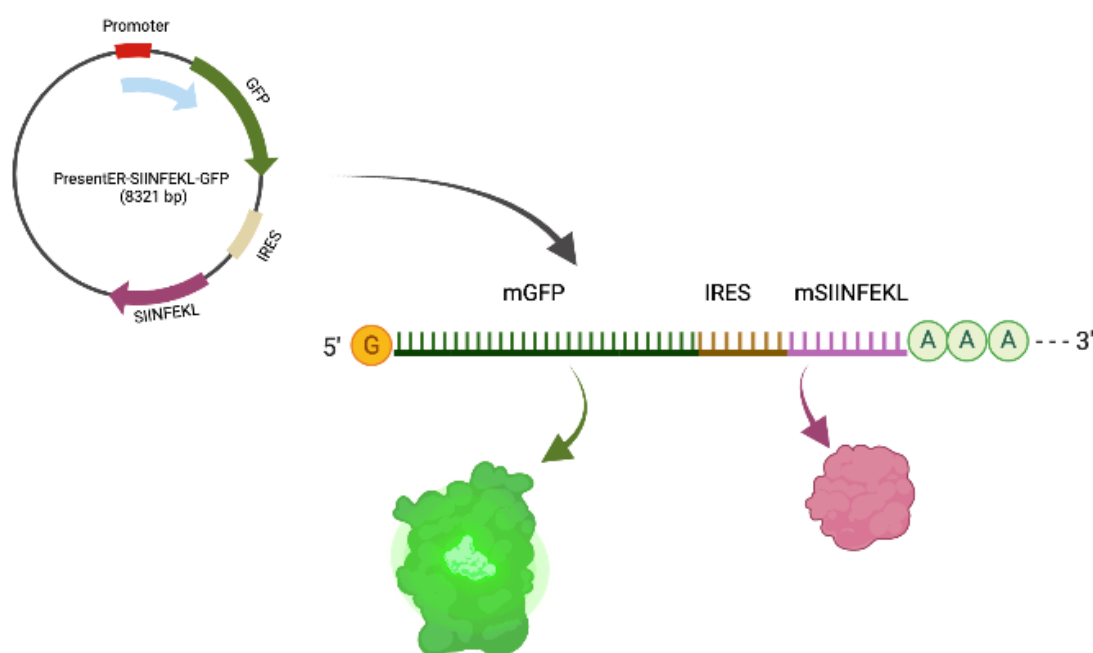


Figure 42: GFP and SIINFEKL Expression Analysis.

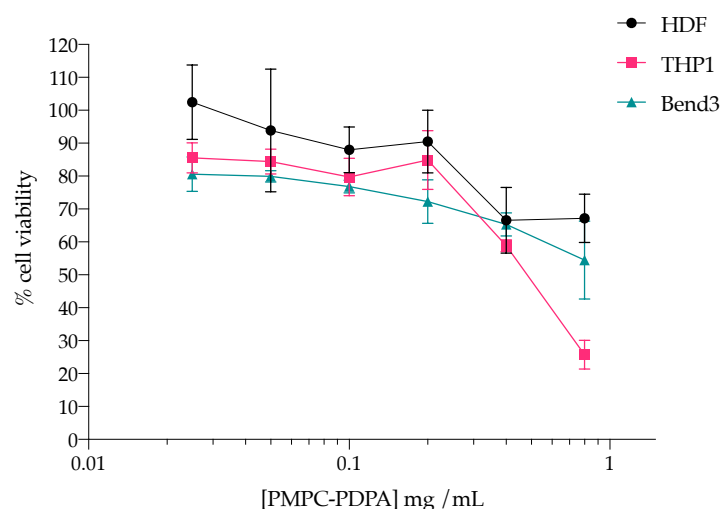
Representative histograms of flow cytometry analysis of HEK293T GFP+ cells (left) and DC2.4 GFP+ (right). Populations are presented in A) untreated (grey), and empty PMPC-PDPA (pink) treatments, used as control for both HEK293T and DC2.4 cells. Populations transfected with pDNA-SFKL:PMPC-PDPA are presented in triplicate in HEK293T (blue) and DC2.4 cells (purple). In B) are presented the percentage of transfections plotted as histogram. Mean \pm SD (n=6, 2 independent experiments). Results in C) show levels of transfection in DC2.4 upon RU.521 treatment looking for GFP expression and SIINFEKL presentation using APC-conjugated antibody. Mean \pm SD (n=9, 3 independent experiments). Statistical analysis using paired student t-test (****p<0.0001). E) Confocal images of DC2.4 without (left) or with RU.521 pre-treatment (right). Green: GFP, Pink: SIINFEKL (pink) channels are presented on the right side of the bright field image. Scale bar = 10 μ m.

5.3 Supplement Material



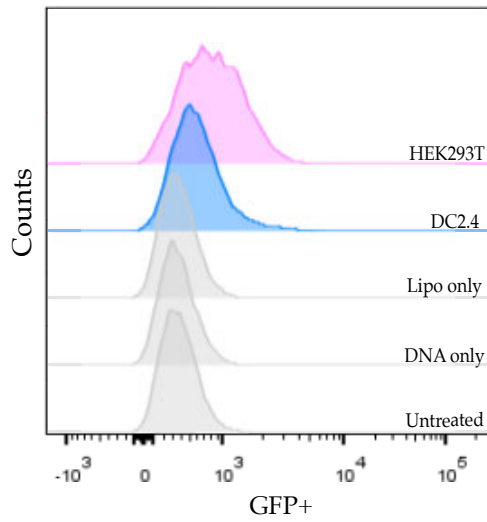
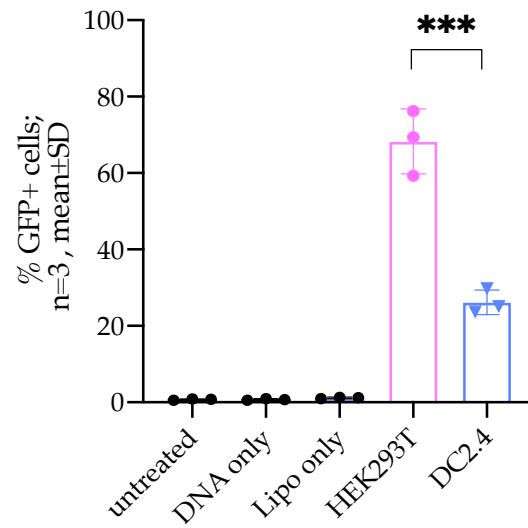
S 1: Schematic representation of pDNA-SIINFEKL (SFKL).

Plasmid encodes for green fluorescent protein (GFP) gene reporter and SIINFEKL antigen under the control of the same mammalian promoter. The internal ribosomal entry sequence (IRES) acts as spacer, translating in two distinct proteins [291].



S 2: PMPC-PDPA effect in cell viability in different cell lines by MTT assay.

To verify the biocompatibility of the polymer, different cell lines, such as HDF, THP1 and Bend3, with different concentrations of POs for 24h. Graphs show that at high concentrations of polymer occurs a reduction of cell viability up to 80% in THP1, while up to 40% of reduction was observed in HDF and Bend3. Thus, a maximum POs concentration (0.2 mg/mL) was used for future studies.

A**B**

S 3: Positive controls for transfection.

Representative data of GFP+ cells upon transfection in HEK293T and DC2.4 using Lipofectamine2000. For the statistical analysis was used the student t-test.

6 cGAMP Encapsulation and Delivery

6.1 Introduction and Aims

As previously described, cancer cells develop aberrant characteristics and the immune system can perceive them as 'foreign' and destroys them. Those mechanisms have been used to pave the way for cancer immunotherapies [292]. The tumour antigen-specific TILs can penetrate the solid tumour to destroy cancer cells effectively and are associated with better patient prognosis [293]. The CD8⁺ T cell activation requires two signals to operate: the tumour antigen and the co-stimulatory molecule. The first is derived from cancer cells expressing aberrant proteins, while the latter is selected to activate the PRRs [294]. It is worthy of attention to the pivotal role of type I IFN response in CD8⁺ T cell activation and tumour infiltration [294]. As mentioned previously, cGAMP plays a pivotal role in the initiation of the IFN type I response. In physiological condition, cGAMP acts as second messenger by binding to the adaptor receptor STING which is localised on the endoplasmic reticulum in proximity of the cellular nucleus [295].

STING agonists have been object of intense investigation lately, thanks to their strong tumour inflammation properties. Alone or in combination with other immunotherapies have been proven to provide a better tumour control [141], [296]. As an example, the biodegradable cationic polymer poly(beta-amino ester) (PBAE) polymer was used to efficiently encapsulate CDNs for the delivery in human monocyte cell line THP1, murine macrophage RAW264.7 and *in vivo* [297]. It was shown that CDN-loaded PBAE NPs were able to activate the transcription factor IRF3, involved in the regulation of several genes of the innate immune response [297],[298]. Intratumoral (i.t.) injections of CDN-loaded NPs were performed in a tumour-bearing animal model and the tumour volume was measured. Results demonstrated that multiple i.t. injections of CDN-NPs, in combination with anti-PD-1

antibody therapy, statistically reduced tumour growth in compared to controls. However, a high dose of non-encapsulated CDN (total mass injected 20µg) resulted in complete tumour eradication in this work [297].

In a very similar work, pH-sensitive poly(ethylene glycol)-block-[(2-(diethylamino)ethyl methacrylate)-co-(butyl methacrylate)-co-(pyridyl disulfide ethyl methacrylate)] (PEG-DBP) was used to encapsulate and deliver to THP1, RAW 264.7 cells and DC2.4 dendritic cell models [299]. The ability to initiate the inflammation was assessed via IFN regulatory factor (IRF)-inducible reporter constructs [299]. The therapeutic efficacy of cGAMP-loaded POs to induce IFN-mediated tumour inflammation were evaluated in a melanoma-bearing immunocompetent mice [299]. In this work, cGAMP-loaded POs were injected repeatedly either i.t. or i.v., obtaining mixed results [299]. While i.t. injected NPs provided a robust and complete response relative to free-cGAMP, eliciting a systemic antitumor response compared to controls. On the other hand, the i.v. injected cGAMP-NPs did not provide better tumour eradication relative to free-cGAMP control. Whilst a therapeutic enhancement through i.v. injected cGAMP-NPs was not reported, the systemic administration of STING agonists might still represent a valid alternative for patients with no accessible tumours location [299].

Thus, pH-sensitive nanocarriers, such as PMPC-PDPA POs, are an ideal nanotechnological platform for the encapsulation and intracellular delivery of cGAMP. It has been hypothesised that PMPC-PDPA POs could act as therapeutic intracellular delivery platform of cGAMP to elicit a strong anti-tumour inflammation response upon i.v. administration.

This chapter aimed to explore the possible therapeutic use of PMPC-PDPA polymer as nanocarrier for the cGAMP intracellular delivery in DCs as potential immunostimulatory molecule (Figure 43). This will be achieved with the following objectives:

- Encapsulation of cGAMP in empty PMPC-PDPA POs;
- Quantification of loaded-cGAMP molecules into POs.

- To assess the power of cGAMP to elicit inflammation in cellular model DC2.4 using B16F10-OVA melanoma cells as negative control.
- To assess the effectiveness of the anti-tumour activity of cGAMP *in vivo* by using a melanoma tumour animal model.

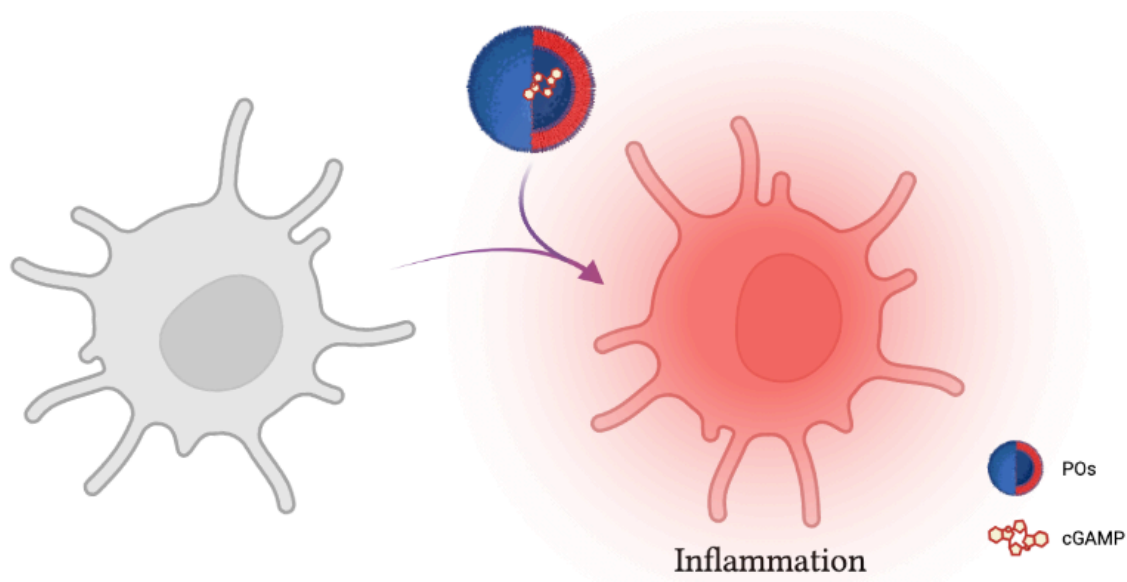


Figure 43: Graphical abstract.

Compound cGAMP encapsulated within PMPC-PDPA PO (in blue and red model) are delivered into dendritic cell model DC2.4 (grey) to evaluate the inflammation response (red) for tumour eradication or vaccine adjuvant.

6.2 Results and Discussion

6.2.1 Polymersomes Preparation and cGAMP Encapsulation

Adjuvants represent a class of small molecules co-administered with the antigen to enhance the immunological response towards a better immunisation. Amongst all adjuvants available, such as alum and poly(I:C) [300], cGAMP has been object of intense studies for its potent inflammatory effect[301], [302]. Its investigation quickly led to its role in tumour inflammation and therapeutic application in cancer immunotherapies, and nowadays has a prominent role as powerful adjuvant in therapeutic and preventive vaccines.

Aiming for an effective delivery of cGAMP for inflammatory studies, cGAMP was encapsulated into PMPC-PDPA POs via electroporation and tested on DC2.4 and B16F10-OVA cells.

First, empty PMPC-PDPA vesicles were self-assembled using solvent switch method and the cGAMP encapsulation was achieved by electroporation, as previously in Paragraph 4.1.2.1.

Upon dialysis in LPS-free PBS and sample concentration by hollow fiber, samples were analysed by DLS and TEM, confirming a homogenous population of spherical POs with a size of 112.89 ± 5.21 nm (Figure 44.A). DLS analysis confirmed a smooth correlation function of the samples, fitting the required parameters of size distribution by intensity and numbers. It was identified a monodisperse population of vesicles with comparable diameters. Additionally, electroporation process did not affect the size or structure of the vesicles, as shown in figure S 6.

To verify that the anionic molecule cGAMP did not affect the membrane potential of POs, the ζ -potential was measured of cGAMP:PMPC-PDPA formulation and its control counterpart were obtained by DLS (Figure 44.B). As previously introduced, the encapsulation of the anionic molecules does not interfere with the neutral charge of the vesicles (Figure 44.B).

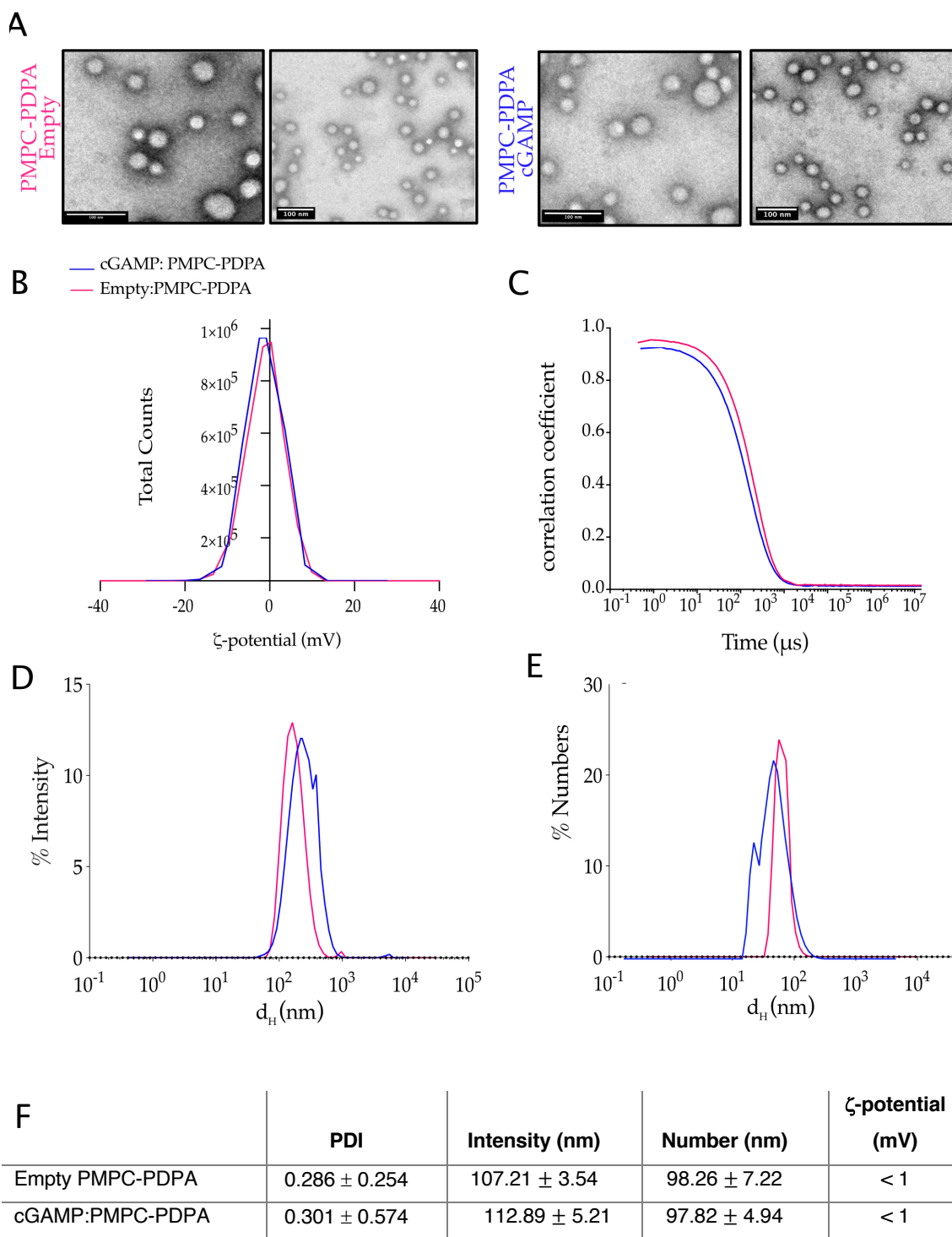


Figure 44: Quality analysis of cGAMP-loaded POs.

In A) are reported images acquired at TEM of empty (left) and cGAMP:PMPC-PDPA (right). Phosphotungstic acid was used as contrast agent. Scale bar is 100 nm. Graphs in B) show the ζ -potential distribution of empty PMPC-PDPA (pink) vs cGAMP:PMPC-PDPA (blue). Correlation function smoothly decaying to zero in time is shown in graph C). Size distribution expressed as % intensity and numbers are reported in graphs D) and E). Numbers and values of the DLS are presented in Table in F).

The encapsulated cGAMP and the PMPC-PDPA polymer were quantified by RP-HPLC using the previously optimised protocol. The anionic molecule cGAMP has a distinctive detectable peak when analysed at 260nm (S 4, S 5) compared to the PMPC-PDPA polymer at 220nm (Figure 24). By the peak area values in a standard curve previously generated for each species, it was possible to estimate the concentrations and, therefore the P.E. and L.E. (Figure 45).

The PO P.E. resulted in being of $57.8 \pm 7.2\%$ for empty vesicles and $35.3 \pm 4.6\%$ for cGAMP-loaded POs. As already observed during pDNA-SFKL encapsulation, a loss of polymer material was expected long the purification steps.

The estimated L.E. was determined to be an average of 1721 molecules per vesicles, with the bigger POs encapsulating around 20000 molecules of cGAMP (Figure 45). As expected, the overall P.E. of cGAMP:PMPC-PDPA formulation was lower than the control counterpart.

Although electroporation is a good methodology for the cargo encapsulation, future optimisation experiments are required to improve the initial concentration in the sample. Several publications have now demonstrated the efficacy of cGAMP and other CDNs in eradicating solid tumours when administered at concentration higher than 20 μ g per injection in animal model, which is around 1000x higher than the current formulation used in this work [303].

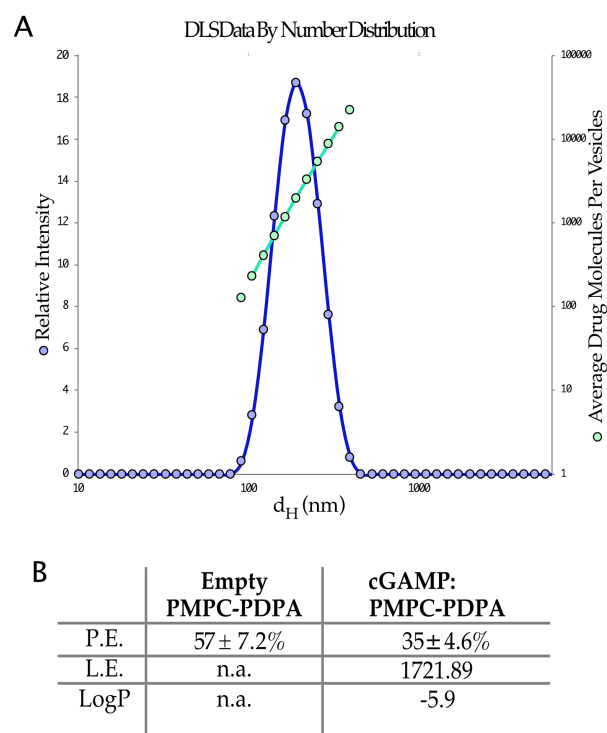


Figure 45: Loading Efficiency (L.E.) of cGAMP in PMPC-PDPA Polymersomes.
 A) Representation of the average number of plasmids per POs in function of dH. Table in B) reports P.E. (%), L.E. (n/POs) and estimated LogP value of cGAMP (Chemspider). The final concentration of cGAMP in the formulation was reported to be of 4.2 µg/mL in 1.5 mg/mL of PMPC-PDPA.

6.2.2 Inflammatory Effect of cGAMP-loaded Polymersomes *in vitro*

Since DC are mainly involved in antigen presentation process, it was decided to test the effect of cGAMP:PMPC-PDPA in a similar cellular model, such as DC2.4. As a model for cold tumour inflammation and for future animal experiments, mouse melanoma B16F10-OVA cells were also tested.

As first step, the metabolic stress triggered upon cGAMP:PMPC-PDPA treatment was assessed by MTT assay in DC2.4 and B16F10-OVA cells.

DC2.4 and B16F10-OVA cells were treated with a broad range of serial dilution concentrations of free-cGAMP, empty PMPC-PDPA, cGAMP:PMPC-PDPA or LPS (initial concentration for the serial concentration MTT are reported in Table 3).

As expected, DC2.4 and B16F10-OVA cells presented distinctive levels of cell viability upon the treatments, indicating intrinsic cellular differences (Figure 46). Indeed, DC2.4 are known to be responsive to stimuli, whereas the B16F10-OVA are known for their refractory phenotype and ‘cold tumour’ characteristics.

LPS treatment induced a strong reduction of cellular viability in both cell lines. However, DC2.4 cells were particularly affected by the treatment with a 50% reduction in cell viability (Figure 46.A).

However, free-cGAMP treatment showed a different response. The treatment perturbed B16F10-OVA only at higher concentrations, whereas DC2.4 exhibited a dramatic behaviour, with initial cell viability reduced by more than 50%. At lower doses, a stress-induced cell proliferation was observed, indicating a dose-dependent behaviour in DC2.4. This behaviour seemed not to be exhibited by the B16F10-OVA. They lost cell viability at high dosages of free-cGAMP. However, they remained above 70% cell viability across the entire spectrum of treatments (Figure 46.B).

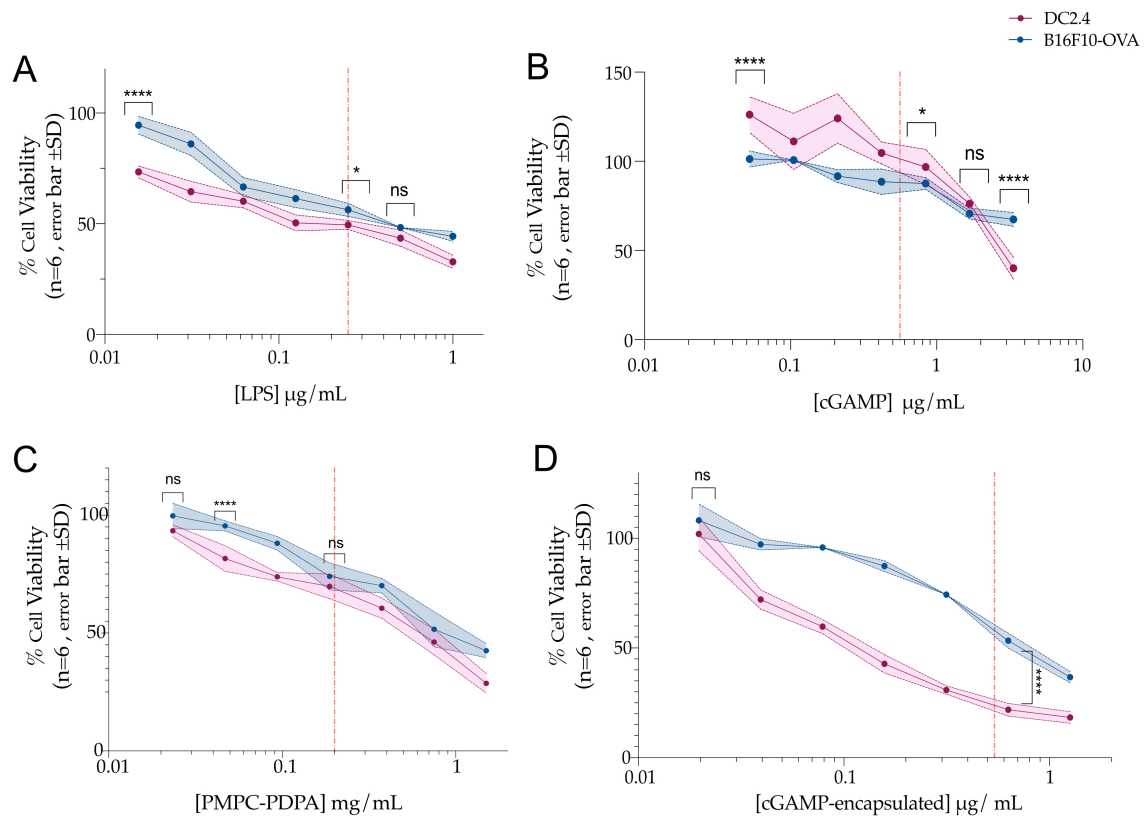


Figure 46: MTT Assay in DC2.4 and B16F10-OVA cells.

Cells were exposed to different range of concentration of each treatment for 24h before performing MTT assay. Values were normalised per PBS and DMSO. Orange dotted vertical line represent the chosen working concentration for single-dose MTT and future experiments *in vitro*. Data collected from two independent experiments with three technical replicates (n=6). Average data is plotted with SD. Two-way ANOVA was used for the statistical analysis (ns with $p > 0.05$).

Empty PMPC-PDPA POs were used as a control to establish the delivery system's basal toxicity level. Both cells were treated with a high concentration of PMPC-PDPA polymer starting at 1.2 mg/mL. As expected, both cells presented a consistent loss of cell viability over the last three highest concentrations of polymer used for the treatment (Figure 46.C). To be consistent with previous experiments on pDNA encapsulation and treatment, the final working solution of 0.2 mg/mL was selected for future experiments.

Lastly, cells were tested with the cGAMP:PMPC-PDPA formulation (Figure 46.D). As expected, the highest concentration showed induced cell viability reduction both cells, around 10% in DC2.4 and 45% in B16F10-OVA cells. Perhaps, it reflects the activated STING-dependent sensing pathway conserved in DC2.4 but not in B16F10-OVA cells. Amongst all treatments, cGAMP:PMPC-PDPA treatment was

associated with the most toxic profile (EC50 reported in S 7). Generally, DC2.4 cells were found to be more susceptible to empty POs or cGAMP:PMPC-PDPA than B16F10-OVA, in agreement with the cold tumour phenotype of the latter.

It was decided to focus the attention on the 0.2 mg/ml of PMPC-PDPA polymer, which is also the concentration where cells responses differed the least, minimising effects introduced by the polymer (Figure 46.D).

The concentration of 0.54 µg/mL of cGAMP-encapsulated in 0.2 mg/mL of PMPC-PDPA was selected for future experiments *in vitro*, such as single-dose MTT assay, quantification of released pro-inflammatory cytokines via ELISA and Caspase 3/7 assay.

The single-dose MTT assay confirmed the toxic effect of cGAMP:PMPC-PDPA formulation and results are presented in Figure 47. Similar to previous observations, cGAMP:PMPC-PDPA formulation had the greatest effect of in DC2.4 cells compared to all other treatments, especially to free-cGAMP, whereas there was no difference in B16F10-OVA. The effect of free-cGAMP was comparable across cell lines, however, differences were registered within the LPS treatment where B16F10-OVA unexpectedly seemed to be more susceptible than DC2.4. Moreover, a stress response to polymer treatment was also observed, comparable to the LPS in DC2.4 cells. As all formulations prepared in sterile environment using only LPS-free reagents, it was hypothesised that PMPC-PDPA polymer might act as adjuvant itself in inflammatory studies, which will be evaluated at high doses in future animal experiment (Figure 50).

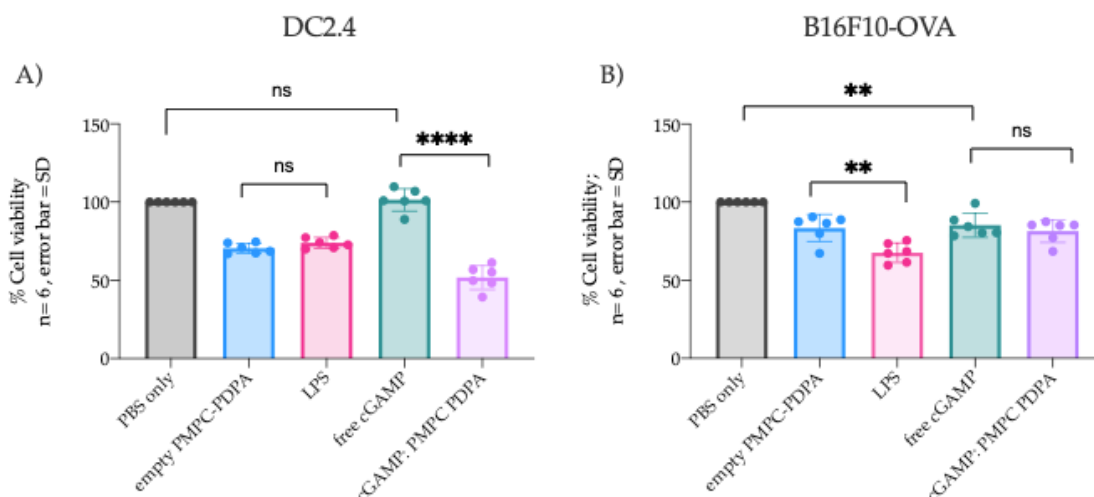


Figure 47: Single-dose MTT Assay in DC2.4 and B16F10-OVA cells. Graph presented in A) reports values obtained from DC2.4 cells, while B16F10-OVA are reported in B). Values were normalised by PBS and DMSO controls. Statistical analysis using one-way ANOVA Tukey's multiple comparison. Data collected from two independent experiments in triplicate. (mean \pm SD, n=6). Legend for data p values: ****p <0.0001, ***p <0.001, **p <0.01, *p <0.05.

6.2.3 Pro-inflammatory Behaviour Induced by cGAMP-POs in DC2.4 and B16F10-OVA Cells

The reduced cell viability previously described in DC2.4 and B16F10-OVA could be an indication of metabolic stress or apoptosis triggered by the inflammation. It was therefore investigated if the cGAMP:PMPC-PDPA formulation was able to trigger type I inflammation, the first step towards immunisation as previously described.

To characterise the inflammatory signature of cGAMP:PMPC-PDPA formulation, a few selected pro-inflammatory cytokines were quantified: INF- β , which belongs to type I IFN response along with IFN- α [304]; IL-6 as key pro-inflammatory cytokines promptly released upon viral infection; TNF- α and IL-12p70 as pro-inflammatory cytokines with direct activation of the expression of INF- γ , mediator of the adaptive immune response [305].

For the experiment, DC2.4 and B16F10-OVA were seeded and cultured overnight before treating them with the final concentration used in single-dose MTT.

The supernatant of DC2.4 and B16F10-OVA cells was collected after 24h, and the pro-inflammatory cytokines were measured by ELISA.

As noticeable in Figure 48, the inflammatory response was not uniform across DC2.4 samples. As example, cGAMP-loaded POs were able to trigger the production of $\text{INF}\beta$, $\text{TNF}\alpha$ and IL-12, but not IL-6. LPS treatment was responsible for most of the cytokines released, except for $\text{INF}\beta$. These findings were in contrast with what observed in the single-dose MTT assay. On the other hand, B16F10-OVA cells confirmed their refractory behaviour to treatments, except for some minimal production of $\text{INF}\beta$ and IL-12 (Figure 48).

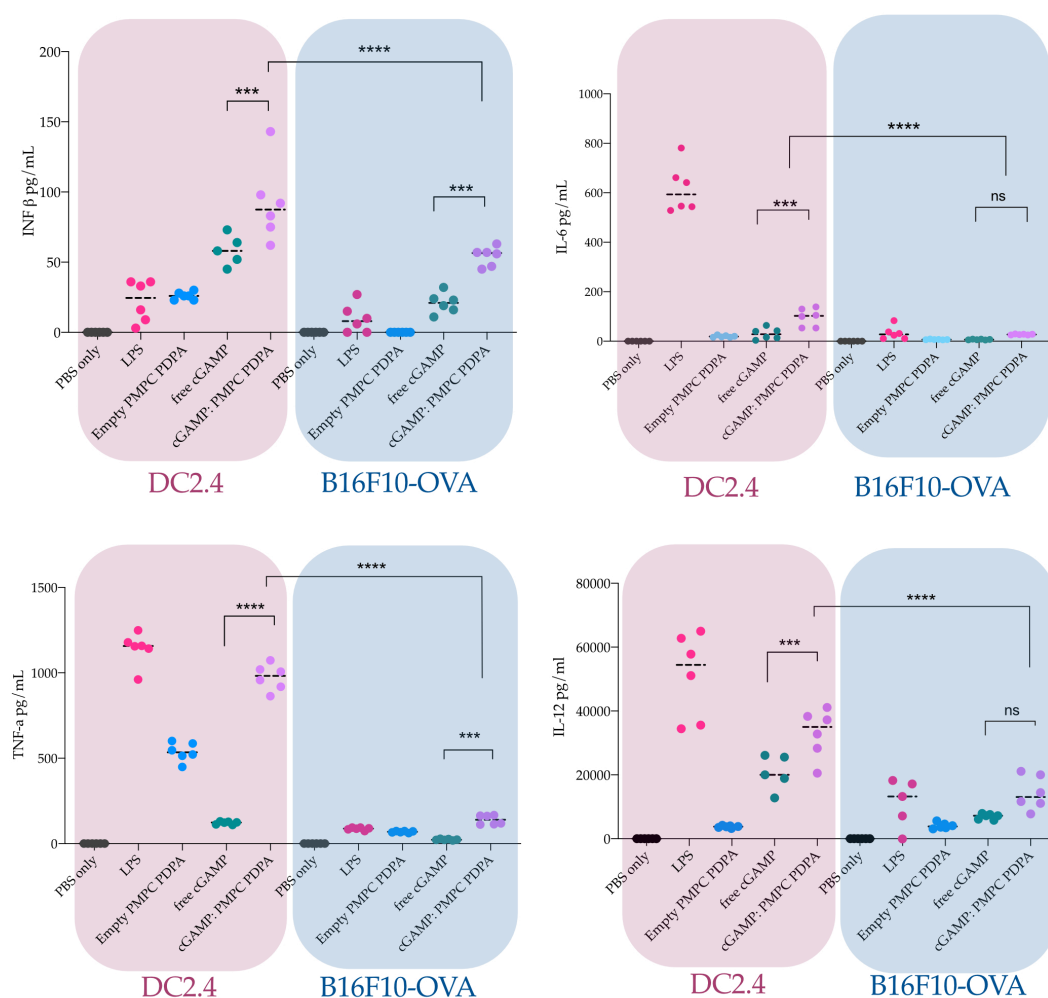


Figure 48: Cytokines Quantification from DC2.4 and B16F10-OVA supernatant. Cells were treated for 24h, followed by MTT assay. Data shown from two independent experiments performed in triplicate (n=6, mean \pm SD). Statistical analysis using one-way ANOVA Tukey's multiple comparison. Legend for data p values: ****p < 0.0001, ***p < 0.001, **p < 0.01, *p < 0.05

6.2.4 Effect of cGAMP-Polymersomes in Cell Death

Apoptosis, or programmed cell death, represents another mechanism of defence developed by the cell to contrast pathogen infection or irreparable DNA damage during the cellular life cycle [76], [306]. In the case of bacterial or DNA viruses or invasion, the infected cell stops the spread by synthesising cGAMP, which alerts neighbouring cells of imminent danger and consequently activates the type I IFN response [33]. Upon type I IFN response, a series of events are activated, culminating with the transcription of CASP3 and CASP7 genes, amongst others. Recent studies have investigated the role of cGAMP-induced apoptosis for therapeutic purposes [32][307].

Since the cGAMP-loaded formulation was found to triggered pro-inflammatory cytokines and Type I IFN response in DC2.4 and less so in B16F10-OVA cells. However, as shown earlier, both DC2.4 and B16F10-OVA cells exhibited a consistent reduction of cell viability assessed by MTT assays. At this point of the investigation, it remained to be determined whether the metabolic stress was followed by apoptotic cell death. [307].

To assess this question, the treated cells were assessed by Cell Event™ Caspase-3/7 kit to detect apoptotic cells.

As reported in Figure 49.A, DC2.4 displayed apoptotic events upon LPS and cGAMP:PMPC-PDPA treatments, in agreement with the results obtained in the MTTs and ELISA. More interestingly, the ELISA indicated LPS as the primary inflammation trigger, but the cGAMP:PMPC-PDPA formulation was responsible for the main apoptotic events (Figure 49.B). B26F10-OVA showed no inflammation-dependent apoptosis, in agreement with their cold tumour behaviour (Figure 49.A and B). It is also plausible that other type of cell death might have been activated (i.e. pyroptosis), which could not have been detected by the apoptosis-specific Caspase3/7 Cell Event kit and remains an open question for future experiments [308], [309].

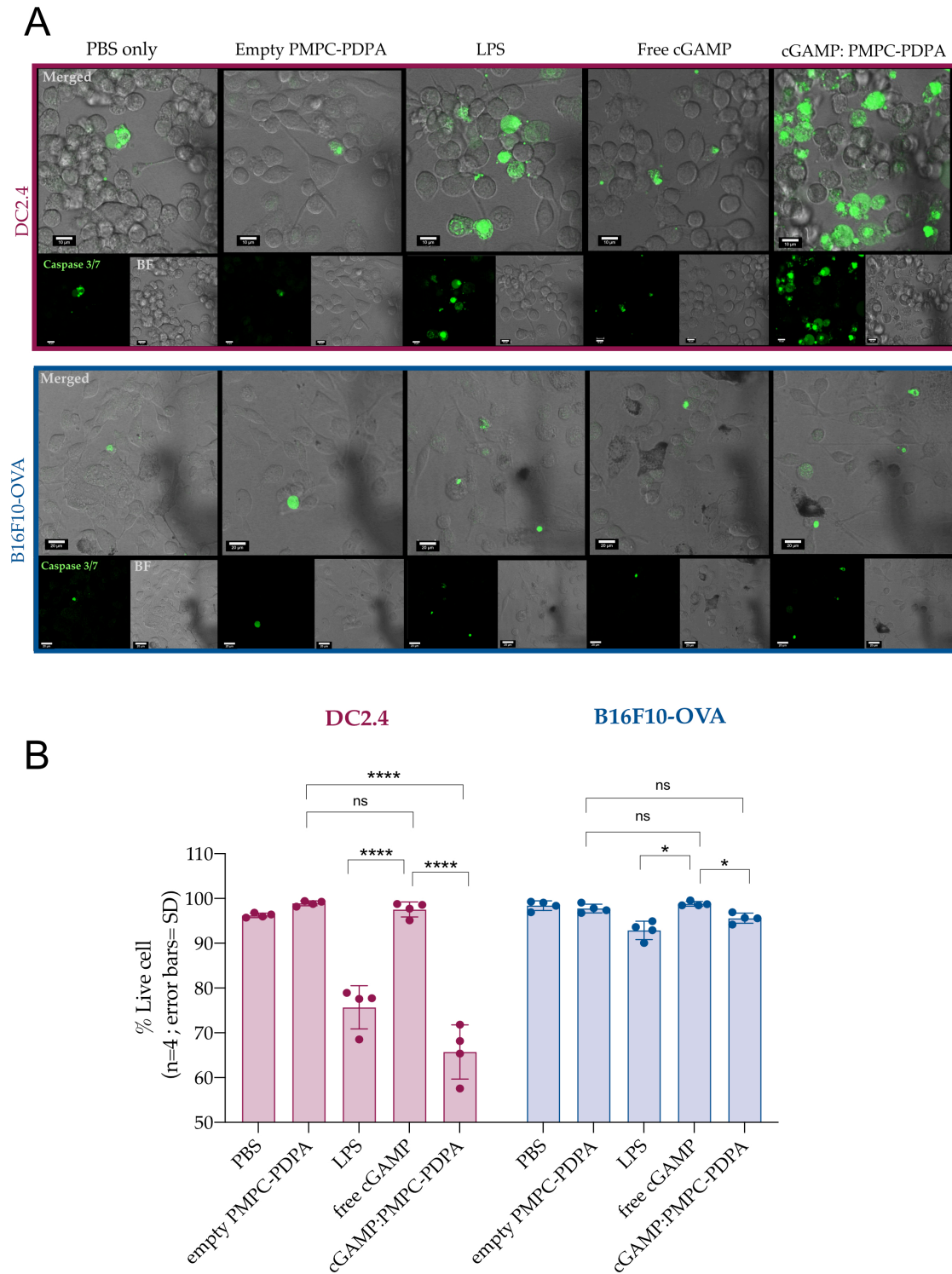


Figure 49: Cell Apoptosis in DC2.4 and B16F10-OVA.

A) Images acquired in bright field for the detection of the green fluorescence emitted by the substrate cleaved by Caspase 3/7. Scale bar is 10um for DC2.4 and 20um for B16F10-OVA cells. Histogram graph in B) reports % of live cells per each treatment in DC2.4 (left) and B16F10-OVA (right). Data collected from two independent experiments in duplicate, 10 images for each condition (mean \pm SD, n=6). Legend for data p values: ****p < 0.0001, ***p < 0.001, **p < 0.01, *p < 0.05.

6.2.5 cGAMP Delivery *In Vivo*

To assess the tumour-inflammatory power of cGAMP-loaded POs, a pilot survival experiment in immunocompetent C57Bl6 mice was performed. First, animals were injected in the flank with B16F10-OVA melanoma mouse cells and treated with multi-injection, as described in Paragraph 4.5.1. A total mass of cGAMP-encapsulated in PMPC-PDPA POs around 100 g in average was administered as treatment to the animal, and the equivalent amount of free-cGAMP was injected, and PBS as a control group.

From observation obtained during the serial dilution MTT assay, PMPC-PDPA polymer at high concentration exhibited similar toxicity profile compared to the cGAMP:PMPC-PDPA formulation. To evaluate the contribution of PMPC-PDPA polymer at high concentration in this experimental set up, it was decided to inject the maximum amount (5mg (w/w) per animal Kg), rather than equivalent amount of polymer of the cGAMP:PMPC-PDPA formulation injected. This was decided in the light of previous observation that pointed PMPC-PDPA having an anti-inflammatory effect in immune cells [179].

The tumour volume was measured daily in agreement with the ASPA-UK and animals were culled as the reaching dimension limits stated in the Project License. Unexpectedly, the statistical analysis conducted on the data did not highlight any significant difference between the PBS control groups and the cGAMP: PMPC-PDPA POs, nor free-cGAMP-treated animals in the tumour growth progression and survival (Figure 50).

One could explain these observations with sub-optimal route of administration and limited amount of drug injected being the main factors of the experimental outcome. As previously mentioned, the choice of route of administration is a rather fundamental aspect for a successful therapy. It is known that i.t. injection of therapeutics provides a better outcome and it is the preferred route in several immunotherapy studies in animal model [89], [228]. However, i.t. route is not always accessible in clinic or easy to perform in patients [89]. As shown in a recent paper, pH-sensitive cGAMP-loaded NPs successfully elicited an immunological response and total tumour remission when injected i.t. or i.v., providing evidence of the feasibility of the system [299].

Therefore, it was decided to perform i.v. injections first, and to leave i.t. injections for future experiments.

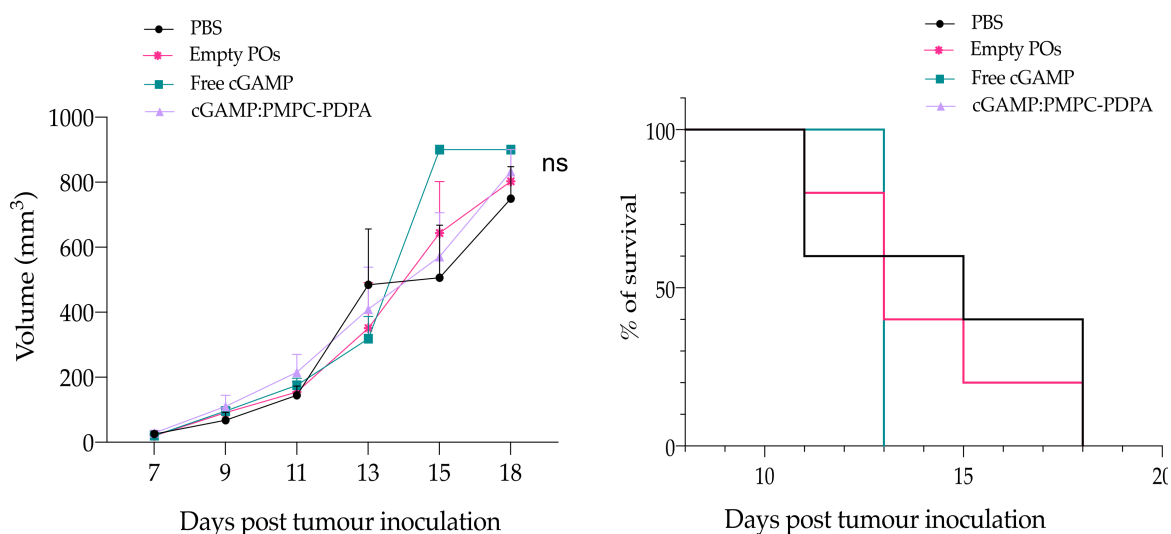


Figure 50: cGAMP-POs delivery in B16F10-OVA tumour bearing mice.

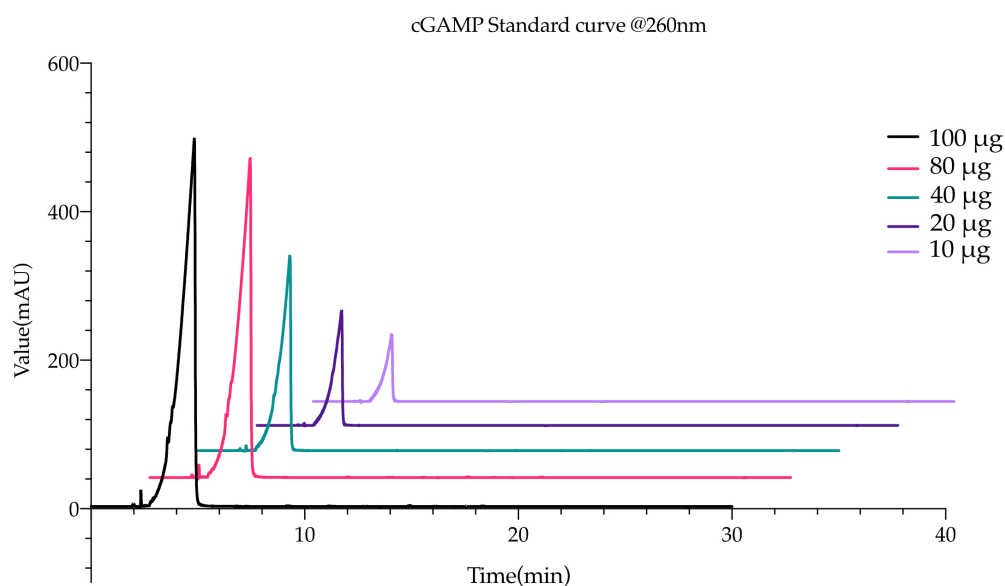
Mice were first injected with B16F10-OVA melanoma cells in the flank to establish the tumour model. Then they were treated at Day 3, 7, 10 and 12 with PBS, empty PMPC-PDPA (at 1.2mg/mL), cGAMP:PMPC-PDPA (at 1.8 μ g/mL of cGAMP in 1.8mg/mL of PMPC-PDPA) or free cGAMP (at 1.8 μ g/mL). No significant difference between control PBS, free cGAMP and cGAMP-loaded POs, with survival curves of cGAMP in PMPC-PDPA overlapping over Empty POs control. Two-way ANOVA was conducted for the statistical analysis using Graph Prism software.

What appeared to be a greater limitation on this experiment was the final amount of encapsulated cGAMP that was injected. When compared to other works, the amount injected of cGAMP in this experiment was around 500 times less than other works that showed an effective tumour control in similar experiments [299].

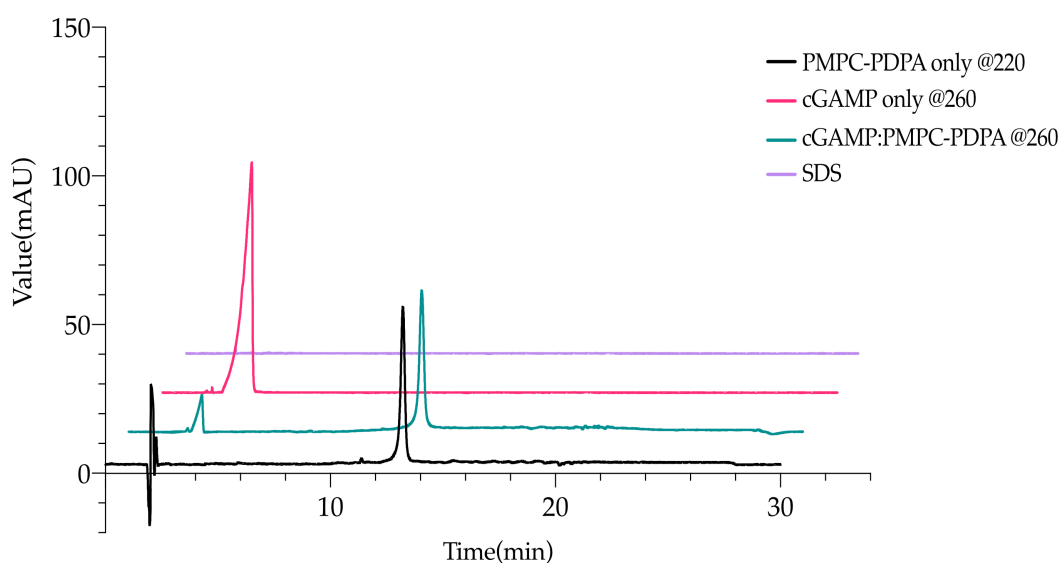
Encapsulation of cGAMP molecules into POs remain a technical challenge, showing variability across different formulations. Future experiments should be focused on the optimisation of the cGAMP encapsulation into PMPC-PDPA or other vesicles first and then best route of administration should be addressed later.

CDNs and other STING-agonists have been intensively investigated in the last years. They were found to bear a powerful effect in tumour control and eradication, especially in combination with immune checkpoint inhibitors antibodies such as anti-PD-L1 and anti-CTLA-4 [303]. Their potential role in future cancer immunotherapies remains unmatched.

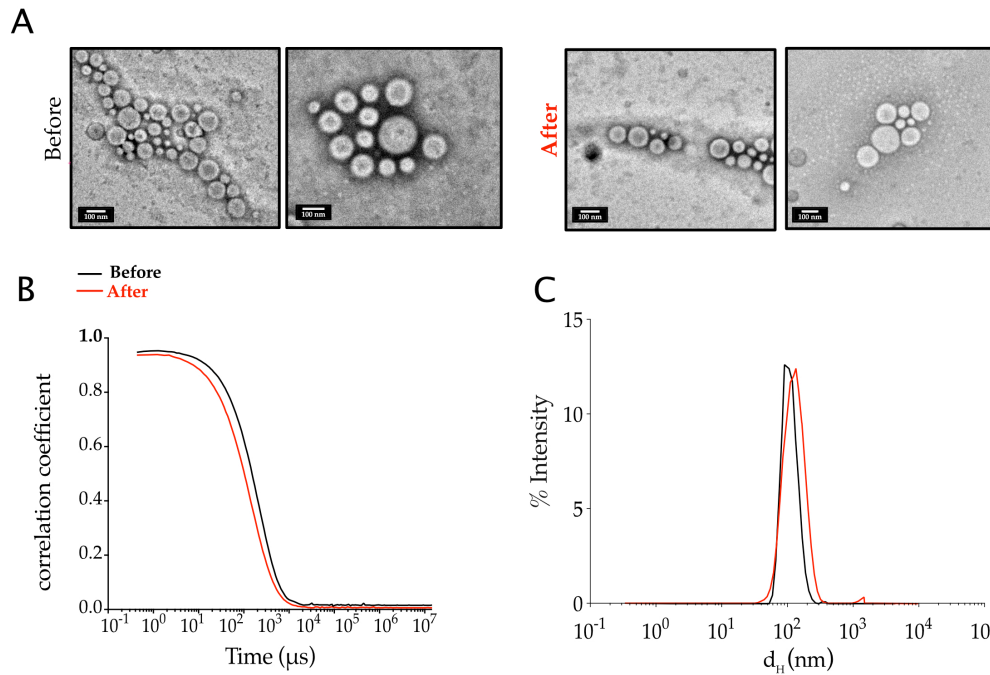
6.3 Supplement Material



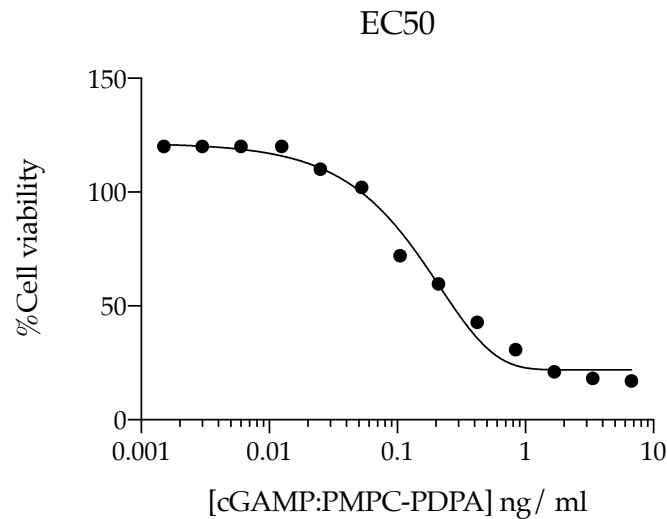
S 4: cGAMP Chromatogram at RP-HPLC.
Absorbance obtained at wavelength of 260nm.



S 5: RP-HPLC Chromatogram of analysis of cGAMP:PMPC-PDPA formulation. Graph shows chromatogram of absorbance detected from 260 or 220 nm. Distinctive peaks were detected from cGAMP only, PMPC-PDPA polymer only and cGAMP:PMPC-PDPA formulation. Quantification of cGAMP was obtained by using UV-vis 260nm to optimise the absorbance of cGAMP, whereas PMPC-PDPA polymer quantification was obtained using 220nm wavelength. This is for illustration only.



S 6: Comparison Analysis of Empty PMPC-PDPA before and after electroporation. No significant difference was found between before and after the electroporation of empty PMPC-PDPA POs. Neither at the TEM imaging in A), nor at DLS analysis in B) and C).



S 7: EC50 of cGAMP:PMPC-PDPA formulation. Value estimated using EC50 shift, X in Log[concentration] in GraphPad Prism8. However, values did not fit into the mathematical model of the non-fit sigmoidal EC50 shift prediction, which resulted in an 'ambiguous' result of EC50= 0.0531 ng/mL.

7 Phenotypic Targeting of DCs

7.1 Introduction and Aims

‘Range Selectivity’ is a new theory for the architectural design of functionalised vesicles for the active targeting [226]. As previously described in Paragraph 2.5, the theory is paving the way for a new concept of selecting suitable multivalent and multiplexing POs for the active targeting, creating the precise phenotype selection. This strategy could be essential for the targeting of key players immune cells for developing an effective cancer vaccine, such as DCs.

Thus, this new approach for the active targeting of DCs amongst all other phenotypes was explored. It was decided to focus the attention on three surface receptors to create a library of POs with the aim of creating the ultimate multivalent and multiplex low-binding affinity PO for the targeting of DCs (Figure 51).

This was achieved with the following objectives:

- To select and validate expression of DCs surface receptor (SR-B1, CD36, CD81, CD207 and CD206);
- To select and validate suitable CD207-targeting ligands obtained by phage display;
- To formulate multivalent and multiplex POs for *in vitro* targeting using receptor-specific ligands in different cell lines (NIH3T3, MutuDC and DC2.4).
- To assess phenotypic targeting *in vivo* upon intradermal injection using multivalent and multiplexing POs.

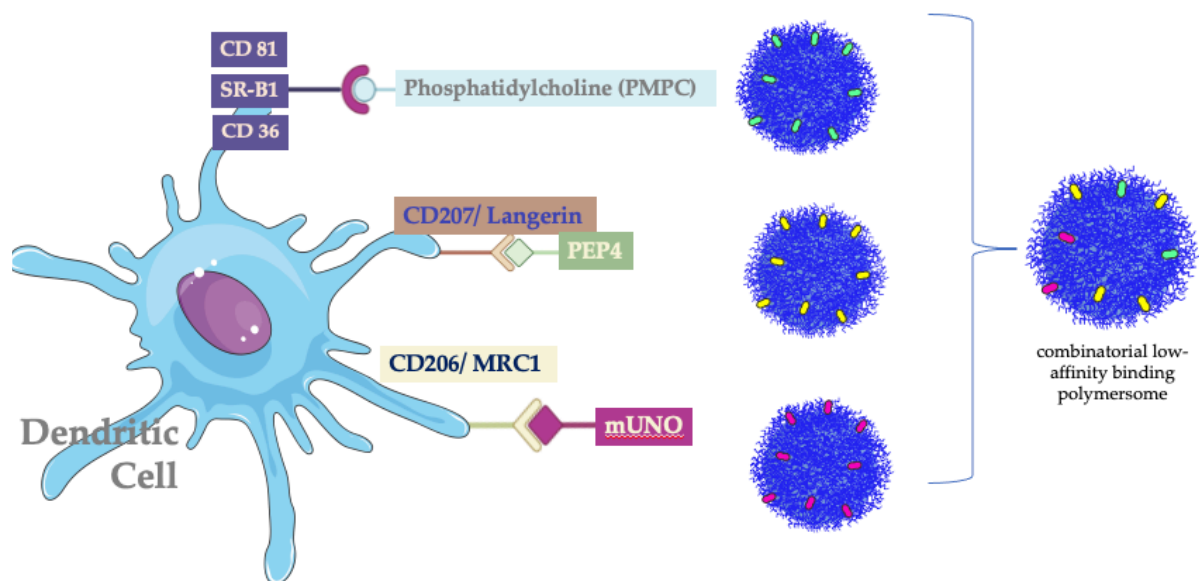


Figure 51: Graphical Abstract.

The range selectivity theory is based on the use of weak multivalent interactions between the receptor and its ligand. For example, the phosphocholine (PC) group of the PMPC block is known to interact with the SR-B1 and CD36 receptors, with some early evidence of potential interaction with CD81 receptor too (Paragraph 2.5.5.3). These receptors are ubiquitously expressed, including DCs [310]. Receptor CD207, also known Langerin, is also expressed in DCs, making it a suitable target to assess the range selectivity theory. The cartoon present one of the peptides (namely PEP4) that was found via phage display and cross-reactive against both the human and mouse CD207 receptor, as described in the next paragraphs. An additional receptor, the CD206, was added to the final library to verify the concept of phenotypic targeting across different cell lines. The receptor CD206 can be targeted using the peptide 'mUNO' (CSPGAK) , which has been recently identified by in vivo phage display and validated for the specific targeting to the receptor [311]–[313].

7.2 Results and Discussion

7.2.1 Protein Expression of Surface Receptors

The 'range selectivity' theory is based on the discrimination between phenotypes based on the number of receptors on the surface, as previously described. It is paramount to evaluate the differential expression of receptors across different cell lines, such as NIH3T3, DC2.4 and MutuDC1940. The receptors of interest, SRB1, CD81, CD36, CD206 and CD207, were validated by WB and confocal imaging. For each protein a housekeeping protein, such as GAPDH or α -tubulin was used for the normalisation and relative quantification (Figure 52). This provided a first glance of the pattern of expression.

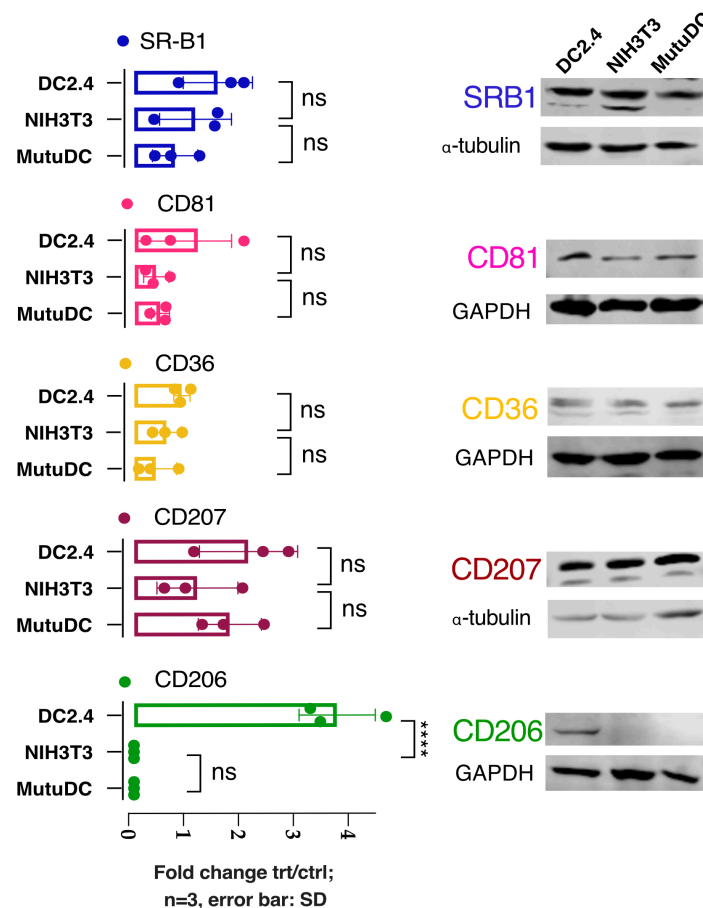


Figure 52: Receptors expression in different cell lines validated by WB assay. Data collected from three independent cell lysate n=3, mean \pm SD. For statistical analysis was used the two-way ANOVA.

As expected, receptors involved in the PMPC binding such as SR-B1, CD81 and CD36 were found expressed in all cell lines, confirming their ubiquitous expression. Receptor CD207 was found to be expressed in DCs cell lines DC2.4 and MutuDC1940, as expected. The CD207 expression was detected in NIH3T3 cells as well, as suggested by other works [314]. Surprisingly, the receptor CD206 was found to be expressed only in DC2.4 cells, in agreement with the immature phenotype of these cells. The DC2.4 cell line was originally derived from bone marrow isolates of C57BL/6 mice and immortalised with retrovirus vectors expressing murine GM-CSF and the *myc* and *raf* oncogenes [315]. In fact, CD206 represents an hallmark of DC maturation [246]

As can be observed from the bright field microscope, the three cell lines NIH3T3, DC2.4 and MutuDC, present different morphology from each other. The different phenotype is reflected at the morphological level and at surface composition, with different levels of receptors and glycosylation (Figure 53 and Figure 54).

These findings are posing the fundamentals to assess the range selectivity theory: the binding of a particle on a surface depends on the number of interactions created, minus the steric hindrance coming from the polymer brush interacting with the glycocalyx of the cell.

The presence of the glycocalyx was assessed by flow cytometry and confocal imaging, using fluorescent-labelled lectin, which is commonly used to detect glycan-binding glycoproteins [274]. Results obtained by flow cytometry (Figure 54) indicated higher expression of glycans in MutuDC cell lines compared to DC2.4 and NIH3T3 cells, potentially suggesting higher steric hindrance between the PO and the cell surface. Whereas DC2.4 and NIH3T3 cells presented similar level of glycans on their surface. These results were corroborated by confocal imaging analysis. Although the protocol for confocal imaging required PFA fixation of the sample, compromising the integrity of the membrane and potentially the composition of the glycocalyx, the qualitative results were confirmed across the two techniques.

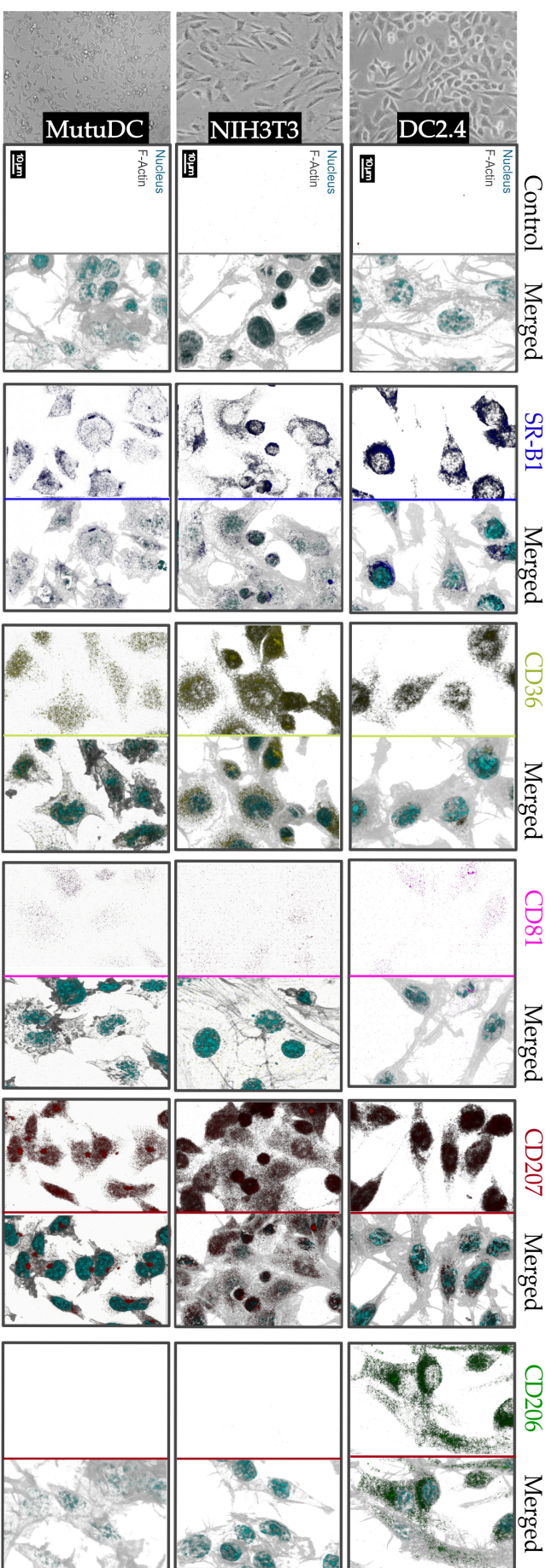


Figure 53: Confocal imaging of surface receptors in cell lines. Confocal imaging confirmed previous findings and the expression of SR-B1, CD36, CD81, and CD207 was confirmed in all three cell lines, except for CD206 which was found only in DC2.4 cell. No subcellular localisation or clustering was detected by the imaging, although receptor CD207 is known to form trimers by the long neck extracellular region (molecular modelling reported in Figure 18). Possibly the confocal imaging does not offer the resolution power intended to confirm the trimerization of the receptor.

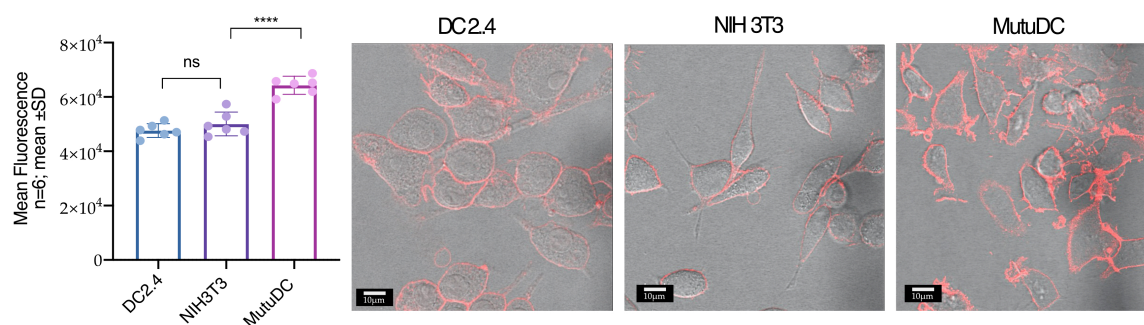


Figure 54: Staining of the cellular surface glycocalyx.

Flow cytometry analysis (left) and confocal imaging of cells (right) stained with fluorescent-labelled lectin (in red). Data are collected from two independent experiment conducted in triplicate, $n=6$; mean \pm SD. Performed one-way ANOVA for the statistical analysis with GraphPad Prism8.

Although lectin staining is a quick, reliable method of detection of glycans and is routinely used in glycobiology ([274]), the method provides only a preliminary quantitative measure. The specific characterisation of the composition of the glycocalyx should be determined in future experiments using mass spectrometry or specific monoclonal antibodies.

7.2.2 Screening and Validation of DC207-targeting Ligands

The CD207-targeting ligands were screened and selected using the phage display technology and ELISA assay, as described in material and methods section. After two rounds of phage display screening, the M13 phage were used for large scale selection using the ELISA assay. Streptavidin-coated plates were first incubated with huCD207 and then with moCD207 receptor. It is worth to notice that the found peptides are cross-reactive against human and mouse, increasing their potential therapeutic applications. Next, anti-M13 antibodies conjugated with HRP were added and the chemiluminescence signal was measured with plate a reader at a wavelength of 450nm. Results obtained for each peptide were ranked by absorbance found in moCD207 and huCD207-coated plates and compared to control plate (streptavidin-coated) to determinate the binding strength. The first four

M13 phage with highest signal were sent for sequencing, revealing the amino acid sequence of binding reported in Figure 55.

CD207 pep1	HSAQISCAHLWSPYFEWCEKAAAE
CD207 pep2	HSAQYNCIGQDWEVFWLCMYAAAE
CD207 pep3	HSAQHSMCALDFMSFPCLIMAAAE
CD207 pep4	HSAQFWCLFTENYEYQECYLAAAE

Figure 55: Sequences of DCs- targeting peptides.

Blue letters identify sequence of amino acids involved in the binding with the receptor. Peptides sequences are flanked by regions of the vector used to engineered bacteriophage clones and for the sequencing.

The peptides selected ((PEP1, PEP2, PEP3 and PEP4) were then synthesised (R&D Systems) with a biotin moiety at the N-terminus for future validation experiments.

The newly synthesised four peptides were used for a validation ELISA experiment to confirm the findings and to identify the binding affinity. Results reported in Figure 56 show the chemiluminescence signal intensities measured from the interaction between the selected CD207-targeting peptides and the huCD207 and moCD207.

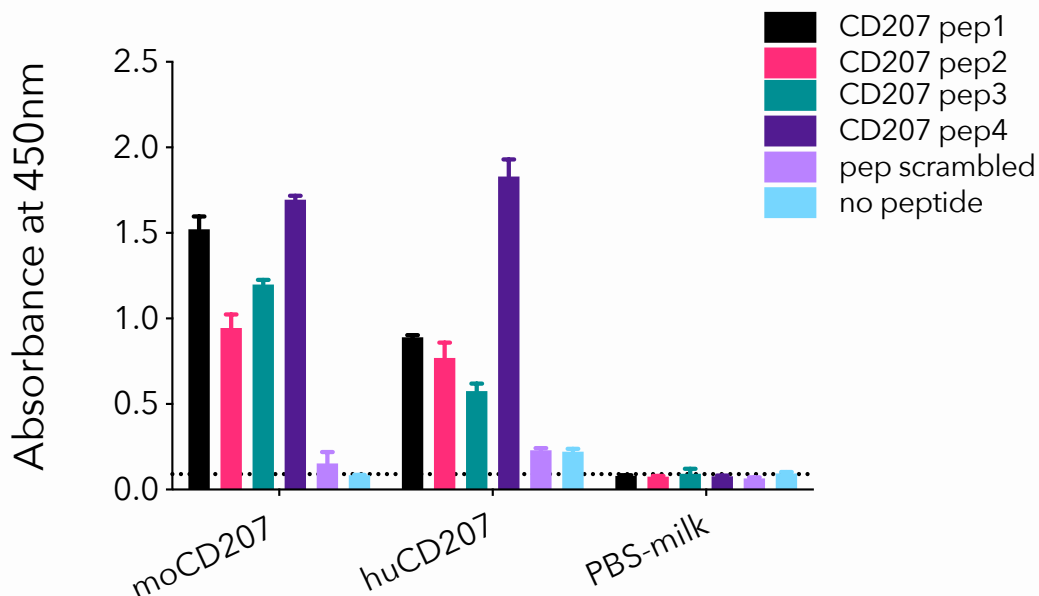


Figure 56: ELISA test for validating synthetic peptides interacting with huCD207 and moCD207.

Scramble peptide (pep C-) and no-peptide were used as negative control for the assay along with PBS with 5% milk. The threshold for the background is indicated with the dotted line.

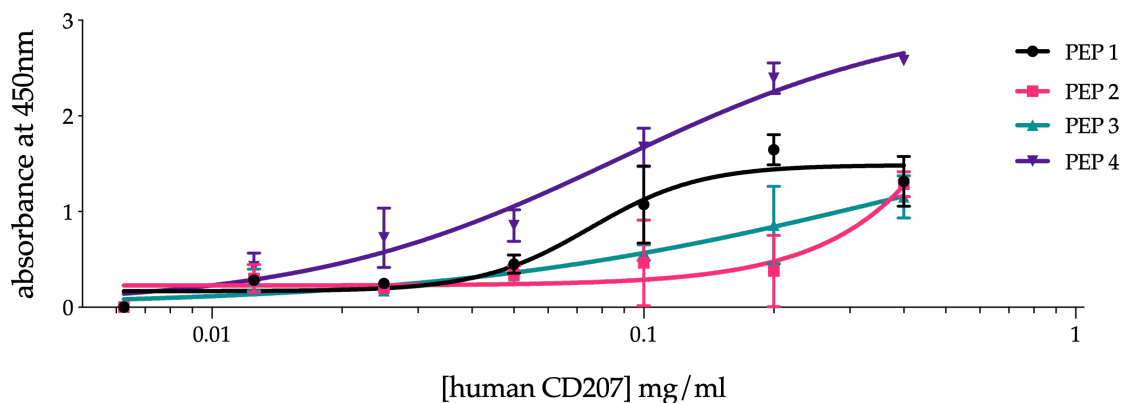
The graph shows a low level of background and a specificity set by the level of signal emitted in control samples such as scrambled peptide (peptide with a random sequence and no relevant to this assay) and no-peptide samples. No relevant signals were detected in the PBS-milk control plate, confirming the absence of false positive interactions between the selected peptides and the streptavidin-coated plates.

All peptides strongly interact with the moCD207 receptor, as their signals are at least twice that of the scramble peptide. It might be possible to argue that PEP1 and PEP4 showed the highest level of binding, while PEP2 and PEP3 showed a lower level of signal that might be due to a minor strength of binding. ELISA on humanCD207 receptor confirmed the cross-reactivity of these peptides across both species, fundamental for potential future experiments and translational purposes. PEP1 and PEP4 are showing the strongest interaction with the huCD207 receptor across the four peptides, however, PEP1, 2, and 3 show similar level of binding, but slightly lower than ones obtained with the moCD207 (Figure 56). For these reasons, PEP4 may have the highest promise for future *in vitro* and *in vivo* experiments since it demonstrated the highest binding affinity for both proteins.

Next, half of the effective concentration (EC50), which represents a concentration value of a drug, antibody or peptide which induces a response halfway between the baseline and maximum after a specified exposure time [316]. At this time, the EC50 was estimated for the four peptides in analysis against the huCD207 only. Technical challenges in expressing and purifying the moCD207 protein made it impossible to estimate the EC50 of peptides binding it. However, Basic Local Alignment Tool (BLAST) identified a similarity of 77% between the human and the mouse CTL domain (Supplement Material S 9), considering that peptides have been selected for binding towards the both species, it might be assumed that PEP1-4 might present very similar binding behaviour towards the moCD207.

The EC50 for the four peptides targeting CD207 was estimated using streptavidin-coated and the biotinylated-peptides. Dilutions of huCD207 protein were added and binding signal was revealed using anti-HisTag-HRP. EC50 values were calculated

and are presented in table in Figure 57. Overall, EC50 values were reported to be between 41- 86 nM for the peptides in analysis and they are showed in Figure 57.



	PEP1	PEP 2	PEP 3	PEP 4
EC50 mg/ml	0.07507	n.a.	0.3958	0.0872
interval mg/ml	0.05517 to 0.1021	n.a.	0.0001178 to 1330	0.05006 to 0.1519
R ²	0.883	0.7069	0.8341	0.9556
EC50 nM	41.46	n.a.	86.8	43.29

Figure 57: EC50 ELISA for the human CD207 receptor with respective EC50 values for each peptide.

The EC50 values were determined for all but PEP 2 (ambiguous/not applicable (n.a.)), which did not reach the point of saturation in this set up and are reported in the table. Values reported in the table were obtained using Graph Prism 8 using nonlinear fit EC50 analysis.

7.2.3 Binding with PMPC-Ligand

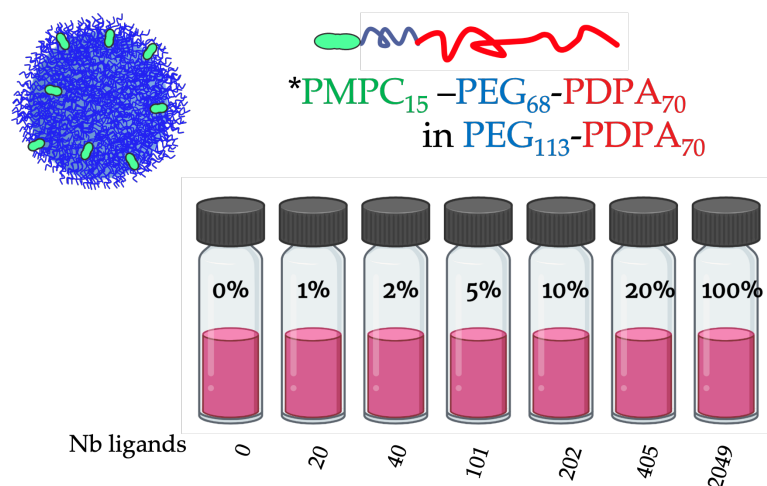
To assess the concept of ‘Range Selectivity’ *in vitro*, it was decided to implement a multivalent system of POs as previously described (Figure 51).

One of the ligands selected is the PMPC block polymer, for its natural capability to bind SR-B1, CD36 and CD81 receptors. Before proceeding with the binding experiments *in vitro*, the PMPC₁₅ block was first added to the PEG₆₈-PDPA₇₀ diblock polymer by cycloaddition (performed by Dr Aroa Duro Castano and Dr Yangwei Deng). Considering the ubiquitous expression of the scavenger receptors and the potential multiple interaction of PMPC with them, it was decided to use a longer block copolymer as main constituent of the PO brush, such as PEG₁₁₃-PDPA₇₀. With this strategy, the resulting POs will have the PMPC ligands embedded within the PO

brush, increasing the repulsion energy of the binding and therefore increasing the selectivity.

For preparing the POs for the binding assays, seven polymers mix ranging with distinct % of Molar mass of PMPC-ligand in PEG-PDPA were prepared. Previous experiments conducted by other members of the group, revealed that the most selective binding is generally comprised between the 0.5 -10 of %Molar mass of PMPC-ligand in the formulation. Based on these findings, it was decided to prepare a batch with a wider range of %Molar PMPC (0-20%) in PEG-PDPA polymer, with the 0%PMPC-PEG-PDPA (100%PEG-PDPA PO, pristine) and 100%PMPC-PDPA formulation as controls. Moreover, a 0.5%Molar mass of Rhodamine B (Rho) was included in the polymer mix to detect the PO binding (Table 9).

POs were prepared by solvent switch as described previously, with the %Molar mass of each polymer as reported in Table 9. The concentration of the total mass of polymer for each formulation was obtained by RP-HPLC. POs were then analysed at TEM and DLS to confirm morphology and dimension (Supplement Material S 10).



Formulation	Nb Ligands	PMPC ₁₅ -PEG ₆₈ -PDPA ₇₀ % Molar mass	PEG ₁₁₃ -PDPA ₇₀ % Molar mass
0% *PMPC-ligand	0	0	0.95
1% *PMPC-ligand	20	0.01	0.94
2% *PMPC-ligand	40	0.02	0.93
5% *PMPC-ligand	101	0.05	0.9
10% *PMPC-ligand	202	0.1	0.85
20% *PMPC-ligand	405	0.2	0.75
100% *PMPC-ligand	2049	0.95 PMPC ₂₅ -PDPA ₇₀	

Table 9: Polymer %Molar mass in *PMPC-PEG-PDPA formulations prepared by solvent switch for the binding experiment.

Figure at the top represent summarise diblock copolymers used, the % of Molar of PMPC-PEG-PDPA with the corresponding number of ligands for each formulation.

Thanks to the geometric considerations described in Paragraph 4.1.6.1 it was obtained an estimation of the number of ligands included in each vesicle.

Before proceeding with the binding assays, it was assessed the kinetic of cellular uptake in DC2.4 cells to minimise the required binding time. PMPC-PDPA POs are known for their quick cellular uptake, which is usually within a few min, as described in previous works [179]. In contrast, PEG polymer is known for its anti-fouling properties and longer cellular uptake time. A first preliminary binding assay was conducted in DC2.4 cells treated with fluorescent 0%PMPC-PEG-PDPA (pristine PO) vesicle at different time points. A fluorescent signal was detected after 1h of incubation by confocal imaging. The dynamic of cellular uptake confirmed the anti-fouling properties of PEGylated vesicles in DC2.4 and the experiment restricted the observational time for the future binding experiments at 1h of incubation (Figure 58).

With DC-targeting PEG-PDPA POs will be expected a quicker cellular binding time and uptake. Therefore, all future binding assay experiments were then performed with a multi-time points at 3, 5, 7, 20, 15, 20, 30, 45 and 60 min after PO incubation.

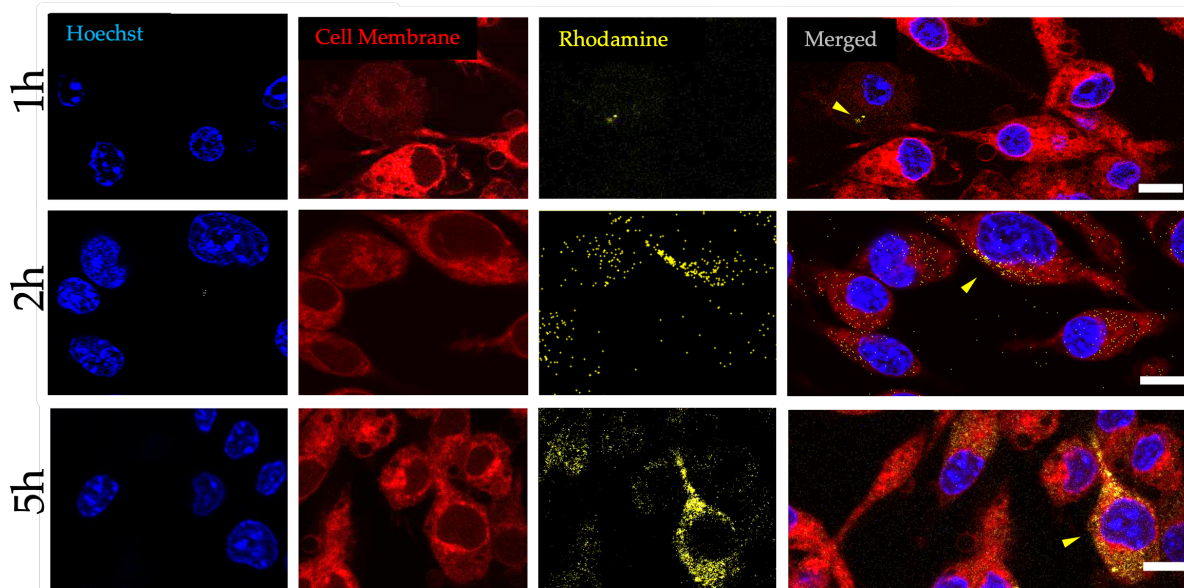


Figure 58: Cellular uptake in DC2.4 cells by confocal microscopy. DC2.4 cells were fixed after the incubation period and stained with Hoechst for nuclei (cyan) and deep red cell mask for plasma cell membranes (red). Rhodamine B released upon polymersomes uptake is visible in yellow. Yellow triangles represent points of cellular uptake and accumulation of the dye. Scale bar is 10 μ m.

Next, it was performed a multi-time points binding assay using the different %Molar mass of PMPC functionalised in PEG-PDPA presented in Table 9. One day before the experiment, NIH3T3, DC2.4 and MutuDC cells were seeded in a 96-well plate as such they presented a 70% confluency on the day of the experiment. In this way the absorption of nanoparticles was consistent across the three different type of cell surface. The media was gently removed and replaced with working solution containing final concentration of 0.2mg/mL of PO in 10% (v/v) FBS in PBS. Each prepared formulation was left incubating a different period of time between 3 and 60 min. At the end of the experiment the supernatant was removed and replaced with PBS looking for fluorescent signal by plate reader.

The signal was normalised and interpolated with the standard curve of the relative formulation previously obtained. With this method, the fluorescent signal detected was used to estimate the % of material uptaken by the cell at each time point. The

results from the binding assays were plotted as 'contour map' and are reported in Figure 59.

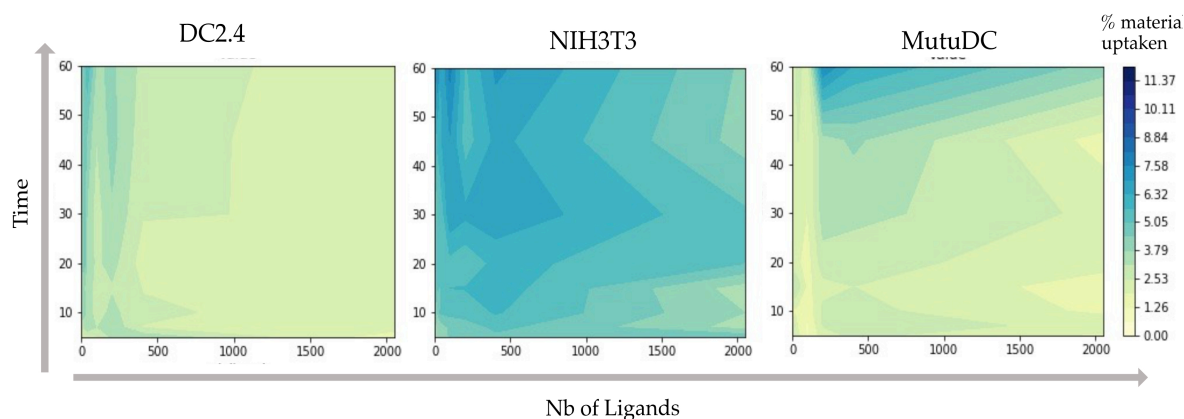


Figure 59: Contour map of multi-time point binding assay with multivalent PMPC-ligand POs.

Each cell line has been incubated with same amount of material (0.2mg/mL final concentration) for different time periods. Time points of incubation are presented on the Y axis, while the Nb of ligands of formulations are reported on X for each contour map. Coloured scale bar represents the average amount of material uptaken or bound to the surface of the cell. Dark-blue colour represents higher amount of material detected by fluorescence. It is worth to notice that the mathematical function used to generate the contour map allows the prediction of the binding behaviour as a continuum between data points. Average values were obtained from 3 independent experiments in triplicates (n=9). Data were plotted also as Heatmap graph reported in Supplement Material S 15.

As noticeable in Figure 59, the binding behaviour presented for each formulation it is rather distinctive for each cell line, aka phenotype. In DC2.4 cells for example, it could be observed a peak of 5-6% of total material uptaken with <500 Nb of ligands. The remaining area of the counter map present unspecific binding (around 2% of material uptaken) of particles to the cellular surface and no other region with contradistinctive binding. In the NIH3T3 cells, it was observed a general binding and uptake across most of the formulations. However, rapid binding kinetic events occurred at <500 Nb of ligands, with an uptake of 6-7.5% of the total material. There were identified two main peaks of binding, one at Nb ligands <100 and the second one at Nb ligands <500. However, taking in consideration the small difference of material between the two peaks identified and the rest of the graph, it could not be excluded unspecificity of binding in these cells.

Instead, MutuDC exhibited a third distinct binding pattern, suggesting a different phenotype. Interestingly, and unexpectedly, it was found no peak of binding at small

Nb ligands as previously observed in DC2.4 and NIH3T3. While observing the binding map for MutuDC, it could be observed a prominent entry of particles at later time point (starting from 45min), which is contrast with DC2.4 and NIH3T3, where the entry of particles was detected at earlier time points (starting from 10min) and with lower amount of Nb ligands.

One explanation of these differences might be represented by the different protein composition of the receptors present on the cellular surface. As previously described, the total energy of binding depends on the affinity ligand-receptor and the repulsion energy generated by the steric hindrance between the surface of absorption and the PO. Hence, different protein expression profiles correlate with different cell phenotypes, therefore with a distinctive phenotypic binding. However, when looked at the overall expression levels of receptors SR-B1, CD81 and CD36 for each cell line, they seemed to not correlate with the phenotypic pattern of binding. For example, the expression level detected for SR-B1 and CD81 is slightly higher in DC2.4 than NIH3T3, but the glycans expression is higher in NIH3T3. These might indicate more but less discriminative binding in DC2.4 due to the glycocalyx. However, it was quite the opposite, with NIH3T3 presenting the higher amount of material uptaken. Considering the juxtaposition of PMPC-ligand within the PO brush, one would assume higher energy of repulsion during the absorption of the particle to the surface, therefore 'less' binding but more selective but as reported in Figure 59 this was not the case.

It was not possible to a direct correlation between the level of expression with the 'phenotypic binding', suggesting a rather complex problem to untangle. It is possible that other unknown factors might have played an important role in the binding behaviour and the empirical method of particle design requires further refining.

It could also be speculated that cellular surface morphology might have played a role in the particle uptake. As observed in bright field and confocal imaging (Figure 53 and Figure 54), the three cell lines presented a distinct phenotypic morphology with DC2.4 and MutuDC been smaller and with a rough surface characterised by dendrimers and filaments, whereas NIH3T3 presented a larger smoother surface in agreement with their original lineage. Empirical observation in transfection

experiments suggest a flat and smooth surface might be favourite for the uptake of lipo-complexed when compared to an irregular and rough surface [317].

Overall, these preliminary experiments of phenotypic binding provided with several information. Firstly, PMPC-ligand was confirmed to be effective in participating in the binding between the PO and cell surface, with early entry time points, as already observed in other cell types in the lab. Secondly, it was observed that the same particle batch binds differently across different cell phenotyping, confirming that, indeed, is possible to reach a range of targeting unique for each cell line, hence the phenotypic targeting, by refining the architecture design of nanoparticles. And lastly, it was confirmed the paradigm shift in the field where 'more ligands' on the particle surface do not necessarily mean better selectivity of binding.

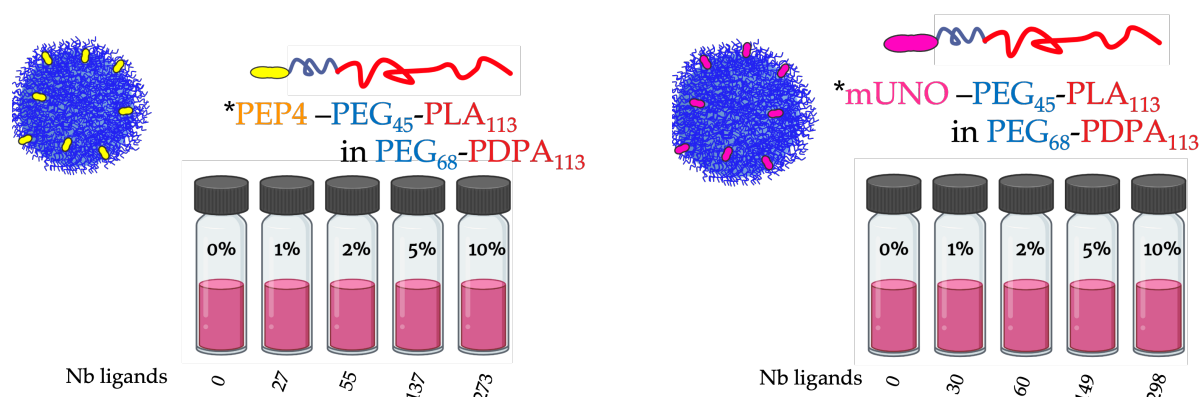
7.2.4 Binding with PEP4 and mUNO-Ligands

To validate the binding activity of the peptides to CD207 and CD206-targeting, it was first necessary to prepare the peptide-polymer *via* cycloaddition as described in Paragraph 4.3. In consideration of the low binding affinity demonstrated in the ELISA experiment by PEP4 and confirmed with the EC50, it was decided to use the PEG₆₈PLA₁₁₃ diblock copolymer for the cyclo-addition, which is longer than the PEG₄₅PLA₁₁₃ polymer (chemical structure in Figure 11) of the PO brush. Thus, the resulting functionalised POs presented a protruding ligand from their brush.

The same strategy was adopted for the CD206-targeting mUNO peptide. In fact, it was demonstrated an effective CD206-targeting only when mUNO formulated as a three-arm branched polyanionic dendrimer, suggesting a low binding affinity of mUNO peptide and the need of cooperativity [318].

Based on previous results from PMPC-ligand binding assay *in vitro*, it was decided to focus the attention a smaller range of number of ligands on the PO surface. The newly prepared batches of *PEP4-PEG-PLA and *mUNO-PEG-PLA POs presented a range of %Molar mass of peptide-polymer comprised between 1% and 10%. PEG-PLA-only PO (%Molar mass of peptide) was used as pristine control. All vesicles were prepared via solvent displacement method as previously described in Paragraph 4.1.3. For the preparation of each formulation, it was taken in

consideration the peptide conjugation efficiency, expressed as ratio between the final mass of peptide (quantified with the BCA assay) and the total mass of peptide used for the click-reaction. The polymer mixes of functionalised POs with the different %Molar mass of polymers are listed in Table 10.



***PEP4-PEG-PLA formulations:**

Formulation ID	Nb Ligands	PEG ₄₅ -PLA ₁₁₃ %Molar mass	PEP4-PEG ₆₉ -PLA ₁₁₃ * %Molar mass
0% PEP4-ligand	0	0.95	0
1% PEP4-ligand	27	0.93	0.012
2% PEP4-ligand	55	0.92	0.025
5% PEP4-ligand	137	0.88	0.064
10% PEP4-ligand	273	0.82	0.128

***mUNO-PEG-PLA formulations:**

Formulation ID	Nb Ligands	PEG ₄₅ -PLA ₁₁₃ %Molar mass	mUNO-PEG ₆₉ -PLA ₁₁₃ * %Molar mass
0% mUNO-ligand	0	0.95	0
1% mUNO-ligand	30	0.93	0.012
2% mUNO-ligand	60	0.92	0.024
5% mUNO-ligand	149	0.89	0.061
10% mUNO-ligand	298	0.82	0.122

Table 10: Schematic representation (figure) and polymer molar percentage (table) of each componen for the self-assembly of PEG-PLA POs used in binding assay experiments. Schematic representation of the POs batch for PEP4 (top left) and mUNO (top right) cartoons. Peptide-polymer Molar percentage breakdown (Table) after considering the conjugation efficiency from the click-reaction. Conjugation efficiency for PEP4 was estimated to be 78%, whereas mUNO was 82%. The Nb of ligands were calculated using geometric consideration explained in paragraph 4.1.6.1.

As previously mentioned, the prepared formulations were first purified by the remaining organic solvents by dialysis, concentrated with hollow fiber and purified from free-dye by SEC. Then they were analysed by TEM and DLS to confirm size and morphology (Supplement Material S 11 and S 12). The method of solvent displacement was revealed to be particularly efficient in the production of a monodisperse samples with an average d_H around 80nm in both collections. As reported in the DLS graphs, all correlation curves and size distribution are perfectly overlapping, indicating non-interference by the peptide-polymer during self-assembly reaction and method consistency. TEM imaging obtained from all the prepared formulation confirmed observations made by DLS, in terms of size and monodispersity. The concentration for each formulation was quantified at RP-HPLC and standard curves for each sample were generated for the interpolation of the fluorescent signal obtained from the binding assays, estimating the % of total material uptaken.

The binding assays of the two new batches of POs were performed using the same protocol previously implemented for the *PMPC-PEG-PDPA POs. The relative fluorescent signal derived from the encapsulated Rho was normalised for the control and interpolated with standard curve previously obtained, from which was possible to estimate the percentage of material uptaken by the cell. The results of the binding assays are reported in Figure 60.

Each 'binding map', or contour map, represents the material uptaken by the cells in function of the Time and the Nb of Ligands displayed on the out layer of functionalised PO. As noticeable, each contour map is showing different regions of 'binding hot-spot' across cell lines (from left to right, DC2.4, NIH3T3 and MutuDC), indicating that the same batch of formulations interact differently with each cellular phenotype, representing the groundwork for achieving the phenotypic targeting with the range selectivity approach.

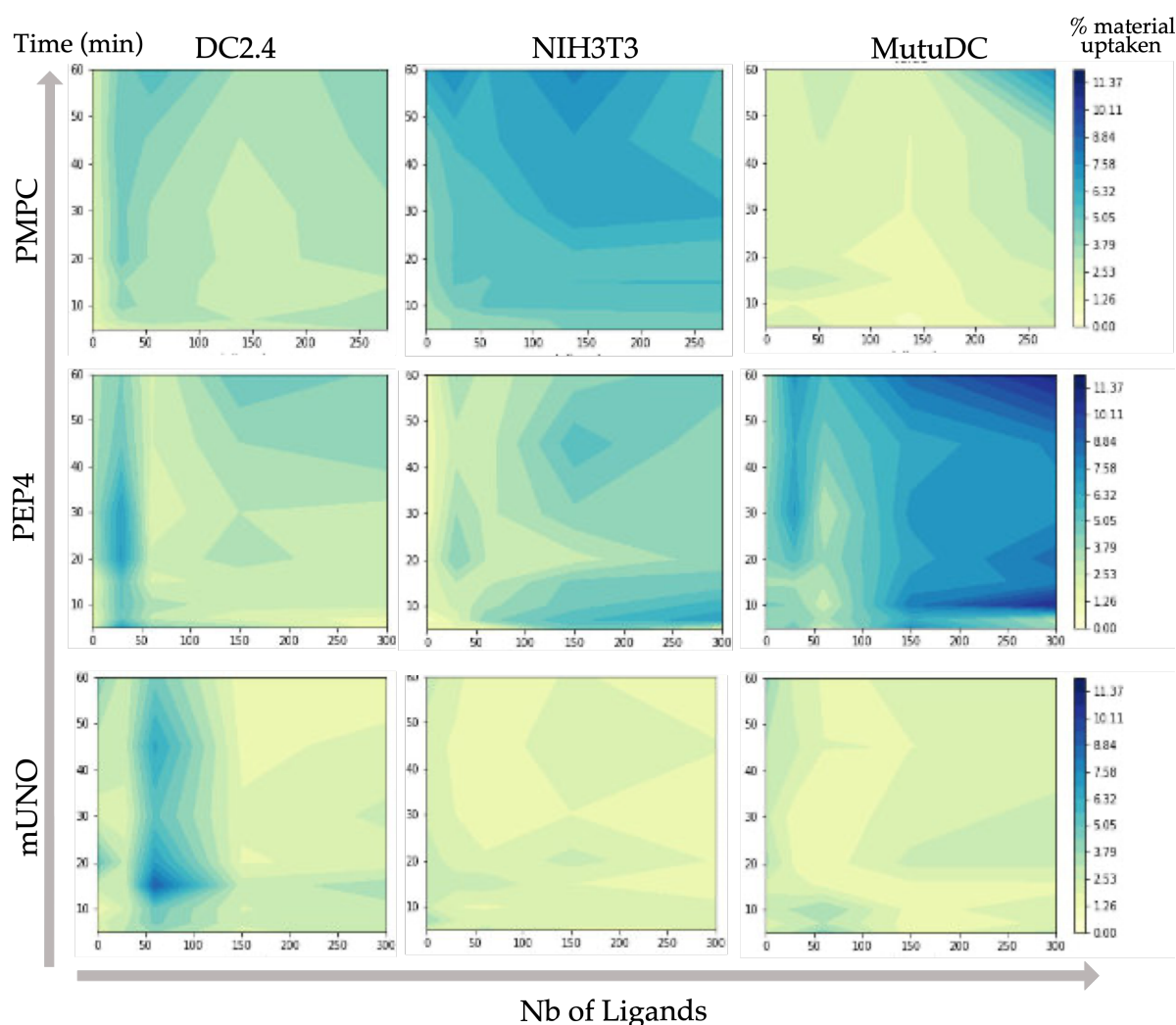


Figure 60: Binding assays using PMPC, PEP4 or mUNO ligands in multivalent POs. Each contour map represents the % of material uptake (coloured bar on the right) in function of the incubation time (between 5 and 60 min, vertical axis) and the relative Nb of ligands estimated on the surface for the batch of PO for that ligand. The first row of contour maps presents the binding kinetic of *PMPC-PEG-PDPA POs batch in DC2.4, NIH3T3 and MutuDC cells. The second row of contour maps shows results obtained from the binding using *PEP4-PEG-PLA POs and third row shows results from *mUNO-PEG-PLA POs. Data were obtained from 3 independent experiments in triplicates (n=9). Data were plotted also as Heatmap graph reported in Supplement Material S 16.

The first row in Figure 60 presents results obtained from binding with PMPC-ligand between 0-10% molar (Nb ligands 0-202) as previously discussed. 'Hot-spots' of binding at 60 min with Nb ligands < 100 in DC2.4 and > 200 in MutuDC were identified, while NIH3T3 presents a general binding across all time points and Nb of ligands.

The second row of binding maps were obtained using *PEP4-PEG-PLA formulations 0-10% Molar of peptide-polymer (Nb ligands 0-273) obtained in DC2.4,

NIH3T3 and MutuDC, respectively. Each binding map reported in here presents a different behaviour of binding across cell phenotypes. In DC2.4, a hot-spot after 20min incubation with 1% Molar PEP4 peptide-polymer (Nb ligands 27) was observed. The same hot-spot was found, although smaller, in NIH3T3, while it appeared to be more noticeable in MutuDC, which however displayed unspecific binding with Nb ligands > 100.

When the levels of expression of CD207 receptor across cell lines are taken into consideration (Figure 52), it can be observed that DC2.4 and MutuDC have same number of receptors on their surface, which could explain why both cell lines present a similar binding hot-spot behaviour. On the other hand, NIH3T3 cells were reported to have a lower amount of receptor which might explain the less general binding. However, the experimental variability behind the protein quantification *via* WB should also be noted, which might represent a limitation in formulating strong conclusions. Moreover, looking at the molecular structure of the receptor CD207, and its tendency to form trimer complex during the binding, it remains unclear what exactly are the kinetics of binding at the molecular level and which supramolecular forces are playing the important role during the particle's absorption on the surface [237]. The effect of the receptor trimerization on the energy of binding is unknown, hence no solid conclusions can be drawn from this observation.

The case of CD206 receptor expression and mUNO-ligand in PEG-PLA binding behaviour is quite different. WB and confocal imaging demonstrated that CD206 receptor is expressed exclusively in DC2.4 cells due to their origin from an immature DC lineage. The binding contour map identified a single hot-spot of binding within 15min using formulation with 1% and 2% of mUNO (Nb ligands 30 and 60), identifying a range of optimal Nb of ligands for the targeting of this cell phenotype. Instead, the signal derived from NIH3T3 and MutuDC, where the receptor was not expressed, might derives from unspecific binding. As mathematically theorised and previously described in Paragraph 2.5, it is conceptually possible to identify an optimal range of ligands in which the total energy is in favour of the binding.

It is plausible that at higher Nb of ligands in the out layer of the PO might introduce too much steric repulsion derived from the 'bulky' CD206 receptors. Receptors might

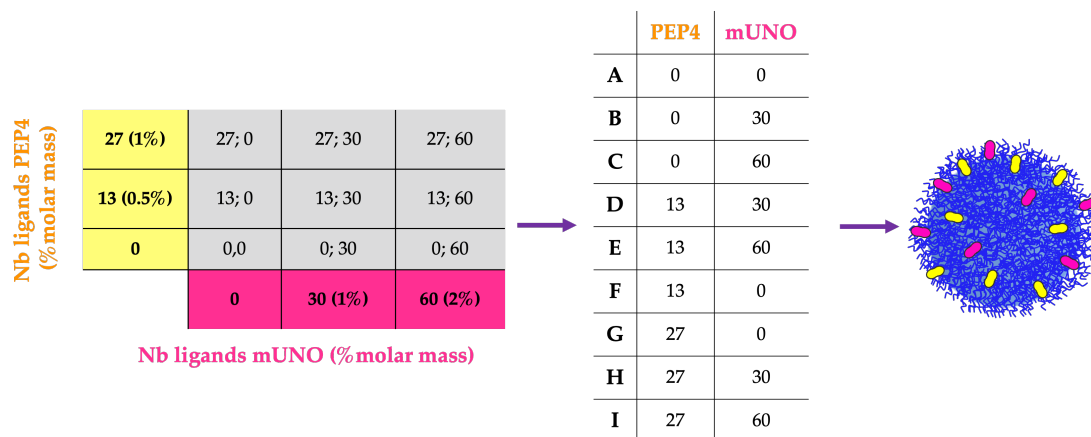
be brought in close proximity by the initial interaction with mUNO-ligands exposed on the out layer of the PO (see computational structure presented in Figure 18), something that should be taken in consideration in future computational modelling. The concept that “the more is not always the merrier” was proven.

7.2.5 Binding Assay with Combinatorial POs

Multivalent particles were found to display a phenotypic binding with a range of Nb of ligands on their surface, yet with a certain degree of unspecificity. To explore the possibility of achieving a higher degree of selectivity of binding, it was tested a new batch of multivalent and multiplexing POs. The previous findings were taken in consideration for the choice of initial %Molar mass of each peptide-polymer to be included into this new batch of POs. Unexpectedly, PMPC-ligand failed to provide a range of Nb ligands for the phenotypic targeting, especially in NIH3T3 and MutuDC cells. For this reason, it was not taken in consideration for the next set of experiments. On the other hand, PEP4-ligand and mUNO-ligand revealed a range of Nb ligands with the potential of achieving the phenotypic targeting. Formulations 1% PEP4-ligand (Nb of ligands 27) and 2% mUNO-ligand (Nb of ligands 60) in PEG-PLA demonstrated a preferential binding in DC2.4 cells, thus focusing the attention on this range of Nb of ligands.

As theorised in a previous work ([217]) and empirically observed by other members of the group, different ligands present on the same surface of the same PO display a synergistic behaviour during the binding, increasing the selectivity and reducing the Nb of ligands needed. Therefore, it was decided to include a lower %Molar mass of peptide-polymer for the next experiments.

The new batch of combinatorial POs (Formulation ID: A-I) was prepared via solvent displacement, analysed and quantified following the same protocols described for the *PEP4- and *mUNO-PEG-PLA formulations. Results are reports in Supplement Material S 13. Polymer mixes were prepared following the %Molar mass listed in Table 11 with the addition of 0.05% Molar mass of Rho fluorophore in each formulation for final fluorescence detection. The number of ligands included in each PO was calculated as previously described in Paragraph 4.1.6.1.



Combinatorial formulations:

Formulation ID	Nb ligands PEP4	Nb ligands mUNO	PEP4-PEG ₆₉ -PLA ₁₁₃ * %Molar mass	mUNO-PEG ₆₉ -PLA ₁₁₃ * %Molar mass	PEG ₄₅ -PLA ₁₁₃ %Molar mass
A	0	0	0	0	0.95
B	0	30	0	0.012	0.93
C	0	60	0	0.024	0.92
D	13	30	0.0064	0.012	0.93
E	13	60	0.0064	0.024	0.91
F	13	0	0.0064	0	0.94
G	27	0	0.0128	0	0.93
H	27	30	0.0128	0.012	0.92
I	27	60	0.0128	0.024	0.91

Table 11: Polymer mix for preparation of combinatorial POs for *in vitro* binding assay.

Figure at the top it is a schematic representation of a matrix used for creating the list of formulation to be tested in the experiment *in vitro*, starting with the previous formulation that exhibited a range selectivity of binding behaviour 1% PEP4-ligand (Nb of ligands 1447) and 2% mUNO-ligand (Nb of ligands 3042) in PEG-PLA. In the matrix were included formulations with half of the %molar mass of peptide to assess the potential synergistic effect during the binding.

A new binding assay was conducted. Cells that were exposed to POs for 5, 20, 40 and 60 min and results are reported as histogram bars in Figure 61.

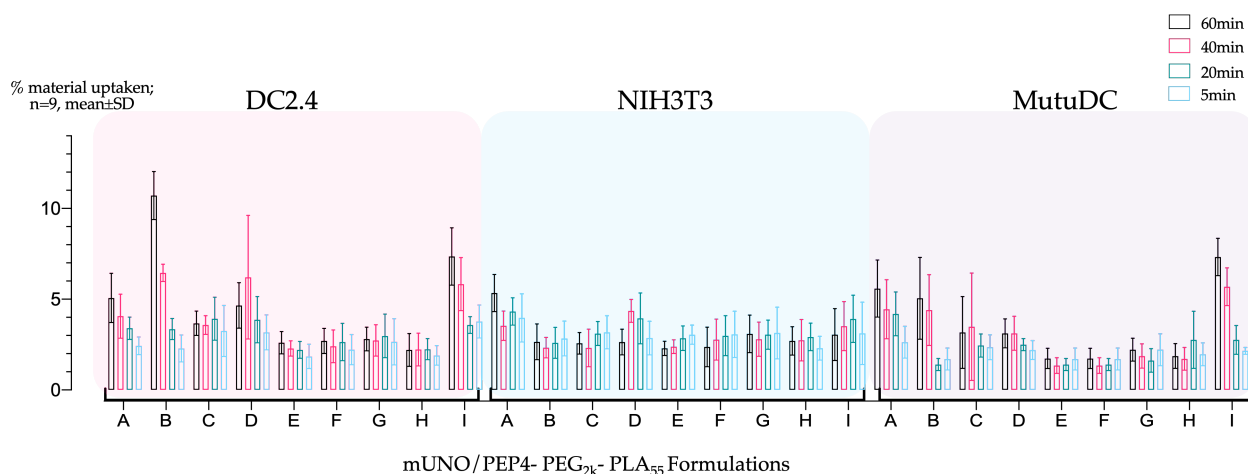


Figure 61: Binding assay of combinatorial POs *in vitro*.

Data were obtained and collected from 3 independent experiments in triplicates (n=9) and the average has been plotted with the SD. Results are also reported as Heatmap in S 17.

The highest binding peaks were observed for formulations B, D and I in DC2.4 cells. The expression of receptor CD206 only in DC2.4 cells might explain the success for some but not all formulations containing mUNO-ligand at different %Molar mass. Interestingly, higher binding was observed for formulation B (0, 30) but not for C (0, 60), confirming the existence of a 'sweet-spot' of number of ligands more favourable to the binding than others.

Conversely, NIH3T3 cells didn't exhibit relevant binding peaks across these set of formulations. A higher uptake level in the pristine control formulation has been observed, compared to the other formulations. Besides pristine control, only formulations D and I displayed a slightly higher level of uptake after 40min incubation, compared to the other formulations. Lack of expression of CD206 receptor might explain the low binding profile of mUNO-containing formulation, still it was expected higher binding with PEP4-containing formulation (F and G) considering the CD207 expression and low level of glycocalyx.

In MutuDC cells, the formulation I (27, 60) displayed the highest level of binding regardless after 40 and 60 min of incubation, despite the lack of expression of CD206 receptor. It could be hypothesised that the presence of peptide mUNO on the PO might facilitate the event of binding through unspecific interactions.

Overall, it is worth of noticing that PEP4-only formulations (F 13; 0 and G 27;0) were the ones with least uptake overall across cell types, despite the CD207 receptor being expressed in all of them.

Generally, it was confirmed the existence of range of number of ligands for each peptide for the phenotypic targeting. However, at this point of the project, results failed to indicate a strong correlation between the binding behaviour of each phenotype with their profile of receptors expression. This might suggest the presence of other key player factors involved during the binding event between the PO and the cellular surface that need further investigation.

7.2.6 Intradermal Injection *In Vivo*

So far, *in vitro* binding assays have demonstrated that there is a potentiality of application for the range selectivity theory to be applied aiming to achieve the phenotypic targeting. Although the current model of NP design needs to be refined with limited correlation with the receptor expression profile, *in vitro* experiments conducted so far indicated a 'sweet-spot' range of Nb of ligands in POs different in each phenotype, paving a new way of designing for active targeting NPs.

Although multivalent POs displayed phenotypic targeting in certain conditions, multivalent and multiplex POs exhibited an unexpected binding behaviour suggesting antagonist effects between ligands or receptors on the same surface. The steric repulsion derived from same receptors brought into proximity during the binding might play another important role during the binding process, which wasn't taken in consideration before.

One of the major limitations of the *in vitro* experiments conducted is lack of the kind of biological complexity found in a physiological tissue/ organ. In fact, all formulations prepared so far were tested in each cell line individually. It remains to investigate how the binding would look in a complex biological environment. Thus, it was decided to test if multivalent and multiplex POs display a differential binding behaviour in complex physiological environment, such as the derma of an animal model aiming for the skin vaccine. Considering the complexity of the experiment, it was decided to start with a short panel of POs to be tested designed from the previous

findings. As example, formulation B (0, 30) was one with highest binding in DC2.4, whilst formulations D (13, 30) and I (27, 60) were the only combinatorial POS with high rate of binding across cell lines. It is worth to notice that formulation I has twice the number of the same ligands as D. It was decided to include in the panel of formulations only the latter, to minimise potential unspecific interactions. For the *in vivo* experiment, besides pristine POs, there were included formulation B (0, 30) and F (13, 0), as control for the combinatorial formulation D (13, 30; refer to Table 12 for further details). As in previous preparations, polymer mixes were prepared following the %molar mass reported in Table 12, with the only difference that this time the fluorescent-labelled Cy5.5-PEG₂₀-PLA₁₀₈ polymer at 0.5% molar mass was included for better detection of fluorescence by flow cytometry and plate reader.

Combinatorial formulations for *in vivo* experiment

Formulation	Nb ligands PEP4	Nb ligands mUNO	PEP4-PEG ₆₉ -PLA ₁₁₃ *	mUNO-PEG ₆₉ -PLA ₁₁₃ *	PEG ₄₅ -PLA ₁₁₃	Nb of animal
Pristine	0	0	0	0	0.95	3
mUNO	0	30	0	0.012	0.93	2
PEP4	13	0	0.0064	0	0.94	2
Comb PO	13	30	0.0064	0.012	0.93	3

Table 12: Polymer mixes for *in vivo* experiment.

Nb of ligands for each formulation is reported on the beginning of the table. Total number of animals used for the i.d. injection *in vivo* is reported at the end of the table

This new set of POs were prepared following the solvent displacement protocol as previously described. As standard procedure, POs were then purified from organic solvent residues by SEC and non-encapsulated fluorescent-labelled polymer by SEC, before being concentrated with hollow fiber. Concentrations of preparations were then quantified by RP-HPLC in acetonitrile/ water gradient flow run. Results of characterisation analysis are reported in Supplement Material S 14.

The prepared formulations were injected into immuno-competent C57BL/6 mice at maximum amount of 10mg per kg of animal. Group control animals were injected with PBS instead.

Considering the therapeutic potential of skin vaccine, it was decided to perform an i.d. injection on the dorsal skin of animals. Mice were sacrificed after 1h, 2h or 4h

from injection. Upon PBS and PFA perfusion, skin area of injection (1 cm²) , the afferent lymph node (l.n.) and internal organs were collected and processed for further analysis and NP biodistribution.

Skin and l.n. were collected, digested and processed for flow cytometry analysis. Single cells were stained with live/dead stain and incubated with mix of antibodies for CD45, CD207 and CD206 markers. Cell population was gated for live cells and then for the respective marker expression and Cy5.5 fluorescent signal of the PO. Gating strategy, FlowJo analysis and results are reported in Supplement Material S 18, S 19, S 20 and S 21.

The experiment was performed to investigate the distribution of the prepared formulations following injection in various group of cells expressing the receptors, both from the skin biopsies and l.n. (Figure 62). The analysis was carried out after 1,2 or 4h from the i.d. injection.

Histogram graphs in Figure 62 report percentage of Cy5.5 positive cells detected from the gating strategy in cells derived from skin (top) and lymph nodes (bottom). Bars represent Mean \pm SD. First, cells were analysed for the expression of CD45 marker (lymphocyte common antigen) and samples were investigated for Cy5.5 fluorescence signal derived from particle internalisation. As depicted in the top graph, skin CD45+, which are immune cells, presented the highest level of Cy5.5 fluorescence overall, indicating higher level of binding than the rest of the receptors. However, at this stage of the work it was not possible to distinguish which exact cell phenotypes gave the most contributions on the uptake of POs. Gating for CD207+ or CD206+ receptor from CD45+ cells did not detect any signal. Further experimental optimisation is needed to better discriminate nanoparticle absorption and cell phenotype.

CD45- cells, such as fibroblasts and endothelia cells, are known to express a certain level of CD207 receptor which might explain the uptake of PEP4-POs but it is unclear the uptake of mUNO-POs and Combinatorial POs, unless by unspecificity. Gating for CD207+ and CD206+ markers reported high signals only after 2h from injections with mUNO-POs, with no evident reason.

It is worth noting that during the skin biopsies preparation, great majority of material injected was still trapped between derma and connective tissue after 4h from the injection. Suggesting the scarce vasculature of the region did not facilitate the diffusion. It seems plausible that considering the vast amount of material present in the tissue interfacing the cell surface, all the targeting specificity is lost. This would explain the general absorption of the POs in all cell type of the skin with no specificity detected.

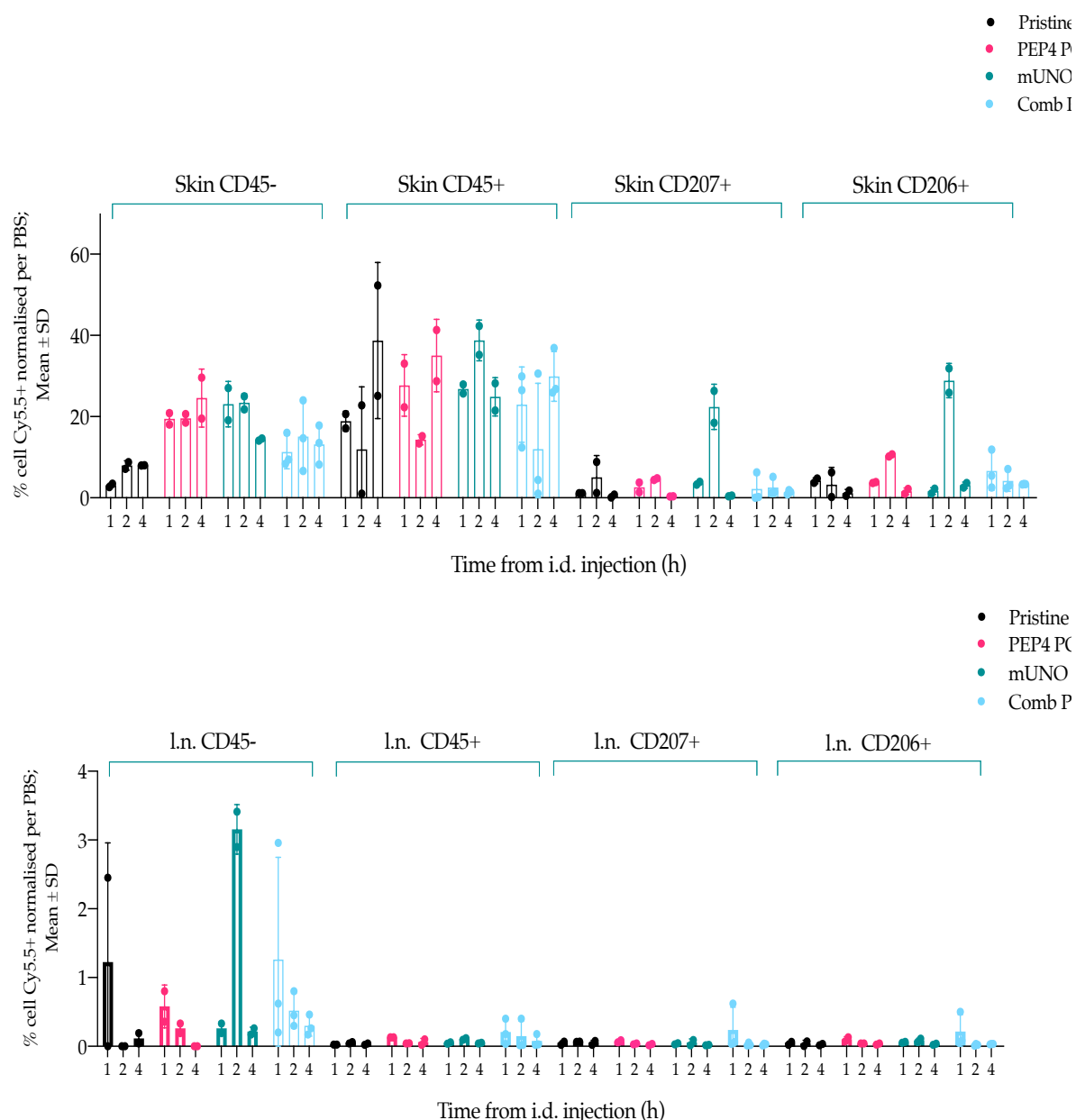


Figure 62: Results from flow cytometry analysis upon i.d. injection from samples derived from skin biopsies (top graph) and I.n. (bottom graph). Histograms bars report the mean \pm SD of %Cy5.5+ live cells detected in the sample gated for CD45, CD207 or CD206, respectively. Signal normalised by PBS. Values from 2 animals for PEP4 and mUNO POs and 3 animals from Comb POs. Mean \pm SD.

At the analysis of samples derived from the afferent I.n., a considerable peak of absorption between the 1 and 3% of Cy5.5+cells for pristine POs and Combinatorial POs in CD45- cells (non-immuno cells) after only 1h from the i.d. injection was observed. It was also observed a 3% of Cy5.5+ cells for mUNO-POs in CD45- cells after 2h from injection. In the remaining groups of cells, CD45+, CD207+ and CD206+, the Cy5.5 signal derived from POs absorption is near the baseline and

negligible for all formulation but Comb-POs. Overall, these observations correlate with other published works demonstrating the early traveling of POs to the l.n., fundamental for an effective vaccine [319].

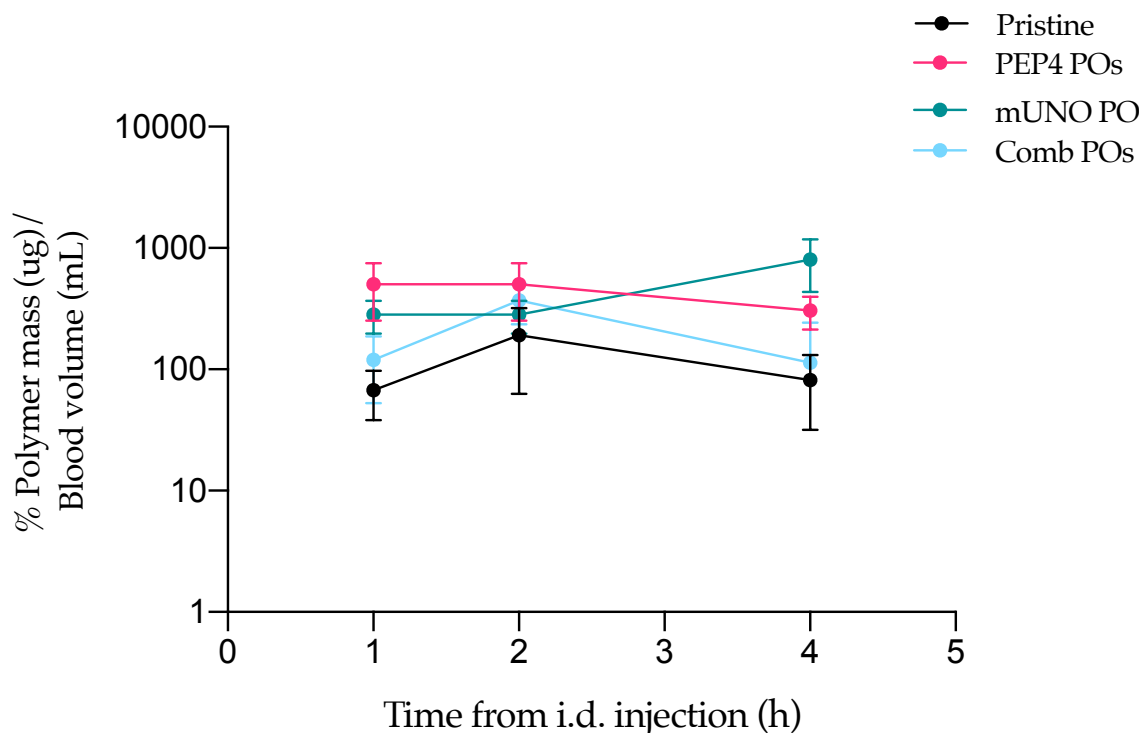


Figure 63: Analysis of fluorescent signal in the serum upon i.d. injection after 1,2 or 4h. Signal normalised by PBS. Values from 2 animals for PEP4 and mUNO POs and 3 animals for pristine and Comb POs. Mean \pm SD.

These data correlate with the circulation time revealed in the blood serum extracted from the animals when scarified and presented in Figure 63. All formulations but mUNO-POs exhibited a maximum peak of retention time of 2h from injection, indicating a different pharmacokinetic in the animal. More interestingly, it can be noticed that the combinatorial formulation presented a similar pharmacokinetic to the pristine control rather than PEP4- or mUNO-POs, potentially suggesting an antagonist effect that would need a better understanding in future experiments. If these results will be confirmed, one of the exploratory points of investigation could be the characterisation of the protein corona of each of these formulations to better understand their retention time and pharmacokinetic.

Finally, it was taken in consideration the organ biodistribution for each formulation at each time point. As seen in Figure 64, fluorescence derived from POs internalisation was prevalently detected in kidneys, spleen, liver, gut. With a minor fluorescent signal detected in lungs and pancreas.

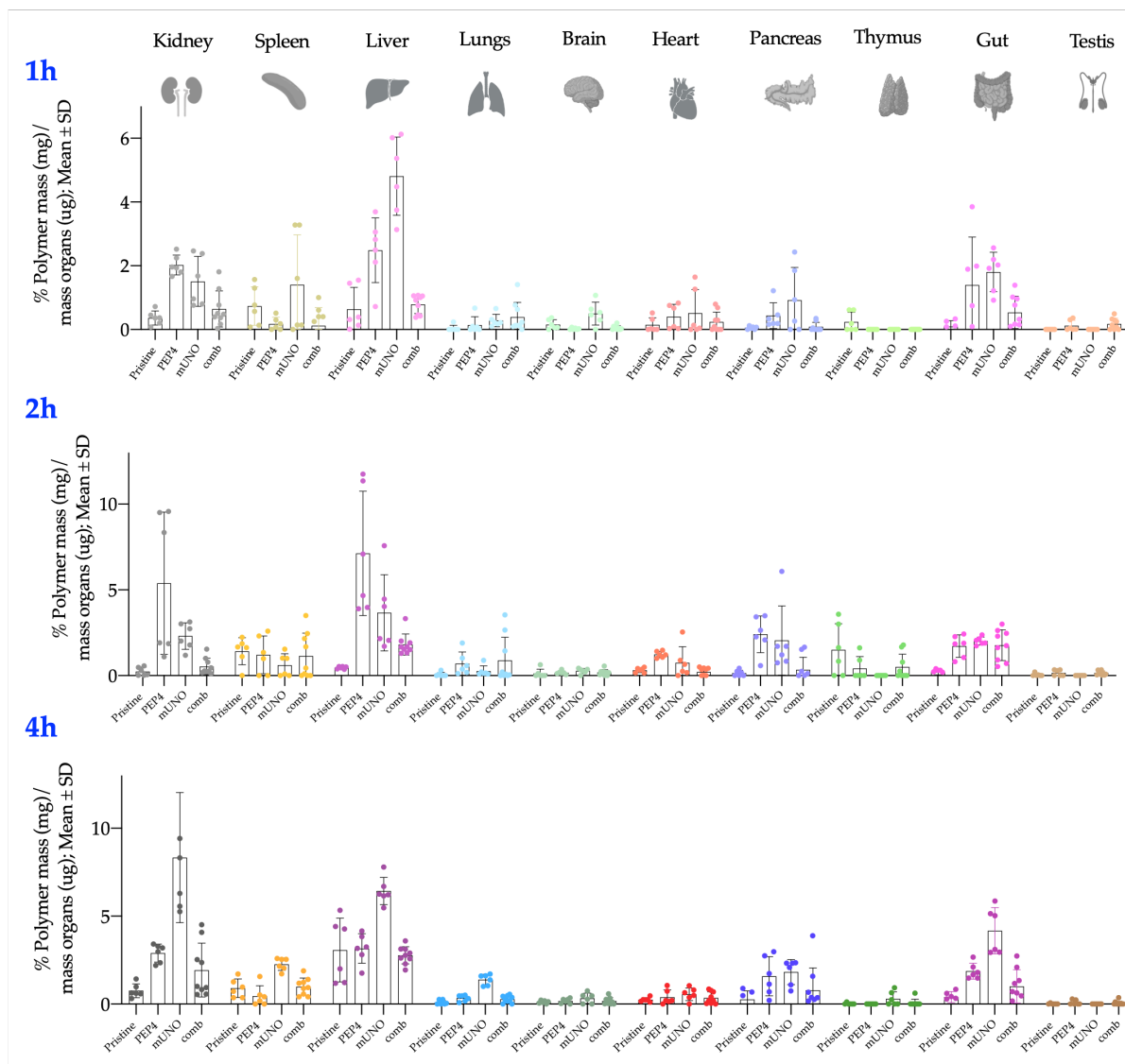
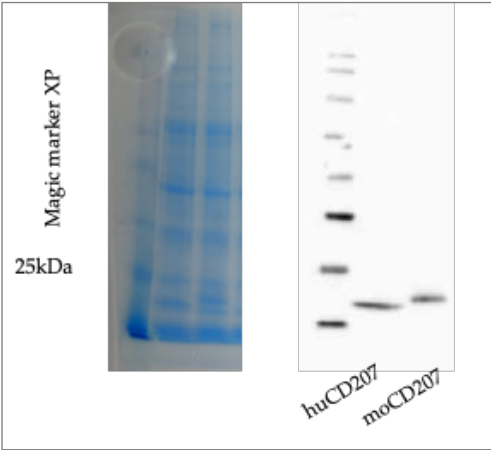


Figure 64: Organ biodistribution for each formulation after 1, 2 or 4 hours from time of i.d. injection.

Signal normalised by PBS. Values from 2 animals for PEP4 and mUNO POs and 3 animals for pristine and Comb POs. Mean \pm SD.

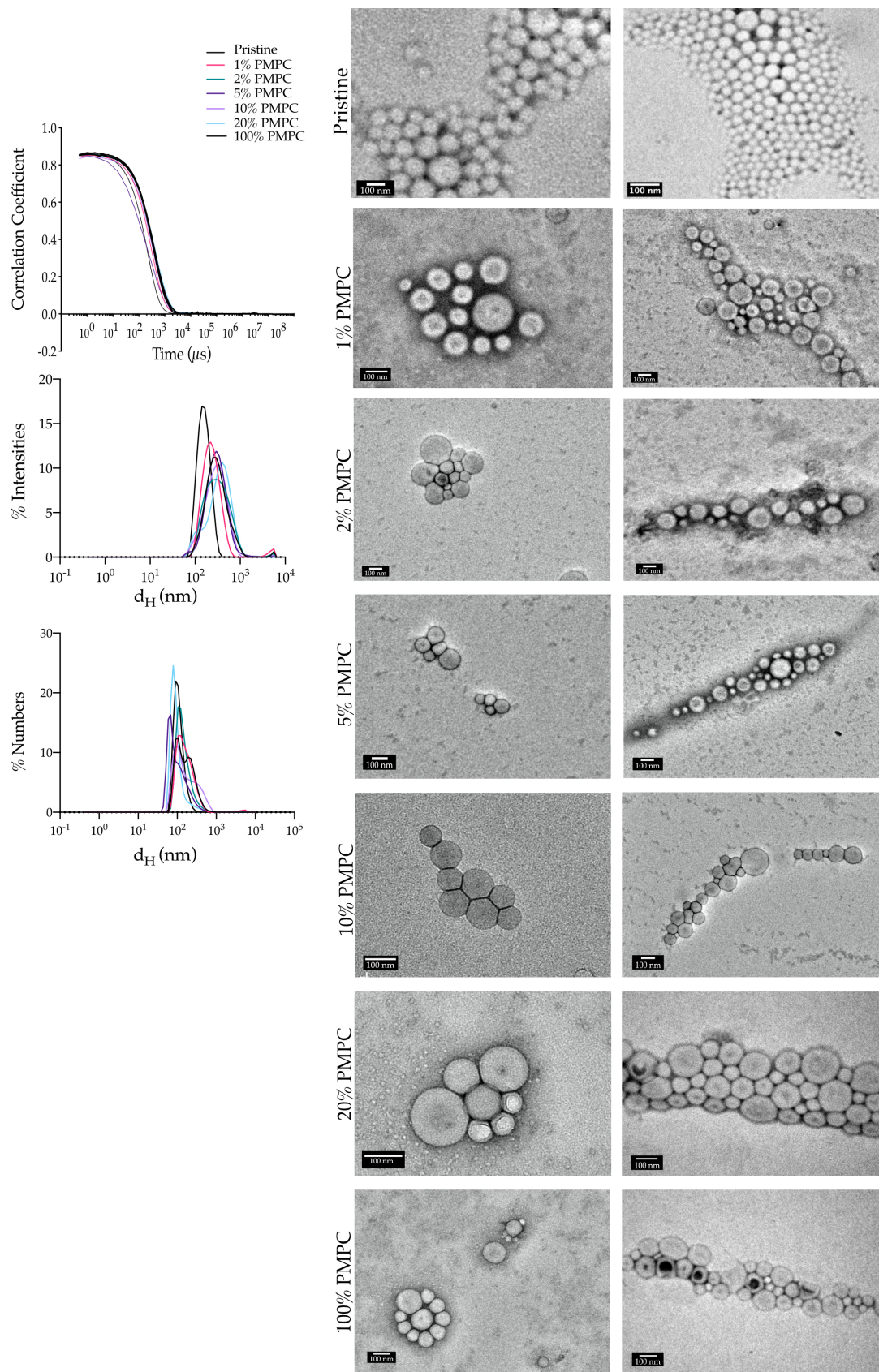
7.3 Supplement Material



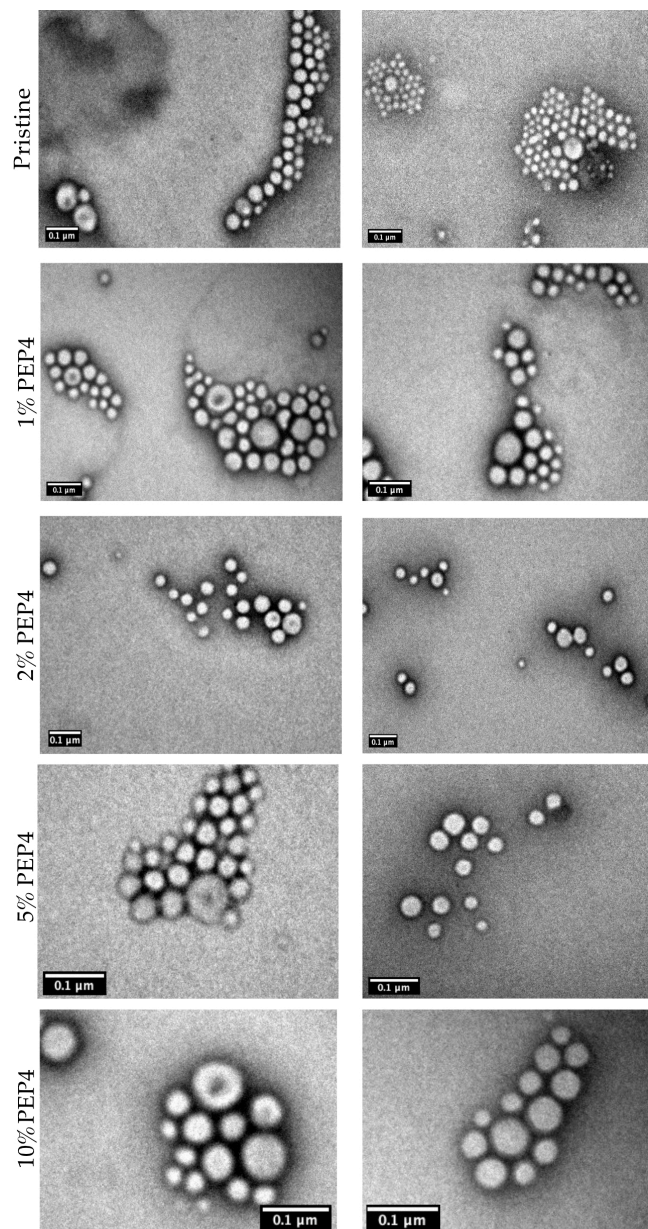
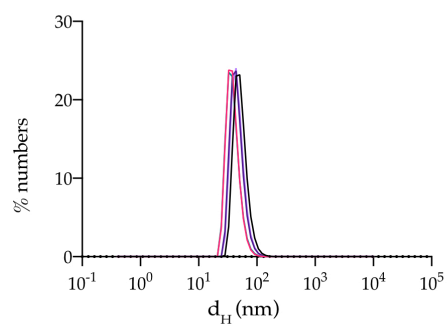
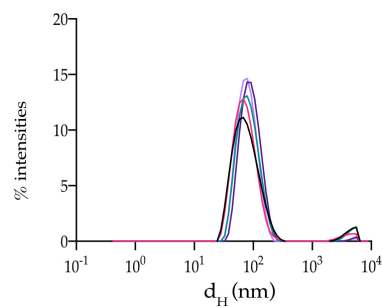
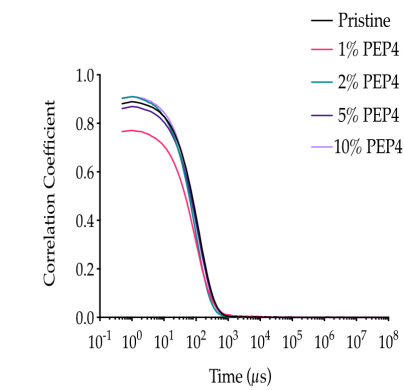
S 8: WB to confirm successfull expression and release in CHO supernant of huCD207 and moCD207.
Difference in size is due to post-transcriptional modification.

Range 1: 201 to 324 GenPept Graphics						▼ Next Match ▲ Previous	
Score	Expect	Method	Identities		Positives	Gaps	
216 bits(551)	1e-71	Compositional matrix adjust.	96/124(77%)		105/124(84%)	0/124(0%)	
Query	1	GWKYFKGNFYFSLIPKTWYSAEQFCVSRNSHLTSVTSESEQEFLYKTAGGLIYWIGLTK					60
Sbjct	201	GWKYF GNFYFYS PKTWYSAEQFC+SR +HLTSV+SESEQ+FLYK A G+ +WIGLTK					260
Query	61	AGMEGDWSWVDDTPFNKVQSVRFWIPGEPNNAGNNEHCNIGAPSLQAWNDA PCDKTFLF					120
Sbjct	261	AG EGDW WVD T FNK QS RFWIPGEPNNAGNNEHC NI+ +L+ WND PCD TFLF					320
Query	121	ICKR					124
Sbjct	321	ICKR					324

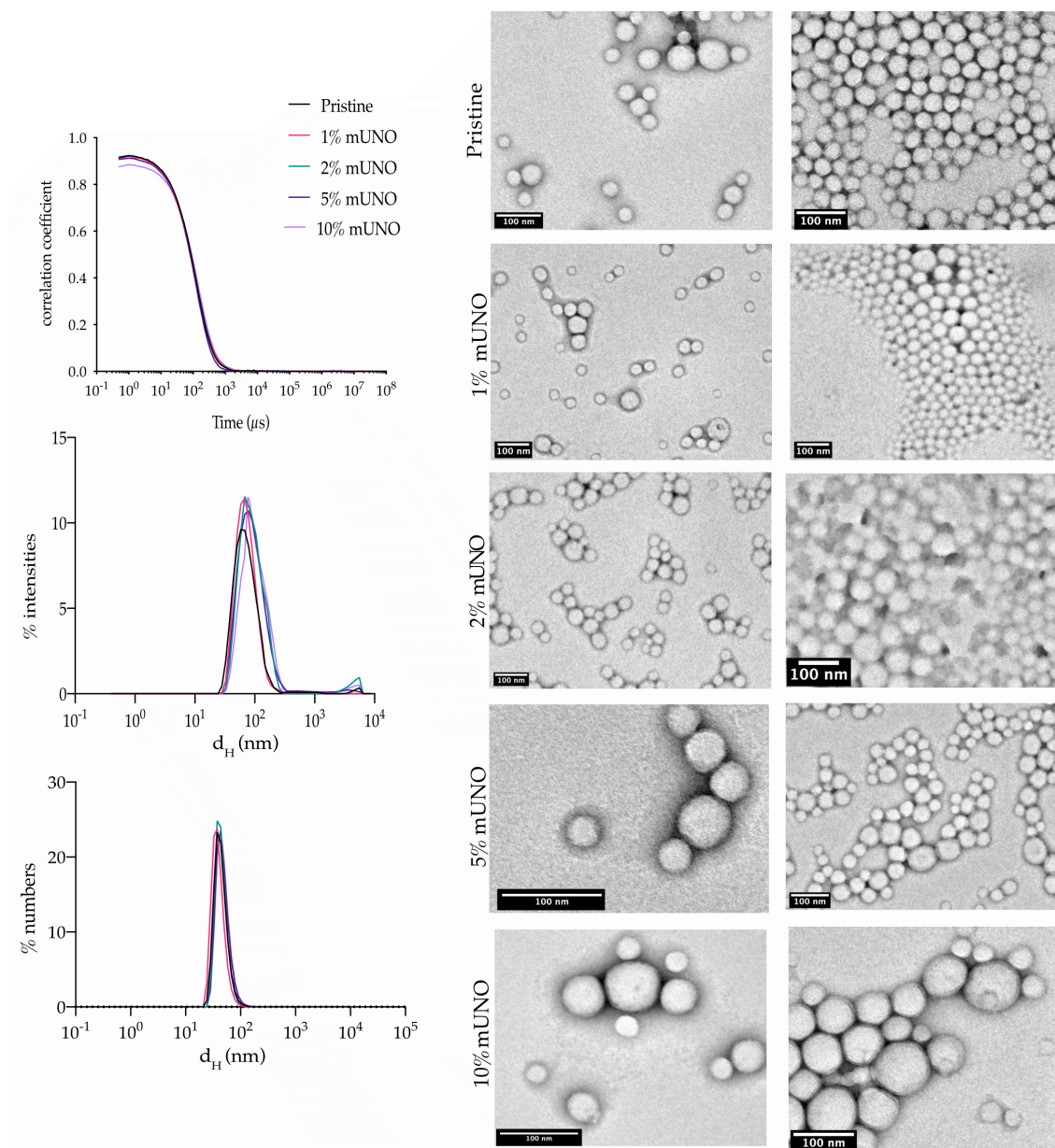
S 9: Homology prediction between huCD207 and moCD207.
The prediction is 77% homology between huCD207 and moCD207 by BLAST alignment for Non-redundant UniProtKB/SwissProt sequences



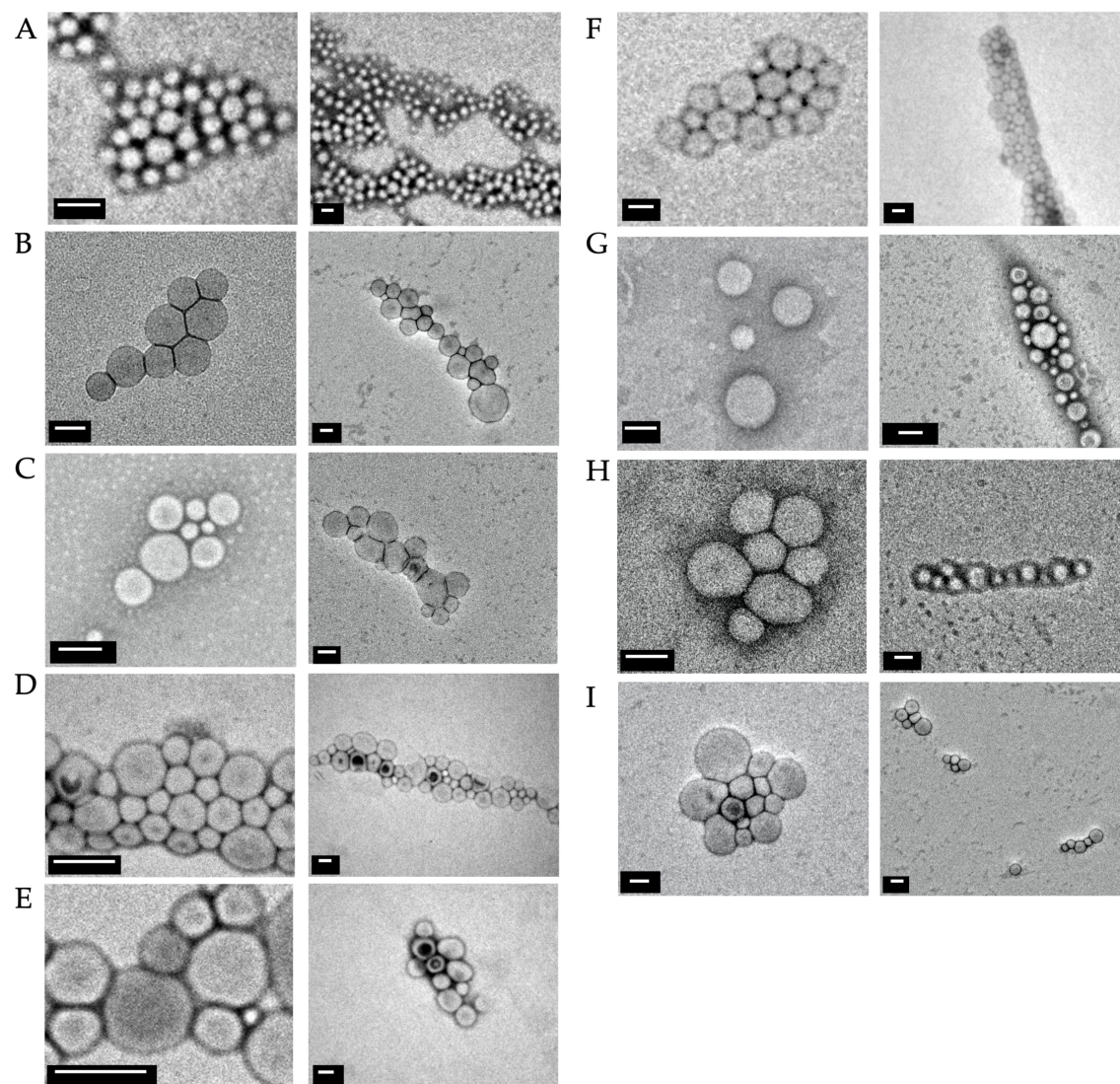
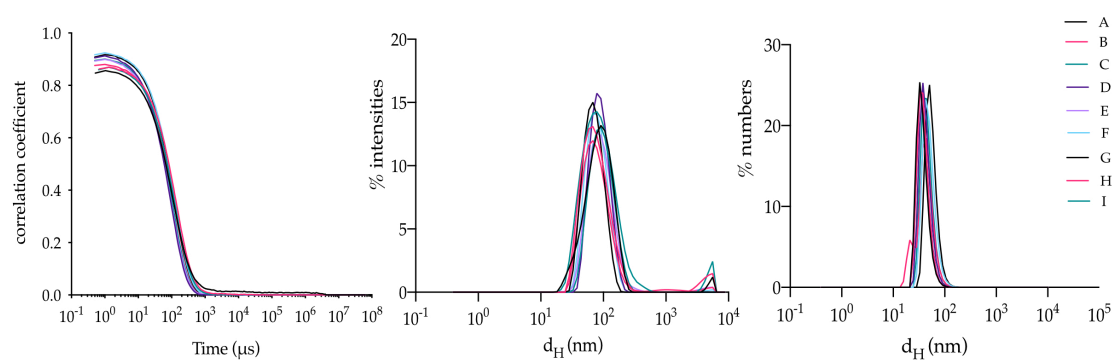
S 10: DLS (left) and TEM (right) analysis of *PMPC-PEG-PDPA POs.



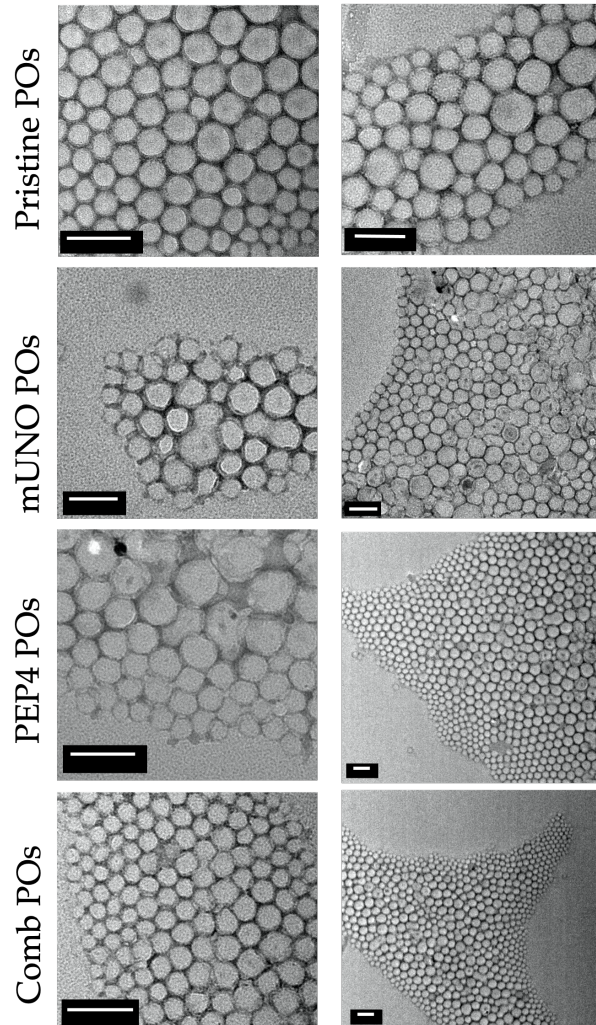
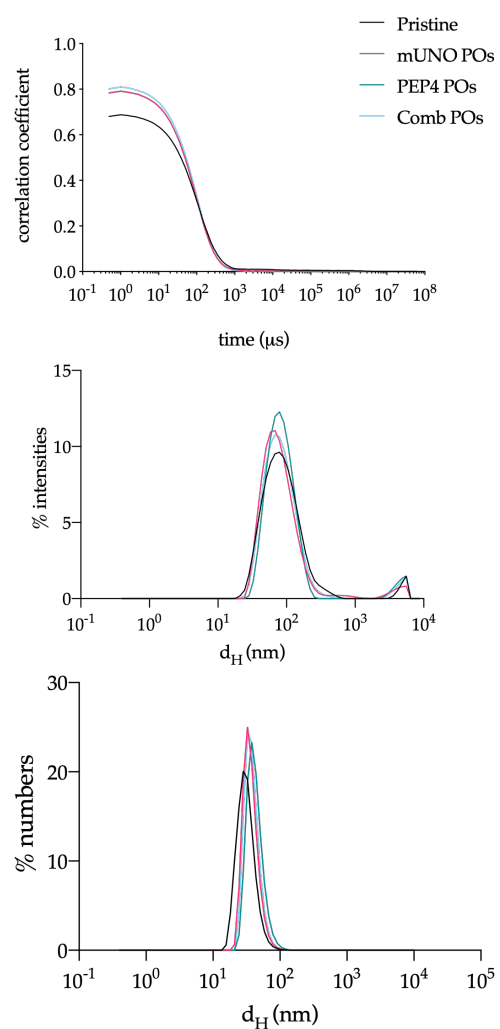
S 11: DLS (left) and TEM (right) analysis of *PEP4-PEG-PLA POs.



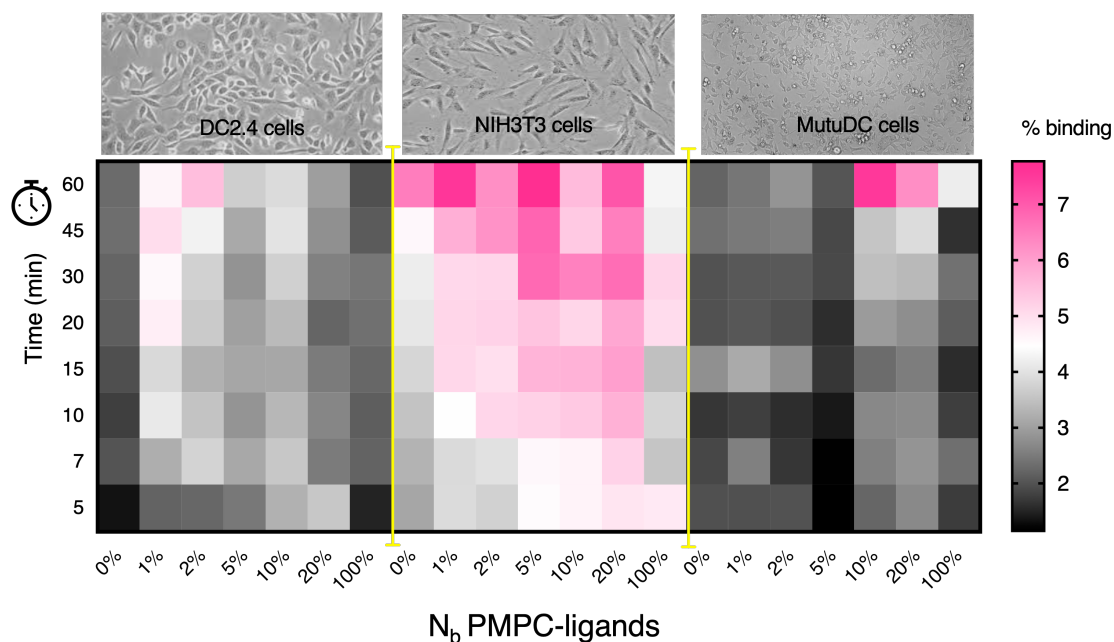
S 12: DLS (left) and TEM (right) analysis of *mUNO-PEG-PLA POs.



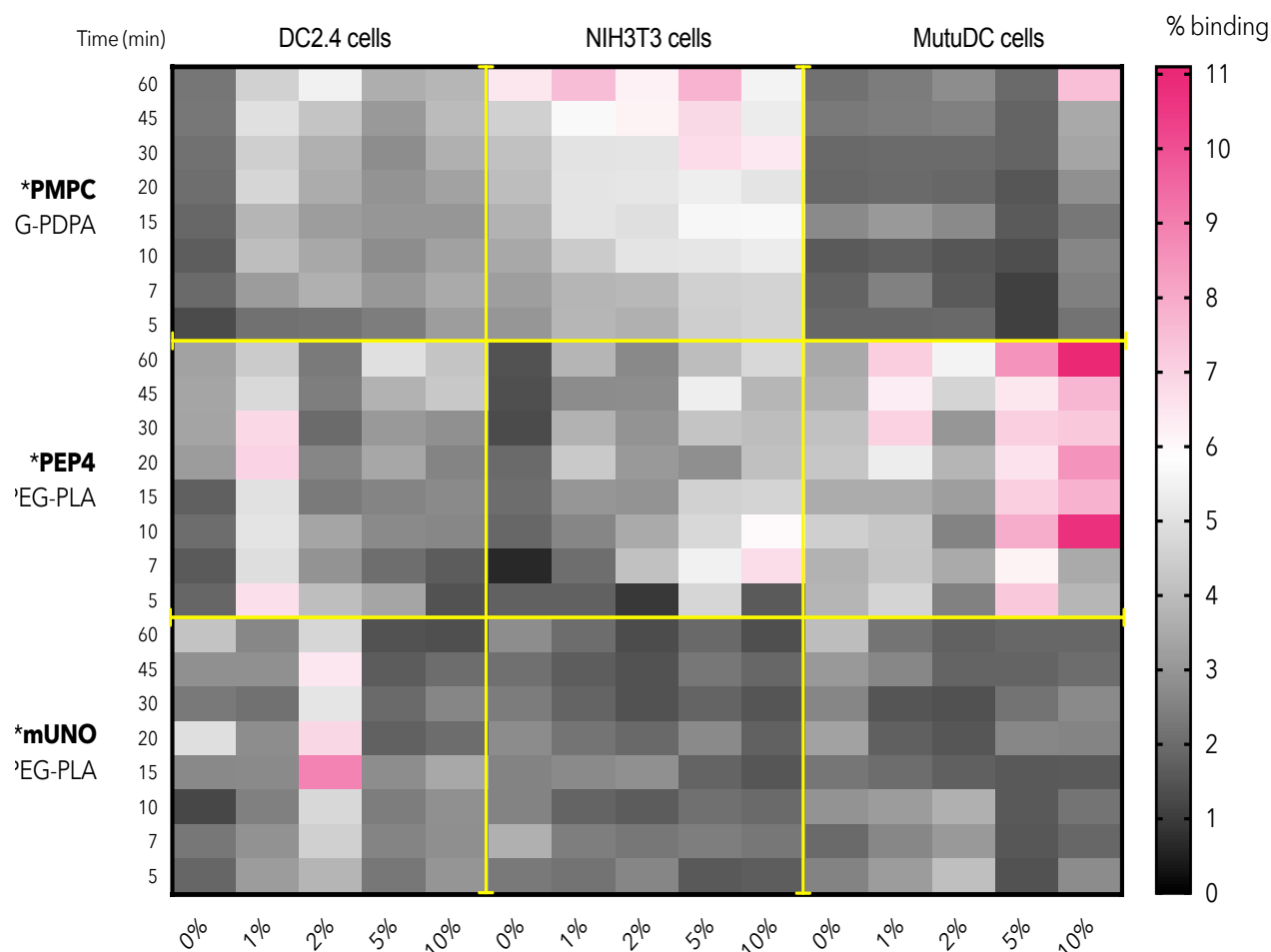
S 13: DLS (top) and TEM (bottom) analysis of combinatorial POs for *in vitro* binding assay.



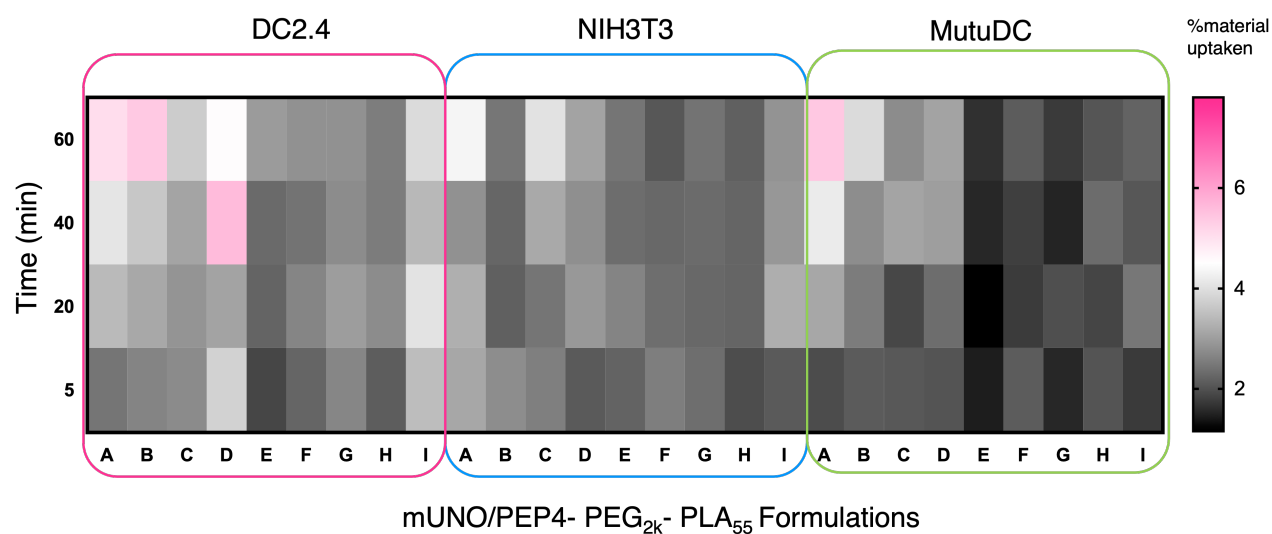
S 14: DLS (left) and TEM (right) analysis of POs batch for *in vivo* i.d. injection.



S 15: Heatmap of Binding for the *PMPC-PEG-PDPA batch formulation on cell models. Each cell line (top picture) was exposed to different formulations (from 0 to 100% molar mass of PMP-PEG-PDPA, left to right) for a various amount of time (between 5 and 60min). Fluorescent signals were collected and analysed. Graph is reporting average values from 3 independent experiments with three technical replicates (n=9). Time is reported on the left and the %of material uptaken is reported as colorimeter bar on the right.

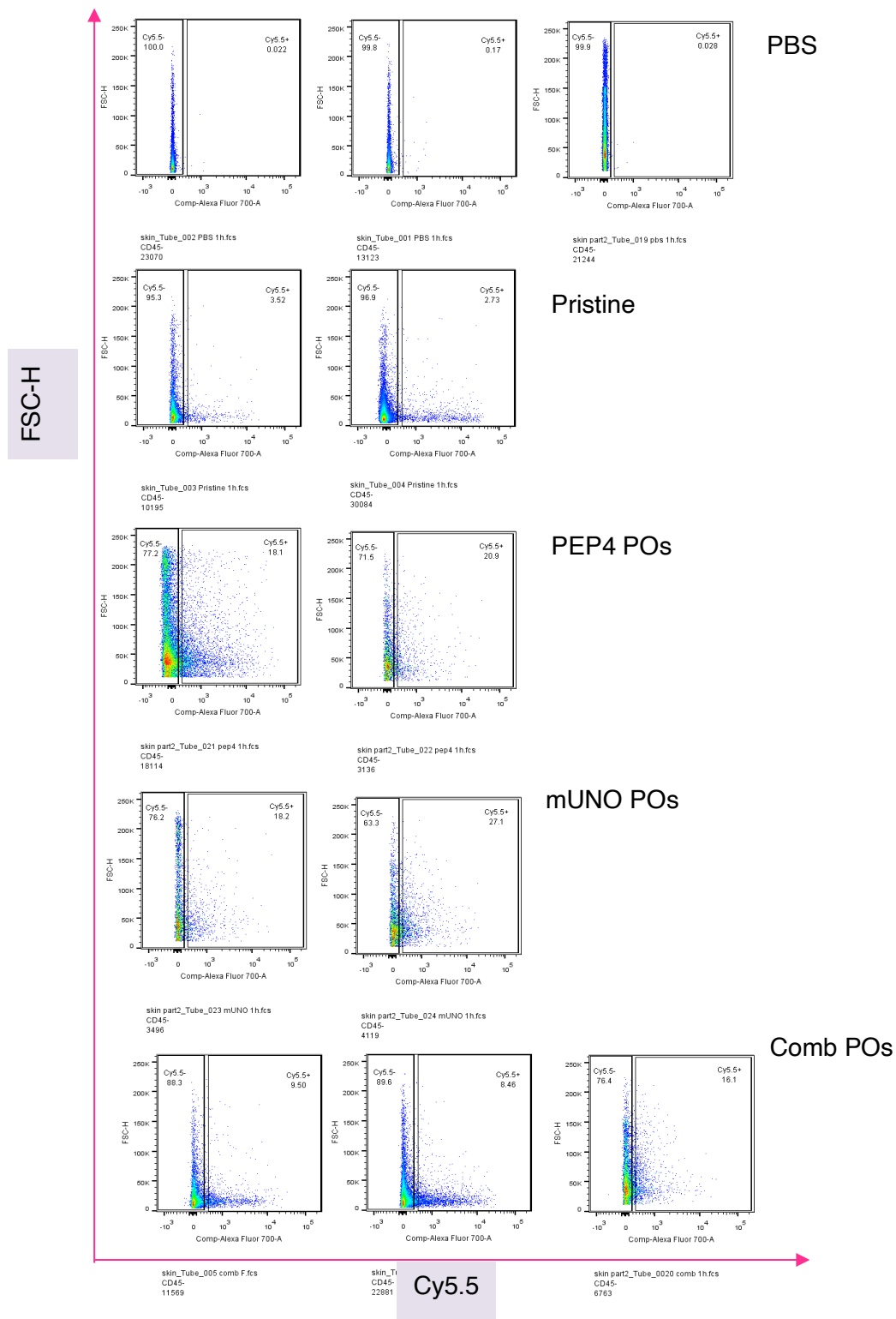


S 16: Heatmap of Binding for *PMPC , *PEP4 and *mUNO ligands on the three cell lines. Each cell line (top picture) was exposed to different formulations (from 0 to 10% molar mass of PMPC-PEG-PDPA, left to right) for a various amount of time (between 5 and 60min). Fluorescent signals were collected and analysed. Graph is reporting average values from 3 independent experiments with three technical replicates (n=9). Time is reported on the left and the %of material uptaken is reported as colorimeter bar on the right.

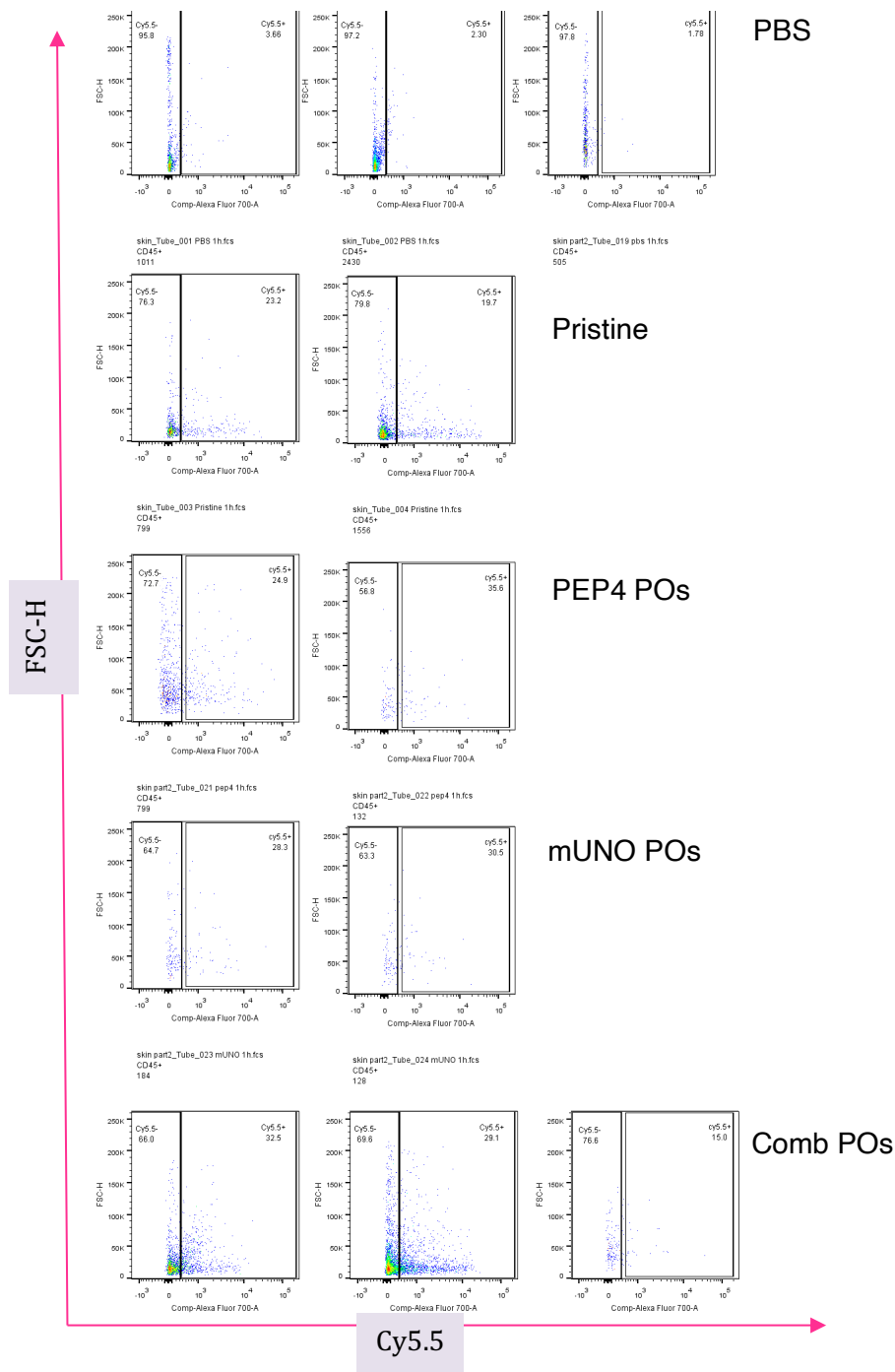


S 17: Combinatorial Formulation binding Heapmap.

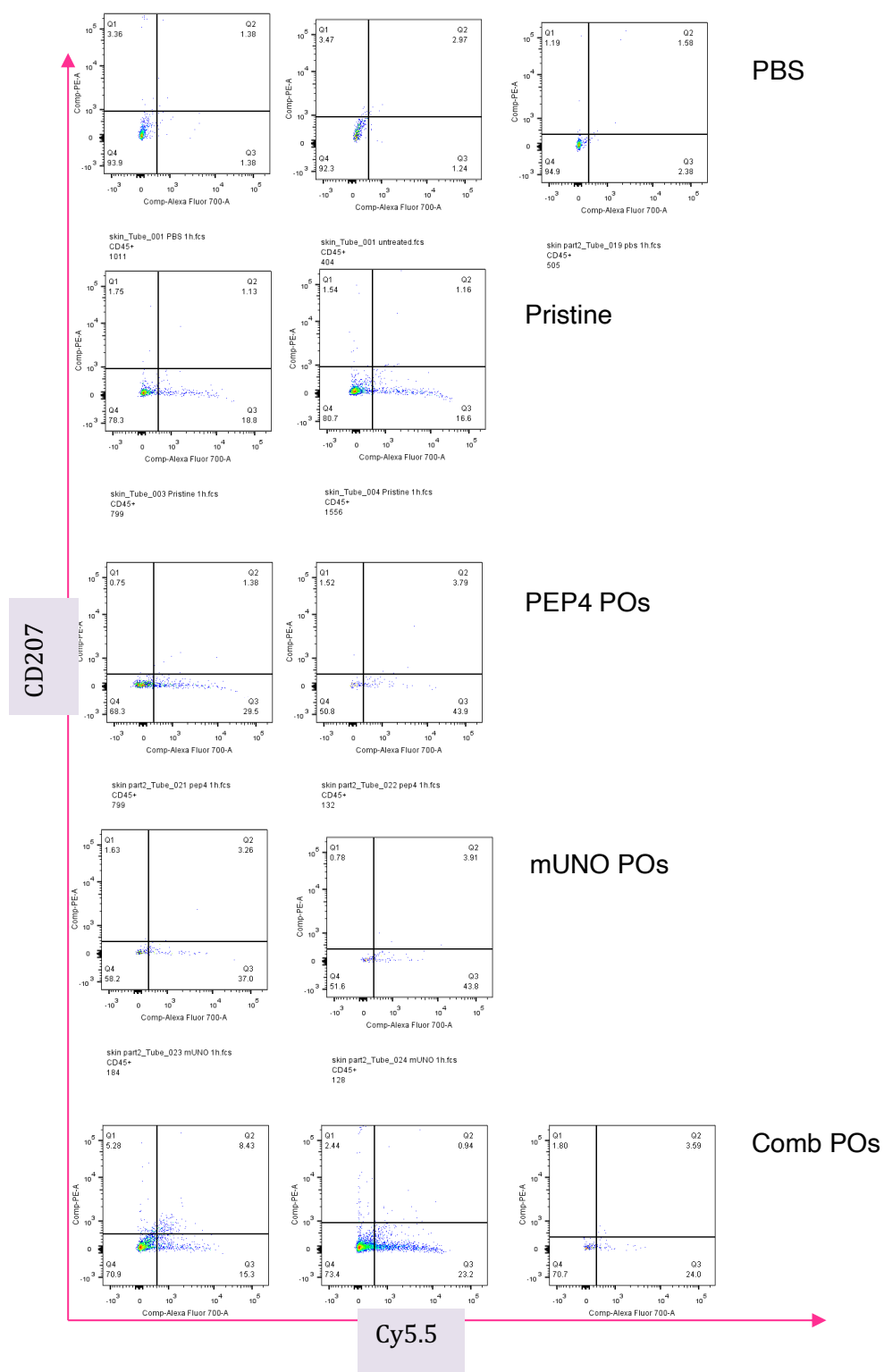
Each cell line was exposed to different formulations (with combinatorial % molar mass of PEP4 or mUNO-PEG-PLA) for a various amount of time (between 5 and 60min). Fluorescent signals were collected and analysed. Graph is reporting average values from 3 independent experiments with three technical replicates (n=9). Time is reported on the left and the %of material uptaken is reported as colorimeter bar on the right.



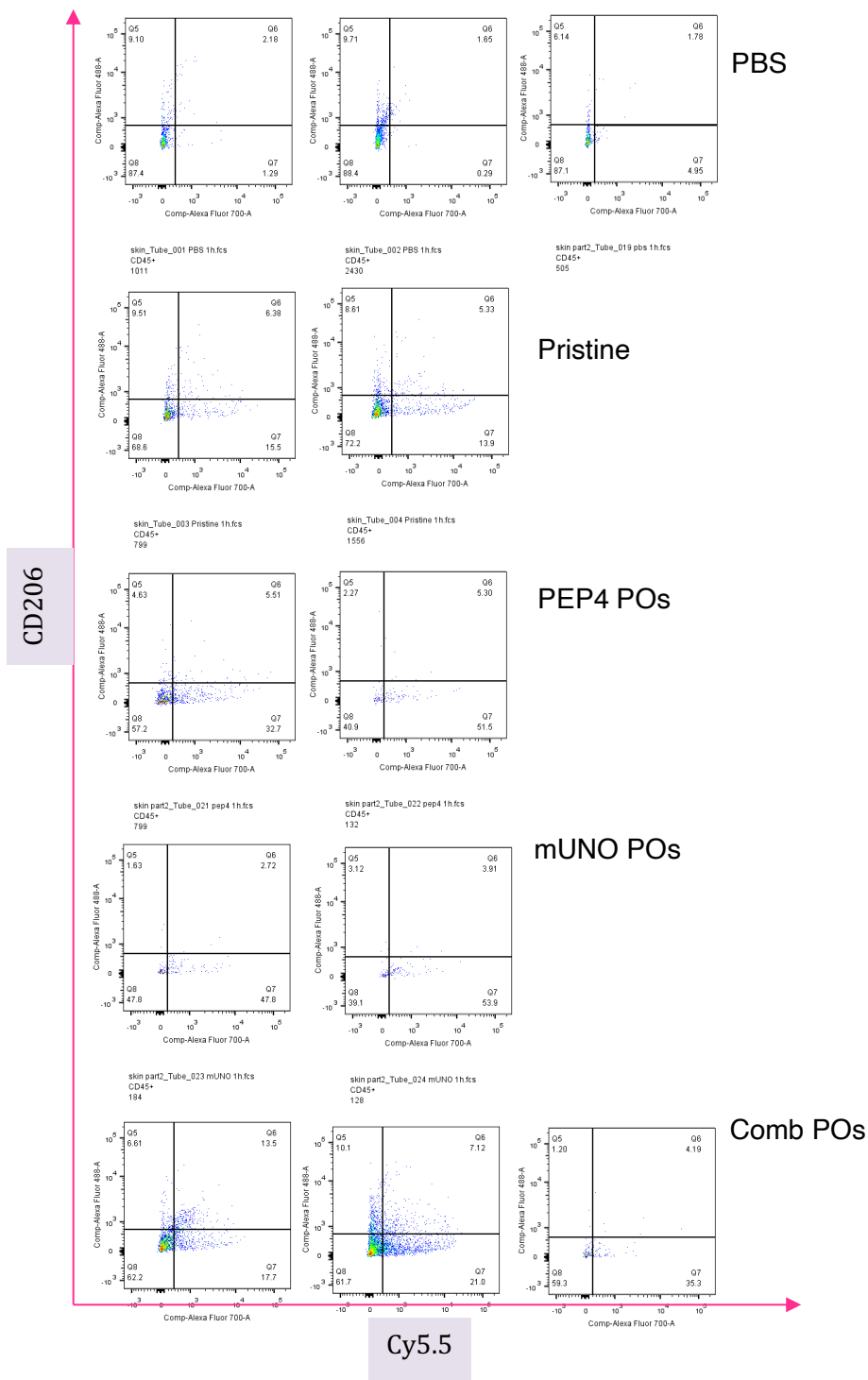
S 18: Gating for Cy5.5 + and CD45- cells.



S 19:Gating for Cy5.5+ and CD45+ cells, representative of gating strategy for analysis of samples after 1h from time of injection



S 20: Cy5.5+ cells indicating PO internalisation gated for CD207+ receptor expression.



S 21: Cy5.5+ cells indicating internalisation of POs gated for CD206+ receptor expression. Cells were collected after 1h from i.d. injection.

8 Final Remarks and Future Directions

Amongst all immunotherapies commercialised or under development, cancer vaccines are the only ones with the least side effects and potential life-long protection [320]. They are one of the few immunotherapies with the greatest potential in personalised medicines, moving away from the concept of ‘one size fits all’. Yet, cancer vaccines are characterised by one of the poorest clinical translations [321]. This is due to several factors precluding an effective adaptive response and TILs, including scarce antigen presentation and a lack of immunostimulatory properties [321]. Perhaps the simple co-delivery of antigen and adjuvant might not be enough to ensure the desired therapeutic effect. Instead, employing PO for the phenotypic targeting of DCs designed using the ‘range selectivity’ approach might result in higher therapeutic efficacy.

In the present study, three key elements for an effective cancer vaccine were evaluated independently within the fabric of a potential new class of intradermal injectables for cancer vaccines.

First, the capacity of pH-sensitive PMPC-PDPA POs to encapsulate and deliver the antigen protein as plasmid DNA into DC2.4 cells was evaluated. Next, the capability of endosome escape, protein expression, and antigen presentation on the cellular surface of a dendritic cell model was assessed. Then, the molecule cGAMP was evaluated for its immunomodulatory capabilities of activating the type I IFN response and pro-inflammatory cytokines. Finally, a DC-targeting multivalent and multiplex delivery platform using the ‘range selectivity’ approach was designed to actively target DCs and specific surface receptors, *in vitro* and *in vivo*.

On the DNA Encapsulation and Delivery

PMPC-PDPA nanocarrier was found to be an effective platform for DNA delivery in DC2.4 cells, a model of antigen presentation in vaccine studies.

POs were prepared via pH-switch, and plasmid pDNA-SFKL was encapsulated during the self-assembly. As a result, a homogenous population was obtained for both empty and loaded POs, as confirmed by DLS and TEM analysis.

However, it was noted that the effective pDNA-SFKL encapsulation was at the expense of material loss during the centrifugation step, which was estimated to be a loss of 60–80% of material (polymer and pDNA). Unfortunately, other methodologies of self-assembly for pDNA-SFKL loading (such as solvent-switch and film re-hydration) could not have been taken into consideration due to the incompatibility of the DNA molecules with the organic solvents.

The direct quantification of the encapsulated pDNA-SFKL represented one of the challenges in this line of work. This setback was overcome by implementing the PicoGreen reagent as a method of quantifying the loaded pDNA while the polymer concentration was obtained using a control counterpart formulation by RP-HPLC. Therefore, the resulting number of plasmids encapsulated and loading efficiency represent an estimation. Although it is possible that the pDNA quantification was greatly underestimated at the time, the results were found to be consistent with the group's previous work [197]. Other methods for quantifying encapsulated pDNA were attempted, such as ethanol: chloroform physical precipitation, and SEC-HPLC, but with evident technical challenges and difficulties in experimental repeatability.

With the numbers obtained by PicoGreen quantification, it was estimated that the average number of copies of pDNA was 1–8 per vesicles characterised by a d_H of 200–400 nm, with an average of 1.15 plasmid delivered by PO.

In a comparable work, a CRISPR-Cas9 plasmid with a similar dimension (8.5 kbp) was successfully encapsulated in PGLA nanoparticles. Authors performed quantification experiments using PicoGreen indicating an average of 2-3 copies of plasmid were encapsulated in their NP [322]. In this work, the quantification of the pDNA was achieved using PicoGreen upon acidification of the solution needed to release molecules from the PGLA polymer. However, in our hands, the acidification of the solution was found to interfere with the assay itself, impeding a reliable read-out of the test.

Further analysis of the ζ -potential demonstrated that self-assembled pDNA-loaded vesicles maintained the neutral surface charge. Both formulations did not exhibit a significant shift of ζ -potential ($\pm 30\text{mV}$) to be considered charged, concluding that the pDNA is fully encapsulated inside the vesicles [323]. The neutral charge is particularly relevant in drug delivery applications. Firstly, for stability of the colloidal solution to prolong shelf life, and secondly, to reduce toxicity and possibility of agglutination in the circulatory system [324]. Several studies have demonstrated that the toxicological effect of NPs is determined by their chemical composition and, most importantly, by their surface charge [325], [326]. In particular, the surface charge of NPs influences the formation of the protein corona (layers of proteins and biomolecules that coat the NP's surface) to the point of drastically modifying their biodistribution and toxicity [325].

Following the characterisation of the PO formulations, the biocompatibility of PMPC-PDPA was evaluated before any cell experiments. PMPC-PDPA was confirmed to induce a level of cytotoxicity at concentrations $> 0.2\text{mg/mL}$ in all range of cell lines, including HEK293T and DC2.4 (Figure 41 and Supplement Material S 2). Therefore, all the following experiments were conducted using a concentration below said range, to ensure viability greater than 80%. Once the safety profile for the PMPC-PDPA POs was established, transfection studies were performed using a pDNA-SFKL:PMPC-PDPA POs. The initial studies consisted in assessing the ability to transfect both HEK293T and DC2.4 with pDNA-SFKL using a common transfection reagent, Lipofectamine 2000 (Supplement Material S 3) [327]. As expected, and in agreement with literature studies, HEK293T exhibited a high rate of transfection, around the 80% of GFP+ cells, whereas DC2.4 was around 20% of GFP+ cells [328]. Once the baseline levels of transfection were determined, the ability of the PMPC-PDPA to deliver pDNA-SFKL was investigated. By using the PO carriers, a transfection efficiency of $\sim 50\%$ and 10% was obtained in HEK293T and DC2.4, respectively (Figure 42). Finally, the capability of the system to present the model antigen SIINFEKL on the cell surface was assessed over time, as a first step towards immunisation.

Overall, Lipofectamine 2000 was confirmed as a high-performance transfection reagent but characterised by tangible cytotoxicity [330]. On the other hand, PMPC-PDPA POs were less effective in DNA transfection. However, they presented a less concerning toxic profile, which must be considered when manipulating sensitive cells, such as DCs.

The transfection results showed a profound mechanistic difference between the two cell types that needed further investigation. Since DC2.4 are derived from immature mouse DC, it is used as a model of antigen presentation and inflammatory response in immunological studies. It was speculated that DC2.4 cells might still have functional intracellular DNA-sensing pathways, such as the cGAS-STING signalling pathway. To overcome such limitation, DC2.4 cells were pre-treated with RU.52, a mouse cGAS inhibitor. The treatment doubled the percentage of GFP+ cells detected in DC2.4 the sample. Although it is an indirect method to assess the involvement of the cGAS-STING pathway, it must be pointed out by other published works its major role in DNA stability and permanence in the cytoplasm, hence in the protein expression [290].

Finally, SIINFEKEL antigen presentation was detected via flow cytometry and by immuno-staining at confocal imaging, validating the delivery system and the chosen cellular model. Interestingly, the levels of SIINFEKL detection seemed to not increase by the pre-treatment with RU.521 cGAS inhibitor. Perhaps the small dimension of the peptide or receptor depletion might be behind this observation. It cannot also be excluded that the inhibition of cGAS might have a detrimental effect on the activation of MHC-I receptor, ultimately interfering with the antigen presentation pathway.

Further experiments in immuno-competent animal model are required to address important questions. It remains unknown if the amount of DNA delivered and SIINFEKL presentation will be sufficient to trigger an adequate immunisation. It would also be interesting to further investigate the role of RU.521 cGAS-inhibitor experiments of co-delivery, which might present a high translational potential. Although RU.521 do not increase the level of SIINFEKL presentation on the cellular surface, it is hypothesised that it might prolong the intracellular survival of pDNA,

consequently reducing the number of pDNA molecules needed. In preparation for these future *in vitro* and *in vivo* experiments, the encapsulation of RU.521 in PMPC-PDPA POs was attempted several times but with no success. Perhaps, the two allogenic group in the molecule might negatively interact with the hydrophobic block of the polymer during the self-assembly process. Different polymers or lipids could be considered to overcome this limitation.

Finally, in future experiments it could be interesting to evaluate the outcome of RU.521 delivery experiments *in vivo* in combination with the DNA delivery, to assess if a more efficient cancer vaccine can be unlocked in the future.

On the cGAMP Encapsulation and Delivery

In consideration of the abundant studies published in the last decade, cGAMP and other CDNs have found a prominent spot in cancer immunotherapy [144]. The powerful pro-inflammatory capacity of the STING-agonists make them powerful activators of the tumour inflammation stimulating their eradication. Evidences in animal model indicate a potential clinical use of STING-agonists alone, or in combination with CIB or other cancer immunotherapies, such as cancer vaccines [302],[329],[330].

To explore the immunostimulatory properties of STING-agonists, cGAMP was loaded into PMPC-PDPA polymersomes via electrophoresis. The obtained POs were purified as usual and analysed by DLS and TEM for morphology and size, and cGAMP-loaded POs were analysed at RP-HPLC for quantification. It was reported an average of 1721 molecules of cGAMP per PO were encapsulated. The P.E. reported before and after the encapsulation reported dropped off around 20%, indicating a loss of material upon encapsulation. Supramolecular interactions between the polymer and the anionic molecule cGAMP might be responsible of such effect, similar to the pDNA-SFKL encapsulation. The cGAMP encapsulation was also attempted by pH switch method using 1mg of cGAMP dissolved in 200uL of sterile water. However, at the RP-HLPC analysis it was not possible to detect a distinguishable peak from cGAMP. This might indicate a null encapsulation, or below the detection limit of the instrument. The inter-sample biomolecule encapsulation

variability in has already been observed across different drug-encapsulating projects and it is known to be one of the focal points of future optimisation protocols of encapsulation.

The limiting cytotoxicity was assessed in DC2.4, antigen presenting cell model, and in B16F10-OVA, common mouse tumour model, *in vitro*. First, a serial dilution MTT assay was performed to explore the potential cytotoxicity of the cGAMP:PMPC-PDPA formulation. The reported results showed a contradistinctive behaviour between DC2.4 and B16F10-OVA cells, confirming fundamental differences in intracellular molecular pathways (Figure 46). In all treatments but cGAMP-only, DC2.4 manifested a reduction in cell viability between 20% and 50%, and up to 80% in cGAMP:PMPC-PDPA POs treatment at high doses. It is worth noticing the increased cell viability in DC2.4 cells when treated with cGAMP-only at low doses. A similar phenomenon has already been observed upon treatment, in a dose-dependent manner, with the immunostimulant pidotimod (PTD) peptide, and could be explained by the cellular hyperproliferation upon the inflammation [331], [332].

In the single-dose MTT assay, previous findings were confirmed. It was observed that the reduced viability in DC2.4 cells treated with empty or cGAMP-loaded PMPC-PDPA POs (Figure 48). The effect of the PMPC-PDPA polymer on DCs might indicate a higher level of sensitivity that is in contrast with what has been observed before, where PMPC-PDPA empty POs exhibited anti-inflammatory properties in a chronically-induced inflamed system and in agreement with other observations of anti-inflammatory properties of the phosphatidylcholine group reported [179], [333].

Future experiments will be aimed at elucidating the pro-inflammatory effect of the phosphatidylcholine group under different circumstances. This could be done by treating DC2.4 cells with the different stimuli, followed by qPCR of ISGs to better characterise the intracellular inflammatory response. Since qPCR technique can investigate only changes at the mRNA transcription level, WBs of a few relevant proteins involved could be performed to corroborate the results (e.g., JAK, STATs and IRF-9, [334]).

Next, the supernatant was tested for the presence of pro-inflammatory cytokines like INF- β , IL-6, TNF- α and IL-12p70 (Figure 48). It was noted that the general higher inflammatory response was in DC2.4 but not in B16F10-OVA cells, as expected, confirming their different phenotypes. This could be of relevance for future experiments *in vivo* where the cGAMP:PMPC-PDPA formulation could be able to initiate the tumour inflammation by initiating a systemic response.

In consideration of the reduced cell viability and the confirmed inflammatory response, it was investigated if the Caspase 3/7 inflammatory-dependent apoptosis had been activated. As reported in Figure 49, a substantial level of apoptosis was induced in DC2.4 cells by the cGAMP:PMPC-PDPA treatment, and not in the B16F10-OVA cells. Future experiments should focus on the better characterisation of the cell death pathways activated by the intracellular delivery of cGAMP. Other intracellular PRR sensors, like the NLRP3 (NOD-like receptor family, pyrin domain-containing-3) inflammasome, could also trigger apoptosis [335]. The inflammasome is a multi-protein complex that assembles in response of inflammatory stimuli or cellular stress, and induces cell death by apoptosis (non-canonical pathway, [335]) and pyroptosis (canonical pathway, [336]) via the release of interleukins IL-1 β and IL-18 [337], [338].

In consideration of the *in vitro* results so far, it was hypothesised the existence of a lower limit of cGAMP sufficient to activate the DCs and their functionality, without inducing apoptosis. Therefore, it was decided to test the formulation in melanoma tumour-bearing mice, monitoring the tumour growth and survival. Unfortunately, no meaningful results were obtained from the *in vivo* animal experiment, and no difference was detected between cGAMP:PMPC-PDPA and the control group. Behind this negative result could be the 1) sub-optimal injection route and 2) the small amount of material encapsulated. Future optimisation experiments will be focused on increasing the loading efficiency of cGAMP molecules into PMPC-PDPA nanocarrier first, and then attempting different routes of administration (i.e., intratumoral). The formulation of cGAMP:PMPC-PDPA prepared was found to have around 500x less material encapsulated compared to other published works. Although the current

formulation failed to demonstrate inflammation power as a *solo* reagent, it is left to investigate if such an amount of cGAMP could have had an impact when co-delivered with the pDNA antigen within the APC.

Furthermore, the intrinsic capability of the PMPC-PDPA polymer to be quickly uptaken by cells might have reduced the amount of material that reached the TME or lymph nodes, thereby minimising the therapeutic effect. In this perspective, could be of relevant to implement a PEG-PDPA PO loaded with cGAMP in *in vivo* experiments, to investigate loading efficiency and the therapeutic effect.

On the Phenotypic Targeting

The design of POs for the active phenotypic targeting of DCs relies on the concepts of the 'range selectivity' previously described (Paragraph 2.5).

The theory is based on the cooperative system of binding between surface receptors and ligands, therefore the cellular expression of the receptors of interest was investigated and characterised. All receptors but CD206 were expressed at different levels in each cellular phenotype. Instead, CD206 protein was detected only in DC2.4 cells, in agreement with their immature lineage phenotype (Figure 52). The results obtained by WB were corroborated by the confocal imaging, but they represent an approximation of the quantitative expression of the receptors. Future experiments shall be direct towards the optimisation of protocols for the precise estimation of numbers of the receptors in each cell lines by flow cytometry for example [339].

The analysis of the glycocalyx (described in Paragraph 2.5.2), showed a small difference in the level of expression across cell lines. However, by the nature of the experiment itself, it was obtained only a quantitative estimation of the presence of the cellular glycocalyx, rather than its qualitative characterisation. In fact, the use of fluorescent-labelled lectin did not allow the fine discrimination amongst all possible contributors of the binding at the surface level. To have a better understanding of the binding dynamics at cell surface level, future experiments should be centred on the qualitative characterisation of the glycocalyx components for each cell lines (e.g., mucins, syndecans and glycosylated lipids).

To experimentally assess the 'range selectivity' theory, ligands for the active targeting were selected, such as PMPC, mUNO and PEP4, and peptide-polymer conjugates were synthesised.

First the binding behaviour of the PMPC-PDPA diblock copolymer embedded into the PEG-PDPA polymer brush was assessed. The analytical characterisation of the batch revealed a larger dispersity of the average diameter dimension. This might be the results of the supramolecular interaction of two different diblock copolymer within the same brush. Although the PMPC in PEG-PDPA batch utilised was freshly prepared for the cell experiments, it cannot be excluded that it would reorganise within the membrane in same-polymer aggregation when mixed with PEG-PDPA diblock copolymer. This could lead to the generation of the so-called 'patchy' POs and future optimisation of PTA staining protocol for TEM imaging could address this question ([340]). If this is the case, it would be worthy of investigation if 'patchy' POs exhibit a different binding behaviour in respect of their control counterparts.

In the binding assays, it was first identified a restricted observational time in DC2.4 cells using PEG-PDPA control formulation (0%PMPC in PEG-PDPA, Figure 58) The antifouling properties of PEG block polymer were once again confirmed by the slow cellular uptake (between 1-2 hours from treatment). Next, different batches of POs were prepared with a different range of ligands on the surface. Generally, it was observed that all PEG-PLA formulations presented very uniform size ranges, regardless the molar composition of peptide, suggesting a negligible interference from the peptide-conjugated polymers (S 11, S 12 and S 13).

All POs batches were tested under identical conditions, and the bindings were observed within 1h of treatment. However, some technical challenges remain in this work and need to be addressed in future experiments.

Firstly, although efforts have been made to have a uniform surface coverage equal to 70% across all cell lines in every binding experiment, a variation of the material taken up due to a higher or lower number of cells seeded cannot be excluded. Few attempts were made to overcome this obstacle. In some settings, cell nuclei were stained with Hoechst for a second normalisation of the signal derived

from the PO. However, this approach resulted in a further detachment and loss of cells, increasing variability and uncertainty. Future experiments should be focused on the detection of the exact surface covered to normalise the bound material across cell lines. This could be achieved by using the Incucyte (Incucyte, Sartorius), a bright field microscope for real-time live-cell imaging and analysis. Through the utilisation of this instrument, it is possible to monitor cellular density on a surface and therefore a more precise distribution of cells across cell lines and experimental replicates. Secondly, it remains unknown if the detected signal was derived from material taken up into or bound to the cell surface. Attempts were made to discriminate and select the bound material to the surface by confocal imaging, however further technical challenges (less precise incubation times, need of membrane fixation, lower fluorescent signals) made impossible to proceed along this path.

From the binding assays obtained and presented in Figure 59, it was observed a distinct binding behaviour across formulations, time and cell lines. However, further optimisation experiments are required to refine the range selectivity design approach. The *PMPC-PED-PDPA and *PEP4-PEG-PLA formulations failed to exhibit selectivity in NIH3T3 and MutuDC cells, for example. This might indicate that either the most selective formulation was not included in the prepared batches, or other unknown factors might be playing a more important role, such as the steric volume occupied by the receptors when forced into proximity by the multiple ligands of the PO's surface. In this case, the binding avidity might not be strong enough to counteract the repulsion forces, resulting in no binding.

Some interesting results were observed in the binding assays with the combinatorial PO batch (Figure 60). Some formulations with only mUNO peptide at different concentrations (B and C) presented opposite results, confirming that not always 'the more the merrier' is the correct approach for particle design. Equally interesting were the results observed from the low binding revealed from combinatorial formulations H and E, across all cell lines. It could be hypothesised that the presence of repulsive energies derived from the different receptors (CD206 and

CD207) forced into proximity during the binding. Future experiments will be aimed towards the preparation of new batches of multivalent and multiplex POs using shorter or longer peptide-conjugated polymers. This manoeuvre would change the position of the ligand with respect of the polymer-brush, altering the binding energy landscape. In fact, a peptide embedded deeper into the PO brush might introduce more steric hindrance, decreasing the energy of binding, if required. A peptide embedded deeper within the PO brush will present higher steric hindrance. *Vice versa*, a protruding peptide from the PO brush might interact more easily with the receptor but might unspecifically interact with the glycocalyx and other moieties (Figure 65).

With this new strategy, it is envisioned that future combinatorial POs might have a mix of short and long peptide-conjugated polymers, suited for the particular phenotypic targeting.

Major efforts are being put in place by several members of the group to translate all the elements discussed so far into a computational model. It is envisioned to create a new computational model for nanoparticle design where machine learning algorithms are combined with parameters obtained experimentally.

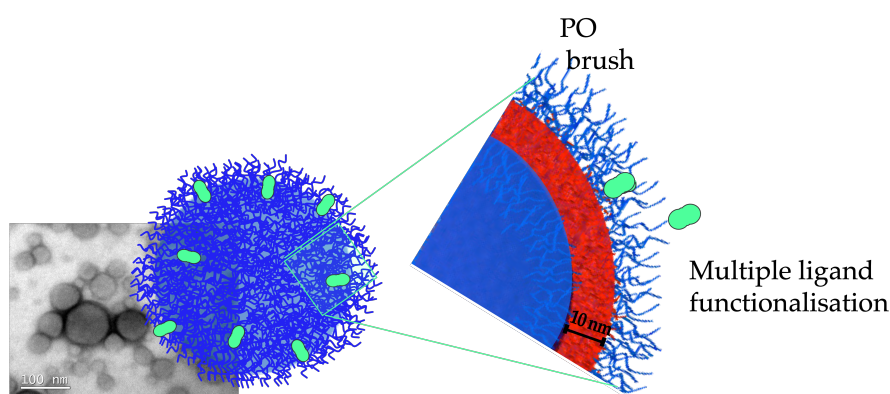


Figure 65: Conceptual model of peptides embedded within the polymer-brush.

Binding obtained with the combinatorial PO batch resulted in only four formulations selected for *in vivo* experiments: pristine, mUNO-POs, PEP4-POs, and Comb POs (Table 12). Cell targeting and biodistribution were the main objectives of the experiments. The fluorescent formulations were i.d. injected, and animals were

sacrificed at different time points (1h, 2h and 4h). Finally, the fluorescent signal derived from the uptaken material was analysed via flow cytometry and plate reader. As observed from the preliminary results discussed in Paragraph 7.2.6, several optimisation experiments are required to provide a more conclusive readout.

Firstly, it was noticed that after 4h post-injection, the great majority of material was still present between the derma and the connective tissue. This represents a major problem for selectivity. Overall, *in vivo* injections provided a preliminary overview of NP organ distribution and other important information for future experiment optimisation. Upon *ex vivo* tissue collection, it was observed that most of the injected material was trapped between the derma and the connective tissue due to the poor vascularisation of the area. As a result, the surface targeted for the phenotypic targeting was overloaded with material, losing selectivity. Future experiments could be focused on optimising the amount of material to be injected and time points of observation of the PO internalisation.

Secondly, the processing of skin samples for flow cytometry is known to be technically challenging. The dorsal skin of the animal was particularly challenging to process to single-cell suspension, and a very harsh digestion protocol was optimised for the scope. Dead cells might increase unspecificity during antibody staining, providing false positive signals and reducing the total viable number of cells acquired by the flow cytometry. Unfortunately, more than 80% of total cells extracted were non-viable at the end of the protocol, with potential loss of information. The gate strategy resulted to be very limited and it did not provide information on skin or lymph node gating CD45+/CD207+ or CD45+/CD206+. That would have allowed to better refine the NP tracking. Before proceeding with the injection, a different location of i.d. injection, such as the back of the ear, was taken in consideration, which unfortunately it was not included in the animal project license at the time of the experiment.

An alternative step could be represented by the implementation of *ex vivo* skin biopsies for the binding assays using functionalised POs. This approach could provide the level of physiological complexity required to identify the best candidates before proceeding with the *in vivo* injections. It could also provide the element of repeatability needed for a refined study of multivalent-multiplex POs and to screen

across libraries of combinatorial POs in search of the best candidates of *in vivo* targeting.

Conventionally, two cellular markers (hence two colours) are selected for each cell type to uniquely identify it in a heterogenous population. However, the prepared formulations already contained a fluorescent dye from the POs, adding an extra colour in each reading. It then proved to be extremely challenging gating for three colours rather than two. Therefore, it was possible to gate cells only for one cell marker and one for the POs, obtaining only a flavour of the targeting, making it impossible to draw definitive conclusions at this time. Future experiments should be focused on the optimisation towards a more detailed and comprehensive marker panel for a better NP tracking and cellular gating.

To sum up, final future directions of the project are directed towards the design and preparation of pH-sensitive, biodegradable and combinatorial POs capable of active targeting of skin DCs. Such POs could be implemented for the co-delivery of antigen DNA+ RU.521, to improve immunisation. Future experiments should aim also to implement cGAMP adjuvant to boost the immune response.

Bibliography

- [1] “2010 to 2015 government policy: cancer research and treatment - GOV.UK.” [Online]. Available: <https://www.gov.uk/government/publications/2010-to-2015-government-policy-cancer-research-and-treatment/2010-to-2015-government-policy-cancer-research-and-treatment>. [Accessed: 26-Mar-2022].
- [2] F. Bray, J. Ferlay, I. Soerjomataram, R. L. Siegel, L. A. Torre, and A. Jemal, “Global cancer statistics 2018: GLOBOCAN estimates of incidence and mortality worldwide for 36 cancers in 185 countries,” *A Cancer Journal for Clinicians*, vol. 68, no. 6, pp. 394–424, Nov. 2018.
- [3] C. J. Sherr, “Cancer Cell Cycles,” *Nature*, vol. 14111, no. 45, pp. 75–1311, 1995.
- [4] R. Fisher, L. Pusztai, and C. Swanton, “Cancer heterogeneity: Implications for targeted therapeutics,” *British Journal of Cancer*, vol. 108, no. 3, pp. 479–485, 19-Feb-2013.
- [5] H. J. Sharp *et al.*, “Synergistic antitumor activity of immune strategies combined with radiation,” *Frontiers in Bioscience*, vol. 12, pp. 4900–4910, 2007.
- [6] G. C. Prendergast and E. M. Jaffee, “Cancer immunologists and cancer biologists: Why we didn’t talk then but need to now,” *Cancer Research*, vol. 67, no. 8, pp. 3500–3504, 2007.
- [7] D. S. Vinay *et al.*, “Immune evasion in cancer: Mechanistic basis and therapeutic strategies,” *Seminars in Cancer Biology*, vol. 35, pp. S185–S198, 2015.
- [8] S. Akira, S. Uematsu, and O. Takeuchi, “Pathogen Recognition and Innate Immunity,” *Cell*, vol. 124, no. 4, pp. 783–801, Feb. 2006.
- [9] D. Ribatti, “The concept of immune surveillance against tumors. The first theories,” *Oncotarget*, vol. 8, no. 4, pp. 7175–7180, 2015.
- [10] R. D. Schreiber, L. J. Old, and M. J. Smyth, “Cancer Immunoediting: Integrating Immunity’s Roles in Cancer Suppression and Promotion,” *Science*, vol. 331, no. 6024, pp. 1565–1570, Mar. 2011.
- [11] L. H. Butterfield, “Cancer vaccines.,” *BMJ (Clinical research ed.)*, vol. 350, p. h988, Apr. 2015.
- [12] B. Aristizábal and Á. González, “Autoimmunity: From Bench to Bedside, Chapter 2: Innate Immune System,” in *Autoimmunity: From Bench to Bedside*, J.-M. Anaya, Y. Shoenfeld, A. Rojas-Villarraga, R. A. Levy, and R. Cervera, Eds. El Rosario University Press, 2013, pp. 237–378.

- [13] R. Medzhitov and C. A. Janeway, "Decoding the patterns of self and nonself by the innate immune system.," *Science (New York, N.Y.)*, vol. 296, no. 5566, pp. 298–300, Apr. 2002.
- [14] C. A. Janeway and R. Medzhitov, "INNATE IMMUNE RECOGNITION," *Annual Review of Immunology*, vol. 20, no. 1, pp. 197–216, 2002.
- [15] C. Basset, J. Holton, R. O'Mahony, and I. Roitt, "Innate immunity and pathogen-host interaction," *Vaccine*. 2003.
- [16] S. Nagata, R. Hanayama, and K. Kawane, "Autoimmunity and the Clearance of Dead Cells," *Cell*, vol. 140, no. 5, pp. 619–630, Mar. 2010.
- [17] M. K. Crow, "Type I interferon in systemic lupus erythematosus," *Current Topics in Microbiology and Immunology*, vol. 316, pp. 359–386, 2007.
- [18] D. Rubio *et al.*, "Crosstalk between the type 1 interferon and nuclear factor kappa B pathways confers resistance to a lethal virus infection.," *Cell host & microbe*, vol. 13, no. 6, pp. 701–10, Jun. 2013.
- [19] R. K. Gupta *et al.*, "Oxidative stress and antioxidants in disease and cancer: A review," *Asian Pacific Journal of Cancer Prevention*, vol. 15, no. 11, pp. 4405–4409, 2014.
- [20] F. Nainu, A. Shiratsuchi, and Y. Nakanishi, "Induction of apoptosis and subsequent phagocytosis of virus-infected cells as an antiviral mechanism," *Frontiers in Immunology*, vol. 8, no. SEP, p. 1220, Sep. 2017.
- [21] M. Tagliamonte, A. Petrizzo, M. L. Tornesello, F. M. Buonaguro, and L. Buonaguro, "Antigen-specific vaccines for cancer treatment.," *Human vaccines & immunotherapeutics*, vol. 10, no. 11, pp. 3332–46, 2014.
- [22] T. Kawai and S. Akira, "Toll-like receptor and RIG-1-like receptor signaling," *Annals of the New York Academy of Sciences*, vol. 1143, pp. 1–20, 2008.
- [23] S. Akira, S. Uematsu, and O. Takeuchi, "Pathogen recognition and innate immunity," *Cell*, vol. 124, no. 4, pp. 783–801, Feb. 2006.
- [24] W. M. Schneider, M. D. Chevillotte, and C. M. Rice, "Interferon-stimulated genes: A complex web of host defenses," *Annual Review of Immunology*, vol. 32. Annu Rev Immunol, pp. 513–545, 2014.
- [25] T. Liu, L. Zhang, D. Joo, and S. C. Sun, "NF-κB signaling in inflammation," *Signal Transduction and Targeted Therapy 2017 2:1*, vol. 2, no. 1, pp. 1–9, Jul. 2017.
- [26] L. Sun, J. Wu, F. Du, X. Chen, and Z. J. Chen, "Cyclic GMP-AMP synthase is a cytosolic DNA sensor that activates the type I interferon pathway," *Science*, vol. 339, no. 6121, pp. 786–791, Feb. 2013.

- [27] A. Takaoka *et al.*, “DAI (DLM-1/ZBP1) is a cytosolic DNA sensor and an activator of innate immune response,” *Nature*, vol. 448, no. 7152, pp. 501–505, Jul. 2007.
- [28] A. M. Krieg *et al.*, “CpG motifs in bacterial DNA trigger direct B-cell activation,” *Nature*, vol. 374, no. 6522, pp. 546–549, Apr. 1995.
- [29] L. Sun, J. Wu, F. Du, X. Chen, and Z. J. Chen, “Cyclic GMP-AMP synthase is a cytosolic DNA sensor that activates the type I interferon pathway,” *Science (New York, N.Y.)*, vol. 339, no. 6121, pp. 786–791, Feb. 2013.
- [30] N. Dobbs, N. Burnaevskiy, D. Chen, V. K. Gonugunta, N. M. Alto, and N. Yan, “STING Activation by Translocation from the ER Is Associated with Infection and Autoinflammatory Disease,” *Cell host & microbe*, vol. 18, no. 2, pp. 157–168, Aug. 2015.
- [31] T. Abe and G. N. Barber, “Cytosolic-DNA-Mediated, STING-Dependent Proinflammatory Gene Induction Necessitates Canonical NF-κB Activation through TBK1,” *Journal of Virology*, vol. 88, no. 10, pp. 5328–5341, May 2014.
- [32] J. Maelfait, L. Liverpool, and J. Rehwinkel, “Nucleic Acid Sensors and Programmed Cell Death,” *Journal of Molecular Biology*, vol. 432, no. 2, pp. 552–568, Jan. 2020.
- [33] C. Zierhut, N. Yamaguchi, M. Paredes, J. D. Luo, T. Carroll, and H. Funabiki, “The Cytoplasmic DNA Sensor cGAS Promotes Mitotic Cell Death,” *Cell*, vol. 178, no. 2, pp. 302–315.e23, Jul. 2019.
- [34] T. Li and Z. J. Chen, “The cGAS-cGAMP-STING pathway connects DNA damage to inflammation, senescence, and cancer,” *Journal of Experimental Medicine*. 2018.
- [35] S. Yum, M. Li, and Z. J. Chen, “Old dogs, new trick: classic cancer therapies activate cGAS,” *Cell Research*, vol. 30, no. 8, p. 639, Aug. 2020.
- [36] R. Lubbers, M. F. van Essen, C. van Kooten, and L. A. Trouw, “Production of complement components by cells of the immune system,” *Clinical and Experimental Immunology*, vol. 188, no. 2. Oxford University Press, pp. 183–194, 01-May-2017.
- [37] M. C. Carroll and M. B. Fischer, “Complement and the immune response,” *Current Opinion in Immunology*, vol. 9, no. 1, pp. 64–69, Feb. 1997.
- [38] P. Vignesh, A. Rawat, M. Sharma, and S. Singh, “Complement in autoimmune diseases,” *Clinica Chimica Acta*, vol. 465. Elsevier B.V., pp. 123–130, 01-Feb-2017.
- [39] “Cytokines, Chemokines and Their Receptors - Madame Curie Bioscience Database - NCBI Bookshelf.” [Online]. Available: <https://www.ncbi.nlm.nih.gov/books/NBK6294/>. [Accessed: 17-May-2022].
- [40] J. M. Zhang and J. An, “Cytokines, inflammation, and pain,” *International*

Anesthesiology Clinics, vol. 45, no. 2. pp. 27–37, Mar-2007.

- [41] L. C. Borish and J. W. Steinke, “Cytokines and chemokines,” *Journal of Allergy and Clinical Immunology*, vol. 111, no. 2, pp. S460–S475, Feb. 2003.
- [42] S. Y. Zhang *et al.*, “Inborn errors of interferon (IFN)-mediated immunity in humans: insights into the respective roles of IFN- α/β , IFN- γ , and IFN- λ in host defense,” *Immunological Reviews*, vol. 226, no. 1, pp. 29–40, Dec. 2008.
- [43] L. B. Ivashkiv and L. T. Donlin, “Regulation of type I interferon responses,” *Nature Reviews Immunology* 2014 14:1, vol. 14, no. 1, pp. 36–49, Dec. 2013.
- [44] V. Shankaran *et al.*, “IFN γ and lymphocytes prevent primary tumour development and shape tumour immunogenicity,” *Nature* 2001 410:6832, vol. 410, no. 6832, pp. 1107–1111, Apr. 2001.
- [45] F. Castro, A. P. Cardoso, R. M. Gonçalves, K. Serre, and M. J. Oliveira, “Interferon-gamma at the crossroads of tumor immune surveillance or evasion,” *Frontiers in Immunology*, vol. 9, no. MAY, p. 847, May 2018.
- [46] S. V. Kotenko *et al.*, “IFN- λ s mediate antiviral protection through a distinct class II cytokine receptor complex,” *Nature Immunology*, vol. 4, no. 1. Nature Publishing Group, pp. 69–77, 16-Dec-2003.
- [47] N. Parameswaran and S. Patial, “Tumor Necrosis Factor- α Signaling in Macrophages,” *Critical reviews in eukaryotic gene expression*, vol. 20, no. 2, p. 87, 2010.
- [48] F. Atzeni and P. Sarzi-Puttini, “Tumor Necrosis Factor,” *Brenner’s Encyclopedia of Genetics: Second Edition*, pp. 229–231, Feb. 2013.
- [49] E. Vivier, E. Tomasello, M. Baratin, T. Walzer, and S. Ugolini, “Functions of natural killer cells,” *Nature Immunology*, vol. 9, no. 5, pp. 503–510, May 2008.
- [50] G. Dranoff, “Cytokines in Cancer Pathogenesis and Cancer Therapy,” *Nature Reviews Cancer*, 2004.
- [51] J. M. Timmerman and R. Levy, “Dendritic Cell Vaccines for cancer immunotherapy,” *Annu. Rev. Med*, no. 2, 1999.
- [52] F. Veglia and D. I. Gabrilovich, “Dendritic cells in cancer: the role revisited.,” *Current opinion in immunology*, vol. 45, pp. 43–51, Apr. 2017.
- [53] R. M. Steinman and Z. A. Cohn, “Identification of a novel cell type in peripheral lymphoid organs of mice: I. Morphology, quantitation, tissue distribution,” *Journal of Experimental Medicine*, vol. 137, no. 5, pp. 1142–1162, May 1973.
- [54] R. M. Steinman, D. S. Lustig, and Z. A. Cohn, “Identification of a novel cell type in

- peripheral lymphoid organs of mice: III. Functional properties in vivo,” *Journal of Experimental Medicine*, vol. 139, no. 6, pp. 1431–1445, Jun. 1974.
- [55] R. M. Steinman and Z. A. Cohn, “Identification of a novel cell type in peripheral lymphoid organs of mice: II. Functional properties in vitro,” *Journal of Experimental Medicine*, vol. 139, no. 2, pp. 380–397, Feb. 1974.
- [56] A. Boltjes and F. van Wijk, “Human Dendritic Cell Functional Specialization in Steady-State and Inflammation,” *Frontiers in Immunology*, vol. 5, p. 131, Apr. 2014.
- [57] M. Haniffa, M. Collin, and F. Ginhoux, “Ontogeny and Functional Specialization of Dendritic Cells in Human and Mouse,” in *Advances in Immunology*, vol. 120, Academic Press, 2013, pp. 1–49.
- [58] M. Collin and V. Bigley, “Human dendritic cell subsets: an update,” *Immunology*, vol. 154, no. 1, p. 3, May 2018.
- [59] M. Merad, P. Sathe, J. Helft, J. Miller, and A. Mortha, “The dendritic cell lineage: ontogeny and function of dendritic cells and their subsets in the steady state and the inflamed setting,” *Annual review of immunology*, vol. 31, pp. 563–604, 2013.
- [60] J. Banchereau and R. M. Steinman, “Dendritic cells and the control of immunity,” *Nature*, vol. 392, no. 6673, pp. 245–252, Mar. 1998.
- [61] D. A. Ferrington and D. S. Gregerson, “Immunoproteasomes: Structure, Function, and Antigen Presentation,” *Progress in molecular biology and translational science*, vol. 109, p. 75, 2012.
- [62] C. P. Larsen, R. M. Steinman, M. Witmer-Pack, D. F. Hankins, P. J. Morris, and J. M. Austyn, “Migration and maturation of Langerhans cells in skin transplants and explants,” *The Journal of Experimental Medicine*, vol. 172, no. 5, p. 1483, Nov. 1990.
- [63] K. L. Medina, *Overview of the immune system*, 1st ed., vol. 133. Elsevier B.V., 2016.
- [64] B. Wootla, A. Denic, and M. Rodriguez, “Polyclonal and monoclonal antibodies in clinic,” *Methods in Molecular Biology*, vol. 1060, pp. 79–110, 2014.
- [65] Y. Takahama, “Journey through the thymus: stromal guides for T-cell development and selection,” *Nature Reviews Immunology 2006 6:2*, vol. 6, no. 2, pp. 127–135, Feb. 2006.
- [66] H. Hosokawa and E. V. Rothenberg, “Cytokines, Transcription Factors, and the Initiation of T-Cell Development,” *Cold Spring Harbor Perspectives in Biology*, vol. 10, no. 5, p. a028621, May 2018.
- [67] M. A. Yui and E. V. Rothenberg, “Developmental gene networks: a triathlon on the course to T cell identity,” *Nature Reviews Immunology 2014 14:8*, vol. 14, no. 8, pp.

529–545, Jul. 2014.

- [68] S. Feske, “Calcium signalling in lymphocyte activation and disease,” *Nature reviews. Immunology*, vol. 7, no. 9, pp. 690–702, Sep. 2007.
- [69] F. A. Bonilla and H. C. Oettgen, “Adaptive immunity,” *J Allergy Clin Immunol.*, vol. 125, no. Suppl 2, pp. S33–S40, Feb. 2010.
- [70] H. W. Schroeder and L. Cavacini, “Structure and function of immunoglobulins,” *The Journal of allergy and clinical immunology*, vol. 125, no. 2 Suppl 2, Feb. 2010.
- [71] M. C. Carroll and D. E. Isenman, “Regulation of Humoral Immunity by Complement,” *Immunity*, vol. 37, no. 2, pp. 199–207, Aug. 2012.
- [72] F. Nimmerjahn and J. V. Ravetch, “Fcγ receptors as regulators of immune responses,” *Nature Reviews Immunology 2007 8:1*, vol. 8, no. 1, pp. 34–47, Jan. 2008.
- [73] G. Wang *et al.*, “Molecular Basis of Assembly and Activation of Complement Component C1 in Complex with Immunoglobulin G1 and Antigen,” *Molecular Cell*, vol. 63, no. 1, pp. 135–145, Jul. 2016.
- [74] E. P. Über, “Über den jetzigen Stand der Karzinomforschung,” *Ned Tijdschr Geneeskde*, vol. 1, no. 5, pp. 273–90, 1909.
- [75] D. Ribatti, “The concept of immune surveillance against tumors. The first theories,” *Oncotarget*, vol. 8, no. 4, pp. 7175–7180, Jan. 2017.
- [76] C. & H. I. Norbury, “Cellular responses to DNA damage,” *Annu Rev Pharmacol Toxicol*, 2001.
- [77] D. Hanahan and R. A. Weinberg, “The hallmarks of cancer,” *Cell*, vol. 100, no. 1, pp. 57–70, 2000.
- [78] D. Hanahan and R. A. Weinberg, “Hallmarks of cancer: The next generation,” *Cell*, vol. 144, no. 5, pp. 646–674, 2011.
- [79] Y.-C. Lu and P. F. Robbins, “Cancer immunotherapy targeting neoantigens,” *Seminars in Immunology*, vol. 28, no. 1, pp. 22–27, Feb. 2016.
- [80] L. Zitvogel, A. Tesniere, and G. Kroemer, “Cancer despite immunosurveillance: immunoselection and immunosubversion,” *Nature Reviews Immunology 2006 6:10*, vol. 6, no. 10, pp. 715–727, Sep. 2006.
- [81] D. Mittal, M. M. Gubin, R. D. Schreiber, and M. J. Smyth, “New insights into cancer immunoediting and its three component phases — elimination, equilibrium and escape,” *Current Opinion in Immunology*, pp. 16–25, 2014.
- [82] C. Asselin-Paturel and G. Trinchieri, “Production of type I interferons: plasmacytoid dendritic cells and beyond,” *The Journal of experimental medicine*, vol. 202, no. 4,

pp. 461–5, Aug. 2005.

- [83] K. Hoshino, T. Kaisho, T. Iwabe, O. Takeuchi, and S. Akira, “Differential involvement of IFN- in Toll-like receptor-stimulated dendritic cell activation,” *International Immunology*, vol. 14, no. 10, pp. 1225–1231, Oct. 2002.
- [84] Y. A. Fouad and C. Aanei, “Revisiting the hallmarks of cancer,” *American Journal of Cancer Research*, vol. 7, no. 5, pp. 1016–1036, 2017.
- [85] G. P. Dunn, A. T. Bruce, H. Ikeda, L. J. Old, and R. D. Schreiber, “Cancer immunoediting: From immunosurveillance to tumor escape,” *Nature Immunology*, vol. 3, no. 11, pp. 991–998, 2002.
- [86] L. Zitvogel, A. Tesniere, and G. Kroemer, “Cancer despite immunosurveillance: immunoselection and immunosubversion,” *Nature Reviews Immunology*, vol. 6, no. 10, pp. 715–727, Oct. 2006.
- [87] W. B. Coley, “The treatment of malignant tumors by repeated inoculations of erysipelas.,” *Clinical orthopaedics and related research*, no. 262, pp. 3–11, 1893.
- [88] W. B. Coley, “The Treatment of Inoperable Sarcoma by Bacterial Toxins (the Mixed Toxins of the Streptococcus erysipelas and the Bacillus prodigiosus),” *Proceedings of the Royal Society of Medicine*, vol. 3, no. Surg Sect, p. 1, Jun. 1910.
- [89] I. Melero, E. Castanon, M. Alvarez, S. Champiat, and A. Marabelle, “Intratumoural administration and tumour tissue targeting of cancer immunotherapies,” *Nature Reviews Clinical Oncology*, vol. 18, no. 9. Nature Publishing Group, pp. 558–576, 18-May-2021.
- [90] Z. Tao *et al.*, “Cellular immunotherapy of cancer: an overview and future directions.,” *Immunotherapy*, vol. 9, no. 7, pp. 589–606, 2017.
- [91] European Medicines Agency, “First two CAR-T cell medicines recommended for approval in the European Union,” London, Jun-2018.
- [92] S. L. Topalian, C. G. Drake, and D. M. Pardoll, “Immune checkpoint blockade: A common denominator approach to cancer therapy,” *Cancer Cell*, vol. 27, no. 4, pp. 451–461, 2015.
- [93] S. L. Topalian, J. M. Taube, R. A. Anders, and D. M. Pardoll, “Mechanism-driven biomarkers to guide immune checkpoint blockade in cancer therapy,” *Nature Reviews Cancer*. 2016.
- [94] P. Sharma, S. Hu-Lieskovan, J. A. Wargo, and A. Ribas, “Primary, Adaptive, and Acquired Resistance to Cancer Immunotherapy,” *Cell*, vol. 168, no. 4, pp. 707–723, Feb. 2017.

- [95] V. Kumar, N. Chaudhary, M. Garg, C. S. Floudas, P. Soni, and A. B. Chandra, "Current Diagnosis and Management of Immune Related Adverse Events (irAEs) Induced by Immune Checkpoint Inhibitor Therapy [Front. Pharmacol(49),8] DOI: 10.3389/fphar.2017.00049," *Frontiers in Pharmacology*, vol. 8, no. MAY, 2017.
- [96] L. Milling, Y. Zhang, and D. J. Irvine, "Delivering safer immunotherapies for cancer," *Advanced Drug Delivery Reviews*, vol. 114, pp. 79–101, May 2017.
- [97] S. Cousin and A. Italiano, "Toxicity profiles of immunotherapy," *Pharmacology and Therapeutics*, vol. 181, pp. 91–100, 2017.
- [98] M. Kostine *et al.*, "Opportunistic autoimmunity secondary to cancer immunotherapy (OASI): An emerging challenge," *Revue de Medecine Interne*, vol. 38, no. 8, pp. 513–525, 2017.
- [99] P. W. Kantoff *et al.*, "Sipuleucel-T immunotherapy for castration-resistant prostate cancer," *New England Journal of Medicine*, 2010.
- [100] D. T. Le *et al.*, "Results from a phase IIb, randomized, multicenter study of GVAX pancreas and CRS-207 compared with chemotherapy in adults with previously treated metastatic pancreatic adenocarcinoma (ECLIPSE study)," *Clinical Cancer Research*, 2019.
- [101] K. F. Bol, G. Schreiber, W. R. Gerritsen, I. J. M. de Vries, and C. G. Figdor, "Dendritic Cell-Based Immunotherapy: State of the Art and Beyond.," *Clinical cancer research : an official journal of the American Association for Cancer Research*, vol. 22, no. 8, pp. 1897–906, Apr. 2016.
- [102] R. E. Hollingsworth and K. Jansen, "Turning the corner on therapeutic cancer vaccines," *npj Vaccines*, vol. 4, no. 1, p. 7, Dec. 2019.
- [103] D. Zamarin and M. A. Postow, "Immune checkpoint modulation: Rational design of combination strategies," *Pharmacology and Therapeutics*, vol. 150, pp. 23–32, 2015.
- [104] T. Niezold *et al.*, "DNA vaccines encoding DEC205-targeted antigens: Immunity or tolerance?," *Immunology*, 2015.
- [105] J. Banchereau and R. M. Steinman, "Dendritic cells and the control of immunity," *Nature*, vol. 392, no. 6673, pp. 245–252, Mar. 1998.
- [106] J. Liu, M. Fu, M. Wang, D. Wan, Y. Wei, and X. Wei, "Cancer vaccines as promising immuno-therapeutics: platforms and current progress," *Journal of Hematology and Oncology*, vol. 15, no. 1, pp. 1–26, Dec. 2022.
- [107] S. Halle, O. Halle, and R. Förster, "Mechanisms and Dynamics of T Cell-Mediated Cytotoxicity In Vivo," *Trends in Immunology*, vol. 38, no. 6, pp. 432–443, Jun. 2017.

- [108] J. Borst, T. Ahrends, N. Bąbała, C. J. M. Melief, and W. Kastenmüller, "CD4+ T cell help in cancer immunology and immunotherapy," *Nature Reviews Immunology* 2018 18:10, vol. 18, no. 10, pp. 635–647, Jul. 2018.
- [109] B. Mastelic-Gavillet, K. Balint, C. Boudousquie, P. O. Gannon, and L. E. Kandalaft, "Personalized Dendritic Cell Vaccines-Recent Breakthroughs and Encouraging Clinical Results," *Frontiers in immunology*, vol. 10, no. APR, 2019.
- [110] M. A. Cheever and C. S. Higano, "PROVENGE (sipuleucel-T) in prostate cancer: The first FDA-approved therapeutic cancer vaccine," *Clinical Cancer Research*, vol. 17, no. 11, pp. 3520–3526, 2011.
- [111] A. H. Banday, S. Jeelani, and V. J. Hruby, "Cancer vaccine adjuvants - Recent clinical progress and future perspectives," *Immunopharmacology and Immunotoxicology*, vol. 37, no. 1, pp. 1–11, 2015.
- [112] E. A. Mittendorf *et al.*, "Clinical trial results of the HER-2/neu (E75) vaccine to prevent breast cancer recurrence in high-risk patients: from US Military Cancer Institute Clinical Trials Group Study I-01 and I-02," *Cancer*, vol. 118, no. 10, pp. 2594–2602, May 2012.
- [113] E. J. Schneble *et al.*, "The HER2 peptide nelipepimut-S (E75) vaccine (NeuVax™) in breast cancer patients at risk for recurrence: Correlation of immunologic data with clinical response," *Immunotherapy*, vol. 6, no. 5, pp. 519–531, Jun. 2014.
- [114] R. Salgia *et al.*, "Vaccination with irradiated autologous tumor cells engineered to secrete granulocyte-macrophage colony-stimulating factor augments antitumor immunity in some patients with metastatic non-small-cell lung carcinoma," *Journal of clinical oncology: official journal of the American Society of Clinical Oncology*, vol. 21, no. 4, pp. 624–630, Feb. 2003.
- [115] E. M. Jaffee *et al.*, "Novel allogeneic granulocyte-macrophage colony-stimulating factor-secreting tumor vaccine for pancreatic cancer: a phase I trial of safety and immune activation," *Journal of clinical oncology: official journal of the American Society of Clinical Oncology*, vol. 19, no. 1, pp. 145–156, Jan. 2001.
- [116] G. Dranoff *et al.*, "Vaccination with irradiated tumor cells engineered to secrete murine granulocyte-macrophage colony-stimulating factor stimulates potent, specific, and long-lasting anti-tumor immunity," *Proceedings of the National Academy of Sciences of the United States of America*, vol. 90, no. 8, pp. 3539–3543, Apr. 1993.
- [117] S. H. Van Der Burg, R. Arens, F. Ossendorp, T. Van Hall, and C. J. M. Melief, "Vaccines for established cancer: overcoming the challenges posed by immune

- evasion,” *Nature Reviews Cancer* 2016 16:4, vol. 16, no. 4, pp. 219–233, Mar. 2016.
- [118] C. Guo, M. H. Manjili, J. R. Subjeck, D. Sarkar, P. B. Fisher, and X.-Y. Wang, *Therapeutic Cancer Vaccines: Past, Present, and Future*, vol. 23, no. 119. 2013.
- [119] D. P. Snider and D. M. Segal, “Targeted antigen presentation using crosslinked antibody heteroaggregates,” *The Journal of Immunology*, vol. 139, no. 5, 1987.
- [120] O. J. Finn, “Human Tumor Antigens Yesterday, Today, and Tomorrow,” *Cancer Immunology Research*, vol. 5, no. 5, pp. 347–354, May 2017.
- [121] L. C. Bonifaz *et al.*, “In Vivo Targeting of Antigens to Maturing Dendritic Cells via the DEC-205 Receptor Improves T Cell Vaccination,” *Journal of Experimental Medicine*, vol. 199, no. 6, pp. 815–824, Mar. 2004.
- [122] L. Zitvogel *et al.*, “Therapy of murine tumors with tumor peptide-pulsed dendritic cells: Dependence on T cells, B7 costimulation, and T helper cell 1-associated cytokines,” *Journal of Experimental Medicine*, 1996.
- [123] D. O’Neill and N. Bhardwaj, “Generation of Autologous Peptide- and Protein-Pulsed Dendritic Cells for Patient-Specific Immunotherapy,” in *Adoptive Immunotherapy*, New Jersey: Humana Press, 2005, pp. 097–112.
- [124] Z. Jahanafrooz *et al.*, “Comparison of DNA and mRNA vaccines against cancer,” *Drug Discovery Today*, vol. 25, no. 3. Elsevier Ltd, pp. 552–560, 01-Mar-2020.
- [125] S. S. Rosa, D. M. F. Prazeres, A. M. Azevedo, and M. P. C. Marques, “mRNA vaccines manufacturing: Challenges and bottlenecks,” *Vaccine*, vol. 39, no. 16, p. 2190, Apr. 2021.
- [126] V. Apostolopoulos, T. Thalhammer, A. G. Tzakos, and L. Stojanovska, “Targeting antigens to dendritic cell receptors for vaccine development,” *Journal of drug delivery*, vol. 2013, p. 869718, 2013.
- [127] W. Li, H. Wei, H. Li, J. Gao, S. S. Feng, and Y. Guo, “Cancer nanoimmunotherapy using advanced pharmaceutical nanotechnology,” *Nanomedicine (Lond)*, vol. 9, no. 16, pp. 2587–2605, 2014.
- [128] G. J. Weiner, H.-M. Liu, J. E. Wooldridge, C. E. Dahle, and A. M. Krieg, “Immunostimulatory oligodeoxynucleotides containing the CpG motif are effective as immune adjuvants in tumor antigen immunization,” *Proceedings of the National Academy of Sciences*, vol. 94, no. 20, pp. 10833–10837, Sep. 1997.
- [129] J. Maelfait, A. Bridgeman, A. Benlahrech, C. Cursi, and J. Rehwinkel, “Restriction by SAMHD1 Limits cGAS/STING-Dependent Innate and Adaptive Immune Responses to HIV-1,” *Cell Reports*, vol. 16, no. 6, pp. 1492–1501, 2016.

- [130] S. R. Woo, L. Corrales, and T. F. Gajewski, "The STING pathway and the T cell-inflamed tumor microenvironment," *Trends in Immunology*. 2015.
- [131] K. Li, S. Qu, X. Chen, Q. Wu, and M. Shi, "Promising Targets for Cancer Immunotherapy: TLRs, RLRs, and STING-Mediated Innate Immune Pathways.," *International journal of molecular sciences*, vol. 18, no. 2, Feb. 2017.
- [132] J. Le Naour, L. Zitvogel, L. Galluzzi, E. Vacchelli, and G. Kroemer, "Trial watch: STING agonists in cancer therapy," *Oncoimmunology*, vol. 9, no. 1, Jan. 2020.
- [133] J. J. Suschak, J. A. Williams, and C. S. Schmaljohn, "Advancements in DNA vaccine vectors, non-mechanical delivery methods, and molecular adjuvants to increase immunogenicity," *Human Vaccines & Immunotherapeutics*, vol. 13, no. 12, p. 2837, Dec. 2017.
- [134] A. Tiptiri-Kourpeti, K. Spyridopoulou, A. Pappa, and K. Chlichlia, "DNA vaccines to attack cancer: Strategies for improving immunogenicity and efficacy," *Pharmacology & Therapeutics*, vol. 165, pp. 32–49, Sep. 2016.
- [135] N. Petrovsky and J. C. Aguilar, "Vaccine adjuvants: Current state and future trends," *Immunology and Cell Biology* 2004 82:5, Sep. 2004.
- [136] M. Pavlenko *et al.*, "A phase I trial of DNA vaccination with a plasmid expressing prostate-specific antigen in patients with hormone-refractory prostate cancer," *British journal of cancer*, vol. 91, no. 4, pp. 688–694, Aug. 2004.
- [137] H. Kim, B. Kwon, and J. I. Sin, "Combined Stimulation of IL-2 and 4-1BB Receptors Augments the Antitumor Activity of E7 DNA Vaccines by Increasing Ag-Specific CTL Responses," *PLOS ONE*, vol. 8, no. 12, p. e83765, Dec. 2013.
- [138] W. K. Decker and A. Safdar, "Cytokine adjuvants for vaccine therapy of neoplastic and infectious disease," *Cytokine Growth Factor Rev*, vol. 22, no. 4, pp. 177–187, Aug. 2011.
- [139] W. Zhao, G. Zhao, and B. Wang, "Revisiting GM-CSF as an adjuvant for therapeutic vaccines," *Cellular & Molecular Immunology* 2018 15:2, vol. 15, no. 2, pp. 187–189, Oct. 2017.
- [140] O. Demaria *et al.*, "STING activation of tumor endothelial cells initiates spontaneous and therapeutic antitumor immunity," *Proceedings of the National Academy of Sciences*, vol. 112, no. 50, pp. 15408–15413, 2015.
- [141] L. Corrales *et al.*, "Direct activation of STING in the tumor microenvironment leads to potent and systemic tumor regression and immunity," *Cell reports*, vol. 11, no. 7, p. 1018, May 2015.

- [142] X. Che *et al.*, “Single Mutations Reshape the Structural Correlation Network of the DMXAA-Human STING Complex,” *Journal of Physical Chemistry B*, vol. 121, no. 9, pp. 2073–2082, 2017.
- [143] M. F. Gulen *et al.*, “Signalling strength determines proapoptotic functions of STING,” *Nature Communications*, vol. 8, no. 1, 2017.
- [144] L. Corrales *et al.*, “Direct Activation of STING in the Tumor Microenvironment Leads to Potent and Systemic Tumor Regression and Immunity,” *Cell Reports*, vol. 11, no. 7, pp. 1018–1030, 2015.
- [145] W. Jiang *et al.*, “Designing nanomedicine for immuno-oncology,” *Nature Biomedical Engineering*, vol. 1, no. 2, p. 0029, Feb. 2017.
- [146] P. Darvin, S. M. Toor, V. Sasidharan Nair, and E. Elkord, “Immune checkpoint inhibitors: recent progress and potential biomarkers,” *Experimental and Molecular Medicine*. 2018.
- [147] P. Bonaventura *et al.*, “Cold tumors: A therapeutic challenge for immunotherapy,” *Frontiers in Immunology*. 2019.
- [148] J. D. Wolchok *et al.*, “Nivolumab plus Ipilimumab in advanced melanoma,” *New England Journal of Medicine*, 2013.
- [149] J. S. Weber *et al.*, “Sequential administration of nivolumab and ipilimumab with a planned switch in patients with advanced melanoma (CheckMate 064): an open-label, randomised, phase 2 trial,” *The Lancet Oncology*, 2016.
- [150] J. Wolfram *et al.*, “Safety of Nanoparticles in Medicine,” *Current Drug Targets*, vol. 16, no. 14, pp. 1671–1681, Dec. 2015.
- [151] T. J. Webster, “Nanomedicine: What’s in a definition?,” *International Journal of Nanomedicine*, vol. 1, no. 2. Dove Press, pp. 115–116, 2006.
- [152] Q. Sun *et al.*, “Nanomedicine and macroscale materials in immuno-oncology,” *Chemical Society Reviews*, vol. 48, no. 1. Europe PMC Funders, pp. 351–381, 01-Jan-2019.
- [153] X. Zang, X. Zhao, H. Hu, M. Qiao, Y. Deng, and D. Chen, “Nanoparticles for tumor immunotherapy,” *European Journal of Pharmaceutics and Biopharmaceutics*, vol. 115, pp. 243–256, Jun. 2017.
- [154] C. LoPresti, H. Lomas, M. Massignani, T. Smart, and G. Battaglia, “Polymersomes: nature inspired nanometer sized compartments,” *Journal of Materials Chemistry*, vol. 19, no. 22, p. 3576, 2009.
- [155] M. E. R. O’Brien *et al.*, “Reduced cardiotoxicity and comparable efficacy in a phase III

- trial of pegylated liposomal doxorubicin HCl (CAELYX™/Doxil®) versus conventional doxorubicin for first-line treatment of metastatic breast cancer,” *Annals of Oncology*, vol. 15, no. 3, pp. 440–449, 2004.
- [156] Y. Liu and J. Guo, “Modulation of tumor microenvironment for immunotherapy: focus on nanomaterial-based strategies,” *Theranostics*, vol. 10, no. 7, pp. 3099–3117, 2020.
- [157] T. Briolay, T. Petithomme, M. Fouet, N. Nguyen-Pham, C. Blanquart, and N. Boisgerault, “Delivery of cancer therapies by synthetic and bio-inspired nanovectors,” *Molecular Cancer*, vol. 20, no. 1. BioMed Central, pp. 1–24, 24-Mar-2021.
- [158] M. S. Goldberg, “Improving cancer immunotherapy through nanotechnology,” *Nature Reviews Cancer*, vol. 19, no. 10. Nature Publishing Group, pp. 587–602, 06-Sep-2019.
- [159] U. Bulbake, S. Doppalapudi, N. Kommineni, and W. Khan, “Liposomal Formulations in Clinical Use : An Updated Review development,” pp. 1–33, 2017.
- [160] W. T. Al-Jamal and K. Kostarelos, “Liposomes: From a clinically established drug delivery system to a nanoparticle platform for theranostic nanomedicine,” *Accounts of Chemical Research*, vol. 44, no. 10. pp. 1094–1104, 2011.
- [161] I. Melero *et al.*, “Therapeutic vaccines for cancer: An overview of clinical trials,” *Nature Reviews Clinical Oncology*, vol. 11, no. 9. Nature Publishing Group, pp. 509–524, 2014.
- [162] L. M. Kranz *et al.*, “Systemic RNA delivery to dendritic cells exploits antiviral defence for cancer immunotherapy,” *Nature*, vol. 534, no. 7607, pp. 396–401, Jun. 2016.
- [163] L. M. Kranz *et al.*, “Systemic RNA delivery to dendritic cells exploits antiviral defence for cancer immunotherapy,” *Nature*, vol. 534, no. 7607, pp. 396–401, Jun. 2016.
- [164] L. Messenger, J. Gaitzsch, L. Chierico, and G. Battaglia, “Novel aspects of encapsulation and delivery using polymersomes,” *Current Opinion in Pharmacology*, vol. 18, no. 1, pp. 104–111, 2014.
- [165] V. Sainz *et al.*, “Regulatory aspects on nanomedicines,” *Biochemical and Biophysical Research Communications*, vol. 468, no. 3, pp. 504–510, Dec. 2015.
- [166] H. J. Jang, C. Y. Shin, and K. B. Kim, “Safety evaluation of polyethylene glycol (PEG) compounds for cosmetic use,” *Toxicological Research*, 2015.
- [167] C. Fetsch, J. Gaitzsch, L. Messenger, G. Battaglia, and R. Luxenhofer, “Self-assembly of amphiphilic block copolypeptoids - Micelles, worms and polymersomes,” *Scientific Reports*, vol. 6, no. 1, p. 33491, Dec. 2016.
- [168] J. N. Israelachvili, “Soft and Biological Structures,” 2011.

- [169] J. Nicolas, S. Mura, D. Brambilla, N. Mackiewicz, and P. Couvreur, "Design, functionalization strategies and biomedical applications of targeted biodegradable/biocompatible polymer-based nanocarriers for drug delivery," *Chem. Soc. Rev.*, vol. 42, no. 3, pp. 1147–1235, 2013.
- [170] T. Smart, H. Lomas, M. Massignani, M. V. Flores-Merino, L. R. Perez, and G. Battaglia, "Block copolymer nanostructures," *Nano Today*, vol. 3, no. 3–4, pp. 38–46, Jun. 2008.
- [171] L. Guan, L. Rizzello, and G. Battaglia, "Polymersomes and their applications in cancer delivery and therapy," *Nanomedicine*, vol. 10, no. 17, pp. 2757–2780, Sep. 2015.
- [172] L. Rodríguez-Arco, A. Poma, L. Ruiz-Pérez, E. Scarpa, K. Ngamkham, and G. Battaglia, "Molecular bionics – engineering biomaterials at the molecular level using biological principles," *Biomaterials*, vol. 192, pp. 26–50, Feb. 2019.
- [173] S. D. Li and L. Huang, "Nanoparticles evading the reticuloendothelial system: Role of the supported bilayer," *Biochimica et Biophysica Acta - Biomembranes*, 2009.
- [174] Y. Zhao, D. Sultan, and Y. Liu, "Biodistribution, excretion, and toxicity of nanoparticles," in *Theranostic Bionanomaterials*, Elsevier, 2019, pp. 27–53.
- [175] F. Barbero *et al.*, "Formation of the Protein Corona: The Interface between Nanoparticles and the Immune System," *Seminars in Immunology*, vol. 34, pp. 52–60, Dec. 2017.
- [176] M. Lundqvist, J. Stigler, G. Elia, I. Lynch, T. Cedervall, and K. A. Dawson, "Nanoparticle size and surface properties determine the protein corona with possible implications for biological impacts," *Proceedings of the National Academy of Sciences of the United States of America*, vol. 105, no. 38, pp. 14265–14270, Sep. 2008.
- [177] and T. T. Lorena Simón-Gracia¹, Hedi Hunt¹, Pablo D. Scodeller^{1, 2}, Jens Gaitzsch³, 4, Gary B. Braun², Anne-Mari A. Willmore¹, Erkki Ruoslahti^{2, 5}, Giuseppe Battaglia^{3,*}, "Paclitaxel-loaded polymersomes for enhanced intraperitoneal chemotherapy," *molecular cancer thera*, vol. 97, no. 12, pp. 5421–5433, 2016.
- [178] H. E. Colley *et al.*, "Polymersome-mediated delivery of combination anticancer therapy to head and neck cancer cells: 2D and 3D in vitro evaluation," *Molecular Pharmaceutics*, vol. 11, no. 4, pp. 1176–1188, 2014.
- [179] V. M. Gouveia *et al.*, "Targeting Macrophages and Synoviocytes Intracellular Milieu to Augment Anti-Inflammatory Drug Potency," *Advanced Therapeutics*, vol. 5, no. 3, p. 2100167, Mar. 2022.
- [180] M. Massignani *et al.*, "Controlling cellular uptake by surface chemistry, size, and

- surface topology at the nanoscale,” *Small*, vol. 5, no. 21, pp. 2424–2432, 2009.
- [181] J. D. Robertson, J. R. Ward, M. Avila-Olias, G. Battaglia, and S. A. Renshaw, “Targeting Neutrophilic Inflammation Using Polymersome-Mediated Cellular Delivery,” *Journal of immunology (Baltimore, Md. : 1950)*, vol. 198, no. 9, pp. 3596–3604, 2017.
- [182] L. K. Mooberry, N. A. Sabnis, M. Panchoo, B. Nagarajan, and A. G. Lacko, “Targeting the SR-B1 receptor as a gateway for cancer therapy and imaging,” *Frontiers in Pharmacology*, vol. 7, no. DEC. Frontiers Media SA, 2016.
- [183] E. Berney, N. Sabnis, M. Panchoo, S. Raut, R. Dickerman, and A. G. Lacko, “The SR-B1 Receptor as a Potential Target for Treating Glioblastoma,” *Journal of Oncology*, vol. 2019, 2019.
- [184] B. Zimmerman *et al.*, “Crystal Structure of a Full-Length Human Tetraspanin Reveals a Cholesterol-Binding Pocket,” *Cell*, vol. 167, no. 4, pp. 1041–1051.e11, Nov. 2016.
- [185] S. Yalaoui *et al.*, “Hepatocyte permissiveness to Plasmodium infection is conveyed by a short and structurally conserved region of the CD81 large extracellular domain,” *PLoS Pathogens*, vol. 4, no. 2, p. e1000010, 2008.
- [186] T. H. Heo, S. M. Lee, B. Bartosch, F. L. Cosset, and C. Y. Kang, “Hepatitis C virus E2 links soluble human CD81 and SR-B1 protein,” *Virus Research*, vol. 121, no. 1, pp. 58–64, Oct. 2006.
- [187] S. Acosta-Gutiérrez *et al.*, “A Multiscale Study of Phosphorylcholine Driven Cellular Phenotypic Targeting,” *ACS Central Science*, 2022.
- [188] J. V. M. Weaver *et al.*, “Stimulus-Responsive Water-Soluble Polymers Based on 2-Hydroxyethyl Methacrylate,” *Macromolecules*, vol. 37, no. 7, pp. 2395–2403, Apr. 2004.
- [189] L. A. Fielding, S. Edmondson, and S. P. Armes, “Synthesis of pH-responsive tertiary amine methacrylate polymer brushes and their response to acidic vapour,” *Journal of Materials Chemistry*, 2011.
- [190] I. Canton *et al.*, “Fully synthetic polymer vesicles for intracellular delivery of antibodies in live cells,” *FASEB Journal*, vol. 27, no. 1, pp. 98–108, 2013.
- [191] D. A. Christian, S. Cai, D. M. Bowen, Y. Kim, J. D. Pajerowski, and D. E. Discher, “Polymersome carriers: From self-assembly to siRNA and protein therapeutics,” *European Journal of Pharmaceutics and Biopharmaceutics*, vol. 71, no. 3, pp. 463–474, Mar. 2009.
- [192] D. E. Discher *et al.*, “Emerging Applications of Polymersomes in Delivery: from

- Molecular Dynamics to Shrinkage of Tumors,” *Progress in polymer science*, vol. 32, no. 8–9, p. 838, Aug. 2007.
- [193] M. Massignani *et al.*, “Controlling Cellular Uptake by Surface Chemistry, Size, and Surface Topology at the Nanoscale,” *Small*, vol. 5, no. 21, pp. 2424–2432, Nov. 2009.
- [194] Y. B. Hu, E. B. Dammer, R. J. Ren, and G. Wang, “The endosomal-lysosomal system: from acidification and cargo sorting to neurodegeneration,” *Translational Neurodegeneration*, vol. 4, no. 1, Sep. 2015.
- [195] J. Du, Y. Tang, A. L. Lewis, and S. P. Armes, “pH-sensitive vesicles based on a biocompatible zwitterionic diblock copolymer,” *Journal of the American Chemical Society*, vol. 127, no. 51, pp. 17982–3, Dec. 2005.
- [196] L. Rizzello *et al.*, “Targeting mononuclear phagocytes for eradicating intracellular parasites,” *bioRxiv*, p. 119297, Mar. 2017.
- [197] H. Lomas *et al.*, “Biomimetic pH Sensitive Polymersomes for Efficient DNA Encapsulation and Delivery,” *Advanced Materials*, 2007.
- [198] S. N. S. Alconcel, A. S. Baas, and H. D. Maynard, “FDA-approved poly(ethylene glycol)–protein conjugate drugs,” *Polymer Chemistry*, vol. 2, no. 7, p. 1442, Jun. 2011.
- [199] Y. Barenholz, “Doxil® — The First FDA-Approved Nano-Drug,” in *Handbook of Harnessing Biomaterials in Nanomedicine*, Pan Stanford Publishing, 2012, pp. 335–398.
- [200] J. Wang *et al.*, “Poly(ethylene glycol)-polylactide micelles for cancer therapy,” *Frontiers in Pharmacology*, vol. 9, no. MAR. Frontiers Media SA, p. 202, 08-Mar-2018.
- [201] D. Garlotta, “A Literature Review of Poly(Lactic Acid),” *Journal of Polymers and the Environment*, vol. 9, no. 2, 2001.
- [202] X. Meng, Z. Zhang, J. Tong, H. Sun, J. P. Fawcett, and J. Gu, “The biological fate of the polymer nanocarrier material monomethoxy poly(ethylene glycol)-block-poly(D,L-lactic acid) in rat,” *Acta Pharmaceutica Sinica B*, vol. 11, no. 4, pp. 1003–1009, Apr. 2021.
- [203] Q. Yang and S. K. Lai, “Anti-PEG immunity: Emergence, characteristics, and unaddressed questions,” *Wiley Interdisciplinary Reviews: Nanomedicine and Nanobiotechnology*, vol. 7, no. 5, pp. 655–677, Sep. 2015.
- [204] T. T. H. Thi, E. H. Pilkington, D. H. Nguyen, J. S. Lee, K. D. Park, and N. P. Truong, “The Importance of Poly(ethylene glycol) Alternatives for Overcoming PEG Immunogenicity in Drug Delivery and Bioconjugation,” *Polymers*, vol. 12, no. 2, Feb. 2020.

- [205] R. P. Garay, R. El-Gewely, J. K. Armstrong, G. Garratty, and P. Richette, "Antibodies against polyethylene glycol in healthy subjects and in patients treated with PEG-conjugated agents," *Expert Opinion on Drug Delivery*, vol. 9, no. 11, pp. 1319–1323, Nov. 2012.
- [206] T. Shimizu *et al.*, "A hydroxyl PEG version of PEGylated liposomes and its impact on anti-PEG IgM induction and on the accelerated clearance of PEGylated liposomes," *European Journal of Pharmaceutics and Biopharmaceutics*, vol. 127, pp. 142–149, Jun. 2018.
- [207] D. Schmid *et al.*, "T cell-targeting nanoparticles focus delivery of immunotherapy to improve antitumor immunity," *Nature Communications*, vol. 8, no. 1, p. 1747, Dec. 2017.
- [208] N. Gong, N. C. Sheppard, M. M. Billingsley, C. H. June, and M. J. Mitchell, "Nanomaterials for T-cell cancer immunotherapy," *Nature Nanotechnology* 2021 16:1, vol. 16, no. 1, pp. 25–36, Jan. 2021.
- [209] T. Curk, J. Dobnikar, and D. Frenkel, "Design Principles for Super Selectivity using Multivalent Interactions," in *Multivalency*, Chichester, UK: John Wiley & Sons, Ltd, 2017, pp. 75–101.
- [210] B. E. Collins and J. C. Paulson, "Cell surface biology mediated by low affinity multivalent protein-glycan interactions," *Current Opinion in Chemical Biology*, vol. 8, no. 6. Elsevier Current Trends, pp. 617–625, 01-Dec-2004.
- [211] G. Vauquelin and S. J. Charlton, "Exploring avidity: understanding the potential gains in functional affinity and target residence time of bivalent and heterobivalent ligands Correspondence," 2013.
- [212] A. M. J. J. Bonvin and P. L. Kastiris, "On the binding affinity of macromolecular interactions: daring to ask why proteins interact."
- [213] T. P. Kenakin, *A pharmacology primer: Theory, application and methods*. 2009.
- [214] M. S. Salahudeen and P. S. Nishtala, "An overview of pharmacodynamic modelling, ligand-binding approach and its application in clinical practice," *Saudi Pharmaceutical Journal*, vol. 25, no. 2. Elsevier, pp. 165–175, 01-Feb-2017.
- [215] J. D. Byrne, T. Betancourt, and L. Brannon-Peppas, "Active targeting schemes for nanoparticle systems in cancer therapeutics," *Advanced Drug Delivery Reviews*. 2008.
- [216] F. J. Martinez-Veracoechea and D. Frenkel, "Designing super selectivity in multivalent nano-particle binding.," *Proceedings of the National Academy of Sciences of the*

- United States of America*, vol. 108, no. 27, pp. 10963–8, Jul. 2011.
- [217] X. Tian, S. Angioletti-Uberti, and G. Battaglia, “On the design of precision nanomedicines,” *Science Advances*, vol. 6, no. 4, p. eaat0919, Jan. 2020.
- [218] M. Mammen, S. K. Choi, and G. M. Whitesides, “Polyvalent interactions in biological systems: Implications for design and use of multivalent ligands and inhibitors,” *Angewandte Chemie - International Edition*, vol. 37, no. 20, pp. 2754–2794, 1998.
- [219] C. B. Calson, P. Mowery, R. M. Owen, E. C. Dykhuizen, and L. L. Kiessling, “Selective tumor cell targeting using low-affinity, multivalent interactions,” *ACS Chemical Biology*, vol. 2, no. 2, pp. 119–127, Feb. 2007.
- [220] J. Wang, J. Min, A. Egtesadi, R. S. Kane, and A. Chilkoti, “Quantitative Study of the Interaction of Multivalent Ligand-Modified Nanoparticles with Breast Cancer Cells with Tunable Receptor Density Article,” *ACS Nano*, vol. 14, p. 39, 2020.
- [221] X. Tian, S. Angioletti-Uberti, and G. Battaglia, “On the design of precision nanomedicines,” *Science Advances*, vol. 6, no. 4, p. eaat0919, Jan. 2020.
- [222] A. S. Zeiger, F. C. Loe, R. Li, M. Raghunath, and K. J. van Vliet, “Macromolecular crowding directs extracellular matrix organization and mesenchymal stem cell behavior,” *PLoS ONE*, vol. 7, no. 5, p. 37904, May 2012.
- [223] M. E. Griffin and L. C. Hsieh-Wilson, “Glycan Engineering for Cell and Developmental Biology,” *Cell Chemical Biology*, vol. 23, no. 1. NIH Public Access, pp. 108–121, 01-Jan-2016.
- [224] E. R. Cruz-Chu, A. Malafeev, T. Pajarskas, I. V Pivkin, and P. Koumoutsakos, “Structure and response to flow of the glycocalyx layer,” *Biophysical Journal*, vol. 106, no. 1, pp. 232–243, 2014.
- [225] X. Tian *et al.*, “LRP-1-mediated intracellular antibody delivery to the Central Nervous System,” *Scientific reports*, vol. 5, p. 11990, Jul. 2015.
- [226] M. Liu *et al.*, “Combinatorial entropy behaviour leads to range selective binding in ligand-receptor interactions,” *Nature Communications*, vol. 11, no. 1, p. 4836, Dec. 2020.
- [227] I. Melero, A. Rouzaut, G. T. Motz, and G. Coukos, “T-cell and NK-cell infiltration into solid tumors: A key limiting factor for efficacious cancer immunotherapy,” *Cancer Discovery*, vol. 4, no. 5, pp. 522–526, 2014.
- [228] T. Ohkuri *et al.*, “Intratumoral administration of cGAMP transiently accumulates potent macrophages for anti-tumor immunity at a mouse tumor site,” *Cancer immunology, immunotherapy: CII*, vol. 66, no. 6, pp. 705–716, Jun. 2017.

- [229] N. Desai *et al.*, “Increased antitumor activity, intratumor paclitaxel concentrations, and endothelial cell transport of cremophor-free, albumin-bound paclitaxel, ABI-007, compared with cremophor-based paclitaxel,” *Clinical Cancer Research*, vol. 12, no. 4, pp. 1317–1324, Feb. 2006.
- [230] B. L. Voth *et al.*, “Intratumor injection of CCL21-coupled vault nanoparticles is associated with reduction in tumor volume in an in vivo model of glioma,” *Journal of Neuro-Oncology*, vol. 147, no. 3, pp. 599–605, May 2020.
- [231] A. Marabelle *et al.*, “Starting the fight in the tumor: Expert recommendations for the development of human intratumoral immunotherapy (HIT-IT),” *Annals of Oncology*, vol. 29, no. 11, pp. 2163–2174, Nov. 2018.
- [232] K. Kabashima, T. Honda, F. Ginhoux, and G. Egawa, “The immunological anatomy of the skin,” *Nature Reviews Immunology*, vol. 19, no. 1. Nat Rev Immunol, pp. 19–30, 01-Jan-2019.
- [233] C. Levin, H. Perrin, and B. Combadiere, “Tailored immunity by skin antigen-presenting cells,” in *Human Vaccines and Immunotherapeutics*, 2015.
- [234] E. E. Kis, G. Winter, and J. Myschik, “Devices for intradermal vaccination,” *Vaccine*, vol. 30, no. 3, pp. 523–538, Jan. 2012.
- [235] E. Larrañeta, R. E. M. Lutton, A. D. Woolfson, and R. F. Donnelly, “Microneedle arrays as transdermal and intradermal drug delivery systems: Materials science, manufacture and commercial development,” *Materials Science and Engineering R: Reports*, vol. 104. Elsevier, pp. 1–32, 01-Jun-2016.
- [236] S. Hamdy *et al.*, “Co-delivery of cancer-associated antigen and Toll-like receptor 4 ligand in PLGA nanoparticles induces potent CD8+ T cell-mediated anti-tumor immunity,” *Vaccine*, vol. 26, no. 39, pp. 5046–5057, Sep. 2008.
- [237] H. Feinberg, A. S. Powlesland, M. E. Taylor, and W. I. Weis, “Trimeric Structure of Langerin,” 2010.
- [238] R. Mc Dermott *et al.*, “Birbeck granules are subdomains of endosomal recycling compartment in human epidermal Langerhans cells, which form where Langerin accumulates,” *Molecular biology of the cell*, vol. 13, no. 1, pp. 317–35, Jan. 2002.
- [239] M. van der Vlist and T. B. H. Geijtenbeek, “Langerin functions as an antiviral receptor on Langerhans cells,” *Immunology and Cell Biology*, vol. 88, no. 4, pp. 410–415, May 2010.
- [240] P. Stoitzner *et al.*, “Langerhans cells cross-present antigen derived from skin,” 2006.
- [241] V. Flacher, F. Sparber, C. H. Tripp, N. Romani, and P. Stoitzner, “Targeting of

- epidermal Langerhans cells with antigenic proteins: attempts to harness their properties for immunotherapy,” *Cancer Immunology, Immunotherapy*, vol. 58, no. 7, pp. 1137–1147, Jul. 2009.
- [242] R. L. Sabado, S. Balan, and N. Bhardwaj, “Dendritic cell-based immunotherapy,” *Cell Research*, vol. 27, no. 1, pp. 74–95, Jan. 2017.
- [243] L. De Witte *et al.*, “Langerin is a natural barrier to HIV-1 transmission by Langerhans cells,” *Nature Medicine*, vol. 13, no. 3, pp. 367–371, Mar. 2007.
- [244] E. C. Wamhoff *et al.*, “A Specific, Glycomimetic Langerin Ligand for Human Langerhans Cell Targeting,” *ACS Central Science*, vol. 5, no. 5, pp. 808–820, May 2019.
- [245] L. East and C. M. Isacke, “The mannose receptor family,” *Biochimica et Biophysica Acta - General Subjects*, vol. 1572, no. 2–3, Elsevier, pp. 364–386, 19-Sep-2002.
- [246] A. Wollenberg, M. Mommaas, T. Oppel, E. M. Schottdorf, S. Günther, and M. Moderer, “Expression and function of the mannose receptor CD206 on epidermal dendritic cells in inflammatory skin diseases,” *The Journal of investigative dermatology*, vol. 118, no. 2, pp. 327–334, 2002.
- [247] A. P. Moseman *et al.*, “Mannose Receptor 1 Mediates Cellular Uptake and Endosomal Delivery of CpG-Motif Containing Oligodeoxynucleotides,” *The Journal of Immunology*, vol. 191, no. 11, pp. 5615–5624, Dec. 2013.
- [248] P. R. Taylor, L. Martinez-Pomares, M. Stacey, H. H. Lin, G. D. Brown, and S. Gordon, “Macrophage receptors and immune recognition,” *Annual Review of Immunology*, vol. 23, Annual Reviews, pp. 901–944, 27-Sep-2005.
- [249] S. Gordon and F. O. Martinez, “Alternative activation of macrophages: Mechanism and functions,” *Immunity*, vol. 32, no. 5, Immunity, pp. 593–604, May-2010.
- [250] P. B. Wright *et al.*, “The mannose receptor (CD206) identifies a population of colonic macrophages in health and inflammatory bowel disease,” *Scientific Reports*, vol. 11, no. 1, pp. 1–12, Oct. 2021.
- [251] P. D. Stahl and R. A. B. Ezekowitz, “The mannose receptor is a pattern recognition receptor involved in host defense,” *Current Opinion in Immunology*, vol. 10, no. 1, pp. 50–55, Feb. 1998.
- [252] J. M. Jaynes *et al.*, “Mannose receptor (CD206) activation in tumor-associated macrophages enhances adaptive and innate antitumor immune responses,” *Science Translational Medicine*, vol. 12, no. 530, Feb. 2020.
- [253] I. A. Zani *et al.*, “Scavenger receptor structure and function in health and disease,”

- Cells*, vol. 4, no. 2. Multidisciplinary Digital Publishing Institute (MDPI), pp. 178–201, 22-May-2015.
- [254] A. Rigotti, B. L. Trigatti, M. Penman, H. Rayburn, J. Herz, and M. Krieger, “A targeted mutation in the murine gene encoding the high density lipoprotein (HDL) receptor scavenger receptor class B type I reveals its key role in HDL metabolism,” *Proceedings of the National Academy of Sciences of the United States of America*, vol. 94, no. 23, pp. 12610–12615, Nov. 1997.
- [255] M. S. Brown and J. L. Goldstein, “A receptor-mediated pathway for cholesterol homeostasis,” *Science*, vol. 232, no. 4746, pp. 34–47, 1986.
- [256] E. Scarselli *et al.*, “The human scavenger receptor class B type I is a novel candidate receptor for the hepatitis C virus,” *The EMBO Journal*, vol. 21, no. 19, pp. 5017–5025, Oct. 2002.
- [257] M. B. Zeisel *et al.*, “Scavenger receptor class B type I is a key host factor for hepatitis C virus infection required for an entry step closely linked to CD81,” *Hepatology*, vol. 46, no. 6, pp. 1722–1731, Dec. 2007.
- [258] W.-J. Shen, S. Azhar, and F. B. Kraemer, “SR-B1: A Unique Multifunctional Receptor for Cholesterol Influx and Efflux,” *Annual Review of Physiology*, vol. 80, no. 1, pp. 95–116, Feb. 2018.
- [259] H. Potter and R. Heller, “Transfection by Electroporation,” *Current protocols in molecular biology / edited by Frederick M. Ausubel ... [et al.]*, vol. CHAPTER, no. SUPPL. 92, p. Unit, Oct. 2003.
- [260] MALVERN, “Zetasizer Nano Series: Research Performance, Operational Simplicity, Application Versatility,” *Malvern Instruments*, p. 20, 2014.
- [261] “Dynamic Light Scattering: An Introduction.”
- [262] L. Instruments, “Dynamic Light Scattering (DLS).” [Online]. Available: <https://lsinstruments.ch/en/technology/dynamic-light-scattering-dls>. [Accessed: 16-Jan-2020].
- [263] K. Canene-Adams, “Reverse-phase HPLC Analysis and Purification of Small Molecules,” *Methods in Enzymology*, vol. 533, pp. 291–301, Jan. 2013.
- [264] L. Wang *et al.*, “Encapsulation of Biomacromolecules within Polymersomes by Electroporation,” *Angewandte Chemie*, 2012.
- [265] S. T. Hyde, “Microstructure of bicontinuous surfactant aggregates,” *Journal of physical chemistry*, vol. 93, no. 4, pp. 1458–1464, 1989.
- [266] T. J. Vaughan *et al.*, “Human Antibodies with Sub-nanomolar Affinities Isolated from

- a Large Non-immunized Phage Display Library,” *Nature Biotechnology*, vol. 14, no. 3, pp. 309–314, Mar. 1996.
- [267] C. Lloyd *et al.*, “Modelling the human immune response: performance of a 1011 human antibody repertoire against a broad panel of therapeutically relevant antigens,” *Protein Engineering Design and Selection*, vol. 22, no. 3, pp. 159–168, Oct. 2008.
- [268] K. S. Lee *et al.*, “Multicenter phase II trial of Genexol-PM, a Cremophor-free, polymeric micelle formulation of paclitaxel, in patients with metastatic breast cancer,” *Breast cancer research and treatment*, vol. 108, no. 2, pp. 241–250, Mar. 2008.
- [269] F. Amblard, J. H. Cho, and R. F. Schinazi, “The Cu(I)-catalyzed Huisgen azide-alkyne 1,3-dipolar cycloaddition reaction in nucleoside, nucleotide and oligonucleotide chemistry,” *Chemical reviews*, vol. 109, no. 9, p. 4207, Sep. 2009.
- [270] L. A. Voloboueva, J. Liu, J. H. Suh, B. N. Ames, and S. S. Miller, “(R)-alpha-lipoic acid protects retinal pigment epithelial cells from oxidative damage.,” *Investigative ophthalmology & visual science*, vol. 46, no. 11, pp. 4302–10, Nov. 2005.
- [271] A. Rhule, B. Rase, J. R. Smith, and D. M. Shepherd, “Toll-like receptor ligand-induced activation of murine DC2.4 cells is attenuated by Panax notoginseng.,” *Journal of ethnopharmacology*, vol. 116, no. 1, pp. 179–86, Feb. 2008.
- [272] H. T. Maecker and J. Trotter, “Flow cytometry controls, instrument setup, and the determination of positivity,” *Cytometry Part A*, vol. 69A, no. 9, pp. 1037–1042, Sep. 2006.
- [273] Š. Belický, J. Katrlík, and J. Tkáč, “Glycan and lectin biosensors,” *Essays in Biochemistry*, vol. 60, no. 1, pp. 37–47, Jun. 2016.
- [274] R. D. Cummings and M. E. Etzler, *Antibodies and Lectins in Glycan Analysis*. Cold Spring Harbor Laboratory Press, 2009.
- [275] A. Lopes, G. Vandermeulen, and V. Pr  at, “Cancer DNA vaccines: current preclinical and clinical developments and future perspectives,” *Journal of Experimental & Clinical Cancer Research*, vol. 38, no. 1, p. 146, Dec. 2019.
- [276] M. E. Gatti-Mays, J. M. Redman, J. M. Collins, and M. Bilusic, “Cancer vaccines: Enhanced immunogenic modulation through therapeutic combinations,” *Human Vaccines and Immunotherapeutics*, vol. 13, no. 11. Taylor & Francis, pp. 2561–2574, 02-Nov-2017.
- [277] A. Tiptiri-Kourpeti, K. Spyridopoulou, A. Pappa, and K. Chlichlia, “DNA vaccines to attack cancer: Strategies for improving immunogenicity and efficacy,” *Pharmacology and Therapeutics*, vol. 165, pp. 32–49, Sep. 2016.

- [278] C. Contini *et al.*, “Bottom-Up Evolution of Vesicles from Disks to High-Genus Polymersomes,” *iScience*, vol. 7, pp. 132–144, Sep. 2018.
- [279] Z. Tang, T. Takarada, and M. Maeda, “Non-Cross-Linking Aggregation of DNA-Carrying Polymer Micelles Triggered by Duplex Formation,” *Langmuir: the ACS journal of surfaces and colloids*, vol. 34, no. 49, pp. 14899–14910, Dec. 2018.
- [280] D. Gudnason, M. Madsen, A. Krissanaprasit, K. V. Gothelf, and V. Birkedal, “Controlled aggregation of DNA functionalized poly(phenylene-vinylene),” *Chemical Communications*, vol. 54, no. 44, pp. 5534–5537, May 2018.
- [281] T. Catherall, D. Huskisson, S. McAdams, and A. Vijayaraghavan, “Self-assembly of one dimensional DNA-templated structures,” *Journal of Materials Chemistry C*, vol. 2, no. 34, pp. 6895–6920, Aug. 2014.
- [282] Hanying Li, Sung Ha Park, John H. Reif, * and Thomas H. LaBean, and H. Yan*, “DNA-Templated Self-Assembly of Protein and Nanoparticle Linear Arrays,” *Journal of the American Chemical Society*, vol. 126, no. 2, pp. 418–419, Jan. 2003.
- [283] D. R. Latulippe and A. L. Zydney, “Size exclusion chromatography of plasmid DNA isoforms,” *Journal of Chromatography A*, vol. 1216, no. 35, pp. 6295–6302, Aug. 2009.
- [284] P. B. Tchounwou, C. Newsome, J. Williams, and K. Glass, “Copper-Induced Cytotoxicity and Transcriptional Activation of Stress Genes in Human Liver Carcinoma (HepG(2)) Cells,” *International Symposium on Metal Ions in Biology and Medicine*, vol. 10, pp. 285–290, 2008.
- [285] R. Di Blasi, M. M. Marbiah, V. Siciliano, K. Polizzi, and F. Ceroni, “A call for caution in analysing mammalian co-transfection experiments and implications of resource competition in data misinterpretation,” *Nature Communications* 2021 12:1, vol. 12, no. 1, pp. 1–6, May 2021.
- [286] L. L. Lesueur, L. M. Mir, and F. M. André, “Overcoming the Specific Toxicity of Large Plasmids Electrotransfer in Primary Cells In Vitro,” *Molecular Therapy. Nucleic Acids*, vol. 5, no. 3, p. e291, 2016.
- [287] D. A. Dean, D. D. Strong, and W. E. Zimmer, “Nuclear entry of nonviral vectors,” *Gene Therapy*, vol. 12, no. 11. Nature Publishing Group, pp. 881–890, 28-Apr-2005.
- [288] A. Elouahabi and J. M. Ruysschaert, “Formation and intracellular trafficking of lipoplexes and polyplexes,” *Molecular Therapy*, vol. 11, no. 3. Elsevier, pp. 336–347, 01-Mar-2005.
- [289] C. Gonçalves, F. Gross, P. Guégan, H. Cheradame, and P. Midou, “A robust transfection reagent for the transfection of CHO and HEK293 cells and production of

- recombinant proteins and lentiviral particles - PTG1," *Biotechnology journal*, vol. 9, no. 11, pp. 1380–1388, Nov. 2014.
- [290] Y. Fu *et al.*, "Inhibition of cGAS-Mediated Interferon Response Facilitates Transgene Expression," *iScience*, vol. 23, no. 4, Apr. 2020.
- [291] E. Renaud-Gabardos, F. Hantelys, F. Morfoisse, X. Chaufour, B. Garmy-Susini, and A.-C. Prats, "Internal ribosome entry site-based vectors for combined gene therapy," *World Journal of Experimental Medicine*, vol. 5, no. 1, p. 11, 2015.
- [292] T. F. Gajewski, H. Schreiber, and Y. X. Fu, "Innate and adaptive immune cells in the tumor microenvironment," *Nature Immunology*. 2013.
- [293] R. Kim, "Cancer Immunoediting: From Immune Surveillance to Immune Escape," *Cancer Immunotherapy*, pp. 9–27, 2007.
- [294] S. R. Woo *et al.*, "STING-dependent cytosolic DNA sensing mediates innate immune recognition of immunogenic tumors," *Immunity*, vol. 41, no. 5, pp. 830–842, Nov. 2014.
- [295] J. Wu *et al.*, "Cyclic GMP-AMP is an endogenous second messenger in innate immune signaling by cytosolic DNA," *Science*, vol. 339, no. 6121, pp. 826–830, Feb. 2013.
- [296] J. Nam, S. Son, K. S. Park, W. Zou, L. D. Shea, and J. J. Moon, "Cancer nanomedicine for combination cancer immunotherapy," *Nature Reviews Materials*, vol. 4, no. 6. Nature Publishing Group, pp. 398–414, 26-Apr-2019.
- [297] D. R. Wilson, R. Sen, J. C. Sunshine, D. M. Pardoll, J. J. Green, and Y. J. Kim, "Biodegradable STING agonist nanoparticles for enhanced cancer immunotherapy," *Nanomedicine: Nanotechnology, Biology and Medicine*, vol. 14, no. 2, pp. 237–246, 2018.
- [298] T. Li *et al.*, "Antitumor Activity of cGAMP via Stimulation of cGAS-cGAMP-STING-IRF3 Mediated Innate Immune Response," *Scientific Reports 2016 6:1*, vol. 6, no. 1, pp. 1–14, Jan. 2016.
- [299] D. Shae *et al.*, "Endosomolytic polymersomes increase the activity of cyclic dinucleotide STING agonists to enhance cancer immunotherapy," *Nature Nanotechnology*, 2019.
- [300] B. Pulendran, P. S. Arunachalam, and D. T. O'Hagan, "Emerging concepts in the science of vaccine adjuvants," *Nature Reviews Drug Discovery 2021 20:6*, vol. 20, no. 6, pp. 454–475, Apr. 2021.
- [301] M. Luo *et al.*, "A STING-activating nanovaccine for cancer immunotherapy.," *Nature nanotechnology*, vol. 12, no. 7, pp. 648–654, Jul. 2017.
- [302] S. Van Herck, B. Feng, and L. Tang, "Delivery of STING agonists for adjuvanting

- subunit vaccines,” *Advanced Drug Delivery Reviews*, vol. 179, p. 114020, Dec. 2021.
- [303] J. Fu *et al.*, “STING agonist formulated cancer vaccines can cure established tumors resistant to PD-1 blockade,” *Science Translational Medicine*, 2015.
- [304] T. Tanaka, M. Narazaki, and T. Kishimoto, “IL-6 in inflammation, immunity, and disease,” *Cold Spring Harbor perspectives in biology*, vol. 6, no. 10, p. a016295, Sep. 2014.
- [305] M. Rincon-Restrepo *et al.*, “Vaccine nanocarriers: Coupling intracellular pathways and cellular biodistribution to control CD4 vs CD8 T cell responses,” *Biomaterials*, vol. 132, pp. 48–58, 2017.
- [306] S. Elmore, “Apoptosis: a review of programmed cell death,” *Toxicologic pathology*, 2007.
- [307] C. H. A. Tang *et al.*, “Agonist-mediated activation of STING induces apoptosis in malignant B cells,” *Cancer research*, vol. 76, no. 8, p. 2137, Apr. 2016.
- [308] S. S. Wright, S. O. Vasudevan, and V. A. Rathinam, “Mechanisms and Consequences of Noncanonical Inflammasome-Mediated Pyroptosis,” *Journal of Molecular Biology*, vol. 434, no. 4, p. 167245, Feb. 2022.
- [309] S. Yokoyama *et al.*, “A novel pathway of LPS uptake through syndecan-1 leading to pyroptotic cell death,” *eLife*, vol. 7, Dec. 2018.
- [310] L. A. Harshyne, M. I. Zimmer, S. C. Watkins, and S. M. Barratt-Boyes, “A Role for Class A Scavenger Receptor in Dendritic Cell Nibbling from Live Cells,” *The Journal of Immunology*, vol. 170, no. 5, pp. 2302–2309, Mar. 2003.
- [311] P. Scodeller *et al.*, “Precision Targeting of Tumor Macrophages with a CD206 Binding Peptide,” *Scientific Reports*, vol. 7, no. 1, Dec. 2017.
- [312] E. K. Asciutto *et al.*, “Phage-Display-Derived Peptide Binds to Human CD206 and Modeling Reveals a New Binding Site on the Receptor,” *Journal of Physical Chemistry B*, vol. 123, no. 9, pp. 1973–1982, 2019.
- [313] A. Lepland *et al.*, “Targeting Pro-Tumoral Macrophages in Early Primary and Metastatic Breast Tumors with the CD206-Binding mUNO Peptide,” *Molecular Pharmaceutics*, vol. 17, no. 7, pp. 2518–2531, Jul. 2020.
- [314] Y. Tada *et al.*, “Identification and Characterization of Endogenous Langerin Ligands in Murine Extracellular Matrix,” *Journal of Investigative Dermatology*, vol. 126, no. 7, pp. 1549–1558, Jul. 2006.
- [315] T. He, C. Tang, S. Xu, T. Moyana, and J. Xiang, “Interferon γ Stimulates Cellular Maturation of Dendritic Cell Line DC2.4 Leading to Induction of Efficient Cytotoxic T

- Cell Responses and Antitumor Immunity,” 2007.
- [316] D. G. Waller and A. P. Sampson, “Principles of pharmacology and mechanisms of drug action,” in *Medical Pharmacology and Therapeutics*, Elsevier, 2018, pp. 3–31.
 - [317] Y. Yang, X. Wang, X. Hu, N. Kawazoe, Y. Yang, and G. Chen, “Influence of Cell Morphology on Mesenchymal Stem Cell Transfection,” *ACS applied materials & interfaces*, vol. 11, no. 2, pp. 1932–1941, Jan. 2019.
 - [318] A. Lepland *et al.*, “Depletion of Mannose Receptor-Positive Tumor-Associated Macrophages via a Peptide-Targeted Star-Shaped Polyglutamate Inhibits Breast Cancer Progression in Mice,” *Cancer Research Communications*, vol. 2, no. 6, pp. 533–551, Jun. 2022.
 - [319] M. Rincon-Restrepo *et al.*, “Vaccine nanocarriers: Coupling intracellular pathways and cellular biodistribution to control CD4 vs CD8 T cell responses,” *Biomaterials*, vol. 132, pp. 48–58, Jul. 2017.
 - [320] K. Palucka and J. Banchereau, “Dendritic-cell-based therapeutic cancer vaccines.,” *Immunity*, vol. 39, no. 1, pp. 38–48, Jul. 2013.
 - [321] C. J. M. Melief, T. Van Hall, R. Arens, F. Ossendorp, and S. H. Van Der Burg, “Therapeutic cancer vaccines,” *The Journal of Clinical Investigation*, vol. 125, no. 9, p. 3401, Sep. 2015.
 - [322] A. Jo *et al.*, “Fabrication and characterization of PLGA nanoparticles encapsulating large CRISPR-Cas9 plasmid,” *Journal of Nanobiotechnology*, vol. 18, no. 1, pp. 1–14, Jan. 2020.
 - [323] J. D. Clogston and A. K. Patri, “Zeta Potential Measurement,” in *Methods in molecular biology (Clifton, N.J.)*, vol. 697, 2011, pp. 63–70.
 - [324] E. Fröhlich, “Action of Nanoparticles on Platelet Activation and Plasmatic Coagulation,” *Current Medicinal Chemistry*, vol. 23, no. 5, p. 408, Jan. 2016.
 - [325] E. Fröhlich, “The role of surface charge in cellular uptake and cytotoxicity of medical nanoparticles,” *International Journal of Nanomedicine*, vol. 7, p. 5577, 2012.
 - [326] M. Weiss *et al.*, “Density of surface charge is a more predictive factor of the toxicity of cationic carbon nanoparticles than zeta potential,” *Journal of Nanobiotechnology*, vol. 19, no. 1, pp. 1–19, Dec. 2021.
 - [327] F. Cardarelli *et al.*, “The intracellular trafficking mechanism of Lipofectamine-based transfection reagents and its implication for gene delivery,” 2016.
 - [328] R. Maurisse *et al.*, “Comparative transfection of DNA into primary and transformed mammalian cells from different lineages,” *BMC Biotechnology*, vol. 10, no. 1, pp. 1–9,

Feb. 2010.

- [329] T. W. Dubensky, D. B. Kanne, and M. L. Leong, "Rationale, progress and development of vaccines utilizing STING-activating cyclic dinucleotide adjuvants," *Therapeutic Advances in Vaccines*, vol. 1, no. 4, pp. 131–143, Nov. 2013.
- [330] O. Demaria *et al.*, "STING activation of tumor endothelial cells initiates spontaneous and therapeutic antitumor immunity," *Proceedings of the National Academy of Sciences of the United States of America*, vol. 112, no. 50, pp. 15408–15413, Dec. 2015.
- [331] A. Mahashur, P. Thomas, P. Mehta, K. Nivangune, S. Muchhala, and R. Jain, "Pidotimod: In-depth review of current evidence," *Lung India: Official Organ of Indian Chest Society*, vol. 36, no. 5, p. 422, Sep. 2019.
- [332] X. Hu *et al.*, "The detailed analysis of the changes of murine dendritic cells (DCs) induced by thymic peptide: Pidotimod(PTD)," *Human Vaccines and Immunotherapeutics*, vol. 8, no. 9, pp. 1250–1258, Sep. 2012.
- [333] M. Cheng *et al.*, "Phosphatidylcholine regulates NF- κ B activation in attenuation of LPS-induced inflammation: evidence from in vitro study," *Animal Cells and Systems*, vol. 22, no. 1, pp. 7–14, 2018.
- [334] W. M. Schneider, M. D. Chevillotte, and C. M. Rice, "Interferon-stimulated genes: A complex web of host defenses," *Annual Review of Immunology*, vol. 32. NIH Public Access, pp. 513–545, 2014.
- [335] K. V. Swanson *et al.*, "A noncanonical function of cGAMP in inflammasome priming and activation," *Journal of Experimental Medicine*, vol. 214, no. 12, pp. 3611–3262, Dec. 2017.
- [336] S. L. Fink and B. T. Cookson, "Caspase-1-dependent pore formation during pyroptosis leads to osmotic lysis of infected host macrophages," *Journal of Immunology*, vol. 202, no. 7, pp. 1913–1926, Jul. 2006.
- [337] K. H. Lee and T. B. Kang, "The molecular links between cell death and inflammasome," *Cells*, vol. 8, no. 9, Sep. 2019.
- [338] D. Zheng, T. Liwinski, and E. Elinav, "Inflammasome activation and regulation: toward a better understanding of complex mechanisms," *Cell Discovery*, vol. 6, no. 1. Nature Publishing Group, pp. 1–22, 09-Jun-2020.
- [339] C. Panke *et al.*, "Quantification of cell surface proteins with bispecific antibodies," *Protein Engineering, Design and Selection*, vol. 26, no. 10, pp. 645–654, Oct. 2013.
- [340] C. Lopresti *et al.*, "Controlling polymersome surface topology at the nanoscale by

membrane confined polymer/polymer phase separation,” *ACS Nano*, vol. 5, no. 3, pp. 1775–1784, Mar. 2011.